

Anomalous Microwave Emission: Theory, Modeling, and Observations

Guest Editors: Clive Dickinson, Roberta Paladini, and Laurent Verstraete





Anomalous Microwave Emission: Theory, Modeling, and Observations

Advances in Astronomy

Anomalous Microwave Emission: Theory, Modeling, and Observations

Guest Editors: Clive Dickinson, Roberta Paladini,
and Laurent Verstraete



Copyright © 2013 Hindawi Publishing Corporation. All rights reserved.

This is a special issue published in “Advances in Astronomy.” All articles are open access articles distributed under the Creative Commons Attribution License, which permits unrestricted use, distribution, and reproduction in any medium, provided the original work is properly cited.

Editorial Board

Joshua S. Bloom, USA
Michael Brotherton, USA
Alberto J. Castro-Tirado, Spain
Michael Disney, UK
Elmetwally Elabbasy, Egypt
Nye Evans, UK
Maurizio Falanga, Switzerland
Duncan Forbes, Australia
Andrew Fruchter, USA
B. T. Gänsicke, UK
Paul Goldsmith, USA
Jonathan Grindlay, USA
Dean Hines, USA

Dieter Horns, Germany
Ivan Hubeny, USA
John Hughes, USA
Wing Huen Ip, Taiwan
Valentina Klochkova, Russia
Gregory Laughlin, USA
M. G. Lee, Republic of Korea
Karen Leighly, USA
Jeffrey Linsky, USA
Mario Mateo, USA
Ronald Mennickent, Chile
Zdzislaw E. Musielak, USA
Valery Nakariakov, UK

Jerome Orosz, USA
George Pavlov, USA
Juri Poutanen, Finland
Somak Raychaudhury, India
William Reach, USA
Peter Roming, USA
Regina Schulte-Ladbeck, USA
Ravi Sheth, USA
Josep M. Trigo-Rodríguez, Spain
Roberto Turolla, Italy
Gary Wegner, USA
Glenn J. White, UK
Paul J. Wiita, USA

Contents

Anomalous Microwave Emission: Theory, Modeling, and Observations, Clive Dickinson, Roberta Paladini, and Laurent Verstraete
Volume 2013, Article ID 134979, 1 page

Anomalous Microwave Emission from Star Forming Regions, Anna M. M. Scaife
Volume 2013, Article ID 390287, 25 pages

The Discovery of Anomalous Microwave Emission, Erik M. Leitch and A. C. R. Readhead
Volume 2013, Article ID 352407, 6 pages

A Characterization of the Diffuse Galactic Emissions at Large Angular Scales Using the Tenerife Data, J. F. Macías-Pérez, R. D. Davies, R. Watson, C. M. Gutierrez, and R. Rebolo
Volume 2013, Article ID 780407, 15 pages

Investigating the Source of Planck-Detected AME: High-Resolution Observations at 15 GHz, Yvette C. Perrott, Anna M. M. Scaife, Natasha Hurley-Walker, and Keith J. B. Grainge
Volume 2013, Article ID 354259, 9 pages

Observations of Anomalous Microwave Emission from HII Regions, Clive Dickinson
Volume 2013, Article ID 162478, 5 pages

Spinning Dust Radiation: A Review of the Theory, Yacine Ali-Haïmoud
Volume 2013, Article ID 462697, 13 pages

Spectrum of the Anomalous Microwave Emission in the North Celestial Pole with WMAP 7-Year Data, Anna Bonaldi and Sara Ricciardi
Volume 2012, Article ID 853927, 8 pages

Spinning Dust Emission from Wobbling Grains: Important Physical Effects and Implications, Thiem Hoang and A. Lazarian
Volume 2012, Article ID 208159, 14 pages

On the Limitations of the Anomalous Microwave Emission Emissivity, Christopher T. Tibbs, Roberta Paladini, and Clive Dickinson
Volume 2012, Article ID 124931, 6 pages

Large Radio Telescopes for Anomalous Microwave Emission Observations, E. S. Battistelli, E. Carretti, P. de Bernardis, and S. Masi
Volume 2012, Article ID 607384, 8 pages

Observations of the Polarisation of the Anomalous Microwave Emission: A Review, J. A. Rubiño-Martín, C. H. López-Caraballo, R. Génova-Santos, and R. Rebolo
Volume 2012, Article ID 351836, 15 pages

Editorial

Anomalous Microwave Emission: Theory, Modeling, and Observations

Clive Dickinson,¹ Roberta Paladini,² and Laurent Verstraete^{3,4}

¹ *Jodrell Bank Centre for Astrophysics, School of Physics and Astronomy, The University of Manchester, Oxford Road, Manchester M13 9PL, UK*

² *NASA Herschel Science Center, California Institute of Technology, Pasadena, CA, USA*

³ *Univ. Paris-Sud, Institut d'Astrophysique Spatiale, UMR-8617, F-91405 Orsay, France*

⁴ *CNRS, F-91405 Orsay, France*

Correspondence should be addressed to Roberta Paladini; paladini@ipac.caltech.edu

Received 19 September 2013; Accepted 19 September 2013

Copyright © 2013 Clive Dickinson et al. This is an open access article distributed under the Creative Commons Attribution License, which permits unrestricted use, distribution, and reproduction in any medium, provided the original work is properly cited.

Anomalous Microwave Emission (AME) was first identified in the late 1990s, through sensitive high frequency radio CMB observations. The usual emission mechanisms (e.g., black-body, synchrotron, and free-free) did not appear to be able to account for the excess emission in the frequency range 10–60 GHz. Since then, a large body of observational evidence has emerged showing that AME appears to be emitted both in the diffuse interstellar medium at large, and from specific clouds within our galaxy. Detections from star-forming regions in an external galaxy have also been made. Nevertheless, detailed measurements have been difficult due to the frequency range (difficult to observe from the ground) and confusion with other emission mechanisms that emit in this frequent range. The most promising candidate for the AME is electric dipole radiation from small spinning dust grains (spinning dust emission). This was first predicted in the late 50s, with major developments in the theory over the last 15 years. The theory predicts a peaked spectrum which emits at frequencies from about 10 GHz to over 100 GHz, but with a wide range of peak frequencies and emissivities, which depend on the local environment and dust grain size distribution. There is still significant debate about the true nature of the AME, and both observations and theory are still relatively unexplored. An exciting possibility is to use detailed radio observations of spinning dust to study the interstellar medium, in a complementary way to the optical, UV, and infrared domains. This special issue is dedicated to the study of AME.

E. M. Leitch and A. C. R. Readhead review the discovery of the AME giving further insights into their early work. A detailed review of observations in star-forming regions is given by A. M. M. Scaife, while a detailed theoretical overview of the spinning dust process is explained by Y. Ali-Haimoud. New theoretical work on the physical effects and implications of grain wobbling is described by T. Hoang and A. Lazarian. E. S. Battistelli et al. discuss the potential and issues involved in using large radio telescopes for AME observations. New observational results and analyses are presented from the Arc Minute Imager (AMI) telescope (Y. C. Perrott et al.), Tenerife experiments (J. F. Macías-Pérez et al.), and WMAP satellite (A. Bonaldi and S. Ricciardi). C. Dickinson summarises observations of AME in HII regions, while C. T. Tibbs et al. discuss the limitation of AME emissivities derived from observations. Finally, J. A. Rubiño-Martín et al. present a comprehensive summary and new results on the polarization of AME.

We hope that researchers from a broad range of astronomical backgrounds (CMB foregrounds, radio astronomy, ISM, and theory) find this special issue useful in bringing the state-of-the-art research in AME into one compendium. We also hope that it may stimulate further research into this fascinating area of astronomy and astrophysics.

*Clive Dickinson
Roberta Paladini
Laurent Verstraete*

Review Article

Anomalous Microwave Emission from Star Forming Regions

Anna M. M. Scaife

Physics & Astronomy, University of Southampton, Highfield, Southampton SO17 1BJ, UK

Correspondence should be addressed to Anna M. M. Scaife; a.scaife@soton.ac.uk

Received 7 June 2012; Accepted 11 January 2013

Academic Editor: Laurent Verstraete

Copyright © 2013 Anna M. M. Scaife. This is an open access article distributed under the Creative Commons Attribution License, which permits unrestricted use, distribution, and reproduction in any medium, provided the original work is properly cited.

The evidence for microwave emission from spinning dust grains has been strengthened considerably by its detection in a number of discrete astrophysical objects associated with star formation. These detections, in combination with statistical constraints on its presence on large angular scales in the diffuse ISM, have provided strong observational confirmation of an emission mechanism still referred to as anomalous. This emission has a peaked spectrum with a maximum in the microwave band; the present review discusses the continuum radio emission mechanisms which can contribute to this region of the electromagnetic spectrum, collects published results on the prevalence of anomalous microwave emission in a variety of star formation regions, presents the overall conclusions that may be drawn from the detections so far, and discusses the prospects for future research on the anomalous microwave emission attributed to spinning dust within star forming regions.

1. Introduction

The interstellar medium (ISM) of our galaxy and others is volume dominated by a small number of components. These components are differentiated by their temperature, ionization state, and density: the cold neutral medium (CNM) with hydrogen density $n_{\text{H}} \approx 30 \text{ cm}^{-3}$ and temperature 100 K, containing very little ionized material and no molecular gas; the warm neutral medium (WNM) with hydrogen density $n_{\text{H}} \approx 0.3 \text{ cm}^{-3}$ and temperatures of 5000–10⁴ K, a low ionization fraction and no molecular component; the warm ionized medium (WIM), which has much in common with the WNM except that it is almost entirely ionized; as well as the low density hot ionized medium (HIM), with $n_{\text{H}} \approx 0.001 \text{ cm}^{-3}$ and temperatures of 10⁶ K, which was first proposed by McKee and Ostriker ([1]; see also [2]) as the result of supernova shocks acting on the ambient ISM, and lead to the phrase “the violent ISM” being coined [3]. Between them these components make up three phases, where they exist with densities regulated by pressure equilibrium: the hot phase of the HIM, the cooler combined warm phase of the WIM and WNM, and the cold CNM phase [4].

In addition to these three phases there also exist quasisstatic, long-lived components with pressures far in excess of the ambient ISM, which have a much smaller volume filling

factor but represent the bulk of mass in the galaxy. These giant cloud components are virialized and gravitationally bound, and their increased pressure is a result of an ongoing internal struggle to produce pressure gradients which will balance their own self-gravity. Unlike the ambient ISM phases, these clouds are largely molecular with little ionized gas. Their high densities make them opaque to optical or ultraviolet radiation and they have very low temperatures of 10–30 K. These molecular clouds have a partly hierarchical structure, with a self-similar density structure thought to arise naturally from a turbulent medium [5]. Simulations of turbulent collapse have demonstrated that turbulent pressure in such regions can support the structure of a molecular cloud against collapse globally while still allowing local collapse to occur (e.g., [6]). It is this local collapse where (in the simplest picture) overdensities from fluctuations become unstable to gravity, which forms the even denser cores which collapse further to become stars. The largest of these structures, with masses in excess of 10⁴ M_⊙, are known as giant molecular clouds (GMCs). Within GMCs, individual overdensities are termed *clumps* and generally correspond to what are loosely termed *dark clouds* in the literature, with densities of 10³–10⁴ cm⁻³. These clouds do not necessarily go on to form stars, but can contain denser cores with $n_{\text{H}} \approx 10^4$ –10⁵ cm⁻³, and it is these cores that go on to form individual or multiple stars.

Once massive stars (typically O or B spectral type) have formed within these clouds, the effect of their energetic UV photon flux ($h\nu > 13.6\text{ eV}$) on both their own surrounding cloud as well as those nearby is to cause photoionization of the molecular hydrogen to produce regions of fully ionized gas (HII regions). Those photons which escape the surrounding clouds completely travel further into the ISM to produce the warm ionized medium, which has similar temperatures to those of the HII regions ($\approx 10^4\text{ K}$). However, HII regions themselves have electron densities that range $1\text{--}10^5\text{ cm}^{-3}$, far higher than those of the WIM. Consequently, with such high densities and large thermal velocities, these HII regions often cause otherwise collapsing clouds to expand into the ambient ISM, tearing apart the larger gravitationally bound molecular cloud.

It is these two higher pressure components of the ISM, molecular clouds, and HII regions which form the basis of this review. Such regions differ from the more diffuse medium where anomalous microwave emission was first detected by Leitch et al. [7] in the NCP. The unbound, low pressure gas of the NCP is often referred to as *cirrus* and may be considered to be composed of a combination of the ambient ISM constituents. Although the higher pressure components differ from this medium, the supposition that AME was related to the dust population presented a strong argument for examining these pre- and protostellar environments, where dust is expected to be ubiquitous.

In spite of the pervasive nature of dust in star formation regions, there is still debate about many of its properties. Dust is composed of carbonaceous, silicate, and/or metallic grains [8], but the actual mixture and structure are not well constrained. The shape of grains varies widely; they may be spherical, spheroidal, and fractal, or in the case of the very smallest grains they may be disk/sheet-like as expected for polycyclic aromatic hydrocarbons (PAHs; [9]) or needle-like [10]. Their sizes vary wildly, between a few tenths of a nanometre for the smallest grains which are expected to produce the anomalous microwave emission attributed to spinning dust, and several centimetres for the largest grains, or *pebbles*, found in the circumstellar/protoplanetary disks around young stars (e.g., [11]). Within cold molecular clouds the surface of these dust grains is expected to be coated by the depletion of molecules from the gas phase and, in the very coldest and densest regions, the formation of ice mantles [10]. All of these factors influence the observational parameters of the dust through their effects on emissivity and opacity as a function of wavelength, as well as the ratio of dust to gas which will vary between different environments [12].

Although star formation regions are generally studied at much shorter wavelengths, the identification of such regions with anomalous microwave emission attributed to spinning dust has led to a surge of observational studies at radio-microwave frequencies. These studies concentrate not only on small angular scales where radio emission is known historically to be associated with protostellar objects, but also on the extended scales of the clouds which contain this activity and indeed the wider complexes of such clouds.

The structure of this review is as follows: in Section 2, I give an overview of the radiation mechanisms contributing

to the total microwave emission of star formation regions other than the anomalous microwave emission attributed to spinning dust; in Section 3, I discuss the possibilities for identifying spinning dust emission in star formation regions based on the theoretical predictions of Draine and Lazarian ([13]; hereafter DL98) and review the observational evidence in each case; in Section 4, I discuss the links to protostellar activity and the environmental conditions within star forming regions; in Section 5, I address the observational issues associated with the identification of the anomalous component; and in Section 6, I discuss the future observational prospects and possible directions for further study.

2. Radio Emission from Star Formation Regions

The mechanism and spectrum of the anomalous microwave emission from spinning dust are described elsewhere in this volume, and so I will not repeat that description here. However, at centimetre wavelengths, there are a number of alternative emission mechanisms which also contribute to the overall spectrum of star forming regions. The measured SED is consequently often a combination of multiple types of radiation processes and identifying the contribution from spinning dust alone requires careful separation of these components. Here I give a brief overview of the major alternative mechanisms which may be found to contribute to the overall spectrum. This overview is not an exhaustive description of these mechanisms, for which I refer the reader to the many more detailed investigations referenced in the text, but is intended to provide the reader with a working “toolkit” with which to understand and interpret the following discussions about the observational constraints on anomalous microwave emission from star formation regions.

Anomalous microwave emission is often discussed in the context of the three major radio emission mechanisms: synchrotron, bremsstrahlung, and thermal (i.e., vibrational) dust emission. Although such mechanisms are usually characterized by canonical spectral indices of $\alpha = -0.7, -0.1,$ and $+3.8$, respectively (where $S_\nu \propto \nu^\alpha$), the detailed spectral dependencies of each vary substantially as a function of environment. Across the microwave band, broadly considered here as 1–100 GHz, the two dominant mechanisms will be thermal bremsstrahlung and thermal (i.e., vibrational) dust emission. As the separation of the anomalous microwave emission from other types of emission is highly important, I here briefly review these two major alternatives in the context of star forming regions.

2.1. Thermal Bremsstrahlung

2.1.1. General Principles. There is a variety of mechanisms expected to give rise to radio emission from star formation regions. The most commonly observed of these is that of thermal bremsstrahlung, or *free-free*, emission. This mechanism operates when charged particles, typically electrons, are accelerated by encountering another charged particle. Consequently radio free-free emission is expected to manifest from any environment populated by an ionized plasma. The

distribution and energy cutoff for scattering in such a plasma are characterized by the Gaunt factor, $\langle g_{ff} \rangle$, which allows one to work out the (ratio of) absorption coefficient, κ_ν , for the plasma,

$$\kappa_\nu = 0.018Z^2 N_e N_i T_e^{-3/2} \nu^2 \langle g_{ff} \rangle. \quad (1)$$

Integration of this quantity along the line of sight, $\int \kappa_\nu d\ell$, gives the optical path length (depth) for the free-free emission,

$$\begin{aligned} \tau_\nu &= 3.014 \times 10^{-2} \left(\frac{T_e}{\text{K}} \right)^{-3/2} \left(\frac{\nu}{\text{GHz}} \right)^{-2} \\ &\times \left\{ \ln \left[4.955 \times 10^{-2} \left(\frac{\nu}{\text{GHz}} \right)^{-1} \right] + 1.5 \ln \left(\frac{T_e}{\text{K}} \right) \right\} \\ &\times \left(\frac{\text{EM}}{\text{cm}^{-6} \text{pc}} \right) \end{aligned} \quad (2)$$

[14, 15], where the emission measure, EM, is defined as the integral $\int N_e N_i d\ell$. This expression is often approximated as

$$\begin{aligned} \tau_\nu &= 8.235 \times 10^{-2} \left(\frac{T_e}{\text{K}} \right)^{-1.35} \\ &\times \left(\frac{\nu}{\text{GHz}} \right)^{-2.1} \left(\frac{\text{EM}}{\text{cm}^{-6} \text{pc}} \right) \end{aligned} \quad (3)$$

(see, Altenhoff et al. [16]). The brightness temperature, T_b , from such emission is given by the product

$$T_b = T_e (1 - e^{-\tau_\nu}). \quad (4)$$

In the Rayleigh-Jeans region of the spectrum, where $S_\nu = 2k_B T_b / \lambda^2$ in units of $\text{W m}^{-2} \text{Hz}^{-1} \text{sr}^{-1}$, and assuming emission extended relative to the resolution of the telescope, the resulting flux density from such emission is then given by

$$\begin{aligned} \left(\frac{S_\nu}{\text{Jy bm}^{-1}} \right) &= 3.07 \times 10^4 \left(\frac{\nu}{\text{GHz}} \right)^2 \\ &\times \left(\frac{T_e}{\text{K}} \right) (1 - e^{-\tau_\nu}) \left(\frac{\Omega_b}{\text{sr}} \right), \end{aligned} \quad (5)$$

where Ω_b is the beam size in steradians. The integrated flux density of a discrete source, in units of Janskys, may be found by replacing Ω_b in (5) by Ω_s , the source size in steradians.

Where the plasma giving rise to the free-free emission is reasonably uniform in density, this leads to a characteristic radio spectrum which has two components delineated by the frequency at which the optical depth equals unity ($\tau_\nu = 1$), marking the transition from optically thick behaviour to optically thin. In the optically thick regime, the optical depth term in (5) becomes approximately unity and the flux density spectrum rises as ν^2 ; in the optically thin regime, the optical depth term becomes $\approx \tau_\nu$, and the frequency dependence of τ_ν (see (3)) cancels with the explicit frequency dependence in (5) resulting in a flux density spectrum which varies as $\nu^{-0.1}$. In the optically thin regime the optical depth term tends to

TABLE 1: Physical parameters for different types of HII regions.

Class	Size (pc)	Density (cm^{-3})	EM ($\text{cm}^{-6} \text{pc}$)
Hypercompact	≤ 0.03	$\geq 10^6$	$\geq 10^{10}$
Ultracompact	≤ 0.1	$\geq 10^4$	$\geq 10^7$
Compact	≤ 0.5	$\geq 5 \times 10^3$	$\geq 10^7$
Classical	~ 10	~ 100	$\sim 10^2$

unity and the frequency dependence follows the Rayleigh-Jeans spectrum with a ν^2 dependence.

The frequency at which an ionized plasma becomes optically thick/thin depends on its size, density, and to a lesser extent its temperature. The first two of these quantities are combined into the emission measure of such a plasma; the turnover frequency where optical depth equals unity is a strong function of the emission measure.

The emission measure of an ionized plasma surrounding a massive young star can be used to establish the relative age of the object with denser, higher emission measure objects corresponding to younger systems. The highest emission measure objects are referred to as hypercompact HII, or HCHII regions, followed by ultracompact (UCHII), compact (CHII), and classical HII regions in order of increasing evolution. Typical parameters for such objects are given in Table 1, which is adapted from Kurtz [17]. Often such objects are found grouped together spatially, as the expansion of an HII region into the ambient ISM is thought to cause *triggered* star formation to occur and hence be responsible in part for the creation of additional local compact cores of HII; see Section 3.1.1.

The integrated flux density spectra, following (5), for the four types of HII region summarized in Table 1 are shown in Figure 1(a). The spectra correspond to the nominal parameters as listed in Table 1, a common electron temperature of 10^4 K and scaled to a distance of 10 kpc. The turnover frequencies for the emission measures of compact/ultracompact (1.76 GHz) and hypercompact (47.2 GHz) regions are indicated by vertical dashed lines. Note that the integrated flux density of the compact region is larger than that of the ultracompact due to having an increased size but comparable emission measure. The turnover frequency from the optically thick to optically thin regime as a function of emission measure is shown for a range of electron temperatures in Figure 1(b).

In practice, the optically thick emission of ultra- and hypercompact HII regions tends to have a somewhat shallower observed spectrum than the $S_\nu \propto \nu^2$ behaviour predicted by the uniform density free-free model, with indices in the range $1 \leq \alpha \leq 2$. This is thought to be due to the fact that such regions are not uniformly smooth, but are instead clumpy along the line of sight [18] with a variety of optical depths present. The morphology of ultra- and hypercompact HII regions is discussed further in Section 3.1.1.

2.1.2. Varying Optical Depth. Frequently the ionized plasma surrounding regions of star formation cannot be well approximated by uniform optical depth but instead has regions of

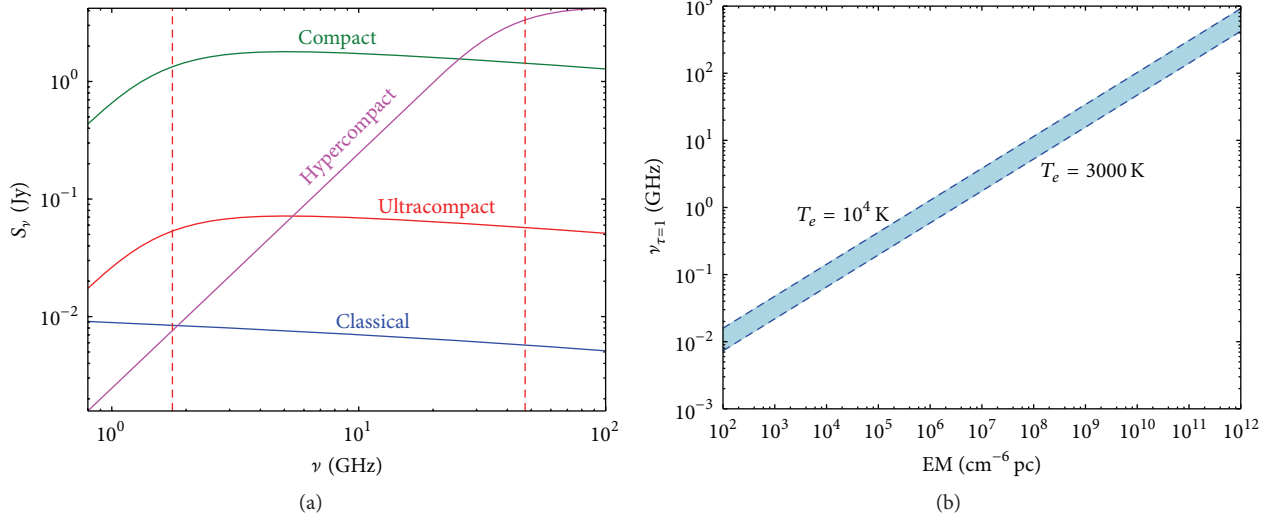


FIGURE 1: (a) Spectra of different types of HII region from Table 1. Red dashed lines indicate turnover frequencies at 1.76 and 47.2 GHz for emission measures of 10^7 and 10^{10} cm^{-6} pc, respectively. (b) Turnover frequency from optically thick to optically thin for free-free emission as a function of emission measure for a range of temperatures.

varying density, resulting in a *partially* opaque plasma. This is particularly the case when considering plasmas in the immediate vicinity of young stellar objects. The spectra from such regions have behaviour that depends not only on the geometry but also on the thermodynamic conditions of the ionized gas. Unlike classical HII regions, where the source of free-free emission is generally due to nearby neutral gas which has been ionized by the strong UV flux from the central star, these plasmas can be associated with stellar winds or ionized jets, both of which are typical in such systems.

The canonical geometry for a stellar wind is that of a spherical region of ionized, isothermal (the polytropic case for the same geometry was considered by Chiuderi and Ciamponi [19], whose derivation preempted the analysis of Reynolds [20] but in a less general form) plasma with a radial density gradient, $n_e(r) = n_0(r/r_0)^{-2}$ [21], where n_0 is the electron density at the inner boundary r_0 , which marks the stellar radius. For such an emission region the optical depth through the plasma varies as a function of projected radius on the sky. The unresolved flux density of such a source can be expressed as

$$\left(\frac{S_\nu}{\text{mJy}}\right) = 32.7 \left(\frac{n_0}{10^6 \text{ cm}^{-3}}\right)^{4/3} \left(\frac{r_0}{10^{15} \text{ cm}}\right)^{8/3} \times \left(\frac{\nu}{\text{GHz}}\right)^{0.6} \left(\frac{T_e}{10^4 \text{ K}}\right)^{0.1} \left(\frac{d}{\text{kpc}}\right)^{-2}. \quad (6)$$

The same spectral behaviour is also expected from a conical isothermal jet [22]. Indeed for a more general outflow where the physical conditions are parameterized by different radial dependencies such that $T_e(r) = (r/r_0)^{q_T}$, $\tau(r) = (r/r_0)^{q_\tau}$, and so forth, the spectral index of the radio emission would have the form

$$\alpha = 2 + \frac{2.1}{q_\tau} (1 + \varepsilon + q_T) \quad (7)$$

with $q_\tau = \varepsilon + 2q_x + 2q_n - 1.35q_T$, where τ denotes optical depth, x denotes ionization, n denotes density, T denotes temperature, and ε relates to the opening angle of the jet such that $w = w_0(r/r_0)^\varepsilon$ with w representing the radius of the jet perpendicular to the direction of outflow. For a range of physical situations, this index varies with values $-0.1 \leq \alpha \leq 1.1$, as listed in Table 1 of Reynolds [22]. For a general outflow, the expression for the integrated radio flux density is

$$\left(\frac{S_\nu}{\text{mJy}}\right) = 4.74F(q_\tau, \alpha) \left(\frac{r_0}{10^{15} \text{ cm}}\right)^2 \left(\frac{\nu}{10 \text{ GHz}}\right)^\alpha \times \left(\frac{\theta_0}{\text{rad}}\right) \left(\frac{\nu_m}{10 \text{ GHz}}\right)^{2-\alpha} \times \left(\frac{d}{\text{kpc}}\right)^{-2} \left(\frac{T_e}{10^4 \text{ K}}\right) \sin i, \quad (8)$$

where $\nu_m = [2 a_k w_0 n_0^2 x_0^2 T_0^{-1.35} (\sin i)^{-1}]^{1/2.1}$ is the turnover frequency from optically thick to optically thin emission, $F(q_\tau, \alpha) = (2.1)^2/q_\tau(\alpha - 2)(\alpha + 0.1)$, and the jet is inclined towards the observer at an angle i . In the specific case of a conical, fully ionized isothermal jet with opening angle $\theta_0 = 2w_0/r_0$ in the plane of the sky, (8) can be rearranged to give an equivalent expression to that of the spherical isothermal wind in (6),

$$\left(\frac{S_\nu}{\text{mJy}}\right) = 1.06 \left(\frac{\theta_0}{\text{rad}}\right)^{5/3} \left(\frac{n_0}{10^6 \text{ cm}^{-3}}\right)^{4/3} \times \left(\frac{r_0}{10^{15} \text{ cm}}\right)^{8/3} \left(\frac{\nu}{\text{GHz}}\right)^{0.6} \times \left(\frac{T_e}{10^4 \text{ K}}\right)^{0.1} \left(\frac{d}{\text{kpc}}\right)^{-2}. \quad (9)$$

Opening angles for outflows from young stellar objects (YSOs) vary with evolution. For example the earliest stage of YSO (Class 0) has highly collimated outflows which become less collimated as they evolve through Class I and, where an outflow remains, leave a wide angle outflow from Class II objects. Typically, however, one may assume that $\theta_0 \leq 0.5$ rad.

Outflows which are collimated ($\epsilon < 1$) will have shallower spectral indices, typically $\alpha = 0.25$, although pressure confined outflows can exhibit much steeper indices approaching unity. Such steep indices can also be produced by recombining or accelerating outflows where the indices may even exceed unity.

2.1.3. Quantifying Thermal Bremsstrahlung Indirectly. There are two major indirect methods for establishing the expected level of free-free emission from a given region. The first is to use of radio recombination lines (RRLs) to determine the local emission measure and use this to predict the free-free flux density. The integrated line temperature is proportional to both the temperature of the electron plasma and the emission measure,

$$\int T_L d\nu = 1.92 \times 10^3 \left(\frac{T_e}{\text{K}} \right)^{-1.5} \left(\frac{\text{EM}}{\text{cm}^{-6} \text{ pc}} \right). \quad (10)$$

By assuming an electron temperature, one may determine the emission measure; however generally RRL measurements record both the line temperature and the continuum brightness temperature. By taking the ratio of these two quantities, $\int T_L d\nu / T_C$, using the expression for brightness temperature in (4), one can find the electron temperature directly,

$$\int T_L d\nu / T_C = 6.985 \times 10^3 \left(\frac{T_e}{\text{K}} \right)^{-1.15} \left(\frac{\nu}{\text{GHz}} \right)^{1.1}, \quad (11)$$

see, for example, Brown et al. [23] for a review.

The width of RRLs towards HII regions provides a good determinant of the type of region being observed. Typically, diffuse classical HII regions have relatively narrow line profiles with widths of $\approx 25 \text{ km s}^{-1}$ [24], compact HII regions have somewhat broader line width, UCHII region RRLs are broader still with $\approx 30\text{--}40 \text{ km s}^{-1}$ [17], and HCHII regions have extremely broad RRLs of $50\text{--}100 \text{ km s}^{-1}$ and often in excess of 100 km s^{-1} (e.g., NGC 7538; [25]).

The second indirect method for predicting free-free emission is to use H α emission, which is thought to trace diffuse free-free emission closely as they both arise from the same plasma and therefore their intensities both depend on the same emission measure. The intensity of free-free is given by (5), whereas the intensity of H α at $\lambda = 6563 \text{ \AA}$ (measured in Rayleighs) is given by

$$\left(\frac{I_\alpha}{\text{R}} \right) = 0.36 \left(\frac{\text{EM}}{\text{cm}^{-6} \text{ pc}} \right) \left(\frac{T_e}{10^4 \text{ K}} \right)^{-\gamma} \quad (12)$$

[26], where $\gamma = 0.942 + 0.031 \ln(T_e/10^4 \text{ K})$ [27]. Under the assumption of optically thin free-free emission, combining

(3) and (5) and replacing the emission measure term with the rearrangement of (12) leads to the relationship

$$\left(\frac{S_\nu}{\text{Jy beam}^{-1}} \right) = 281 \left(\frac{T_e}{10^4 \text{ K}} \right)^{\gamma-0.35} \times \left(\frac{\nu}{\text{GHz}} \right)^{-0.1} \left(\frac{I_\alpha}{\text{R}} \right) \left(\frac{\Omega_b}{\text{sr}} \right). \quad (13)$$

Although broadly correct, this treatment is somewhat simplistic in its treatment of the emitting species. Whereas free-free emission will arise from *all* ions in the plasma, H α emission will only arise from $\text{H}^+ + \text{e}^-$. Consequently the ratio of free-free to H α emission will also depend on both the ionization fraction, $x_{\text{H}} \equiv n(\text{H}^+)/n_{\text{H}}$, and the gas-phase elemental abundance. Without exact knowledge of these conditions the variation in this ratio can be a factor of several (Dong and Draine, 2010).

2.2. Thermal Dust Emission. The spectral behaviour of continuum thermal dust emission is far more coherently expressed than that of free-free emission. Dust spectra are heavily dominated by modified blackbody emission, with an additional subdominant component from the emission lines of individual dust species. The observed continuum flux density from such emission in the Rayleigh-Jeans limit and optically thin limit is characterized as

$$S_\nu \propto \nu^{2+\beta/(1+\Delta)} B_\nu(T_d), \quad (14)$$

where β is the opacity index of the dust population with opacity $\kappa_\nu = \kappa_0(\nu/\nu_0)^\beta$ (cf. [28]), T_d is the dust temperature, and $B_\nu(T_d)$ is the Planck function.

The opacity index, β , depends on the dust composition and grain size distribution. Smaller grains have larger opacity indices, leading to steeper spectra at longer wavelengths, whereas larger grains such as those found in circumstellar or protoplanetary disks exhibit flatter spectra with low values of β . The opacity index, β , is related to the spectral index of flux density measurements as $\beta = (1 + \Delta)(\alpha - 2)$, where Δ is the ratio of optically thick to optically thin emission. This ratio decreases at longer wavelengths and has been observationally determined in the region $350 \mu\text{m}$ to 1.3 mm for dark clouds as $\Delta \approx 0.2$ [29, 30]. Although negative values of β are unphysical, values approaching zero (e.g., [31]) are proposed for the long wavelength tail of the greybody spectrum for young stellar objects, which is dominated by large dust grains in circumstellar/protoplanetary disks. This is substantially lower than that expected for the more diffuse interstellar medium of $\beta_{\text{ISM}} \approx 1.8\text{--}2.0$. This difference is due to the change in expected grain size distribution within the dust population, as described previously. For grains with a size distribution $dn/da \propto a^{-p}$, where the grain size $a \leq a_{\text{max}}$ and $a_{\text{max}} \geq 3\lambda$, where λ is the wavelength of observation, the measured opacity index will be

$$\beta(\lambda) \approx (p - 3) \beta_{\text{ISM}}. \quad (15)$$

For a typical power-law index of $p = 3.5$ (MRN distribution; [32]), grains with $\beta_{\text{ISM}} \approx 2$ will have $\beta \approx 1$ when

$a_{\max} > \lambda$ and by extension $\beta \leq 1$ when $a_{\max} > 3\lambda$ [33]. Power-law indices, p , for grain size distributions have been shown to be as low as $p = 3$ for protoplanetary disks (e.g., [34]), which can reduce the expected value of β even further.

Consequently the contribution from thermal dust at microwave frequencies ($\lambda > 3$ mm) is expected to come from the largest grains in the overall population. The additional log normal grain size distribution for very small grains appended to the MRN distribution by Draine and Lazarian [13], as inferred from 12 and 25 μm IRAS data [35], to predict the rotational emission of the small grain population has no effect on the greybody tail of the thermal dust population at these longer wavelengths.

The flux density of dust emission at a single frequency can be used directly to characterize the dust properties of the emitting region. Specifically, the hydrogen column density can be found using

$$\left(\frac{N_{\text{H}}}{\text{cm}^{-2}}\right) = \frac{\Psi}{2.8 m_{\text{H}}} \left(\frac{S_{\nu}}{\text{Jy beam}^{-1}}\right) \times \left[\left(\frac{\kappa_{\nu}}{\text{cm}^2 \text{g}^{-1}}\right) \left(\frac{B_{\nu}(T_d)}{\text{Jy sr}^{-1}}\right) \left(\frac{\Omega}{\text{sr}}\right)\right]^{-1}, \quad (16)$$

where Ψ is the gas-to-dust ratio and m_{H} is the atomic mass of hydrogen. The total (gas + dust) mass can be estimated from the integrated flux density when the distance to the source, d , is known,

$$\left(\frac{M}{M_{\odot}}\right) = 4.8 \times 10^9 \Psi \left(\frac{S_{\nu}}{\text{Jy}}\right) \left(\frac{d}{\text{kpc}}\right)^2 \times \left[\left(\frac{\kappa_{\nu}}{\text{cm}^2 \text{g}^{-1}}\right) \left(\frac{B_{\nu}(T_d)}{\text{Jy sr}^{-1}}\right)\right]^{-1}, \quad (17)$$

see, for example, Anderson et al. [36]. Both of these quantities also depend on the opacity index β through the dependence of κ_{ν} on this parameter. Typical normalizations of the opacity function at sub-mm wavelengths are in the range 0.001–0.05 $\text{cm}^2 \text{g}^{-1}$, and the dust to gas mass ratio, Ψ , is typically assumed to be 100 although there is a large degree of uncertainty in both of these parameters (e.g., [37]). In this paper a dust emissivity of $\kappa_{850} = 0.012 \text{ cm}^2 \text{g}^{-1}$ (gas + dust), from Ossenkopf and Henning [10] model 5 for icy coagulated grains, and a gas-to-dust mass ratio of 161 (1.5×10^{-26} g of dust per H atom; [38]), assuming gas is 0.89% H by number [39], are assumed.

2.2.1. Free-Free Absorption by Dust. If only free-free emission is involved then the radio spectral index of the flux density with increasing frequency should never be substantially negative. However, this is not the case when free-free is obscured by a dust cloud along the line of sight. The dust and the free-free will have differing optical depths, τ_{ν}^d and τ_{ν}^{ff} , respectively, and consequently the recovered flux density will be, following the approach of Rodriguez et al. [40],

$$S_{\nu} = \frac{2k_B \nu^2}{c^2} \Omega \left[T_e \left(1 - e^{-\tau_{\nu}^{\text{ff}}}\right) e^{-\tau_{\nu}^d} + T_d \left(1 - e^{-\tau_{\nu}^d}\right) \right]. \quad (18)$$

Since the optical depth of the dust will be $\tau_{\nu}^d = N(d)\kappa_0(\nu/\nu_0)^{\beta}$ where $N(d)$ is the mass column density of the dust and including the Gaunt factor dependence in the free-free optical depth, the resulting absorbed free-free spectral index assumes the complicated form

$$\alpha = 2 + \left\{ \beta \tau_{\nu}^d e^{-\tau_{\nu}^d} \left[T_d - T_e \left(1 - e^{-\tau_{\nu}^{\text{ff}}}\right) \right] - 2 \left[1 + \left(\ln \frac{T_e^3}{\nu^2} + 35.4 \right)^{-1} \right] \tau_{\nu}^{\text{ff}} T_e e^{-\tau_{\nu}^{\text{ff}} + \tau_{\nu}^d} \right\} \times \left[T_e \left(1 - e^{-\tau_{\nu}^{\text{ff}}}\right) e^{-\tau_{\nu}^d} + T_d \left(1 - e^{-\tau_{\nu}^d}\right) \right]^{-1}. \quad (19)$$

This kind of absorption can produce highly negative spectral indices in principle. However, in practice the dust column densities required are extremely large compared to the expected value in the ambient ISM; see Section 3.1.1.

3. Where Should We Expect to Find Spinning Dust?

Of the seven different environments considered as possible sites for producing spinning dust emission by Draine and Lazarian [13], three are representative of the large scale diffuse interstellar medium or cirrus: the cold neutral medium (CNM), the warm neutral medium (WNM), and the warm ionized medium (WIM); five are directly associated with star formation: dark clouds, molecular clouds, the warm ionized medium, reflection nebulae, and photodissociation regions. The warm ionized medium is a cross-over component as it may be representative not only of large scale diffuse ionized plasmas, but also of hot ionized objects with compact support such as HII regions.

There is some confusion in the literature over terminology in this area, and here I explicitly define my nomenclature. Clouds or dark clouds (DC) are regions of high visual extinction on scales of a few parsecs. They contain large quantities of molecular gas, which often harbours *cores* and active star formation. Cores are defined as compact objects on scales of a few tenths of a parsec and are typically identified at sub-mm wavelengths. Cores can be protostellar or starless, a distinction made on the basis of their SEDs, the presence of an IR source, a molecular outflow, or a compact cm-wave source [41]. Cores identified in the sub-mm are suffixed “SMM,” whilst those identified in the infrared are suffixed “IRS.” Correspondingly I will refer to dark clouds as being “starless” or “star-forming” based on whether they are known to contain protostellar cores or not. On larger scales of a few parsecs to a few tens of parsecs I will refer to extended regions of presumably interconnected clouds as molecular clouds (MCs), or molecular cloud complexes.

Reflection nebulae (RN) are regions of gas subject to UV flux from nearby stars insufficient to ionize the neutral medium, but strong enough to cause scattering effects which illuminate the dust. Typically they are associated with high mass star formation or particularly luminous premain sequence (PMS; low-mass) stars. In general these low-mass PMS

stars are Herbig Ae/Be stars [42] or FU Orionis objects [43], but in a few cases they may also be illuminated by T Tauri stars (TTs; Class II/III). One such case is the bright reflection nebulae Parsamian 3 [44] associated with a weak-line T Tauri star (WTTS; Class III) binary (possibly triplet; [45]) pair HBC 515 at the apex of the star-forming dark cloud LDN 1622, which will be discussed in more detail later in this review.

Photodissociation regions (PDRs), also sometimes called photon-dominated regions, contain ultraviolet photons from nearby stars, which are not energetic enough to ionize hydrogen and create HII regions, but which can dissociate most molecules. The term remains sufficiently general to include regions that are mostly H₂ or CO but where ultraviolet fluxes still appreciably dissociate other species. In broad terms nearly all phases of the ISM which are not dominated by ionized hydrogen can be considered to be PDRs. The degree of dissociation in PDRs covers a spectrum which includes regions where the penetration of photons leads to a predominantly atomic component with molecular oxygen and hydrogen and atomic carbon, as well as regions where molecular hydrogen and carbon monoxide remain intact and only molecular oxygen is dissociated and which include all gradations of dissociation intermediate to the two. These gradations can also be described by considering the balance between the atomic hydrogen density and the interstellar radiation field (ISRF; e.g., Hollenbach [46]). DL98 defined their PDR scenario as regions with hydrogen density of $n_{\text{H}} = 10^5 \text{ cm}^{-3}$, an ionized hydrogen fraction of 10^{-4} and a more general fraction of ionized species double that of hydrogen. These conditions are typical of PDRs such as those associated with the HII region S140 [47], which represents what might traditionally be termed a PDR, that is a region where neutral hydrogen substantially dominates both ionized and molecular hydrogen, but where other ionized species (such as carbon, oxygen, and silicon) are significant. These other ionized species are identified by their IR emission lines: CII (158 μm), OI (63 μm), and SiII (35 μm). Typically such regions are found predominantly in the outer layers of molecular clouds and in what follows the term PDR will be used in the sense defined by DL98 to denote those regions identified in the literature specifically as these predominantly neutral outer layers where significant line emission from other ionized species has been recorded.

3.1. Targeted Observations. The earliest targeted observations of star formation regions for the purpose of detecting spinning dust emission were made with the Green Bank 43 (140 foot) telescope [48] shortly before it was decommissioned in 1999. These observations targeted a selection of 10 dark clouds, HII regions and infrared sources at 5 and 8–10 GHz, with the intention of constraining an excess at 8–10 GHz relative to any free-free continuum at 5 GHz. Tentative detections were reported towards the dark cloud LDN 1622 and the HII region LPH 201.6+1.6. Later observations revealed that the detection towards LPH 201.6+1.6 was in error [49, 50], but LDN 1622 still remains one of the best candidates for hosting emission from spinning dust grains. These early observations and potential detections lead to a slew of further targeted studies towards a range of objects.

3.1.1. Warm Ionized Medium: HII Regions. The early tentative detection of spinning dust from the HII region LPH 201.6+1.6 [48] had a spectrum which matched the theoretical predictions of DL98 very well, but a magnitude of intensity excess far larger than predicted. This predicted free-free contribution to the flux densities was determined from the H α survey of Gaustad et al. [51] as described in Section 2.1.3, which indicated an emission measure of $\text{EM} \approx 400 \text{ cm}^{-6} \text{ pc}$, consistent with a classical HII region (see Table 1).

As described in Section 2.1.1, HII regions are well known as bright radio sources. Although classical HII regions typically have flat radio spectra, with flux density measurements only on the longer wavelength (rising) side of the expected spinning dust spectrum for LPH 201.6+1.6, McCullough and Chen [52] suggested that the excess could in fact be due to the presence of an ultracompact HII region either embedded in or projected against LPH 201.6+1.6 contaminating the data, which would produce such an inverted spectrum at higher frequencies.

Although the emission measure recovered from H α data did not support the presence of HCHII, see Section 2.1.3, predictions from H α are strongly affected by optical depth effects and so this alone could not rule out such a theory. However, when combined with low IRAS fluxes as pointed out by McCullough and Chen [52], which would suggest an improbably large distance to the potential UCHII region, this possibility seemed remote. In addition, I note that the RRL width towards LPH 201.6+1.6 [24] from observations with a resolution large enough to encompass the IRAS source postulated as the potential contaminant (IRAS 06337+1051; [52]) is only $\Delta V = 22.8 \pm 2.9 \text{ km s}^{-1}$. This is low even for diffuse HII regions, which have typical line widths of $\approx 25 \text{ km s}^{-1}$ (see Section 2.1.3) as opposed to ultra- and hypercompact HII regions which possess much broader lines widths. Furthermore, the original excess was brought into question by results from the CBI telescope [49], which were subsequently confirmed by the VSA telescope [50], and indeed further observations made with the 100 m Green Bank telescope were unable to reproduce the original rising spectrum seen with the 140-foot telescope (footnote, [49]).

Further studies of HII regions concentrated on larger samples. However, the results were somewhat contradictory. A sample of six HII regions in the Southern hemisphere [53] showed a possible small excess of dust correlated emission relative to IRAS 100 μm data with an average emissivity of $3.3 \pm 1.7 \mu\text{K} (\text{MJy sr}^{-1})^{-1}$ at 31 GHz over the full sample and a 95% confidence limit of $< 6.1 \mu\text{K} (\text{MJy sr}^{-1})^{-1}$. The most significant detection was towards RCW 49 which indicated a 3.3σ excess at 31 GHz; see Figure 2. This provided further tentative evidence of some additional mechanism producing emission over the cm-wave band. In contrast a sample of sixteen HII regions in the Northern hemisphere [54] showed no statistically significant excess towards any individual object and on average found a decrease in emission relative to free-free predictions extrapolated from lower frequencies, consistent with the expected steepening of the free-free spectrum at shorter wavelengths [55]. Those objects where a positive

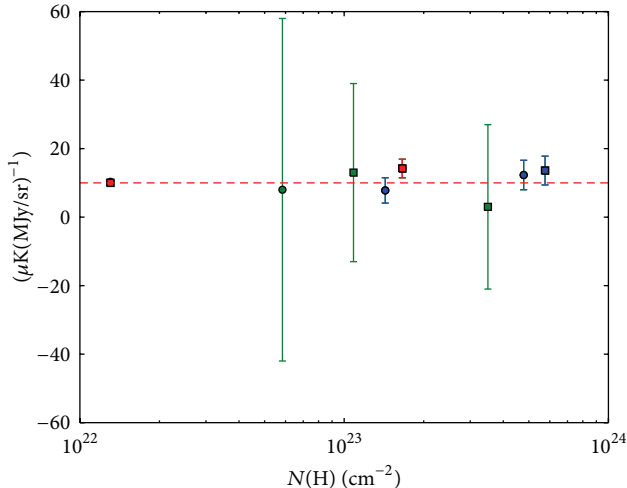


FIGURE 2: Relative emissivity of *excess* microwave emission to $100\ \mu\text{m}$ FIR emission as a function of hydrogen column density, $N(\text{H})$, for HII regions where an excess is detected. Data are shown for excess emission relative to spectra extrapolated using spectral indices fitted to lower frequency data (squares) and using canonical spectral indices for free-free emission (circles) for detections of anomalous microwave emission from Dickinson et al. ([53]; blue points), Scaife et al. ([54]; green points), RCW 175 ([64]; red square), and G159.6–18.5 ([91]; red square). A red dashed line indicates a relative emissivity of $10\ \mu\text{K}\ (\text{MJy}/\text{sr})^{-1}$ typical of that observed on large scales at high galactic latitudes [80].

excess was observed are shown in Figure 2 where it can be seen that none are statistically distinct from zero.

Aside from the difference in observing frequency, a further potential cause of the discrepancy in AME detection between these two samples of HII regions may be the range of angular scales probed. Anomalous microwave emission was initially detected on large-scales and it should be noted that not only was the sample of Southern HII regions [53] observed with an instrument that had sensitivity to marginally larger angular scales than the Northern sample [54], but also that the Northern sample of HII regions had less associated diffuse emission relative to the resolution of the telescope. Such a differing response to sample composition and spatial sensitivity might indicate that the anomalous microwave emission is present either on larger scales than free-free emission, or may be a consequence of an inverse relationship between VSG abundance and density resulting in a lower spinning dust emissivity as suggested by DL98. The second of these possibilities was proposed by DL98 in the context of dark clouds, which have high densities of molecular gas, rather than HII regions but may also be relevant in this case, although it should be noted that the range of emission measures covered by the two samples was not substantially different.

A significant possibility for misidentification of anomalous microwave emission from HII regions is provided by the presence of ultra- or hypercompact HII regions, such as that suggested by McCullough and Chen [52] for LPH 201.6+1.6, as these may also provide a rising spectral index

from lower frequencies. Without additional data at $\nu > 50\ \text{GHz}$ to confirm the peak of the spinning dust SED such contamination is very hard to distinguish.

Unlike low-mass stars, the earliest stages of high-mass star formation where the central object is still undergoing accretion are generally undetectable at radio frequencies. This is because, even though the protostar produces a high enough UV flux to cause significant ionization, the absorption from infalling matter prevents the photons travelling very far from the central source [56]. The radio emission that is seen from ultra- and hypercompact HII regions is thought to occur after accretion finishes and the star evolves onto the main sequence (possibly immediately after or even during the final stages of accretion for hypercompact HII regions) but is still cloaked in the surrounding molecular cloud. During its lifetime on the main sequence, the HII region will evolve from a dense region with the star embedded and expand, revealing the central object, and form a classical nebula. During this expansion the HII region interacts with surrounding or neighbouring molecular clouds by sweeping up material. If the expansion scale is smaller than the size of individual clouds, then this triggers new star formation by effectively “squeezing” the extant dense clumps; if the expansion scale is larger than the size of an individual cloud then a cavity forms surrounded by a rim of collected material which then goes on to form clumps which then collapse triggering new star formation [57]. The first of these mechanisms is considerably faster than the second; however both are observed (e.g., Deharveng et al. [58]; Zavagno et al. [59]; Choudhury et al. [60]). The consequence of this triggered star formation is that different classes of HII region are often found in close proximity. For microwave measurements made with large beam sizes, the contributions of multiple regions of HII of varying emission measure must therefore be accounted for spectrally.

Radio recombination lines (RRLs) provide a useful method for establishing the degree of contamination from denser plasma HII within an unresolved source. Figure 4 shows the distribution of the ratio of microwave excess flux density to $100\ \mu\text{m}$ flux density (following Todorović et al. [61]) with RRL widths, for sources from the VLA Galactic Plane Survey of Todorović et al. [61] and Scaife et al. [54], which have a counterpart in the RRL catalogue of Lockman (see [62]; the HII regions from [53] fall outside the survey area for this catalogue). The average value of RRL width for a classical HII region, see Section 2.1.3, is indicated by a dashed line. Naively, one might interpret these data as indicating that UCHII regions are more likely to exhibit a microwave excess; however, if we assume that the dust-to-gas ratio is relatively uniform across these classes, then the ratio of excess microwave emission to $100\ \mu\text{m}$ dust emission should be constant as a function of RRL width. Indeed the dust abundance is expected to be depleted in dense regions (DL98), moreso towards the central star in UC and HCHII regions where temperatures are higher than the dust sublimation temperature. In which case one might expect a negative correlation between RRL width and the excess ratio. It is more likely therefore that the data in Figure 4 indicate that the microwave excess for the two UCHII regions shown is significantly contaminated by an unresolved contribution from dense plasma.

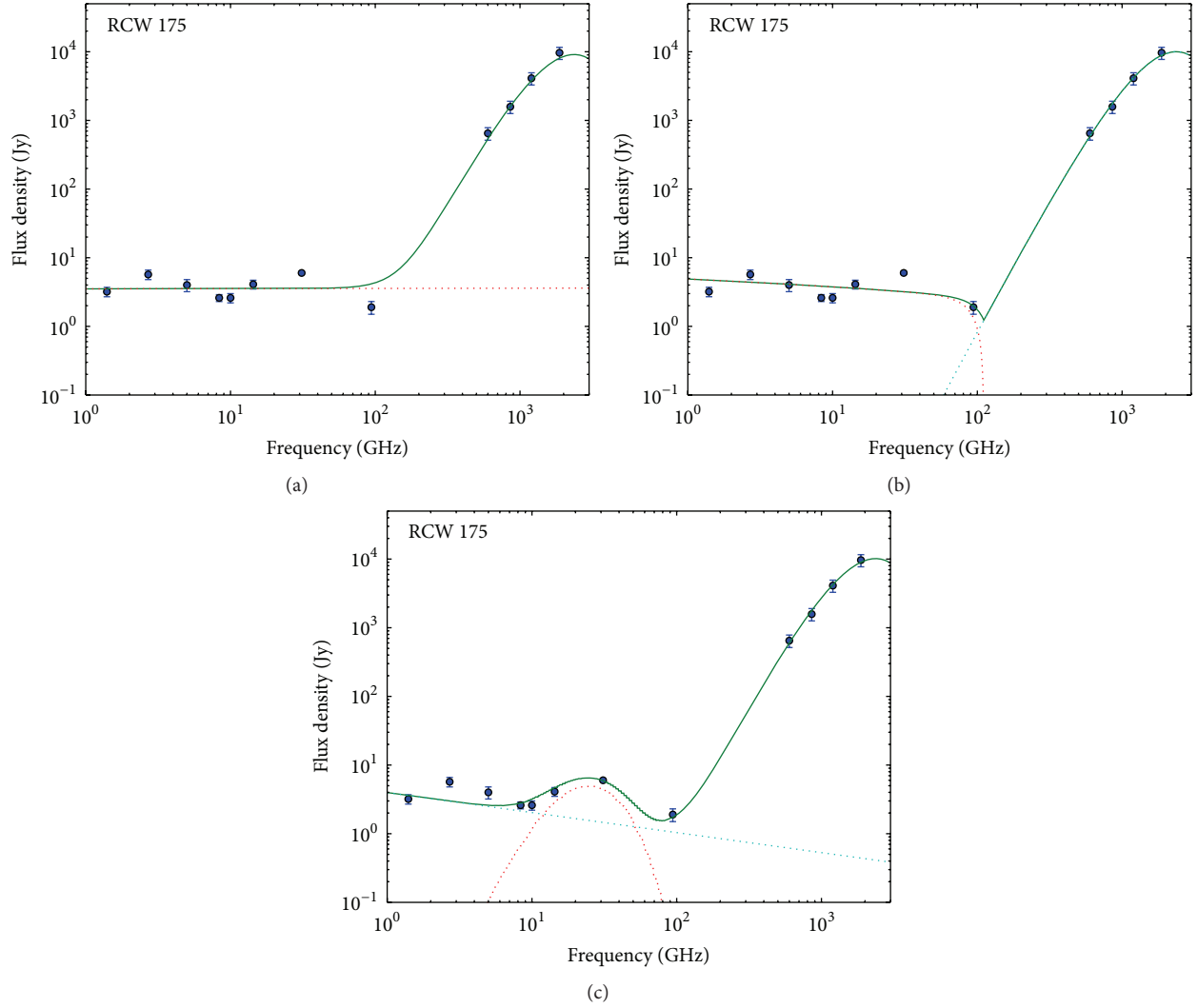


FIGURE 3: SED of RCW 175. (a) Power-law radio emission plus thermal dust greybody. (b) Thermal bremsstrahlung with dust absorption plus thermal dust greybody. (c) Power-law radio emission plus spinning dust (WIM model; DL98) plus thermal dust greybody.

The data point at $\Delta V = 45.1 \pm 3.9 \text{ km s}^{-1}$ corresponds to the HII region S211 [63]. Although the measured excess is consistent with zero this object showed the *largest* excess in the sample of 16 Northern HII regions [54], which may also have been due to contamination by an UC/HCHII region.

RCW 175, a more convincing detection of microwave excess from an HII region came from RCW 175 [64], where an excess at 31–33 GHz was reported with an 8.6σ significance. Although RCW 175 is described as an HII region, it is also listed as a *Spitzer* Infrared Dark Cloud (IRDC). Such objects were originally discovered by the *MSX* [65, 66] and *ISO* [67] surveys as dark regions seen against the mid-infrared (MIR) background, in the same way that traditional dark clouds were first identified by Herschel as voids in the optical sky. IRDCs are considered to represent the earliest stages of high-mass star formation in the same way that traditional dark clouds such as those identified by Lynds [68] represent the earliest stages of low-mass star formation, that is, dark clouds will go on to form low-mass stars, whereas the densest IRDCs

will go on to form high-mass (massive) stars [69]. IRDCs have low temperatures of $<25 \text{ K}$ [66, 70] and high densities $n_{\text{H}} > 10^5 \text{ cm}^{-3}$ [66, 71]. Whereas low mass pre- and protostellar cores within dark clouds have masses of a few solar masses, the cores which form in IRDCs can be up to $10^3 M_{\odot}$ (e.g., [72–74]). Current estimates of the ionization degree in IRDCs are similar to those found in PDRs, with upper limits of $\approx 10^{-4}$ [75].

More recently the RCW 175 region was examined in detail by Tibbs et al. [76] who compiled a full SED from radio to infrared wavelengths. The anomalous excess of emission seen at 31 GHz from RCW 175 is largely constrained relative to data at 94 GHz from the *WMAP* satellite. Data at lower radio frequencies have a large amount of systematic scatter, likely due to the extended nature of this object causing difficulties with both flux density estimation and baseline subtraction for single dish telescopes.

In Figure 3 three different scenarios to explain the SED of RCW 175 are examined, based on the physical mechanisms

TABLE 2: Maximum likelihood parameters from the three models described in Section 3.1.1 fitted to data for RCW 175 [76]. Model fits are shown in Figure 3.

Model	$S_{5\text{GHz}}$ (Jy)	α	$N(H)$ (10^{21} cm^{-2})	$S_{100\text{GHz}}$ (Jy)	$\Delta \ln Z$
PL+GB	3.54 ± 0.20	0.00 ± 0.03	—	0.75 ± 0.08	—
PL+SD+GB	2.49 ± 0.22	-0.29 ± 0.09	18.6 ± 1.8	0.83 ± 0.08	51.27 ± 0.16
	T_e (K)	EM ($\text{cm}^{-6} \text{ pc}$)	$N(d)$ (g cm^{-2})	$S_{100\text{GHz}}$ (Jy)	
abFF+GB	5800	762 ± 33	0.005 ± 0.002	0.82 ± 0.08	-1.72 ± 0.11

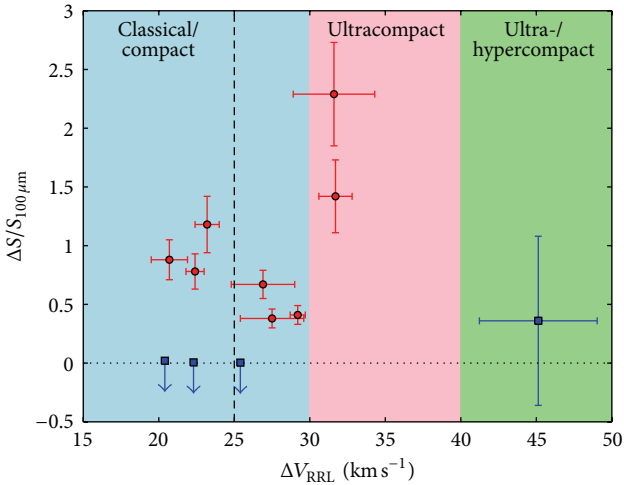


FIGURE 4: Distribution of excess microwave emission relative to $100 \mu\text{m}$ emission with RRL width for HII regions. Data are shown from Todorović et al. (see [61]; red points) and Scaife et al. ([54]; blue points). The range of RRL widths corresponding to different types of HII region are indicated, as is the average RRL width for a classical HII region [24].

described in Section 2. Maximum likelihood (ML) parameters for each model were determined using an MCMC based method [77], and the models were ranked using the common dataset [76, Table 4] through calculation of their Bayesian evidence, Z , over a 3σ prior volume around the ML values. The difference in the logarithm of this quantity, $\Delta \ln Z$, with respect to the first scenario is listed in column 6 of Table 2. As the major source of uncertainty in this spectrum arises from the radio data, in each scenario fixed greybody parameters of $\beta = 2.0$ and $T_d = 22.9 \text{ K}$ [76] were assumed, with only the 100 GHz normalization, $S_{100\text{GHz}}$, being left as a free parameter.

The first scenario is a simple power-law radio spectrum plus a greybody thermal dust spectrum (PL+GB; Table 2). The radio emission is best fitted by a flat power-law with spectral index $\alpha = -0.00 \pm 0.03$. Although this is close to the canonical value for optically thin free-free emission, see Section 2.1.1, there is significant scatter of the measured data about the fit and notably the data at 31 and 94 GHz are heavily under- and overestimated, respectively.

A model including a thermal bremsstrahlung emission component suffering from dust absorption at high frequencies (scenario 2; abFF+GB), see Section 2.2.1, can account for the dip in flux density at 94 GHz, see Figure 3, relative to

lower frequencies. However, in order to produce this degree of absorption, the dust mass column density along the line of sight needs to be high, $N(d) = 0.005 \pm 0.002 \text{ g cm}^{-2}$. Although such dust mass column densities are not unknown in HII regions they are typically associated with compact cores (e.g., [78]) and not the diffuse medium on large scales. Consequently this degree of absorption is highly unlikely to occur on average towards RCW 175. In addition, these data show no preference for the absorbed free-free model above the simple power-law (PL+GB) model with a Bayes factor of $\Delta \ln Z = -1.72 \pm 0.14$ indicating weak evidence for the preference of the power-law model [79].

A model with both a power-law component and a spinning dust component (scenario 3; FF+SD+GB) is strongly preferred ($\gg 5\sigma$) over both alternative models. The maximum likelihood spectral index, $\alpha = -0.29 \pm 0.09$, is consistent with that found by Tibbs et al. [76]. This is steeper than typically expected from free-free; however the flux densities for this object are found using aperture photometry rather than source fitting due to the extended nature of the emission and, as suggested by Tibbs et al. [76], it is possible that there is some contamination from residual nonthermal background emission which has not been completely excised by the background subtraction.

The emissivity of the excess emission at 31 GHz relative to $100 \mu\text{m}$ FIR emission for RCW 175 is $14.2 \pm 2.7 \mu\text{K (MJy/ sr)}^{-1}$. Indeed, for all those objects where an excess is detected, the emissivity is reasonably uniform and similar to that observed on large scales at high galactic latitudes of $10 \mu\text{K (MJy/ sr)}^{-1}$ [80]. The relative emissivity of such objects is plotted as a function of hydrogen column density in Figure 2. The column densities in this figure have been derived from the dust extinction map of Schlegel et al. [81] assuming a conversion factor of $N(H) = 8 \times 10^{21} \text{ cm}^{-2}$ for one magnitude $E(B - V)$ [48]. This uniformity would imply that the degree of excess emission is reasonably independent of local column density. However, not all objects exhibit an excess and averaged over larger samples the value of the relative emissivity falls [53, 54, 82]. It is still uncertain why particular objects show an excess and others do not: the nondetections of a microwave excess span the range of column densities shown in Figure 2 and are far more numerous than the known detections.

3.1.2. Molecular Clouds. The Perseus molecular cloud is a well-known star forming cloud nearby in the galaxy. It is associated with three clusters containing pre-main sequence stars: IC 348, with an estimated age of 2 Myr (and spread of $\pm 1.5 \text{ Myr}$; [83]); NGC 1333, which is less than 1 Myr in

age [84, 85]; and the Per OB2 association, which contains a B0.5 star [86] and therefore must be less than 13 Myr in age [87]. These clusters therefore all show evidence of star formation activity within the last $\sim 10^7$ years. The molecular cloud itself contains a number of previously known protoclusters and isolated protostars and the first full census of its star formation activity was done by Hatchell et al. [88–90] in the sub-mm using a combination of the SCUBA and Harp instruments on the JCMT.

Anomalous emission within Perseus was originally identified using data from the COSMOSOMAS telescope [91] towards the HII region G159.6–18.5 using a combination of COSMOSOMAS data and archival *WMAP* data was well fitted by a combination of WNM and MC spinning dust models from DL98. This detection was confirmed by the VSA telescope [92], which was further able to provide evidence that an excess was seen in multiple separate regions of the cloud. *Planck* data towards Perseus confirmed an excess of microwave emission at 17.1σ [93]. The first measurement of the polarization of anomalous microwave emission was also made towards the Perseus molecular cloud [94], with a detection of 3% fractional polarization. This result was particularly notable as it appeared to rule out the competing mechanism of magnetic dipole fluctuations [13] which would be expected to produce polarized emission approximately an order of magnitude larger.

Additional *Spitzer* analysis of the anomalous regions within Perseus [95] showed that they had no particular enhancement of PAH or VSG population, but that the strength of the ISRF was locally higher. These results indicated that the presence of a VSG population alone was not sufficient to produce the anomalous microwave emission but that the environment of those grains, specifically the ISRF and consequently the equilibrium temperature of the dust, might result in increased emission from spinning dust.

The ρ Ophiuchi molecular cloud [93, 96, 97] lies in the Gould Belt at a distance $d = 135 \pm 15$ pc [98]. It is a region of intermediate-mass star formation and has a high degree of photoionization towards its periphery due to UV flux from its hottest young stars, which heats and dissociates these exposed layers creating photodissociation regions (PDRs), but does not ionise the bulk of the molecular hydrogen in the cloud. The most prominent of these PDRs is ρ Oph W, with $n(\text{H}) = 10^4\text{--}10^5 \text{ cm}^{-3}$ [99, 100], which is excited by HD 147889, the earliest star in the ρ Oph star formation complex. The bulk of the mass in the ρ Ophiuchi cloud is situated in the Oph A molecular core [101, 102], a range of values are available for $N(\text{H}_2)$ in ρ -Ophiuchus generally (see, e.g., van Dishoeck and Black [103]; K azmierczak et al. [104]) although the line of sight towards HD 147889 can be used to form rough ideas about the environmental conditions.

An excess of microwave emission was detected towards ρ -Ophiuchus at a significance of 8.4σ by the *Planck* satellite [93]. Both this detection and that of the Perseus molecular cloud were shown to have conical microwave spectra, consistent with the curved peak of the spinning dust SED. The peak itself was found to be flattened in both cases suggesting that several different spinning dust components with different environment conditions were present. This superposition of

spectra is perhaps unsurprising given the internal complexity of these molecular clouds and the large angular scales probed by the *Planck* beam, although the extended nature of the microwave emission seen towards both targets relative to this beam once more indicates that AME may be a large-scale phenomenon and is ideally identified using such observations.

3.1.3. Dark Clouds. The dark cloud L1622 has been extensively studied since it provided the first confirmed detection of an anomalous microwave excess in its SED [48]. Although included in a number of catalogues of starless clouds [105, 106] it in fact contains a host of low-mass star formation with at least 32 [107] young stellar objects and pre-main sequence stars contained in its depths. Notable amongst these is the binary weak-line T Tauri system HBC 515 at the cometary head of the cloud, which is one of the visually brightest known low-mass young stars [108] and is surrounded by the bright reflection nebula Parsamian 3 [44]. The larger cloud is bright-rimmed indicating that the exterior has been ionized by UV flux from a nearby OB type star, probably σ Ori [45], and this is evident both optically and from $\text{H}\alpha$ images of this region (e.g., [51, 109]). The distance to L1622 is uncertain, with estimates favouring distances of either 120–160 pc [109, 110] or 400–500 pc [110–115]. The current weight of favoured distance is the latter, which I will adopt here.

Unlike HII regions, no radio emission is expected from dark clouds as the ionized fraction is thought to be very low. Casassus et al. [116] made the first resolved centimetre-wave image of L1622 using the CBI telescope [117] and confirmed an excess of emission at $\nu > 20$ GHz consistent with the rising radio spectrum first measured by the Green Bank 140 foot telescope [48]. They also demonstrated that the excess emission was more strongly correlated with *IRAS* $12 \mu\text{m}$ emission than $100 \mu\text{m}$ emission and suggested that this was evidence for the radio emission arising from the small grain population, which is better traced by the $12 \mu\text{m}$ emission. A further interesting detail noted for L1622 was that the cm-wave emission was not correlated spatially with the bright ionized rim of L1622, but was rather distributed across the central regions of the cloud. An investigation of the polarization of this emission [118] found a limit of 2.7 (3.5)% at 2 (3) σ , consistent with that expected from spinning dust models and in line with the findings of Battistelli et al. [94] towards the Perseus molecular cloud.

The well-constrained spectrum of the anomalous emission in L1622 was used to investigate the possibility that the excess could be due to rotational emission from fullerenes and fulleranes (hydrogenated fullerenes; [119]). It was found that the excess could be well fitted by a two component model, with the bulk of the species residing in the dark cloud itself and 10 percent in the surrounding cold neutral medium. Much like PAHs, fullerenes are expected to produce strong line emission in the optical and infrared [120] visible with *Spitzer* observations (e.g., [121, 122]).

The first directed sample of a larger number of dark clouds [123] targeted fourteen small diameter clouds selected from previous submillimetre surveys of isolated star forming regions [124]. From identifications in the sub-mm and

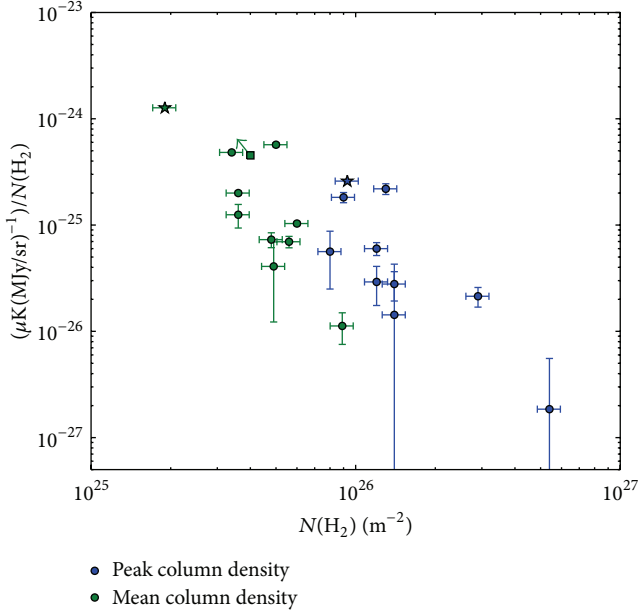


FIGURE 5: Relative emissivity of microwave emission to $100\ \mu\text{m}$ FIR emission as a function of molecular hydrogen column density, $N(\text{H}_2)$, for dark clouds. Clouds from Scaife et al. [123, 125] are shown as filled circles, LDN 1622 [116] is shown as filled stars, and LDN 1621 [128] is shown as a filled square.

infrared, only three of these clouds were assumed to be star-forming, with the remainder classified as starless. Of the fourteen selected clouds two were identified as showing clear signs of an anomalous microwave excess, L675 and L1111 (see also [125]), whilst three further clouds were identified as *possible* candidates, L944, L1103, and L1246. These candidates included two of the three clouds known to be protostellar, L944 and L1246.

The relative emissivity of the two clear detections was found to be in excess of that seen on large scales at high galactic latitude with values of 16.4 ± 1.8 and $28.5 \pm 3.3\ \mu\text{K}\ (\text{MJy}\ \text{sr}^{-1})^{-1}$ for L675 and L1111, respectively, although there are of course clear environmental differences between diffuse emission at high galactic latitudes and the dense molecular gas of dark clouds. Since these sources were selected from sub-mm data, the column density for each object could be constrained directly from the sub-mm flux density using (16).

The five positive detections from this sample of dark clouds were reobserved at higher resolution at radio frequencies [126, 127] in order to establish whether the microwave emission could be localized more precisely and particularly to investigate whether it followed the same distribution as the cold dust traced by sub-mm observations. A significant finding from these observations was that the dark cloud L675, which was assumed to be starless, hosted a compact radio source coincident with the peak of the $850\ \mu\text{m}$ sub-mm emission. A peak in the sub-mm is not sufficient evidence to demonstrate the presence of star formation as starless cores may also exhibit peaked structure. However, the coincidence of a compact sub-mm peak with a radio point

source is strong evidence for protostellar activity [41]. The lack of an infrared point source can be accounted for by the opacity of the dense core, which can often obscure the very earliest stages of protostellar evolution. The presence of a protostar within L675 raised the question of whether it is possible to accurately investigate any correlation of anomalous microwave emission with protostellar activity based on infrared classifications. Investigating this correlation is important not only for providing constraints on physical conditions necessary to produce anomalous microwave emission, but also for assessing the degree of contamination at radio frequencies from protostellar activity. Such contamination is discussed further in Section 4.1.

A further significant result from these high resolution follow-up observations was the first clear morphological correlation of cm-wave radio emission with mid-infrared emission concentrated in *Spitzer* Band 4, indicative of a PAH population [126, 127]. This correlation was detected in the L1246 region, where it had a clear arc-like structure. The remaining objects had no complementary *Spitzer* data available, with the exception of L675, and so the possibility of a similar correlation could not be investigated. However, of the remaining objects only L944 (also star forming) exhibited an unusual morphology in the high resolution observations, with a nebulous radio emission region to the north of the sub-mm core.

For those dark clouds where a microwave excess is detected the degree of emission relative to the FIR $100\ \mu\text{m}$ dust emission appears to be inversely correlated with the column density of molecular hydrogen in the cloud; see Figure 5. The dark cloud sample of Scaife et al. [123] was selected from the sub-mm survey of Visser et al. [124]; and consequently for those objects column densities of molecular hydrogen can be derived directly from the sub-mm flux density (see Table 3 of [124]). Also included in this plot are the dark clouds L1622 and L1621. For L1622 the peak and average column density of molecular hydrogen was derived from the CO measurements of Kun et al. [115] using the relation $N(\text{H}_2)/W(\text{CO}) = 1.8 \times 10^{20}\ \text{cm}^{-2}/\text{K}\ \text{km}\ \text{s}^{-1}$. For L1621 [128], the column density of molecular hydrogen was derived from the ^{13}CO measurements of Park et al. [106] assuming a $^{13}\text{CO}/\text{H}_2$ ratio of 1.7×10^{-6} [129]. These later molecular line measurements are taken along discrete lines of sight through the cloud and, by comparison to the similar measurements for L1622, will provide values intermediate to the peak and average column densities. Consequently the position of L1621 is shown as a limit on the emissivity relative to the mean column density in Figure 5. It is possible that this negative correlation represents the depletion of small grains in denser environments, as proposed by DL98 when considering the environmental conditions in dark clouds. The microwave excess is correlated in a very similar manner with both the peak and mean column density of molecular hydrogen, which have Pearson correlation coefficients of $r = -0.81$ ($P = 0.004$) and $r = -0.83$ ($P = 0.003$), respectively. The slopes of the correlations are correspondingly consistent with values of -2.08 ± 0.53 and -2.77 ± 0.67 .

A similar correlation of 31 GHz intensity with $N(\text{H})$ was demonstrated by Vidal et al. [130], albeit for a less homogeneous sample of clouds, and was also interpreted

as evidence for the microwave emission being associated with the small grain population. The presence of such a correlation is remarkable across so diverse a sample of objects where other environmental conditions such as ionization and temperature vary from source to source, indicating a strong dependence on density.

3.1.4. Reflection Nebulae. Much like dark clouds, reflection nebulae are not expected to emit at radio frequencies as they lack a high degree of ionization. However, significant microwave emission was detected towards the M78 reflection nebula [131], which has been attributed to anomalous microwave emission from spinning dust.

The M78 region is part of the dark cloud L1630 within the Orion molecular cloud. It contains a number of reflection nebulae including NGC 2068, NGC 2071, NGC 2064, and NGC 2067. The nebula NGC 2023, which was used to typify the environmental conditions in reflection nebulae by DL98, is also found in the L1630 dark cloud at a distance of approximately 2.7° from M78. An excess of centimetre-wave emission was detected here using the CBI telescope [131] which was found to be strongly correlated with the infrared emission, although notably here the $12\ \mu\text{m}$ correlation was not stronger than the $100\ \mu\text{m}$ correlation as previously noted by Casassus et al. [116] for L1622, which also hosts a reflection nebula. I note however that the reflection nebulae in these two objects differ somewhat as L1622 is illuminated by low-mass protostars, whereas M78 hosts massive protostars.

3.1.5. Photodissociation Regions. The first, tentative, detection of anomalous microwave emission from a PDR was made with the VSA telescope [50]. This PDR was unusual in nature as it was associated with the supernova remnant (SNR) 3C396 (G39.2–0.3; Green [132]). 3C396 was identified in the *Spitzer* survey of SNRs [133] as having IRAC colours which were not representative of normal interstellar emission; IRAC colours indicated the presence of both shocked ionized gas and two very bright infrared filaments which were identified as PDRs within the SNR, possibly the remnants of old shocks. The excess emission at 33 GHz was significant at the 7σ level, relative to a well-constrained synchrotron spectrum at longer wavelengths.

Strong 31 GHz emission from the ρ -Ophiuchus W PDR was detected with the CBI telescope [134]. Spectrally the emission could not be distinguished from free-free in this case due to a lack of complementary data at lower radio frequencies, and following a detailed study it was concluded that the strong cm-wave emission could have arisen either from spinning dust or from a CII region. Caveats to this were that the CII would have to be optically thick at frequencies $\nu < 10$ GHz, requiring densities and order of magnitude higher than previously supported by the literature for such a region and leading to the conclusion that were such emission to be a real possibility the CII regions would have to be distributed in clumps along the line of sight. Such a situation is not unreasonable as it is also invoked to explain the intermediate radio spectral indices seen in HC/UCHII regions; see Section 2.1.1. However, in this case it was suggested that an AME solution was more preferable, a suggestion supported by the

later results of the *Planck* satellite towards this region; see Section 3.1.2.

3.2. Other Targeted Observations. In addition to the regions suggested by DL98 as potential sources of spinning dust emission there have been a number of other objects associated with star formation which have been targeted.

3.2.1. Planetary Nebulae. An excess of microwave emission towards 18 planetary nebulae was investigated as possibly arising from spinning dust emission by Casassus et al. [135]. The excess in this case was relative to the higher frequency 250 GHz data from the *SIMBA* telescope. In this case the excess was not found to be consistent with a spinning dust spectrum, but instead proposed as dust extinction, as outlined in Section 2, from a population of needle-like grains. A caveat to this explanation is that it requires extremely low temperatures of ≤ 1 K, which are unphysical. The alternative mechanism of synchrotron emission was also considered, but additional caveats such as the lack of evidence for a CRE population in the vicinity of these objects were also raised. The spectral behavior of these objects at radio frequencies is not typical of spinning dust. The SEDs of the sources tend to be flat at radio wavelengths with a dip at $\nu > 100$ GHz, similar to the absorbed free-free spectral model shown in Figure 3(b).

Additional large surveys of 442 planetary nebulae at 30 GHz from the OCRA-p instrument on the Toruń telescope [136] and 62 planetary nebulae (there is substantial overlap between the samples) at 43 GHz, the 32 m INAF-IRA Noto telescope [137], were also examined for any possible excess emission above a free-free spectrum extrapolated from lower radio frequencies. It was concluded that there was no evidence for an excess of emission which could be considered anomalous.

3.2.2. Extragalactic Spinning Dust. The first detection of anomalous microwave emission from an extragalactic star-formation region was made towards the nearby face-on spiral galaxy NGC 6946 [138, 139]. The detection was made during a series of observations targeting 10 star forming regions within NGC 6946 including the starbursting nucleus, as part of a complementary program to the *Spitzer* Infrared Nearby Galaxies Survey (SINGS; [140]) and the project Key Insights on Nearby Galaxies: a Far-Infrared Survey with *Herschel* (KINGFISH; PI: R. Kennicutt) at 33 GHz with the 100 m Green Bank Telescope. In one of the ten regions (extranuclear region 4), an $\approx 7\sigma$ excess was detected with a spectrum that fitted the high frequency side of the spinning dust peak with a column density of $N_{\text{H}} = 3.3 \times 10^{21}\ \text{cm}^{-2}$, within a factor of two of the column density derived from HI measurements [141]. The low frequency side of the spinning dust spectrum was confirmed to be rising by the AMI telescope [126, 127] where a Bayesian model comparison was used to find that a spinning dust spectrum was preferred by the data above a spectrum which included an UCHII component, although the preference was not at a very high level.

4. Connecting Anomalous Microwave Emission to Protostellar Activity

4.1. Radio Emission from YSOs. Observational studies of dark clouds for identifying anomalous microwave emission have largely concentrated on the arcminute scale emission, neglecting the known small-scale radio emission detected from a significant fraction of protostars [142, 143]. As these investigations become more detailed and explore smaller spatial scales, it is necessary to quantify correctly this emission in order to avoid confusing it with that arising from spinning dust when observing at resolutions where the two may not be easily distinguishable. Historically, a large number of radio protostar searches and surveys (e.g., [143–145]) have been made at 3.6 and 6 cm wavelengths due to the general availability and instrumental efficiency of these frequencies. However, most observations targeted at detecting anomalous microwave emission are made at higher radio frequencies where the spectrum of emission due to spinning dust is thought to peak, ~ 1 -2 cm (DL98). Protostellar observations at such frequencies are available towards a number of discrete sources (e.g., [146–150], hereafter AMB99) as well as through the *Spitzer* follow-up surveys of the AMI telescope at 16 GHz [151–153], which were specifically initiated to investigate the potential relationship between radio emission from YSOs and spinning dust following the identification of a new radio YSO in the AME source L675, which was previously classified as starless [126, 127].

The dense natal dust envelopes which surround YSOs can often conceal their embedded protostars at infrared wavelengths. However, the longer wavelength radiation in the radio band does not suffer to the same extent and is capable of penetrating the dust shell to make such objects detectable at radio frequencies. This radio emission is in addition to that of thermal dust, which is expected to have a spectrum that falls off steeply at long wavelengths, and has been observed to possess a spectrum rising with frequency, indicating that it occurs as a consequence of free-free from partially optically thick ionized plasma, see Section 2.1.2, with spectral indices in the range $0.1 \leq \alpha \leq 2$. In more high-mass stars the physics behind the ionization required to produce radio free-free emission is reasonably well understood as arising from photoionization due to the strong UV flux from such objects. For low-mass objects, multiple mechanisms have been proposed to produce the ionization responsible for free-free emission in the immediate vicinity of YSOs. Similarly to the high-mass case, where a high enough ionizing flux is present (generally in later type T Tauri stars), photoionization may also support an embedded HII region [39]. Otherwise a fully ionized stellar wind, again associated more often with premain sequence stars than YSOs, could be responsible for radio emission [21, 154], as could a partially ionized, collimated outflow [20]; see Section 2.1.2 for expected flux densities. Shock ionization, such as that arising from the accretion shock on the surface of protostellar discs, may heat infalling gas sufficiently to produce radio emission [155, 156]. Alternatively the powerful molecular outflows from young protostars may also cause shock ionization as they encounter the surrounding envelope [154, 157, 158], which will produce

a free-free flux density proportional to the outflow force (also called momentum flux), F_{out} , which is equivalent to the rate of outflow momentum and is often calculated as $F_{\text{out}} = P/\tau_{\text{dyn}}$. At a wavelength of 2 cm the expected flux density from such shock ionization can be computed as

$$\left(\frac{S_{\lambda=2\text{cm}}}{\text{mJy}} \right) = 3.4 \times 10^3 \eta \xi(\tau)^{-1} \times \left(\frac{F_{\text{out}}}{M_{\odot} \text{ yr}^{-1} \text{ km s}^{-1}} \right) \left(\frac{d}{\text{kpc}} \right)^{-2} \quad (20)$$

(see [126, 127, 159]), where $\eta = (\Omega/4\pi)$ is the fraction of the stellar wind being shocked and the factor $\xi(\tau) = \tau/(1 - e^{-\tau})$ allows for the fact that the radio emission may not be optically thin [160], although this dependence on the optical depth, τ , is very weak.

In the case of low-luminosity protostars, the last of these mechanisms, that of shock ionization associated with the outflow, is often favoured. Although there is considerable uncertainty in measurements of outflow force, most recovered values for observed protostellar jets are considered energetically viable to explain the observed cm-wave radio emission [143]. Shock ionization along the length of these outflows is also supported by very high angular resolution maps of the radio emission [159, 161]; which have revealed radio emission distributed along molecular outflows or extended in a direction consistent with those outflows. In a few cases, however, the increasing sensitivity of the molecular observations required to determine the outflow force has revealed weaker and weaker outflows (e.g., [162, 163]) where the momentum flux appears insufficient to explain the measured radio emission (e.g., [151]). Again this may be explained in specific cases by uncertainties in estimation of momentum flux [164], although it is likely that in others a combination of the above mechanisms is required to account for the observed radio emission.

A strong correlation between radio and bolometric luminosity has been known for some time in the case of YSOs [143], and recent surveys have shown that this correlation appears to hold towards lower luminosities [153]; see Figure 6(a). These recent surveys have also altered the historical bias of radio observations of protostars towards higher luminosities, as can be seen in the grey hatched area of Figure 6(b). This bias was largely a consequence of observational constraints and ongoing improvements in instrumental sensitivity have allowed this distribution increasingly to tend more towards that recovered from blind infrared surveys, although there are still substantial improvements to be made. At low luminosities, potentially large populations of YSOs, as predicted by theoretical models of YSO evolution (e.g., [165]; red hatched area), still remain to be discovered. However, the measured correlation may allow one to predict the contribution of protostars, where identified, to the integrated microwave emission from star forming regions based on their measured bolometric luminosities. The level of this ‘‘contamination’’ when identifying the amount of anomalous microwave emission on large scales is expected to be low given current observational evidence, with typical radio flux densities

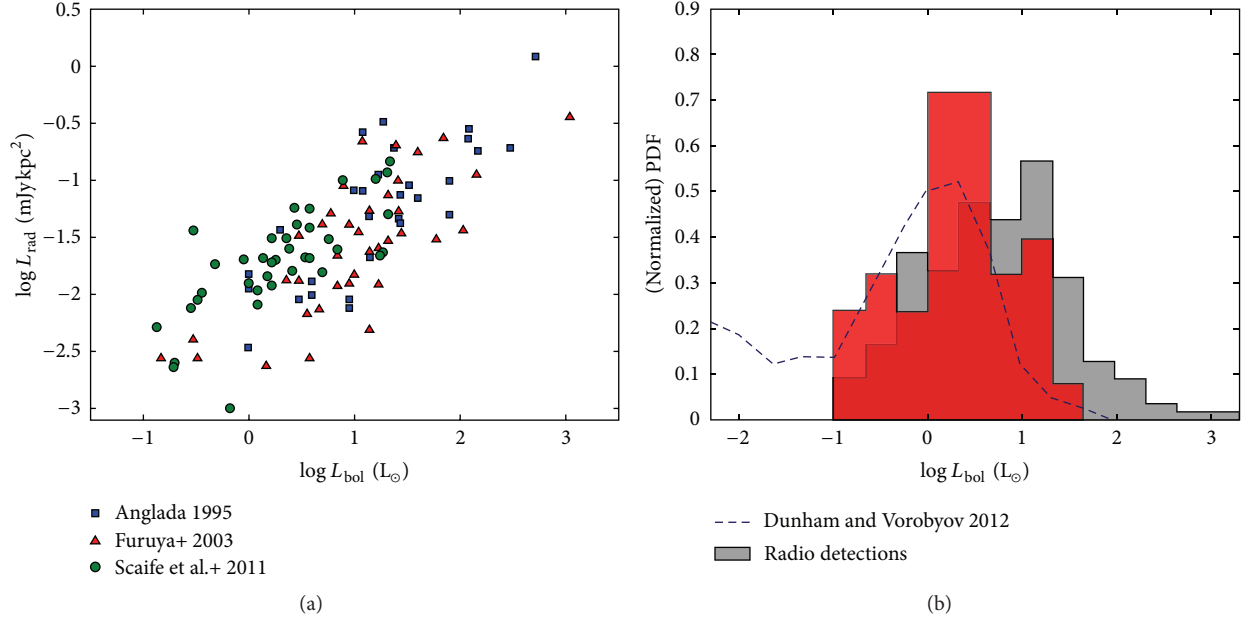


FIGURE 6: (a) Distribution of radio luminosity, L_{rad} , with bolometric luminosity, L_{bol} , for YSOs (figure reproduced from [164]); (b) distribution of radio detected YSOs as a function of bolometric luminosity, compared to the expected distribution of YSOs from Dunham and Vorobyov [165]. Grey hatching indicates objects from the combined catalogues of Anglada [143], Furuya et al. [188], and Scaife et al. [151–153]. Red hatching indicates the objects detected at 16 GHz [151–153].

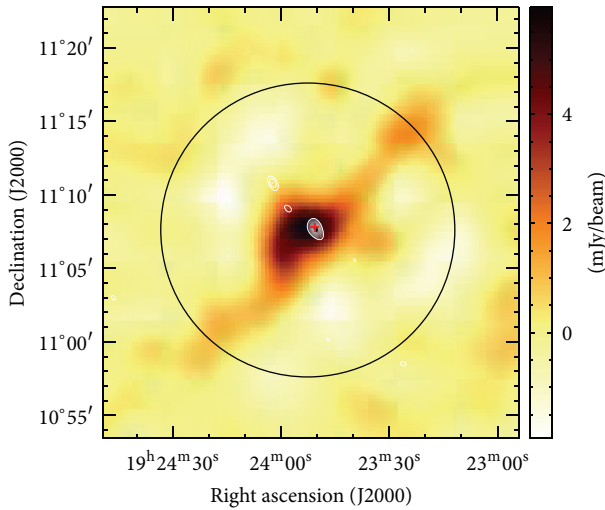


FIGURE 7: L675 star-forming dark cloud. Greyscale shows the anomalous emission on large scales as observed with the AMI telescope [123, 125], and white contours show the compact radio emission from the proposed YSO [126, 127] with contours at intervals of $5\sigma_{\text{rms}}$. The position of the sub-mm peak from 850 μm data [124] is marked as a red cross.

for young stellar objects in the range 100–500 μJy . Even considering the possibility of a population of YSOs missed by infrared surveys due to opacity effects, it seems unlikely that such radio emission can account for the anomalous component due to spinning dust as, in addition to the low flux densities expected from such objects, the emission from YSOs is in general highly compact (although there are

notable exceptions, e.g., CB188; [151]), whereas the anomalous microwave emission attributed to spinning dust appears on much larger scales; see Figure 7.

A connection between the presence of active star formation within a dark cloud and the identification of a spinning dust component is more difficult to quantify. The observational uncertainties surrounding the identification of heavily embedded, low luminosity YSOs have led to the proposition that many clouds currently considered to be starless, including a number not previously thought to even be undergoing collapse, do in fact host star formation. This possibility creates complications when investigating the correlation of those clouds hosting star formation with those which are associated with anomalous microwave emission, as highlighted by the case of L675 [126, 127] and this remains an important open question. However, the possibility that the excess radio emission associated with spinning dust may be confused by radio emission from YSOs seems remote.

Indeed the inverse correlation of spinning dust emissivity with column density of molecular hydrogen, see Figure 5, suggests that the anomalous emission is in particular *not* associated with the earliest stages of star formation, which tend to occur in more dense environments. This premise also seems to be supported by the distribution of large scale anomalous radio emission in the Perseus molecular cloud. The morphology of this emission avoids the densest regions of star formation traced by sub-mm emission, Figure 8, where the youngest objects are found [89, 90] but are more correlated with the 24 μm emission traced by *Spitzer* MIPS [95].

4.2. PAH Populations in Star Formation Regions and the Interstellar Radiation Field. The connection between anomalous

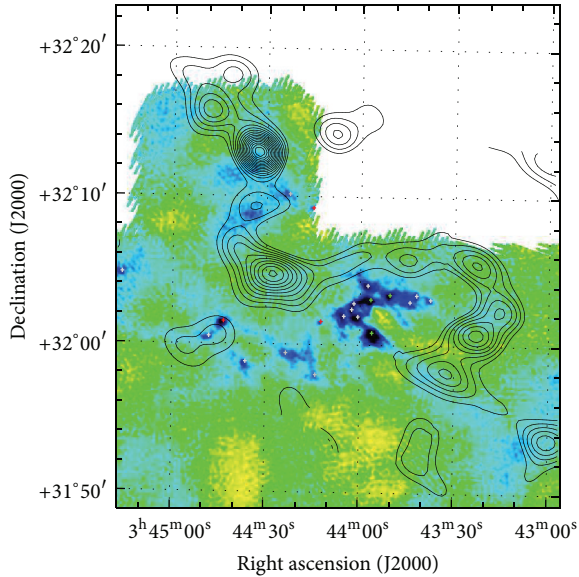


FIGURE 8: Perseus molecular cloud. Contours show radio emission at 16 GHz from the AMI telescope [189] with contours at intervals of $0.25 \text{ mJy beam}^{-1}$ ($\sim 5\sigma$) overlaid on greyscale $850 \mu\text{m}$ data from SCUBA ([89, 90]; J. Hatchell, priv. comm.). The greyscale has been saturated at $500 \text{ mJy beam}^{-1}$ (dark blue) to bring out the large-scale features. Crosses indicate the positions of Class 0 (green), Class I (red), and starless cores (grey).

microwave emission and polycyclic aromatic hydrocarbon (PAH) molecules was suggested by DL98, who attributed the emission to such very small grains. These PAH molecules represent the extension at small sizes of the standard grain size distribution (e.g., MRL; see Section 2.2) to molecular dimensions. Such grains are abundant and ubiquitous in the ISM and are generally identified in the mid-infrared (MIR) where stochastic heating from UV photons leads to spectral emission lines at $3.3, 6.2, 7.7, 8.6,$ and $11.3 \mu\text{m}$ [166]. Within the dust population it is largely these very small grains/molecules control the overall heating and ionization balance in the ISM and they consequently constitute a very important component in the evolution and chemical balance of star formation regions [167]. Since the strength and prevalence of PAH emission features trace the UV flux, PAH emission has also been proposed as a tracer of star formation [168]. PAH features are particularly bright in the local environment of early type stars such as those associated with HII regions and reflection nebulae (RNe), although they are also detected in the diffuse ISM, planetary nebulae (PNe), and on the surface of protoplanetary disks, as well as in low redshift extragalactic sources such as AGN. The PAH molecules themselves are expected to be produced by fragmentation of larger graphitic grains primarily through the action of interstellar shocks such as those produced by supernovae [169]. However, identifying regions of PAHs associated directly with known supernova remnants (SNRs) is problematic due to projection effects as well as a potential lack of UV illumination necessary for PAH line emission. In a sample of 95 supernova remnants only four were identified in a *Spitzer* survey as having IR

colours suggestive of PAH populations [133], including the SNR 3C396 (see Section 3.1.5).

Although PAH emission is seen from such a wide variety of galactic objects, the relative strength of this emission to the FIR continuum varies as a function of source type. This is of course true for the dust continuum also; HII regions show a strong dust continuum from thermal dust emission with relatively weak PAH spectral features, whereas objects such as RNe have much weaker thermal dust continua due to their lower temperature, but stronger PAH line emission. There is a reasonably smooth trend in the emission of such objects from those with a strong thermal continuum and little PAH line emission, such as that seen in compact HII regions, to those with stronger line emission and weaker continuum, such as the diffuse ISM and RNe. This evolution is illustrated in Figure 9(a), which is adapted from the empirical results of Peeters et al. [168]. Certainly this evolution also has a dependence on local conditions and environment, and a key example of this is the Orion Bar (indicated in Figure 9(a)) which is considered an optically visible, that is, more transparent, HII region and is more similar in terms of the ratio of line emission to continuum to RNe than compact HII regions.

The strength of PAH line emission is also related to the interstellar radiation field (ISRF), which is typically normalized to the measurements of Habing (an alternately used normalization is that of Draine [170]) [171] from which the energy density of the ISRF is $1.6 \times 10^{-3} \text{ erg cm}^{-2} \text{ s}^{-1}$. The normalized ISRF is denoted G_0 (see, e.g., [172]). The ratio of this PAH strength to FIR continuum is an indicator of the abundance ratio of PAH molecules to larger dust grains as it measures the relative number of photons from the ISRF absorbed by the PAH molecules relative to those dust grains. For HII regions the amount of PAH line emission relative to the FIR continuum is reasonably uniform for a broad range of G_0 (approximately three orders of magnitude), see Figure 9(b), before sharply decreasing at $G_0 \approx 10^6$. Observationally more compact regions of HII have higher values of G_0 due to their higher UV photon flux but their PAH line emission is reduced, possibly due to destruction of the PAH molecules by strong UV flux or alternatively by increased absorption of the UV photons by larger dust grains in the higher density environment. Certainly PAH molecules “compete” more successfully for UV photons in diffuse regions [168] such as RNe, as indicated in Figure 9(b). The Orion Bar is also indicated in this plot as it is a well-known outlier. The microwave emission from very small spinning dust grains, proposed to be PAH molecules, is expected to be largely independent of the ISRF (DL98), while the strength of line emission from PAH molecules is expected to depend approximately linearly on the ISRF [173]. Consequently the ratio of continuum microwave emission to PAH emission line strength, both arising from a population of PAHs, should be inversely proportional to the ISRF [134]. Accordingly direct correlation studies between microwave emission and MIR tracers of PAH emission should have the MIR data corrected for the ISRF, and indeed this has shown to lead to tighter correlation of these data [130].

In spite of the global trends illustrated in Figure 9 the relationship between PAH emission and the ISRF in

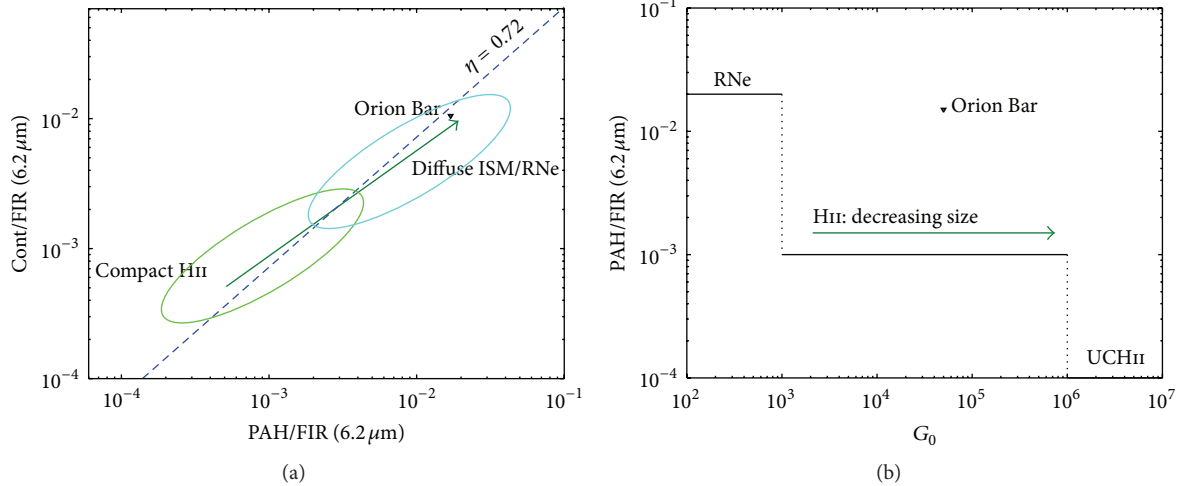


FIGURE 9: (a) Relationship between the ratio of $6.2 \mu\text{m}$ emission line feature to the FIR continuum and the ratio of $6.2 \mu\text{m}$ continuum to FIR continuum for typical galactic objects such as HII regions, RNe, and the diffuse ISM. The dashed line indicates the PAH continuum ratio of 0.72; see text for details. (b) Ratio of $6.2 \mu\text{m}$ emission line feature to the FIR continuum as a function of the ISRF, G_0 , for a range of galactic objects. Figures adapted from Peeters et al. [168].

individual objects is heavily dependent on local conditions and can vary by a significant degree within a source. Furthermore, in contrast to the proposed connection of anomalous microwave emission to PAHs (DL98), the observed correlation of anomalous microwave emission within individual regions has been shown to be a stronger function of ISRF than PAH mass abundance on both large scales in the Perseus molecular cloud [92] and smaller scales within the RCW 175 HII region [76].

5. Observational Issues

There are a number of observational issues which affect the identification of spinning dust emission. These stem from the fact that in order to make a (nonstatistical) detection the SED of the observed object must be well constrained from 1–100 GHz. This presents an immediate problem in terms of available data, with objects that are heavily studied at $\nu \approx 1$ GHz generally not being studied at $\nu \approx 100$ GHz and vice versa. Consequently there is often a gap in available data on either the rising, or the falling, side of the spinning dust SED leaving an uncertainty. This was the case for the Helix planetary nebula which was originally misidentified as having a spinning dust component to its spectrum [174] due to a lack of data at lower radio frequencies concealing the fact that it in fact had a spectrum consistent with free-free emission [123, 125]. Aside from this issue there are also two other circumstances which may contribute significantly to the limitation of identifying an excess of emission at microwave frequencies relative to other mechanisms.

5.1. Calibration Scales. The majority of radio telescopes operating from 1–15 GHz are calibrated from the scale of Baars et al. ([175]; B77), although notable exceptions to this are the Effelsberg 100 m telescope and the Westerbork Synthesis Radio Telescope (WSRT) which employ subtly different flux

density scales. Outside this frequency range, the B77 flux scale is known to have a number of issues. At low frequencies it is affected by the secular decrease of Cas A (e.g., [176]), and at higher frequencies it is both incomplete and the resolved structure of Cas A which becomes visible at the higher resolution of many telescopes at shorter wavelengths starts to become an issue. Additionally, for comparison of datasets compiled over long periods of time, the secular decrease of Cas A (and indeed Tau A) must also be accounted for.

Unlike radio telescopes, submillimetre instruments are typically calibrated from planets or bright planetary nebulae. For example the *SCUBA* instrument at the JCMT uses Mars, Uranus, and Neptune as primary calibrators. Long term radio monitoring of Mars has shown that the flux scale of B77 is low relative to the Mars scale at $\nu > 4$ GHz (Rick Perley, priv. comm.). Without correction, this discrepancy can create an artificial excess of emission at frequencies above 4 GHz relative to longer wavelengths. CMB instruments also tend to utilise planets for calibration, notably Jupiter for the ground-based CBI and VSA telescopes [177] as well as for space-based missions such as *WMAP* [178].

More recently the Perley-Butler 2010 flux scale which uses the emission of Mars at frequencies $\nu > 5$ GHz as predicted by the model of Rudy et al. [179] and adjusted to the absolute *WMAP* emission scale [178] has become a broad frequency standard for 1–50 GHz. However, older archival flux densities may often be tied to scales which differ by several percents and are only valid over certain frequency ranges.

5.2. Flux Loss Issues. A further issue with compiling spectra over a range of frequencies is that in the case of extended objects two telescopes operating at the same frequency may measure completely different flux densities depending on the range of angular scales to which they are sensitive. For synthesis telescopes (interferometers), this may involve the loss of flux density not only on angular scales larger than the

shortest separation of their elements, but also on intermediate scales where there is a gap in the *uv*-coverage. This is a particular problem when comparing flux densities from CMB synthesis telescopes which are specifically designed to be sensitive to larger angular scales, with lower radio frequency telescopes designed for examining extragalactic radio sources on small angular scales. This difference can artificially create an excess of emission, which may then be interpreted as anomalous. Particular care must be taken in cases where aperture photometry is used to ensure that appropriate angular scales are measured in all constituent datasets.

6. Where Do We Go from Here?

Currently the bulk of observational data on anomalous microwave emission comes from CMB experiments, which probe large angular scales, and these studies are aimed at detecting the continuum radio emission. Large angular scales are important for identifying regions where anomalous microwave emission is significant as available data indicates that the bulk of the radio signal occurs on these scales. However, information on small angular scales is crucial for probing star formation and circumstellar environments in more detail and understanding the anomalous microwave emission with respect to different ISM conditions requires sufficient resolution to separate distinct environments. Increasingly, galactic surveys undertaken from a non-CMB perspective are expected to contribute to the field of AME science, including those mentioned later in this section, and probe the connections between star formation and spinning dust. Understanding this relationship is important not only in terms of examining the microwave emission itself, but also in terms of probing the VSG and PAH dust populations. VSGs play an important role in the chemical and thermal balance of the ISM; see Section 4.2; in addition to controlling the ionization fraction and temperature of the ISM, the smallest grains account for most of the surface area available for catalysis of molecular formation and the potential information which might be provided by the AME data in this regard is currently largely unexplored.

The existence of VSGs is supported by the physical manifestations of their reprocessing of incident starlight. Such reprocessing by a substantial population of carbonaceous nanoparticles could potentially account for both IR emission features and the strong mid-infrared emission component seen by IRAS. However, the true size distribution of VSGs is poorly known as studies of interstellar extinction are relatively insensitive to its details. The MRN dust size distribution is assumed to significantly underestimate the fraction of ISM carbon content contained in this nanoparticle population and was accordingly modified by DL98 in their spinning dust model to include a significant population of VSGs, assumed to be largely PAH molecules.

Observationally determining the true extent of this VSG/PAH population is nontrivial. The MIR spectral emission features produced by PAHs are only produced when the molecules are subjected to a strong UV flux, which is often absent in the case of heavily embedded pre- and protostellar objects due to local opacity effects. In this respect, spinning

dust emission will provide a highly complementary measure of the small grain population to MIR PAH emission in the absence of favorable excitation conditions. At high resolution the anticipated MeerGAL survey at 14 GHz, and additionally the proposed ALMA Band 1 instrument [180] will constrain the spinning dust SED at similar resolution to, for example, *Spitzer* or the forthcoming MIRI instrument on the JWST. With such resolution it may be possible to measure the size distribution of VSGs directly from the data. These constraints will also be important in the context of circumstellar and protoplanetary disks, where the proposed population of VSGs may have important implications for disk evolution. Indeed MIR emission lines from PAH molecules have been detected from the disks around Herbig Ae/Be stars [181], indicating that there is a substantial population of these VSGs present—at least on the surface of the disk where they are irradiated by the central star. However, they have not yet been detected in protoplanetary disks due to a lack of strong UV flux. Since spinning dust emission has been observed to be spatially correlated with PAH emission [123], spinning dust may provide a unique window on the small grain population of these disks. Measurements of the true density and mixing of the PAHs through the disk are not possible using their MIR emission, which is dependent on a strongly ionizing incident UV flux to which only the thin exterior layers of the disk are exposed. In contrast, the rotational emission from these grains that occurs in the microwave regime is dependent on the integrated column density through the disk and may provide useful constraints on whether the VSGs contribute substantially to the disk dust population [182].

In addition to targeted studies with ALMA Band 1, at high angular resolution the new MeerKAT telescope will provide an invaluable resource with its uniquely fast survey speed at 14 GHz. The MeerKAT telescope will have a smaller aperture than the currently available Jansky Very Large Array (JVLA), the consequence of which is that the number of pointings for a 14 GHz survey is comparable to that of an JVLA 5 GHz survey (e.g., CORNISH; [183]). Combining this field-of-view with broadband feeds and the large collecting area resulting from 80 antennas means that MeerKAT has a 14 GHz survey speed over 3 times faster than the JVLA (SKA Memo 40). By working at high frequencies, it gains an additional factor for positive spectral index sources: a MeerKAT 14 GHz survey is over 14 times faster than an JVLA 5 GHz survey would be [184]. The planned MeerGAL survey, the first sensitive arc-second resolution 12–14 GHz survey of the galactic plane, will be carried out using MeerKAT. The primary aim of this survey is to discover and characterise the population of steep positive spectrum objects in the galaxy and search for variability in their flux densities.

A balance between the high resolution data that will be available from instruments such as MeerKAT, ALMA, and the JVLA and the low resolution data from CMB experiments such as *Planck* will be provided by surveys such as the AMI 16 GHz galactic plane survey (AGPS; [185]). With sensitivity to arcminute scales, the AGPS will provide a highly useful resource for identifying regions of anomalous emission on scales of 2–16 arcmin. At this resolution it will be highly effective at isolating this emission relative to the larger scales

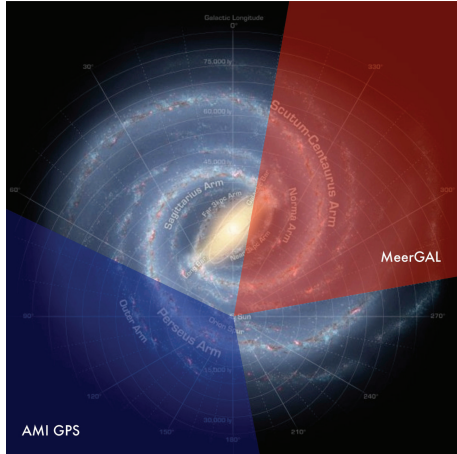


FIGURE 10: Galactic coverage of the MeerGAL [184] and AMI Galactic Plane Survey [185]. Background image credit: Robert Hurt (SSC Caltech)/NASA/JPL-Caltech.

(≈ 30 arcmin) measured from all-sky data at 30 GHz with the *Planck* satellite. The AGPS covers the outer galactic plane between $55 \leq \ell \leq 187$ and galactic latitudes of $|b| < 5$; see Figure 10. The AMI telescope has already been successful in providing new identifications of spinning dust and the AGPS offers an excellent opportunity to search new areas of sky aside from pointed observations of known objects.

There is a paucity of surveys currently available in this frequency range due to the comparative expense in terms of observing time of working at higher radio frequencies for fixed aperture telescopes. The cost of a survey with a given sensitivity using a fixed aperture telescope scales as steeply as $\nu^{3.4}$ for objects with negative or slowly falling spectral indices and consequently a 14 GHz survey is 150–2500 times as expensive as a 1.4 GHz survey depending on the spectral index of the objects searched for [184]. This has led to a prevalence of low radio frequency surveys, optimal for identifying steep spectrum nonthermal sources. Unfortunately these surveys therefore have a strong selection bias against rising spectrum objects, such as the ultra- and hypercompact HII regions described in Section 2.1.1 and allowing HCHII regions to remain completely undetected in radio surveys at frequencies below 5 GHz until being discovered serendipitously in high frequency observations of UCHII regions. The linear dependence of the turn-over frequency from the optically thick to optically thin thermal bremsstrahlung regime on emission measure, see Section 3.1.1, means that these low frequency surveys preferentially detect objects with low plasma densities and select against dense plasmas. These dense plasmas include not only UC/HCHII regions but also massive stellar winds, ionized jets from low-mass YSOs, and young planetary nebulae [186]. Sources which exhibit anomalous microwave emission due to spinning dust are not dense plasma objects, but due to their rising spectrum from low frequencies they suffer the same bias, which may explain the only relatively recent observational identification of this emission mechanism. It is in part due to this bias that we currently have an incomplete understanding of the

physical properties of the objects listed above, not only on an individual basis but also in terms of their underlying populations. From the few major surveys that have been carried out at ~ 15 GHz, for example, the 9C Ryle Telescope survey [187] and the AT20G survey [138, 139], data are too shallow and/or have sensitivity to a restricted range of (small) angular scales, making it difficult to adequately identify different populations in the highly confused galactic plane.

7. Conclusions

Although observational correlations between the degree of detected anomalous microwave emission and other physical characteristics are emerging for a range of physical conditions, see, for example, Sections 3.1.3 and 4.2, one of the remaining issues is the number of objects that are not detected yet have physical conditions similar to those which are detected. This suggests the existence of a further important physical parameter in the study of spinning dust which has not currently been identified. Doubtless, larger datasets will assist with this characterization but it may be that clues exist in the current data.

Certainly the emerging impression is that those regions of lower density where the ISRF is high provide the most promising environments for detecting anomalous microwave emission. These conditions are linked in the sense that the effective incidence of UV photons on the small grain population is affected by both: a higher ISRF provides a larger incidence rate whereas higher density regions suffer from absorption of UV photons by larger grains. However, a balance is required as the very high ISRF found in some regions may also lead to destruction of the very small grain population.

The prospects for rapid progress in this field are good. Starting from what remains a low level of understanding concerning the necessary triggering mechanisms or local environments suitable for anomalous microwave emission, many questions will be asked and answered with every new dataset that is taken. Whilst information on large scales will be provided by instruments such as the *Planck* satellite, on the smaller scales necessary for probing different environments internal to and in the vicinity of star-formation regions the current and future centimetre-wave surveys with AMI, MeerKAT, and ALMA will undoubtedly contribute extensively to improving our understanding in this area, as will advanced mid-infrared data from instruments such as MIRI on the JWST. In conjunction with further theoretical developments, this combination offers an excellent vehicle for furthering our comprehension of an emission mechanism which is becoming increasingly less anomalous.

References

- [1] C. F. McKee and J. P. Ostriker, “A theory of the interstellar medium—three components regulated by supernova explosions in an inhomogeneous substrate,” *The Astrophysical Journal*, vol. 218, pp. 148–169, 1977.
- [2] S. R. Kulkarni and C. Heiles, “The atomic component,” *Astrophysics and Space Science Library*, vol. 134, pp. 87–122, 1987.

- [3] R. McCray and T. P. Snow Jr., "The violent interstellar medium," *Annual Review of Astronomy & Astrophysics*, vol. 17, pp. 213–240, 1979.
- [4] D. J. Hollenbach and A. G. G. Tielens M., "Photodissociation regions in the interstellar medium of galaxies," *Reviews of Modern Physics*, vol. 71, pp. 173–230, 1999.
- [5] R. B. Larson, "Turbulence and star formation in molecular clouds," *Monthly Notices of the Royal Astronomical Society*, vol. 194, pp. 809–826, 1981.
- [6] M. M. Mac Low and R. S. Klessen, "Control of star formation by supersonic turbulence," *Reviews of Modern Physics*, vol. 76, pp. 125–194, 2004.
- [7] E. M. Leitch, A. C. S. Readhead, T. J. Pearson, and S. T. Myers, "An anomalous component of galactic emission," *Astrophysical Journal Letters*, vol. 486, no. 1, pp. L23–L26, 1997.
- [8] B. T. Draine, "Interstellar dust grains," *Annual Review of Astronomy & Astrophysics*, vol. 41, pp. 241–289, 2003.
- [9] A. Leger and J. L. Puget, "Identification of the "unidentified" IR emission features of interstellar dust?" *Astronomy & Astrophysics*, vol. 137, no. 1, pp. L5–L8, 1984.
- [10] V. Ossenkopf and T. Henning, "Dust opacities for protostellar cores," *Astronomy & Astrophysics*, vol. 291, no. 3, pp. 943–959, 1994.
- [11] J. S. Greaves and W. K. M. Rice, "Do all Sun-like stars have planets? Inferences from the disc mass reservoirs of Class 0 protostars," *Monthly Notices of the Royal Astronomical Society*, vol. 412, pp. L88–L92, 2011.
- [12] D. Burstein and C. Heiles, "H I, galaxy counts, and reddening—variation in the gas-to-dust ratio, the extinction at high galactic latitudes, and a new method for determining galactic reddening," *The Astrophysical Journal*, vol. 225, pp. 40–55, 1978.
- [13] B. T. Draine and A. Lazarian, "Electric dipole radiation from spinning dust grains," *Astrophysical Journal Letters*, vol. 508, no. 1, pp. 157–179, 1998.
- [14] L. Oster, "Emission and absorption of thermal radio radiation," *The Astrophysical Journal*, vol. 134, pp. 1010–1013, 1961.
- [15] L. Oster, "Free-free emission in the radio-frequency range," *The Astronomical Journal*, vol. 66, p. 50, 1961.
- [16] W. Altenhoff, P. G. Mezger, H. Wendker, and G. Westerhout, "Meßprogramme bei der Wellenlänge 11 cm am 25 m-Radioteleskop Stockert," *Veröffentlichungen der Königlichen Sternwarte zu Bonn*, no. 59, p. 48, 1960.
- [17] S. Kurtz, "Hypercompact HII regions," in *Proceedings of the International Astronomical Union (IAUS '05)*, Symposium 227, pp. 111–119, 2005.
- [18] R. Ignace and E. Churchwell, "Free-free spectral energy distributions of hierarchically clumped H II regions," *The Astrophysical Journal*, vol. 610, no. 1, pp. 351–360, 2004.
- [19] C. Chiuderi and G. T. Ciamponi, "Polytropic models of radio stars," *Astronomy & Astrophysics*, vol. 69, pp. 333–339, 1978.
- [20] S. P. Reynolds, "Continuum spectra of collimated, ionized stellar winds," *The Astrophysical Journal*, vol. 304, pp. 713–720, 1986.
- [21] N. Panagia and M. Felli, "The spectrum of the free-free radiation from extended envelopes," *Astronomy & Astrophysics*, vol. 39, pp. 1–5, 1975.
- [22] S. P. Reynolds, "Continuum spectra of collimated, ionized stellar winds," *The Astrophysical Journal*, vol. 304, pp. 713–720, 1986.
- [23] R. L. Brown, F. J. Lockman, and G. R. Knapp, "Radio recombination lines," *Annual Review of Astronomy & Astrophysics*, vol. 16, pp. 445–485, 1978.
- [24] F. J. Lockman, D. J. Pisano, and G. J. Howard, "Detection of 130 "diffuse" galactic H II regions," *Astrophysical Journal Letters*, vol. 472, no. 1, pp. 173–182, 1996.
- [25] R. A. Gaume, W. M. Goss, H. R. Dickel, T. L. Wilson, and K. J. Johnston, "The NGC 7538 IRS 1 region of star formation: observations of the H66 α recombination line with a spatial resolution of 300 AU," *Astrophysical Journal Letters*, vol. 438, no. 2, pp. 776–783, 1995.
- [26] G. F. Smoot, "Galactic Free-free and H-alpha Emission," <http://arxiv.org/abs/astro-ph/9801121>.
- [27] R. Dong and B. T. Draine, "H α and free-free emission from the warm ionized medium," *The Astrophysical Journal*, vol. 727, p. 35, 2011.
- [28] R. H. Hildebrand, "The determination of cloud masses and dust characteristics from submillimetre thermal emission," *Quarterly Journal of the Royal Astronomical Society*, vol. 24, pp. 267–282, 1983.
- [29] J. Rodmann, T. Henning, C. J. Chandler, L. G. Mundy, and D. J. Wilner, "Large dust particles in disks around T Tauri stars," *Astronomy & Astrophysics*, vol. 446, no. 1, pp. 211–221, 2006.
- [30] D. Lommen, C. M. Wright, S. T. Maddison et al., "Investigating grain growth in disks around southern T Tauri stars at millimetre wavelengths," *Astronomy & Astrophysics*, vol. 462, pp. 211–220, 2007.
- [31] J. B. Pollack, D. Hollenbach, S. Beckwith, D. P. Simonelli, T. Roush, and W. Fong, "Composition and radiative properties of grains in molecular clouds and accretion disks," *Astrophysical Journal Letters*, vol. 421, no. 2, pp. 615–639, 1994.
- [32] J. S. Mathis, W. Rumpl, and K. H. Nordsieck, "The size distribution of interstellar grains," *The Astrophysical Journal*, vol. 217, pp. 425–433, 1977.
- [33] B. T. Draine, "On the submillimeter opacity of protoplanetary disks," *The Astrophysical Journal*, vol. 636, no. 2, pp. 1114–1120, 2006.
- [34] H. Tanaka, Y. Himeno, and S. Ida, "Dust growth and settling in protoplanetary disks and disk spectral energy distributions. I. Laminar disks," *Astrophysical Journal Letters*, vol. 625, no. 1, pp. 414–426, 2005.
- [35] F. Boulanger and M. Perault, "Diffuse infrared emission from the galaxy. I—solar neighborhood," *The Astrophysical Journal*, vol. 330, pp. 964–985, 1988.
- [36] L. D. Anderson, A. Zavagno, L. Deharveng et al., "The dust properties of bubble H II regions as seen by *Herschel*," *Astronomy & Astrophysics*, vol. 542, article A10, 2012.
- [37] T. Preibisch, V. Ossenkopf, H. W. Yorke, and T. Henning, "The influence of ice-coated grains on protostellar spectra," *Astronomy & Astrophysics*, vol. 279, pp. 577–588, 1993.
- [38] B. T. Draine and H. M. Lee, "Optical properties of interstellar graphite and silicate grains," *The Astrophysical Journal*, vol. 285, pp. 89–108, 1984.
- [39] E. Churchwell, M. G. Wolfire, and D. O. S. Wood, "The infrared emission from dust surrounding newly formed O stars," *Astrophysical Journal Letters*, vol. 354, no. 1, pp. 247–261, 1990.
- [40] L. F. Rodriguez, J. Marti, J. Canto, J. M. Moran, and S. Curiel, "Possible radio spectral indices from inhomogeneous free-free sources," *Revista Mexicana De Astronomia Y Astrofisica*, vol. 25, no. 1, pp. 23–229, 1993.
- [41] P. Andre, D. Ward-Thompson, and M. Barsony, in *Proceedings of the Protostars and Planets Conference*, p. 59.
- [42] G. H. Herbig, "The spectra of Be- and Ae-TYPE stars associated with nebulosity," *The Astrophysical Journal*, vol. 4, p. 337, 1960.

- [43] G. H. Herbig, "Eruptive phenomena in early stellar evolution," *The Astrophysical Journal*, vol. 217, pp. 693–715, 1977.
- [44] E. S. Parsamian, "Catalogue of cometary nebulae discovered on Palomar maps," *Izv. Akad. Nauk Armyan*, vol. 18, pp. 146–148, 1965.
- [45] B. Reipurth, G. Herbig, and C. Aspin, "The multiple pre-main-sequence system HBC 515 in L1622," *The Astronomical Journal*, vol. 139, no. 4, pp. 1668–1680, 2010.
- [46] D. J. Hollenbach, in *Astronomical Society of the Pacific Conference Series (ASPC '90)*, vol. 12, p. 167, 1990.
- [47] R. Timmermann, F. Bertoldi, C. M. Wright et al., "H₂ infrared line emission from S140: a warm PDR," *Astronomy & Astrophysics*, vol. 315, no. 2, pp. L281–L284, 1996.
- [48] D. P. Finkbeiner, D. J. Schlegel, C. Frank, and C. Heiles, "Tentative detection of electric dipole emission from rapidly rotating dust grains," *Astrophysical Journal Letters*, vol. 566, no. 2, pp. 898–904, 2002.
- [49] C. Dickinson, S. Casassus, J. L. Pineda, T. J. Pearson, A. C. S. Readhead, and R. D. Davies, "An upper limit on anomalous dust emission at 31 GHz in the diffuse cloud [LPH96] 201.663+1.643," *The Astrophysical Journal*, vol. 643, no. 2, pp. L111–L114, 2006.
- [50] A. Scaife, D. A. Green, R. A. Battye et al., "Constraints on spinning dust towards Galactic targets with the Very Small Array: a tentative detection of excess microwave emission towards $_3C_{39.6}$," *Monthly Notices of the Royal Astronomical Society*, vol. 377, pp. L69–L73, 2007.
- [51] J. E. Gaustad, P. R. McCullough, W. Rosing, and D. Van Buren, "A robotic wide-angle H α survey of the southern sky," *Publications of the Astronomical Society of the Pacific*, vol. 113, no. 789, pp. 1326–1348, 2001.
- [52] P. R. McCullough and R. R. Chen, "An alternative to spinning dust for the microwave emission of LPH 201.663+1.643: an Ultracompact H II Region," *The Astrophysical Journal Letters*, vol. 566, no. 1, article L45, 2002.
- [53] C. Dickinson, R. D. Davies, L. Bronfman et al., "CBI limits on 31 GHz excess emission in southern H II regions," *Monthly Notices of the Royal Astronomical Society*, vol. 379, no. 1, pp. 297–307, 2007.
- [54] A. M. M. Scaife, N. Hurley-Walker, M. L. Davies et al., "AMI limits on 15-GHz excess emission in northern H II regions," *Monthly Notices of the Royal Astronomical Society*, vol. 385, pp. 809–822, 2008.
- [55] C. Dickinson, R. D. Davies, and R. J. Davis, "Towards a free-free template for CMB foregrounds," *Monthly Notices of the Royal Astronomical Society*, vol. 341, pp. 369–384, 2003.
- [56] E. Churchwell, "Ultra-compact H II regions and massive star formation," *Annual Review of Astronomy and Astrophysics*, vol. 40, pp. 27–62, 2002.
- [57] B. G. Elmegreen, "Triggered star formation," *EAS Publications Series*, vol. 51, pp. 45–58, 2011.
- [58] L. Deharveng, F. Schuller, L. D. Anderson et al., "A gallery of bubbles. The nature of the bubbles observed by *Spitzer* and what ATLASGAL tells us about the surrounding neutral material," *Astronomy & Astrophysics*, vol. 523, article A6, 2010.
- [59] A. Zavagno, L. Deharveng, F. Comerón et al., "Triggered massive-star formation on the borders of Galactic H II regions II. Evidence for the collect and collapse process around RCW 79," *Astronomy & Astrophysics*, vol. 446, no. 1, pp. 171–184, 2006.
- [60] R. Choudhury, B. Mookerjee, and H. C. Bhatt, "Triggered star formation and young stellar population in bright-rimmed cloud SFO 38," *Astrophysical Journal Letters*, vol. 717, no. 2, pp. 1067–1083, 2010.
- [61] M. Todorović, R. D. Davies, C. Dickinson et al., "A 33-GHz very small array survey of the Galactic plane from $\ell = 27^\circ$ to 46° ," *Monthly Notices of the Royal Astronomical Society*, vol. 406, pp. 1629–1643, 2010.
- [62] F. J. Lockman, "A survey of radio H II regions in the northern sky," *The Astrophysical Journal Supplement Series*, vol. 71, pp. 469–479, 1989.
- [63] S. Sharpless, "A catalogue of H II regions," *The Astrophysical Journal Supplement Series*, vol. 4, p. 257, 1959.
- [64] C. Dickinson et al., "Anomalous microwave emission from the H II region RCW175," *The Astrophysical Journal*, vol. 690, no. 2, article 1585, 2009.
- [65] S. J. Carey, F. O. Clark, M. P. Egan, S. D. Price, R. F. Snipman, and T. A. Kuchar, "The physical properties of the Midcourse Space Experiment galactic infrared-dark clouds," *Astrophysical Journal Letters*, vol. 508, no. 2, pp. 721–728, 1998.
- [66] M. P. Egan, R. F. Shipman, S. D. Price, S. J. Carey, F. O. Clark, and M. Cohen, "A population of cold cores in the galactic plane," *Astrophysical Journal Letters*, vol. 494, no. 2, pp. L199–L202, 1998.
- [67] M. Perault et al., "First ISOCAM images of the Milky Way," *Astronomy & Astrophysics*, vol. 315, p. L165, 1996.
- [68] B. T. Lynds, "Catalogue of dark nebulae," *The Astrophysical Journal*, vol. 7, p. 1, 1962.
- [69] J. Kauffmann and T. Pillai, "How many infrared dark clouds can form massive stars and clusters?" *The Astrophysical Journal Letters*, vol. 723, no. 1, article L7, 2010.
- [70] D. Teyssier, P. Hennebelle, and M. Perault, "Radio-millimetre investigation of galactic infrared dark clouds," *Astronomy & Astrophysics*, vol. 382, pp. 624–638, 2002.
- [71] S. J. Carey, P. A. Feldman, R. O. Redman, M. P. Egan, J. M. MacLeod, and S. D. Price, "Submillimeter observations of Midcourse Space Experiment galactic infrared-dark clouds," *The Astrophysical Journal*, vol. 543, no. 2, pp. L157–L161, 2000.
- [72] J. M. Rathborne, J. M. Jackson, R. Simon, and Q. Zhang, "Infrared dark clouds as precursors to star clusters," *Astrophysics and Space Science*, vol. 324, pp. 155–162, 2009.
- [73] N. Peretto and G. A. Fuller, "A statistical study of the mass and density structure of infrared dark clouds," *Astrophysical Journal Letters*, vol. 723, no. 1, pp. 555–562, 2010.
- [74] L. A. Wilcock, J. M. Kirk, D. Stamatellos et al., "The initial conditions of high-mass star formation: radiative transfer models of IRDCs seen in the *Herschel* Hi-GAL survey," *Astronomy & Astrophysics*, vol. 526, article A159, 2011.
- [75] O. Miettinen, M. Hennemann, and H. Linz, "Deuterium fractionation and the degree of ionisation in massive clumps within infrared dark clouds," *Astronomy & Astrophysics*, vol. 534, article A134, 2011.
- [76] C. T. Tibbs, R. Paladini, M. Compiegne, M. C. et al., "A multi-wavelength investigation of RCW175: an HII region harboring spinning dust emission," *The Astrophysical Journal*, vol. 754, no. 2, article 94, 2012.
- [77] M. P. Hobson and J. E. Baldwin, "Markov-chain Monte Carlo approach to the design of multilayer thin-film optical coatings," *Applied Optics*, vol. 43, pp. 2651–2660, 2004.
- [78] K. Arvidsson and C. R. Kerton, "Submillimeter and molecular views of three galactic ring-like H II regions," *The Astronomical Journal*, vol. 141, no. 5, article 153, 2011.
- [79] C. Gordon and R. Trotta, "Bayesian calibrated significance levels applied to the spectral tilt and hemispherical asymmetry," *Monthly Notices of the Royal Astronomical Society*, vol. 382, pp. 1859–1863, 2007.

- [80] R. D. Davies, C. Dickinson, A. J. Banday, T. R. Jaffe, K. M. Górski, and R. J. Davis, "A determination of the spectra of Galactic components observed by the *Wilkinson Microwave Anisotropy Probe*," *Monthly Notices of the Royal Astronomical Society*, vol. 370, pp. 1125–1139, 2006.
- [81] D. J. Schlegel, D. P. Finkbeiner, and M. Davis, "Maps of dust infrared emission for use in estimation of reddening and cosmic microwave background radiation foregrounds," *Astrophysical Journal Letters*, vol. 500, no. 2, pp. 525–553, 1998.
- [82] C. Dickinson, "Anomalous Emission from HII regions," <http://arxiv.org/abs/0808.0473>.
- [83] K. L. Luhman, J. R. Stauffer, A. A. Muench et al., "A census of the young cluster IC 348," *Astrophysical Journal Letters*, vol. 593, no. 2, pp. 1093–1115, 2003.
- [84] C. J. Lada, J. Alves, and E. A. Lada, "Near-infrared imaging of embedded clusters: NGC 1333," *The Astronomical Journal*, vol. 111, no. 5, pp. 1964–1976, 1996.
- [85] B. A. Wilking, M. R. Meyer, T. P. Greene, A. Mikhail, and G. Carlson, "Low-mass stars and substellar objects in the NGC 1333 molecular cloud," *The Astronomical Journal*, vol. 127, no. 2, pp. 1131–1146, 2004.
- [86] K. C. Steenbrugge, J. H. J. De Bruijne, R. Hoogerwerf, and P. T. De Zeeuw, "Radial velocities of early-type stars in the Perseus OB2 association," *Astronomy & Astrophysics*, vol. 402, no. 2, pp. 587–605, 2003.
- [87] G. Meynet and A. Maeder, "Stellar evolution with rotation V. Changes in all the outputs of massive star models," *Astronomy & Astrophysics*, vol. 361, no. 1, pp. 101–120, 2000.
- [88] J. Hatchell, J. S. Richer, G. A. Fuller, C. J. Qualtrough, E. F. Ladd, and C. J. Chandler, "Star formation in Perseus: clusters, filaments and the conditions for star formation," *Astronomy & Astrophysics*, vol. 440, no. 1, pp. 151–161, 2005.
- [89] J. Hatchell, G. A. Fuller, and J. S. Richer, "Star formation in Perseus III. Outflows," *Astronomy & Astrophysics*, vol. 472, no. 1, pp. 187–198, 2007.
- [90] J. Hatchell, G. A. Fuller, J. S. Richer, T. J. Harries, and E. F. Ladd, "Star formation in Perseus II. SEDs, classification, and lifetimes," *Astronomy & Astrophysics*, vol. 468, no. 3, pp. 1009–1024, 2007.
- [91] R. A. Watson, R. Rebolo, J. A. Rubiño-Martín et al., "Detection of anomalous microwave emission in the perseus molecular cloud with the COSMOSOMAS experiment," *The Astrophysical Journal Letters*, vol. 624, no. 2, article L89, 2005.
- [92] C. T. Tibbs, R. A. Watson, C. Dickinson and et al., "Very Small Array observations of the anomalous microwave emission in the Perseus region," *Monthly Notices of the Royal Astronomical Society*, vol. 402, pp. 1969–1979, 2010.
- [93] P. J. Encrenaz, "A new source of intense molecular emission in the rho ophiuchi complex," *The Astrophysical Journal*, vol. 189, p. L135, 1974.
- [94] E. S. Battistelli, R. Rebolo, J. A. Rubiño-Martín et al., "Polarization observations of the anomalous microwave emission in the perseus molecular complex with the COSMOSOMAS experiment," *The Astrophysical Journal Letters*, vol. 645, no. 2, article L141, 2006.
- [95] C. T. Tibbs, N. Flagey, R. Paladini et al., "Spitzer characterization of dust in an anomalous emission region: the Perseus cloud," *Monthly Notices of the Royal Astronomical Society*, vol. 418, pp. 1889–1900, 2011.
- [96] C. A. Kulesa, A. L. Hungerford, C. K. Walker, X. Zhang, and A. P. Lane, "Large-scale CO and [C I] emission in the ρ ophiuchi molecular cloud," *The Astrophysical Journal*, vol. 625, no. 1, pp. 194–209, 2005.
- [97] K. E. Young, M. L. Enoch, N. J. Evans II et al., "Bolocam survey for 1.1 mm dust continuum emission in the c2d legacy clouds. II. Ophiuchus," *The Astrophysical Journal*, vol. 644, no. 1, article 326, 2006.
- [98] M. A. C. Perryman, L. Lindegren, J. Kovalevsky, E. Hoeg et al., "The HIPPARCOS Catalogue," *Astronomy & Astrophysics*, vol. 323, pp. L49–L52, 1997.
- [99] R. Liseau, G. J. White, B. Larsson et al., "Looking at the bright side of the ρ Ophiuchi dark cloud. Far infrared spectrophotometric observations of the ρ Oph cloud with the ISO-LWS," *Astronomy & Astrophysics*, vol. 344, pp. 342–354, 1999.
- [100] E. Habart, F. Boulanger, L. Verstraete, G. Pineau des Forêts, E. Falgarone, and A. Abergel, " H_2 infrared line emission across the bright side of the ρ ophiuchi main cloud," *Astronomy & Astrophysics*, vol. 397, no. 2, pp. 623–634, 2003.
- [101] A. Wootten, R. Snell, and A. E. Glassgold, "The determination of electron abundances in interstellar clouds," *The Astrophysical Journal*, vol. 234, pp. 876–880, 1979.
- [102] A. Wootten, N. J. Evans, N. J. II, R. Snell, and P. vanden Bout, "Molecular abundance variations in interstellar clouds," *The Astrophysical Journal*, vol. 225, pp. L143–L148, 1978.
- [103] E. F. van Dishoeck and J. H. Black, "Interstellar C2, CH, and CN in translucent molecular clouds," *The Astrophysical Journal*, vol. 340, pp. 273–297, 1989.
- [104] M. Kámierczak, M. R. Schmidt, A. Bondar, and J. Krełowski, "Abundances and rotational temperatures of the C_2 interstellar molecule towards six reddened early-type stars," *Monthly Notices of the Royal Astronomical Society*, vol. 402, pp. 2548–2558, 2010.
- [105] C. W. Lee, P. C. Myers, and M. Tafalla, "A survey for infall motions toward starless cores. II. CS (2-1) and N_2H^+ (1-0) mapping observations," *The Astrophysical Journal*, vol. 136, no. 2, p. 703, 2001.
- [106] Y. S. Park, C. W. Lee, and P. C. Myers, "A CO Survey toward Starless Cores," *The Astrophysical Journal*, vol. 152, no. 1, article 81, 2004.
- [107] B. Reipurth, S. T. Megeath, J. Bally, and J. Walawender, "The L1617 and L1622 cometary clouds in orion," in *Handbook of Star Forming Regions, Volume I*, p. 782, 2008.
- [108] G. H. Herbig and K. R. Bell, *cels.book*, 1988.
- [109] B. A. Wilson, T. M. Dame, M. R. W. Masheder, and P. Thaddeus, "A uniform CO survey of the molecular clouds in Orion and Monoceros," *Astronomy & Astrophysics*, vol. 430, no. 2, pp. 523–539, 2005.
- [110] J. Knude, C. Fabricius, E. Høg, and V. Makarov, "Distances of absorbing features in the LDN 1622 direction: an application of Tycho-2 photometry and Michigan Classification," *Astronomy & Astrophysics*, vol. 392, no. 3, pp. 1069–1079, 2002.
- [111] R. F. Garrison, "The σ orionis clustering," *Publications of the Astronomical Society of the Pacific*, vol. 79, no. 470, p. 433, 1967.
- [112] R. J. Maddalena, M. Morris, J. Moscowitz, and P. Thaddeus, "The large system of molecular clouds in Orion and Monoceros," *The Astrophysical Journal*, vol. 303, pp. 375–391, 1986.
- [113] W. H. Sherry, F. M. Walter, S. J. Wolk, and N. R. Adams, "Main-sequence fitting distance to the σ Ori cluster," *The Astronomical Journal*, vol. 135, no. 4, pp. 1616–1623, 2008.
- [114] J. Bally, J. Walawender, B. Reipurth, and S. T. Megeath, "Outflows and young stars in orion's large cometary clouds L1622and L1634," *The Astronomical Journal*, vol. 137, no. 4, p. 3843, 2009.

- [115] M. Kun, Z. Balog, N. Mizuno et al., “Lynds 1622: a nearby star-forming cloud projected on Orion B?” *Monthly Notices of the Royal Astronomical Society*, vol. 391, pp. 84–94, 2008.
- [116] S. Casassus, G. F. Cabrera, F. Forster, T. J. Pearson, A. C. S. Readhead, and C. Dickinson, “Morphological analysis of the centimeter-wave continuum in the dark cloud LDN 1622,” *The Astrophysical Journal*, vol. 639, no. 2, article 951, 2006.
- [117] S. Padin, M. C. Shepherd, J. K. Cartwright et al., “The cosmic background imager,” *Publications of the Astronomical Society of the Pacific*, vol. 114, pp. 83–97, 2002.
- [118] B. S. Mason, T. Robishaw, C. Heiles, D. Finkbeiner, and C. Dickinson, “A limit on the polarized anomalous microwave emission of Lynds 1622,” *Astrophysical Journal Letters*, vol. 697, no. 2, pp. 1187–1193, 2009.
- [119] S. Iglesias-Groth, “Hydrogenated fullerenes and the anomalous microwave emission of the dark cloud LDN 1622,” *Monthly Notices of the Royal Astronomical Society*, vol. 368, pp. 1925–1930, 2006.
- [120] C. C. Henderson and P. A. Cahill, “C₆₀H₂: synthesis of the simplest C₆₀ hydrocarbon derivative,” *Science*, vol. 259, no. 5103, pp. 1885–1887, 1993.
- [121] J. Cami, J. Bernard-Salas, E. Peeters, and S. E. Malek, “Fullerenes in circumstellar and interstellar environments,” in *Proceedings of the International Astronomical Union (IAUS '11)*, vol. 7 of *Symposium S280*, pp. 216–227, 2011.
- [122] A. Garcia-Hernandez, “On the formation of fullerenes in H-rich circumstellar environments,” in *Proceedings of the International Astronomical Union (IAUS '11)*, Symposium 280, 2011.
- [123] A. M. M. Scaife, N. Hurley-Walker, D. A. Green et al., “An excess of emission in the dark cloud LDN1111 with the Arcminute Microkelvin Imager,” *Monthly Notices of the Royal Astronomical Society*, vol. 394, pp. L46–L50, 2009.
- [124] A. E. Visser, J. S. Richer, and C. J. Chandler, “A SCUBA survey of compact dark Lynds clouds,” *Monthly Notices of the Royal Astronomical Society*, vol. 323, no. 2, pp. 257–269, 2001.
- [125] A. M. M. Scaife, N. Hurley-Walker, D. A. Green et al., “AMI observations of Lynds dark nebulae: further evidence for anomalous cm-wave emission,” *Monthly Notices of the Royal Astronomical Society*, vol. 400, pp. 1394–1412, 2009.
- [126] A. M. M. Scaife, M. Scaife, B. Nikolic et al., “Microwave observations of spinning dust emission in NGC6946,” *Monthly Notices of the Royal Astronomical Society*, vol. 406, pp. L45–L49, 2010.
- [127] A. M. M. Scaife, D. A. Green, G. G. Pooley et al., “High-resolution AMI Large Array imaging of spinning dust sources: spatially correlated 8 μm emission and evidence of a stellar wind in L675,” *Monthly Notices of the Royal Astronomical Society*, vol. 403, pp. L46–L50, 2010.
- [128] C. Dickinson, S. Casassus, R. D. Davies et al., “Infrared-correlated 31-GHz radio emission from Orion East,” *Monthly Notices of the Royal Astronomical Society*, vol. 407, pp. 2223–2229, 2010.
- [129] T. L. Wilson and R. T. Rood, “Abundances in the interstellar medium,” *Annual Review of Astronomy & Astrophysics*, vol. 32, no. 1, pp. 191–226, 1994.
- [130] M. Vidal, S. Casassus, C. Dickinson et al., “Dust-correlated cm wavelength continuum emission from translucent clouds ζ Oph and LDN 1780,” *Monthly Notices of the Royal Astronomical Society*, vol. 414, pp. 2424–2435, 2011.
- [131] P. Castellanos, S. Casassus, C. Dickinson et al., “Dust-correlated centimetre-wave radiation from the M78 reflection nebula,” *Monthly Notices of the Royal Astronomical Society*, vol. 411, no. 2, pp. 1137–1150, 2011.
- [132] D. A. Green, “A revised Galactic supernova remnant catalogue,” *Bulletin of the Astronomical Society of India*, vol. 37, pp. 45–61, 2009.
- [133] W. T. Reach, J. Rho, A. Tappe et al., “A Spitzer Space Telescope Infrared Survey of supernova remnants in the inner Galaxy,” *The Astronomical Journal*, vol. 131, no. 3, article 1479, 2006.
- [134] S. Casassus, C. Dickinson, K. Cleary et al., “Centimetre-wave continuum radiation from the ρ Ophiuchi molecular cloud,” *Monthly Notices of the Royal Astronomical Society*, vol. 391, pp. 1075–1090, 2008.
- [135] S. Casassus, L. Å. Nyman, C. Dickinson, and T. J. Pearson, “A centimetre-wave excess over free-free emission in planetary nebulae,” *Monthly Notices of the Royal Astronomical Society*, vol. 382, no. 4, pp. 1607–1622, 2007.
- [136] B. M. Pazderska, M. P. Gawroński, R. Feiler et al., “Survey of planetary nebulae at 30 GHz with OCRA-p,” *Astronomy & Astrophysics*, vol. 498, pp. 463–470, 2009.
- [137] G. Umana, P. Leto, C. Trigilio et al., “Millimeter observations of planetary nebulae,” *Astronomy & Astrophysics*, vol. 482, no. 2, pp. 529–534, 2008.
- [138] E. J. Murphy, G. Helou, J. J. Condon et al., “The detection of anomalous dust emission in the nearby galaxy ngc 6946,” *The Astrophysical Journal Letters*, vol. 709, no. 2, article L108, 2010.
- [139] T. Murphy, E. M. Sadler, R. D. Ekers et al., “The Australia Telescope 20 GHz Survey: the source catalogue,” *Monthly Notices of the Royal Astronomical Society*, vol. 402, pp. 2403–2423, 2010.
- [140] R. C. Kennicutt Jr., L. Armus, G. Bendo et al., “SINGS: The SIRTf Nearby Galaxies Survey,” *Publications of the Astronomical Society of the Pacific*, vol. 115, pp. 928–952, 2003.
- [141] F. Walter, E. Brinks, W. J. G. De Blok et al., “Things: the Hi nearby galaxy survey,” *The Astronomical Journal*, vol. 136, no. 6, pp. 2563–2647, 2008.
- [142] L. F. Rodriguez, “Radio observations of outflows,” *Bulletin of the American Astronomical Society*, vol. 21, p. 786, 1989.
- [143] G. Anglada, “Centimeter continuum emission from outflow sources,” in *Revista Mexicana de Astronomia y Astrofisica Serie de Conferencias*, vol. 1, p. 67, 1995.
- [144] P. Andre, T. Montmerle, and E. D. Feigelson, “A VLA survey of radio-emitting young stars in the Rho Ophiuchi dark cloud,” *The Astronomical Journal*, vol. 93, pp. 1182–1198, 1987.
- [145] D. Stamatellos, D. Ward-Thompson, A. P. Whitworth, and S. Bontemps, “A VLA search for young protostars embedded in dense cores,” *Astronomy & Astrophysics*, vol. 462, no. 2, pp. 677–682, 2007.
- [146] L. F. Rodriguez and J. Canto, “Stellar winds and molecular clouds—a search for ionized stellar winds,” *Revista Mexicana De Astronomia Y Astrofisica*, vol. 8, no. 2, p. 163, 1983.
- [147] J. H. Bieging, M. Cohen, and P. R. Schwartz, “VLA observations of T Tauri stars. II—a luminosity-limited survey of Taurus-Auriga,” *The Astrophysical Journal*, vol. 282, pp. 699–708, 1984.
- [148] S. H. Pravdo, L. F. Rodriguez, S. Curiel et al., “Detection of radio continuum emission from Herbig-Haro objects 1 and 2 and from their central exciting source,” *The Astrophysical Journal*, vol. 293, pp. L35–L38, 1985.
- [149] L. F. Rodriguez and B. Reipurth, “VLA detection of the exciting sources of HH 83, HH 117, HH 124, HH 192, HH 300, HH 366, and HH 375,” *Revista Mexicana De Astronomia Y Astrofisica*, vol. 34, p. 13, 1998.

- [150] P. Andre, F. Motte, and A. Bacmann, "Discovery of an extremely young accreting protostar in Taurus," *The Astrophysical Journal Letters*, vol. 513, no. 1, article L57, 1999.
- [151] A. M. M. Scaife, J. Hatchell, M. Davies et al., "AMI-LA radio continuum observations of *Spitzer* c2d small clouds and cores: Perseus region," *Monthly Notices of the Royal Astronomical Society*, vol. 415, pp. 893–910, 2011.
- [152] A. M. M. Scaife, E. I. Curtis, M. Davies et al., "AMI Large Array radio continuum observations of *Spitzer* c2d small clouds and cores," *Monthly Notices of the Royal Astronomical Society*, vol. 410, no. 4, pp. 2662–2678, 2011.
- [153] A. M. M. Scaife, J. Hatchell, R. E. Ainsworth et al., "AMI-LA radio continuum observations of *Spitzer* c2d small clouds and cores: Serpens region," *Monthly Notices of the Royal Astronomical Society*, vol. 420, pp. 1019–1033, 2012.
- [154] S. Curiel, L. F. Rodriguez, J. Bohigas, M. Roth, J. Canto, and J. M. Torrelles, "Extended radio continuum emission associated with V645 CYG and MWC1080," *Astrophysical Letters and Communications*, vol. 27, pp. 299–309, 1989.
- [155] K. H. A. Winkler and M. J. Newman, "Formation of solar-type stars in spherical symmetry. I—the key role of the accretion shock," *The Astrophysical Journal*, vol. 236, pp. 201–211, 1980.
- [156] P. Cassen and A. Moosman, "On the formation of protostellar disks," *Icarus*, vol. 48, no. 3, pp. 353–376, 1981.
- [157] S. Curiel, J. Canto, and L. F. Rodriguez, "A model for the thermal radio continuum emission produced by a shock wave and its application to the Herbig-Haro objects 1 and 2," *Revista Mexicana de Astronomia y Astrofisica*, vol. 14, pp. 595–602, 1987.
- [158] L. F. Rodriguez and B. Reipurth, "VLA detection of the exciting sources of HH 34, HH 114, and HH 199," *Revista Mexicana De Astronomia Y Astrofisica*, vol. 32, pp. 27–33, 1996.
- [159] G. Anglada, "Radio Jets in young stellar objects," in *Astronomical Society of the Pacific Conference Series (ASPC '96)*, vol. 93, University of Barcelona, Barcelona, Spain, July 1996.
- [160] G. Anglada, E. Villuendas, R. Estalella et al., "Spectral indices of centimeter continuum sources in star-forming regions: implications on the nature of the outflow exciting sources," *Astronomical Journal*, vol. 116, no. 6, pp. 2953–2964, 1998.
- [161] M. Simon, M. Felli, L. Cassar, J. Fischer, and M. Massi, "Infrared line and radio continuum emission of circumstellar ionized regions," *The Astrophysical Journal*, vol. 266, pp. 623–645, 1983.
- [162] T. L. Bourke, A. Crapsi, P. C. Myers et al., "Discovery of a low-mass bipolar molecular outflow from L1014-IRS with the sub-millimeter array," *The Astrophysical Journal Letters*, vol. 633, no. 2, article L129, 2005.
- [163] A. Crapsi, C. H. DeVries, T. L. Huard et al., "Dynamical and chemical properties of the "starless" core L1014," *Astronomy & Astrophysics*, vol. 439, pp. 1023–1032, 2005.
- [164] A. Scaife, "Radio Emission from Young Stellar Objects," *AstRv*, vol. 7, Article ID 040000, 2012.
- [165] M. M. Dunham and E. I. Vorobyov, "Resolving the luminosity problem in low-mass star formation," *The Astrophysical Journal*, vol. 747, no. 1, article 52, 2012.
- [166] A. G. G. Tielens M, S. Hony, C. van Kerckhoven, and E. Peeters, "Interstellar and circumstellar PAHs," *ESA-SP 427*, 579, 1999.
- [167] A. G. G. Tielens M, "Interstellar polycyclic aromatic hydrocarbon molecules," *Annual Review of Astronomy & Astrophysics*, vol. 46, pp. 289–337, 2008.
- [168] E. Peeters, H. W. W. Spoon, and A. G. G. M. Tielens, "Polycyclic aromatic hydrocarbons as a tracer of star formation?" *The Astrophysical Journal*, vol. 613, no. 2, pp. 986–1003, 2004.
- [169] A. P. Jones, A. G. G. M. Tielens, and D. J. Hollenbach, "Grain shattering in shocks: the interstellar grain size distribution," *Astrophysical Journal Letters*, vol. 469, no. 2, pp. 740–764, 1996.
- [170] B. T. Draine, "Photoelectric heating of interstellar gas," *The Astrophysical Journal*, vol. 36, pp. 595–619, 1978.
- [171] H. J. Habing, "The interstellar radiation density between 912 Å and 2400 Å," *Bulletin of the Astronomical Institutes of the Netherlands*, vol. 19, p. 421, 1968.
- [172] N. Ysard and L. Verstraete, "The long-wavelength emission of interstellar PAHs: characterizing the spinning dust contribution," *Astronomy & Astrophysics*, vol. 509, article A12, 2010.
- [173] B. T. Draine and A. Li, "Infrared emission from interstellar dust. IV. The Silicate-Graphite-PAH Model in the Post-*Spitzer* Era," *The Astrophysical Journal*, vol. 657, no. 2, article 810, 2007.
- [174] S. Casassus, A. C. S. Readhead, T. J. Pearson, L. Å. Nyman, M. C. Shepherd, and L. Bronfman, "Anomalous radio emission from dust in the Helix," *The Astrophysical Journal*, vol. 603, no. 2, pp. 599–610, 2004.
- [175] J. W. M. Baars, R. Genzel, I. I. K. Pauliny-Toth, and A. Witzel, "The absolute spectrum of CAS A—an accurate flux density scale and a set of secondary calibrators," *Astronomy & Astrophysics*, vol. 61, no. 1, pp. 99–106, 1977.
- [176] N. Rees, "Comments on the absolute flux density scale at low radio frequencies," *Monthly Notices of the Royal Astronomical Society*, vol. 243, pp. 637–639, 1990.
- [177] Y. A. Hafez, R. D. Davies, R. J. Davis et al., "Radio source calibration for the very small array and other cosmic microwave background instruments at around 30 GHz," *Monthly Notices of the Royal Astronomical Society*, vol. 388, no. 4, pp. 1775–1786, 2008.
- [178] J. L. Weiland, N. Odegard, R. S. Hill et al., "seven-year *wilkinson microwave anisotropy probe (wmap *)* observations: planets and celestial calibration sources," *The Astrophysical Journal*, vol. 192, no. 2, article 19, 2011.
- [179] D. J. Rudy, D. O. Muhleman, and G. L. Berge, "Mapping of the 2 and 6cm thermal emission from mars using the very large array," *Bulletin of the American Astronomical Society*, vol. 19, p. 834, 1987.
- [180] D. Johnstone, J. Di Francesco, B. Matthews et al., "The science case for building a band 1 receiver suite for ALMA," <http://arxiv.org/abs/0910.1609>.
- [181] B. Acke and M. E. Van Den Ancker, "ISO spectroscopy of disks around Herbig Ae/Be stars," *Astronomy & Astrophysics*, vol. 426, no. 1, pp. 151–170, 2004.
- [182] R. R. Rafikov, "Microwave emission from spinning dust in circumstellar disks," *The Astrophysical Journal*, vol. 646, pp. 288–296, 2006.
- [183] C. R. Purcell, M. G. Hoare, and P. Diamond, "The CORNISH Survey of the galactic plane," in *Astronomical 2008 Society of the Pacific Conference Series (ASPC '08)*, vol. 387, p. 389, 2008.
- [184] M. Thompson, S. Goedhart et al., The MeerKAT Galactic Plane Survey (MeerGAL), http://star.herts.ac.uk/progs/surveys_mw_radio.html.
- [185] Y. Perrott, A. M. M. Scaife, D. A. Green et al., "AMI Galactic Plane Survey at 16 GHz: I. Observing, mapping and source extraction," *Monthly Notices of the Royal Astronomical Society*, 2013.
- [186] I. Bains, M. Cohen, J. M. Chapman, R. M. Deacon, and M. P. Redman, "Revealing the transition from post-AGB stars to planetary nebulae: non-thermal and thermal radio continuum observations," *Monthly Notices of the Royal Astronomical Society*, vol. 397, no. 3, pp. 1386–1401, 2009.

- [187] E. M. Waldram, G. G. Pooley, K. J. B. Grainge et al., “9C: a survey of radio sources at 15 GHz with the Ryle Telescope,” *Monthly Notices of the Royal Astronomical Society*, vol. 342, no. 3, pp. 915–925, 2003.
- [188] R. S. Furuya, Y. Kitamura, A. Wootten, M. J. Claussen, and R. Kawabe, “Water maser survey toward low-mass young stellar objects in the northern sky with the Nobeyama 45 meter telescope and the very large array,” *The Astrophysical Journal Supplement Series*, vol. 144, no. 1, pp. 71–134, 2003.
- [189] C. T. Tibbs, A. M. M. Scaife, C. Dickinson et al., “AMI observations of the anomalous microwave emission in the perseus molecular cloud,” <http://arxiv.org/abs/1303.5501>.

Review Article

The Discovery of Anomalous Microwave Emission

Erik M. Leitch¹ and A. C. R. Readhead²

¹ Department of Astronomy, University of Chicago, Chicago, IL 60637, USA

² Department of Astronomy, California Institute of Technology, Pasadena, CA 91125, USA

Correspondence should be addressed to Erik M. Leitch; eml@astro.caltech.edu

Received 21 November 2012; Accepted 14 January 2013

Academic Editor: Clive Dickinson

Copyright © 2013 E. M. Leitch and A. C. R. Readhead. This is an open access article distributed under the Creative Commons Attribution License, which permits unrestricted use, distribution, and reproduction in any medium, provided the original work is properly cited.

We discuss the first detection of anomalous microwave emission, in the Owens Valley RING5M experiment, and its interpretation in the context of the ground-based cosmic microwave background (CMB) experiments of the early 1990s. The RING5M experiment was one of the first attempts to constrain the anisotropy power on sub-horizon scales, by observing a set of $7'$ -size fields around the North Celestial Pole (NCP). Fields were selected close to the NCP to allow continuous integration from the Owens Valley site. The experiment detected significant emission at both 14.5 GHz and 30 GHz, consistent with a mixture of CMB and a flat-spectrum foreground component, which we termed *anomalous*, as it could be explained neither by thermal dust emission, nor by standard models for synchrotron or free-free emission. A significant spatial correlation was found between the extracted foreground component and structure in the IRAS $100\ \mu\text{m}$ maps. While microwave emission from spinning dust may be the most natural explanation for this correlation, spinning dust is unlikely to account for all of the anomalous emission seen in the RING5M data.

1. Introduction

From the perspective of the 21st century cosmology, it can be hard to imagine how primitive the state of our knowledge was a short twenty years ago and how rapidly the landscape was changing at the time. Today, ground-based experiments like the South Pole Telescope (SPT) and the Atacama Cosmology Telescope (ACT) have measured the high- ℓ power spectrum with enough resolution to detect the first nine Doppler peaks (SPT [1, 2], ACT [3]) and enough sensitivity to detect the background of SZ power from unresolved galaxy clusters [4]. The combination of ground, balloon-borne, and space-based missions have already determined fundamental cosmological parameters to uncertainties of a few percent (c.f. DASI [5], ACBAR [6], Boomerang [7], WMAP [8]), and new data from Planck are poised to refine these further. The E-mode polarization of the CMB, whose detection was unthinkable twenty years ago, is now routinely measured by ground-based experiments (first detected by DASI [9, 10], with progressive improvements in resolution and sensitivity by CBI [11], QUaD [12], BICEPI [13], and QUIET [14]), while ever more sensitive limits on the B-mode power spectrum are beginning to place interesting constraints on the tensor-to-scalar ratio r [13]

(with the next generation cameras like SPTpol, BICEPII, the Keck Array, PolarBear, and ACTpol already in operation).

By contrast, the early 1990s had just witnessed the first ever detection of CMB anisotropy on super-horizon scales by the COBE satellite [15]. A small number of Antarctic ground-based experiments were trying to detect any indication of a rise toward the first Doppler peak and where that peak might lie (e.g., ACME [16], Python [17], MAX [18], IAB [19]). It is indicative of the state of the field that model power spectra were routinely displayed in log space, since the only feature anyone hoped to detect at the time was the rise in power at intermediate ℓ .

The Owens Valley RING5M experiment was one of a small complement of experiments designed to probe the CMB anisotropy spectrum at arcminute scales; these scales were assumed to be sub-horizon, but that had yet to be demonstrated. At the time of its inception, only upper limits had been achieved by a small handful of experiments (at $12'$ by Tucker et al. [20] and at $2'$ by the OVRO NCP experiment [21]). Collectively these instruments constituted the deepest probes of the microwave spectrum to date, and by contrast with the large-scale experiments, the resolution

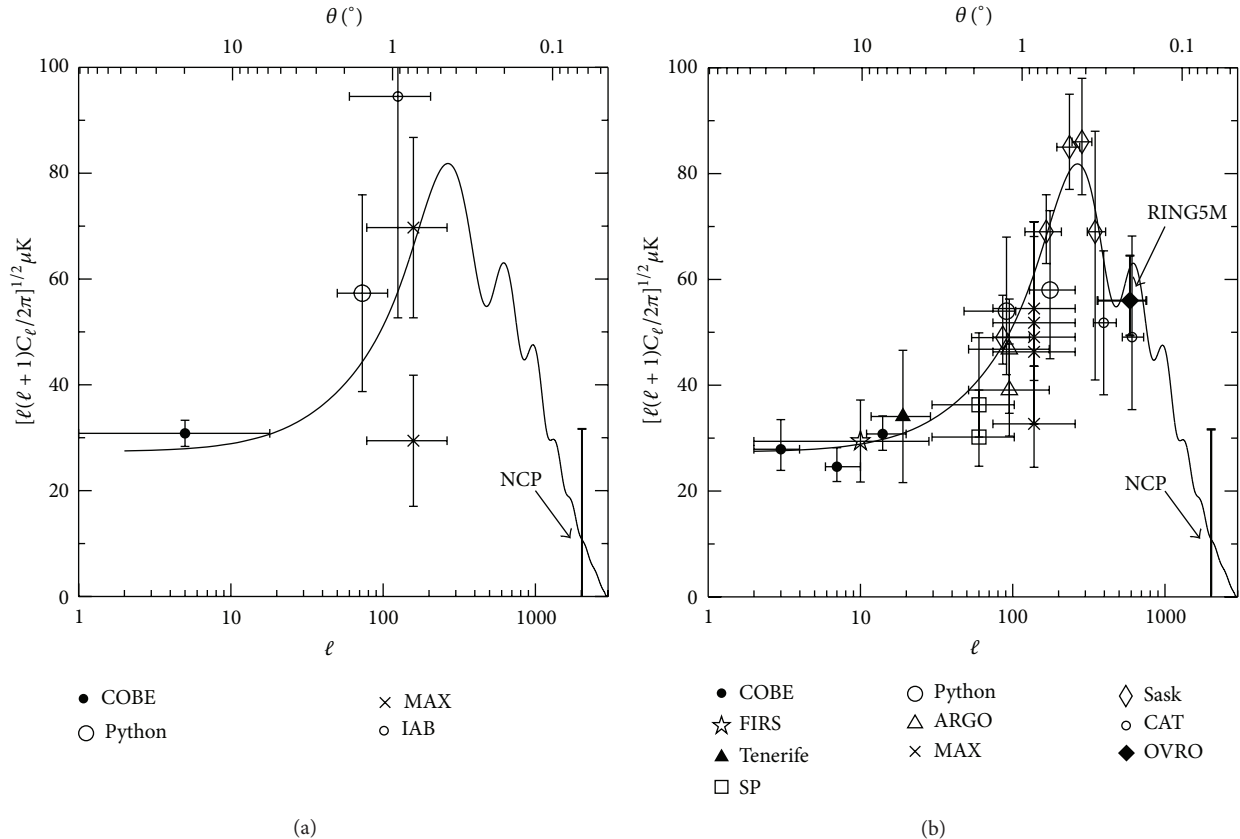


FIGURE 1: (Reproduced from [22]) (a) The state of CMB anisotropy detections in 1993. The points are from COBE [15], Python [17], MAX [18] and IAB [19]. Also shown is the upper limit from the OVRO NCP experiment [21]. (b) The state of the field in early 1998. Shown are COBE [36], FIRS [37], Tenerife [38], SP94 [39], Python [40], ARGO [41], MAX [42], Saskatoon [24], CAT [25], and the OVRO RING5M [23]. (The solid line is a CDM model with $H_0 = 30$, $\Omega_0 = 1$ and $\Omega_b = 0.05$, and is also indicative of the state of late 20th century cosmology).

of the RING5M instruments presented one of the first opportunities for probing microwave emission from specific galactic features. It is therefore not surprising, in retrospect, that these observations resulted in the first detection of anomalous microwave emission from the Galaxy, as we discuss in Section 3.

In the following section, we review details of the RING5M experiment design relevant to understanding the data. In Section 3, we present the evidence for anomalous emission in the RING5M data and discuss its interpretation in the context of multifrequency observations of the NCP in Section 4. Finally, in Section 5 we consider the relation of the anomalous emission detected near the NCP to the dust correlated components seen in degree-scale CMB experiments.

2. The RING5M Experiment

Figure 1, reproduced from [22], shows the state of anisotropy detections when the RING5M experiment was constructed. Taken together, results from the early Antarctic experiments were somewhat suggestive of a rise in power at scales approaching $\sim 1^{\circ}$, while the NCP upper limit (also shown in

Figure 1) demonstrated that the power had dropped significantly at $\sim 2'$ scales. The RING5M experiment was, therefore, designed to operate at $7' - 22'$ scales, where the peak of the power spectrum might lie in an $\Omega < 1$ universe, but which should nonetheless be detectable even in an $\Omega = 1$ cosmology. Like our counterparts in the southern hemisphere, we were driven to observe near the celestial pole; in our case, the North Celestial Pole (NCP) was the only part of the northern hemisphere sky available for round-the-clock observations.

The experiment consisted of two independent telescopes operating at widely separated frequencies. A 30 GHz channel was provided by a dual-feed receiver installed on a 5.5-meter telescope at the Owens Valley Radio Observatory (OVRO), with a beam of approximately $7'$ FWHM. To provide leverage against potential foreground contamination, a second 14.5 GHz receiver was constructed on the OVRO 40-meter telescope, with optics designed to underilluminate the dish, so that matched beams were produced at both frequencies. A Dicke switch provided fast azimuthal switching between two positions on the sky separated by $22'$, while a second, slower level of differencing was achieved by slewing the telescope to alternate the beams on the target field, producing an effective beam pattern indicated in Figure 2. In all, 36 fields were

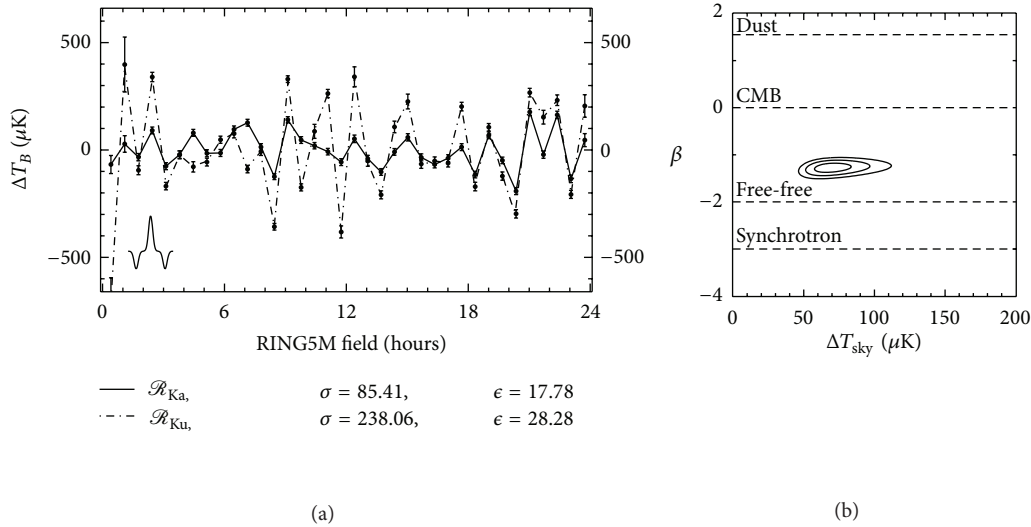


FIGURE 2: (a) Source-subtracted Ka (30 GHz) and Ku-band (14.5 GHz) data plotted to equal brightness temperature scale. Both represent sky amplitudes, convolved with the double-switched beam pattern of the RING5M observations, indicated at the bottom left of the figure. Approximately half of the RING5M fields show CMB-like signals (equal brightness temperature at both frequencies), while the other half show temperature signals with a steep spectral dependence. (b) The likelihood of the spectral index of the RING5M data, assuming that a single process is responsible for the signals at both frequencies. Clearly pure CMB ($\beta = 0$) is ruled out with high significance.

observed and spaced evenly in a ring around the NCP. The fields were observed only during transit, so that common mode contamination from the ground would be removed by the double switching.

As detailed in [23], over three years of observation, a variety of null tests demonstrated high signal-to-noise detection of structure in the RING5M data at both frequencies, consistent from year-to-year. These data were ultimately used to place a sensitive new constraint on the small-scale ($\ell \sim 600$) CMB anisotropy [23] that remains in excellent agreement with modern measurements (see Figure 1). By 1997, the Saskatoon experiment had released data that started to resolve some of the scatter at low- ℓ into a more convincing picture of a primary Doppler peak [24], and the CAT experiment had also released its preliminary results, which were in good agreement with ours [25].

3. Detection of Anomalous Emission

The analysis of the RING5M data was, however, not as simple as that story might imply. Taken together, the two frequency channels showed signals consistent with CMB (equal brightness temperature at 14.5 and 30 GHz) in roughly half the fields and signals consistent with a steep-spectrum foreground (comparable intensity at 14.5 and 30 GHz) in the other half, as can be seen in Figure 2. Modeling the dual-frequency data as a single Gaussian process with $T(\nu) \propto \nu^\beta$, we found that a pure CMB signal could be ruled out with high confidence, with the likelihood peaking for $\beta \sim -1$.

Modeling the data as the sum of a CMB component and a power-law foreground enabled us to place only a weak constraint of $\beta < -2$ on the foreground spectral index from the RING5M data alone. However, from the absence of

structure in 325 MHz maps of the NCP regions from the Westerbork Northern Sky Survey (WENSS, [26]), we were able to place a lower bound of $\beta > -2.2$ on the spectral index of a single foreground, making synchrotron emission an untenable model for the 14.5 GHz signals, unless the fields happen to be associated with an active region where the normally steep synchrotron spectrum is kept unusually flat by the injection of high-energy electrons, for example, a supernova remnant that has undergone recent repowering (see for example [27]). The lack of any correlation with the WENSS synchrotron maps, however, makes synchrotron of any variety an unlikely explanation.

Moreover, although the spectral index was consistent with free-free emission, the amplitude of the signals was not. Maps of the NCP from the Wisconsin H α Mapper (WHAM, [28]) were almost featureless; when convolved with the double-switched RING5M beam, the H α template for the RING5M fields predicted a free-free *rms* at 14.5 GHz from a warm ($\sim 10^4$ K) component that is nearly two orders of magnitude lower than the amplitude of the signals we detected. To reconcile the radio emission with the absence of structure in the H α maps would require a plasma temperature of at least 10^6 K. These considerations, and the lack of any correlation with the low-frequency synchrotron maps, led us to consider the radio emission “anomalous” (Leitch et al. [29]).

The dual-frequency data were ultimately used to separate this foreground component from the CMB signal to produce the bandpower reported in [23]. As can be seen in Figure 3, when this anomalous component was extracted from the 14.5 GHz and 30 GHz data assuming that $\beta = -2.2$, we found a remarkable correlation between the extracted anomalous component and the emission in the IRAS 100 μm

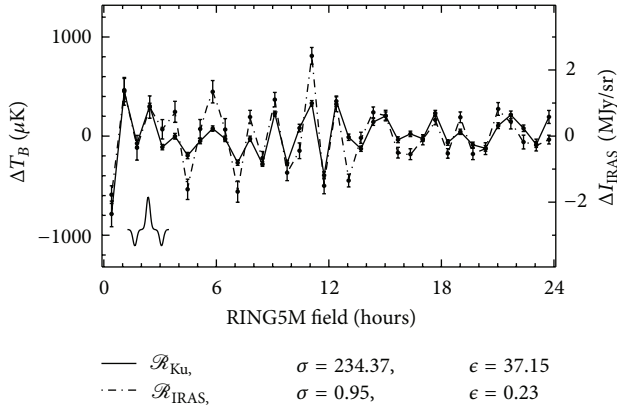


FIGURE 3: Extracted anomalous component, assuming that $\beta = -2.2$ (solid line) is overplotted with amplitudes from the IRAS $100\ \mu\text{m}$ map (dashed line). Both represent sky amplitudes, convolved with the double-switched beam pattern of the RING5M observations, indicated at the bottom left of the figure.

maps. The correlation is quite significant, as noted in [29]. Factoring in the artificial correlation introduced by the double-switched observing strategy, an analysis of the rank correlation between these two data sets indicates a probability to exceed of 10^{-6} , prompting a closer examination of the morphology of the NCP region, which we review in the next section.

4. Interpretation of the Anomalous Emission

A wide-field IRAS $100\ \mu\text{m}$ image of the NCP is shown in Figure 4, with the locations of the RING5M fields near $\delta = 88^\circ$ indicated for reference. As is clear from the figure, the fields are embedded in the wall of a prominent HI feature known as the North Celestial Pole Loop (after Heiles [30]). Heiles concludes from an examination of HI column densities, that the NCP Loop is unlikely to be a shell, but instead is probably filamentary in nature. (Note that the NCP Loop, near the north *Celestial* pole, is not to be confused with the North Polar Spur, a prominent feature near the north *galactic* pole, which is well understood as a supernova remnant.) The abundance of molecular species in individual clouds in the NCP Loop was extensively studied from 1970–1990 (see [31] for a review), and the magnetic fields and pressure support were investigated by Heiles [30], from Zeeman-splitting measurements of the 21-cm line at locations within and around the NCP Loop.

In the comprehensive study of Meyerdierks et al. [31], who analyze the radio continuum, X-ray, and far infrared properties of the NCP Loop, this structure is understood as the massive shell of an expanding cylindrical cavity in the galactic HI disk. At 408 MHz, the radio continuum shows a deep deficit within the Loop [32], consistent with expulsion of magnetized material from the interior of the shell. The model that best matches the HI velocity data, and at the same time explains the depth of the radio continuum deficit, has the cylinder inclined nearly along the line of sight.

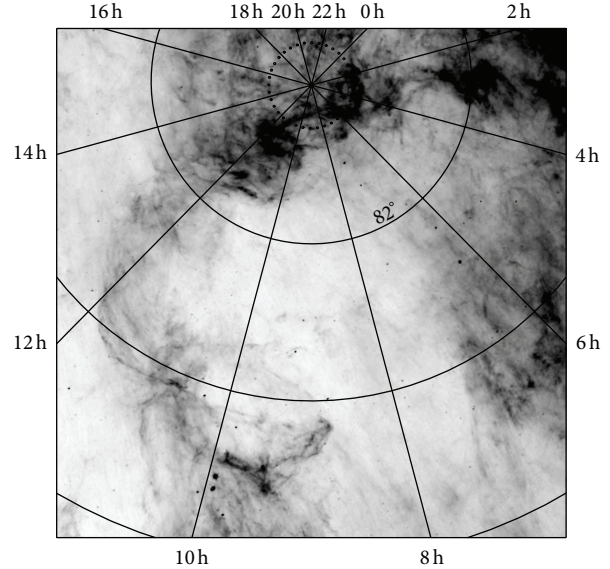


FIGURE 4: IRAS $100\ \mu\text{m}$ map, showing the NCP Loop and the locations of the RING5M fields (near $\delta = 88^\circ$, top center). (Note that this figure is intended to illustrate the large-scale morphology of the NCP Loop—the location of the RING5M fields is indicated for reference only).

Given the morphology of the Loop, it is perhaps not surprising that interpretation of the high-frequency radio emission observed in the RING5M experiment as either synchrotron or free-free suggests an unusual kinematic environment. As noted earlier, the spectral flatness of the anomalous component could be explained most naturally by synchrotron emission if the Loop is associated with a supernova remnant that has undergone recent repowering. As previously pointed out by Heiles [30], however, the nonspherical nature of the shock inferred from the HI column densities suggests a different mechanism. Meyerdierks et al., furthermore, cite the absence of OB stars within the Loop and the deep radio deficit within the Loop that requires expulsion of magnetic material for a long distance along the line of sight, and suggest that infall of a cloud from the galactic halo may be a more natural explanation for the source of the shell [31].

Similarly, the shocked morphology of the Loop also makes high-temperature free-free a potentially viable explanation for the anomalous emission in this region. Meyerdierks et al. [31] also found an enhancement of soft X-ray emission in the interior of the shell, suggesting the presence of a thin hot medium within the cavity; they estimate that the temperature could be as high as $5 \times 10^5\ \text{K}$, with large uncertainties due to the estimated HI absorption.

We have argued for the reasonableness of interpreting the anomalous emission near the NCP as either flat-spectrum synchrotron or high-temperature free-free in the light of the $100\ \mu\text{m}$ morphology, HI velocity structure, radio continuum deficit, and soft X-ray emission, all of which indicate a shocked environment in the vicinity of the NCP. In the next section, however, we discuss an alternative explanation that explains the emission as arising from the dust itself, obviating

the need to invoke any special kinematic environment near the boundary of the Loop.

5. Discussion: Spinning Dust

Either of the explanations proposed earlier would rely on the superposition of emission from a shocked component at the edge of the cavity with emission from the dense neutral medium in the wall of the Loop to explain the extraordinary correlation of the anomalous component with the IRAS maps. In 1998, Draine and Lazarian proposed a more natural explanation for the dust correlation observed in the RING5M data, with the anomalous component arising from dipole emission from very small dust grains [33].

The model could also explain the all-sky dust-correlated component seen at $>7^\circ$ scales in the COBE DMR maps by Kogut et al. [34], and the marginal correlation with DIRBE reported at 1° by the Saskatoon experiment [35]. We note, however, that no new mechanism was required to explain these results, as neither of those authors found anything anomalous about the large-scale dust-correlated components. Both results were adequately explained by free-free emission from a warm-ionized component, with amplitudes consistent with predicted levels.

Kogut et al. cross-correlated the all-sky COBE DMR 2-year sky maps with far infrared COBE DIRBE maps and found evidence for a component of microwave emission that correlates with the large-scale structure in the infrared maps. They interpret this component as a free-free emission from 10^4 K ionized gas and interpret the correlation with the dust maps as due to evaporating cloud surfaces embedded in that ionized medium. Kogut et al. further note that the amplitude of this correlated free-free component is in good agreement with the predicted *rms* variation in the free-free signal at 7° scales, as inferred from fluctuations in the $H\alpha$ emission.

Similarly, de Oliveira-Costa et al. found that a cross-correlation of the 30 and 40 GHz Saskatoon data with the COBE DIRBE maps detects a correlated free-free component at 1° scales. They note that assuming an ℓ^{-3} power spectrum for the diffuse free-free emission, the amplitude of the correlated signal detected in the Saskatoon data is also in good agreement with the amplitude of the correlated signal detected by Kogut et al. on large scales. Accordingly, de Oliveira-Costa et al. argued that free-free contamination was the most likely explanation for the correlated emission at degree angular scales as well.

While the spinning dust model is certainly the simplest explanation for the observed dust correlations, it is likely that the anomalous component detected toward the NCP in the RING5M data represents a mixture of emission from several components. While the spinning dust models can reproduce the amplitude of the anomalous component at 30 GHz, a significant increase in the assumed grain dipole moment would be required to match the amplitude of the signals at 14.5 GHz [33]. At the same time, the coincidence of the RING5M fields with the wall of the NCP Loop is consistent with some or all of the emission arising from either flat-spectrum synchrotron or high-temperature free-free. We note that Draine and Lazarian advanced an argument

rejecting high-temperature free-free emission as a possible source of the anomalous component on energetic grounds [33]. That argument, however, was based on a conflation of two unrelated results: the localized small-scale emission from the wall of the NCP Loop, for which high-temperature free-free poses no energetic problems, and the full-sky dust-correlated component detected by COBE, for which high-temperature free-free was neither required nor suggested as an explanation.

The combination of increasingly sophisticated models and observations with better frequency resolution will ultimately decide whether spinning dust can explain the anomalous emission detected in the RING5M fields. What is clear from the results in this volume, however, is that the evidence for anomalous microwave emission is mounting in a variety of astrophysical contexts and that spinning dust may provide a cogent model for its origin.

References

- [1] R. Keisler, C. L. Reichardt, K. A. Aird et al., "A measurement of the damping tail of the cosmic microwave background power spectrum with the south pole telescope," *The Astrophysical Journal*, vol. 743, no. 1, article 28, 2011.
- [2] K. Story, C. L. Reichardt, Z. Hou et al., "A measurement of the cosmic microwave background damping tail from the 2500-square-degree SPT-SZ survey," <http://arxiv.org/abs/1210.7231>.
- [3] S. Das, T. Louis, M. R. Nolte et al., "The Atacama Cosmology Telescope: temperature and gravitational lensing power spectrum measurements from three seasons of data," <http://arxiv.org/abs/arXiv:1301.1037>.
- [4] C. L. Reichardt, L. Shaw, O. Zahn et al., "A measurement of secondary cosmic microwave background anisotropies with two years of South Pole Telescope observations," *The Astrophysical Journal*, vol. 755, no. 1, 2012.
- [5] C. Pryke, N. W. Halverson, E. M. Leitch et al., "Cosmological parameter extraction from the first season of observations with the degree angular scale interferometer," *Astrophysical Journal Letters*, vol. 568, no. 1, pp. 46–51, 2002.
- [6] J. H. Goldstein, P. A. R. Ade, J. J. Bock et al., "Estimates of cosmological parameters using the cosmic microwave background angular power spectrum of ACBAR," *Astrophysical Journal*, vol. 599, no. 2, pp. 773–785, 2003.
- [7] C. J. Mactavish, P. A. R. Ade, J. J. Bock et al., "Cosmological parameters from the 2003 flight of Boomerang," *Astrophysical Journal*, vol. 647, no. 2, pp. 799–812, 2006.
- [8] D. Larson, J. Dunkley, G. Hinshaw et al., "Seven-year wilkinson microwave anisotropy probe (WMAP*) observations: power spectra and WMAP-derived parameters," *Astrophysical Journal, Supplement Series*, vol. 192, no. 2, article 16, 2011.
- [9] J. M. Kovac, E. M. Leitch, C. Pryke, J. E. Carlstrom, N. W. Halverson, and W. L. Holzapfel, "Detection of polarization in the cosmic microwave background using DASI," *Nature*, vol. 420, no. 6917, pp. 772–787, 2002.
- [10] E. M. Leitch, J. M. Kovac, N. W. Halverson, J. E. Carlstrom, C. Pryke, and M. W. E. Smith, "Degree angular scale interferometer 3 year cosmic microwave background polarization results," *Astrophysical Journal*, vol. 624, no. 1, pp. 10–20, 2005.
- [11] A. C. S. Readhead, S. T. Myers, T. J. Pearson et al., "Polarization observations with the cosmic background imager," *Science*, vol. 306, no. 5697, pp. 836–844, 2004.

- [12] C. Pryke, P. Ade, J. Bock et al., "Second and third season quad cosmic microwave background temperature and polarization power spectra," *Astrophysical Journal*, vol. 692, no. 2, p. 1247, 2009.
- [13] H. C. Chiang, P. A. R. Ade, D. Barkats et al., "Measurement of cosmic microwave background polarization power spectra from two years of BICEP data," *Astrophysical Journal*, vol. 711, no. 2, pp. 1123–1140, 2010.
- [14] C. Bischoff, A. Brizius, I. Buder et al., "First season quiet observations: measurements of cosmic microwave background polarization power spectra at 43 GHz in the multipole range $25 \leq \ell \leq 475$," *Astrophysical Journal*, vol. 741, no. 2, article 111, 2011.
- [15] G. Smoot, C. Bennett, E. Wright et al., "Structure in the COBE differential microwave radiometer first-year maps," *Astrophysical Journal*, vol. 396, no. 1, pp. L1–L5, 1992.
- [16] T. Gaier, J. Schuster, J. Gundersen et al., "A degree-scale measurement of anisotropy of the cosmic background radiation," *Astrophysical Journal Letters*, vol. 398, no. 1, pp. L1–L4, 1992.
- [17] M. Dragovan, J. E. Ruhl, G. Novak et al., "Anisotropy in the microwave sky at intermediate angular scales," *Astrophysical Journal Letters*, vol. 427, no. 2, pp. L67–L70, 1994.
- [18] J. O. Gundersen, A. C. Clapp, M. Devlin et al., "A degree scale anisotropy measurement of the cosmic microwave background near the star gamma Ursae minoris," *Astrophysical Journal Letters*, vol. 413, no. 1, pp. L1–L5, 1993.
- [19] L. Piccirillo and P. Calisse, "Measurements of cosmic background radiation anisotropy at intermediate angular scale," *Astrophysical Journal Letters*, vol. 411, no. 2, pp. 529–533, 1993.
- [20] G. S. Tucker, G. S. Griffin, H. T. Nguyen, and J. B. Peterson, "A search for small-scale anisotropy in the cosmic microwave background," *Astrophysical Journal Letters*, vol. 419, no. 2, pp. L45–L48, 1993.
- [21] A. C. S. Readhead, C. R. Lawrence, S. T. Myers, W. L. W. Sargent, H. E. Hardebeck, and A. T. Moffet, "A limit on the anisotropy of the microwave background radiation on arcminute scales," *Astrophysical Journal*, vol. 346, pp. 566–587, 1989.
- [22] E. M. Leitch, *A measurement of anisotropy in the microwave background on $7' - 22'$ scales [Ph.D. thesis]*, California Institute of Technology, 1998.
- [23] E. M. Leitch, A. C. S. Readhead, T. J. Pearson, S. T. Myers, S. Gulkis, and C. R. Lawrence, "A measurement of anisotropy in the cosmic microwave background on $7' - 22'$ scales," *Astrophysical Journal*, vol. 532, no. 1, pp. 37–56, 2000.
- [24] C. B. Netterfield, M. J. Devlin, N. Jarosik, L. Page, and E. J. Wollack, "A measurement of the angular power spectrum of the anisotropy in the cosmic microwave background," *Astrophysical Journal Letters*, vol. 474, no. 1, pp. 47–66, 1997.
- [25] P. F. Scott, R. Saunders, G. Pooley et al., "Measurements of structure in the cosmic background radiation with the Cambridge cosmic anisotropy telescope," *Astrophysical Journal Letters*, vol. 461, no. 1, pp. L1–L4, 1996.
- [26] R. B. Rengelink, Y. Tang, A. G. de Bruyn et al., "The Westerbork Northern Sky Survey (WENSS). I. A 570 square degree mini-survey around the North Ecliptic Pole," *Astronomy and Astrophysics Supplement Series*, vol. 124, pp. 259–280, 1997.
- [27] I. Lerche, "On the spectral index distribution of supernova remnants," *Astronomy & Astrophysics*, vol. 85, pp. 141–143, 1980.
- [28] R. J. Reynolds, S. L. Tufte, L. M. Haffner, K. Jaehnig, and J. W. Percival, "The Wisconsin H α Mapper (WHAM): a brief review of performance characteristics and early scientific results," *Publications of the Astronomical Society of Australia*, vol. 15, no. 1, pp. 14–18, 1998.
- [29] E. M. Leitch, A. C. S. Readhead, T. J. Pearson, and S. T. Myers, "An anomalous component of galactic emission," *Astrophysical Journal Letters*, vol. 486, no. 1, pp. L23–L26, 1997.
- [30] C. Heiles, "Magnetic fields, pressures, and thermally unstable gas in prominent H I shells," *Astrophysical Journal*, vol. 336, pp. 808–821, 1989.
- [31] H. Meyerdierks, A. Heithausen, and K. Reif, "The north celestial pole loop," *Astronomy and Astrophysics*, vol. 245, pp. 247–256, 1991.
- [32] C. G. T. Haslam, C. J. Salter, H. Stoffel, and W. E. Wilson, "A 408 MHz all-sky continuum survey. II—the atlas of contour maps," *Astronomy and Astrophysics Supplement Series*, vol. 47, p. 1, 1982.
- [33] B. T. Draine and A. Lazarian, "Diffuse galactic emission from spinning dust grains," *Astrophysical Journal Letters*, vol. 494, no. 1, pp. L19–L22, 1998.
- [34] A. Kogut, A. J. Banday, C. L. Bennett, K. M. Górski, G. Hinshaw, and W. T. Reach, "High-latitude galactic emission in the COBE differential microwave radiometer 2 year sky maps," *Astrophysical Journal Letters*, vol. 460, no. 1, pp. 1–9, 1996.
- [35] A. de Oliveira-Costa, A. Kogut, M. J. Devlin, C. B. Netterfield, L. A. Page, and E. J. Wollack, "Galactic microwave emission at degree angular scales," *Astrophysical Journal Letters*, vol. 482, no. 1, pp. L17–L20, 1997.
- [36] G. Hinshaw, A. J. Banday, C. L. Bennett et al., "Band power spectra in the COBE 1 DMR four-year anisotropy maps," *Astrophysical Journal Letters*, vol. 464, no. 1, pp. L17–L20, 1996.
- [37] K. Ganga, L. Page, E. Cheng, and S. Meyer, "The amplitude and spectral index of the large angular scale anisotropy in the cosmic microwave background radiation," *Astrophysical Journal Letters*, vol. 432, no. 1, pp. L15–L18, 1994.
- [38] S. Hancock, C. M. Gutierrez, R. D. Davies et al., "Studies of cosmic microwave background structure at Dec. = + 40°—II. Analysis and cosmological interpretation," *Monthly Notices of the Royal Astronomical Society*, vol. 289, no. 3, pp. 505–514, 1997.
- [39] J. O. Gundersen, M. Lim, J. Staren et al., "Degree-scale anisotropy in the cosmic microwave background: SP94 results," *Astrophysical Journal Letters*, vol. 443, no. 2, pp. L57–L60, 1995.
- [40] S. R. Platt, J. Kovac, M. Dragovan, J. B. Peterson, and J. E. Ruhl, "Anisotropy in the microwave sky at 90 GHz: results from python III," *Astrophysical Journal Letters*, vol. 475, no. 1, pp. L1–L4, 1997.
- [41] P. De Bernardis, E. Aquilini, A. Boscaleri et al., "Degree-scale observations of cosmic microwave background anisotropies," *Astrophysical Journal Letters*, vol. 422, no. 2, pp. L33–L36, 1994.
- [42] S. T. Tanaka, A. C. Clapp, M. J. Devlin et al., "Measurements of anisotropy in the cosmic microwave background radiation at 0.5° scales near the stars HR 5127 and ϕ Hercules," *Astrophysical Journal Letters*, vol. 468, no. 2, pp. L81–L84, 1996.

Research Article

A Characterization of the Diffuse Galactic Emissions at Large Angular Scales Using the Tenerife Data

J. F. Macías-Pérez,^{1,2} R. D. Davies,² R. Watson,² C. M. Gutierrez,³ and R. Rebolo³

¹ LPSC, Université Joseph Fourier Grenoble 1, CNRS/IN2P3, Institut National Polytechnique de Grenoble, 53 avenue des Martyrs, 38026 Grenoble Cedex, France

² Jodrell Bank Centre for Astrophysics, Alan Turing Building, School of Physics and Astronomy, The University of Manchester, Oxford Road, Manchester M13 9PL, UK

³ Instituto de Astrofísica de Canarias, C/Vía Láctea s/n, La Laguna, 65 Tenerife, Spain

Correspondence should be addressed to J. F. Macías-Pérez; macias@lpsc.in2p3.fr

Received 9 July 2012; Revised 13 January 2013; Accepted 13 January 2013

Academic Editor: Roberta Paladini

Copyright © 2013 J. F. Macías-Pérez et al. This is an open access article distributed under the Creative Commons Attribution License, which permits unrestricted use, distribution, and reproduction in any medium, provided the original work is properly cited.

The anomalous microwave emission (AME) has been proved to be an important component of the galactic diffuse emission in the range from 20 to 60 GHz. To discriminate between different models of AME, low frequency microwave data from 10 to 20 GHz are needed. We present here a reanalysis of published and unpublished Tenerife data from 10 to 33 GHz at large angular scales (from 5 to 15 degrees). We cross-correlate the Tenerife data to templates of the main galactic diffuse emissions: synchrotron, free-free, and thermal dust. We find evidence of dust-correlated emission in the Tenerife data that could be explained as spinning dust grain emission.

1. Introduction

The anomalous microwave emission (AME) is an important contributor of the galactic diffuse emission in the range from 20 to 60 GHz. It was first identified by [1, 2] as free-free emission from electrons with temperature, $T_e > 10^6$ K. Draine and Lazarian [3] argued that AME may result from electric dipole radiation due to small rotating grains, the so-called *spinning dust*. Models of the *spinning dust* emission, Draine and Lazarian [4] show that an emissivity spectrum peaking at around 20–50 GHz is able to reproduce the observations [5–12]. The initial *spinning dust* model has been refined regarding the shape and rotational properties of the dust grains [13–15]. An alternative explanation of AME was proposed by Draine and Lazarian [16] based on magnetic dipole radiation arising from hot ferromagnetic grains. Observations have placed limits of a few percent on the fractional polarization towards AME targets [9, 17–20]. This excludes perfectly aligned single-domain magnetic grains; however, other alignments and grain compositions produce similarly low levels of polarization [21].

A correlation between microwave and infrared maps, mainly dominated by dust thermal emission [22], was observed for various experiments, for example, on COBE/DMR [23, 24], OVRO [1, 2], Saskatoon [25, 26], survey at 19 GHz [27, 28], and Tenerife [29, 30]. A similar signal was found in compact regions by [5] and in some molecular clouds based on data from COSMOSMAS [7, 31], AMI (Ami-Consortium: [32, 33]), CBI [9, 34], VSA [12], and Planck [35]. A recent study of the Small Magellanic Cloud also claims a detection of AME [36].

Independently, Bennett et al. [41] proposed an alternative explanation of AME based on flat-spectrum synchrotron emission associated to star-forming regions to explain part of the WMAP first-year observations. This hypothesis seems to be in disagreement with results from de Oliveira-Costa et al. [6]; Fernández-Cerezo et al. [42]; Hildebrandt et al. [43]; Ysard et al. [44] which showed that spinning dust best explained the excess below 20 GHz. Furthermore, Davies et al. [45] showed the existence of important correlation between microwave and infrared emission in regions outside star-forming areas. More recently, Kogut et al. [46] discussed

the fact that *spinning dust* fits better to ARCADE data (3.8 and 10 GHz) than a flat-spectrum synchrotron.

To discriminate between the different AME models and the alternative explanations such as those discussed earlier low frequency microwave data in the range, from 10 to 20 GHz at different angular resolutions are needed. Indeed in this frequency range, we expect the AME spectrum to be significantly distinct from magnetic dust and flat-spectrum synchrotron. At this respect, the Tenerife data set, from 10 to 33 GHz and at large angular scales (from 5 to 15 degrees), is unique. We present in the following a re-analysis of these data including previously published data by Gutierrez et al. [47] and un-published data since January 1998 to December 2000. The paper is structured as follows. Section 2 presents the Tenerife data and discusses the reprocessing of these data. In Section 3 we describe the main galactic emission mechanisms and the associated templates used in the analysis. Section 4 discusses the point source contribution to the Tenerife data. In Section 5, we present the cross correlation between the Tenerife data and the galactic templates. The main results are discussed in Section 6. Finally, we draw conclusions in Section 7.

2. The Tenerife Data

The Tenerife experiment observed unidimensional scans at constant declination at 10, 15, and 33 GHz using a triple beam pattern of FWHM 5° and of 8.1° beam spacing. The region of the sky centered at declination 40° was chosen for observations because it corresponds to the largest area of the sky at high latitudes where contamination from foregrounds is a minimum. To reconstruct 2D maps of the sky, consecutive declinations separated by half the beamwidth (2.5°) are observed. Each single declination is repeatedly observed until sufficient sensitivity and full RA coverage is achieved. The scheduling of the observations takes into account the position of the sun so that its contribution to the data is a minimum. This requires observations of the same declination at different times of the year for full RA coverage. Observations were performed day and night. Day-time observations present an increase in total power and noise with respect to night-time observations due to receiver gain changes. In extreme cases, data observed at day time have to be removed.

The atmospheric contribution to the data depends on frequency, being severe at 33 GHz and relatively small at 10 GHz. The observing efficiency depends mainly on the weather conditions. Data strongly affected by atmospheric contamination cannot be used. In addition, technical problems, such as power cutoff, warmed and oscillating HEMT amplifiers, RF interference, and failure in the electronic systems, can also affect the data. At 10 and 15 GHz, more than 80% of the observed data are useful. However, at 33 GHz only about 10% of data are kept, due mainly to atmospheric effects.

We use in the following the full Tenerife data set which includes new data (taken from January 1998 to December 2000) with respect to previously published releases (see, e.g., [47, 48]). These data have been completely reprocessed

TABLE 1: 10 GHz data. Mean temperature, mean noise per beam, and r.m.s per 1° pixel for the 10 GHz final stacks in the RA interval 150° to 250° .

Declination (deg)	Mean T (μK)	σ (μK)	r.m.s (μK)
30.0	-3.7	52.9	150.5
32.5	-5.0	45.9	147.8
35.0	10.0	47.1	140.5
37.5	7.5	51.0	153.1
40.0	13.6	49.6	147.4
42.5	7.9	54.1	146.0
45.0	-7.8	59.2	215.5

TABLE 2: 15 GHz data. mean, mean noise per beam, and r.m.s per 1° pixel for the 15 GHz final stacks in the RA interval 150° to 250° .

Declination	Mean T (μK)	σ (μK)	r.m.s (μK)
25.0	3.6	18.1	51.7
27.5	4.6	16.3	48.7
30.0	3.4	19.3	61.1
32.5	3.9	22.7	67.2
35.0	0.25	20.6	74.6
37.5	8.3	22.4	78.6
40.0	7.8	20.7	75.7
42.5	5.0	22.6	81.3
45.0	-8.2	21.3	75.8
47.5	-5.9	19.3	70.5

TABLE 3: 33 GHz data. Mean, mean noise per beam, and r.m.s per 1° pixel for the 33 GHz final stacks in the RA interval 150° to 250° .

Declination	Mean T (μK)	σ (μK)	r.m.s (μK)
40.0	-3.1	27.2	80.8
42.5	0.2	43.7	167.7

including hand editing to remove clearly systematic contaminated regions and accurate removal of the atmospheric emission using an MEM-based baseline removal technique as described in Gutierrez et al. [47]. The latter has been improved to enlarge the sky region for which atmospheric residuals are negligible. In particular, this allows us to consider in the following analysis regions at low galactic latitudes. Figures 1, 2, and 3 present the cleaned Tenerife data at 10, 15, and 33 GHz, respectively. The main properties of these clean data: central declination of the scan, mean temperature, mean noise per beam, and r.m.s per 1° pixel in the RA interval 150° to 250° , are presented in Tables 1, 2 and 3 for the 10, 15, and 33 GHz channels, respectively.

3. Galactic Diffuse Emission

We present in this section the main known galactic diffuse mechanisms: synchrotron, free-free, and vibrational and rotational dust.

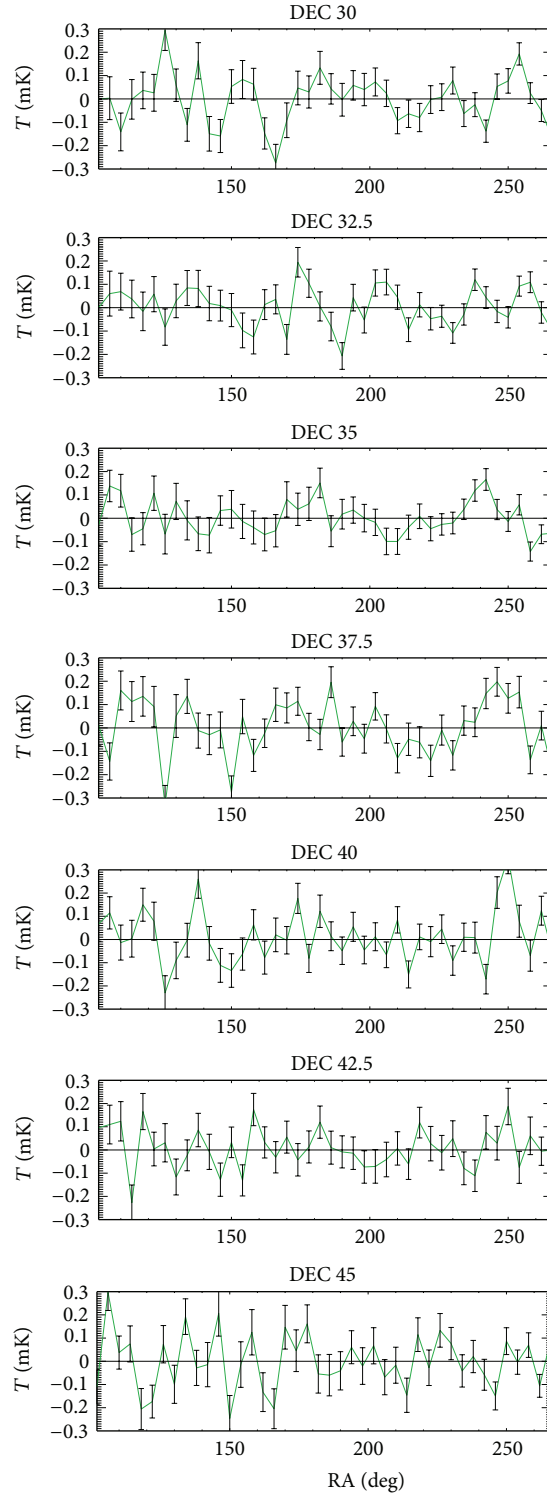


FIGURE 1: 10 GHz stacked scans. From top to bottom we plot the stacked scans for the 10 GHz radiometer from declination 30° to 45° . The data have been binned into 4° pixels.

3.1. Synchrotron. Synchrotron emission results from cosmic-ray electrons accelerated in magnetic fields, and thus, depends on the energy spectrum of the electrons and the intensity of the magnetic field [49, 50]. The local energy

spectrum of the electrons has been measured to be, for energies contributing to the observed radio synchrotron emission, a power law to good approximation with index from about -2.7 to -3.3 over this energy range [51]. Such an

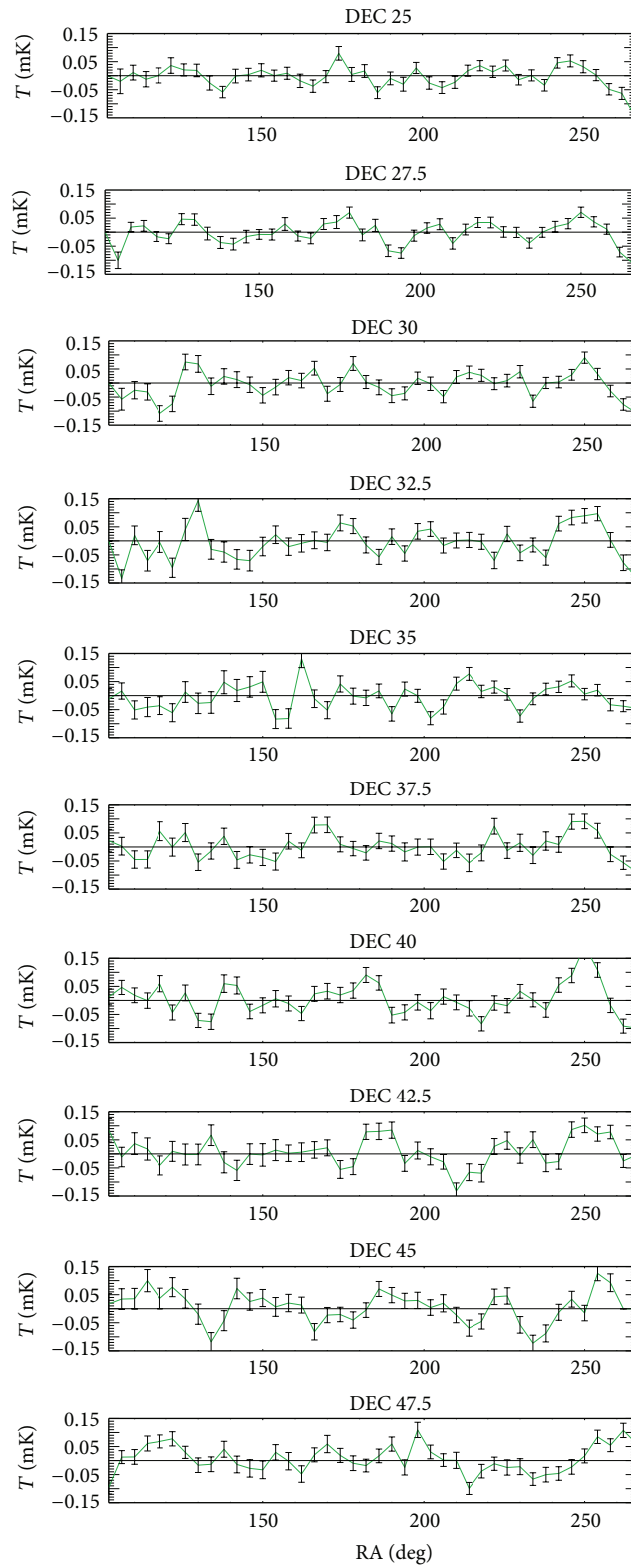


FIGURE 2: 15 GHz stacked scans. From top to bottom we plot the 15 GHz stacked scans in the declination range 25° to 47.5° . The data have been binned into 4° pixels.

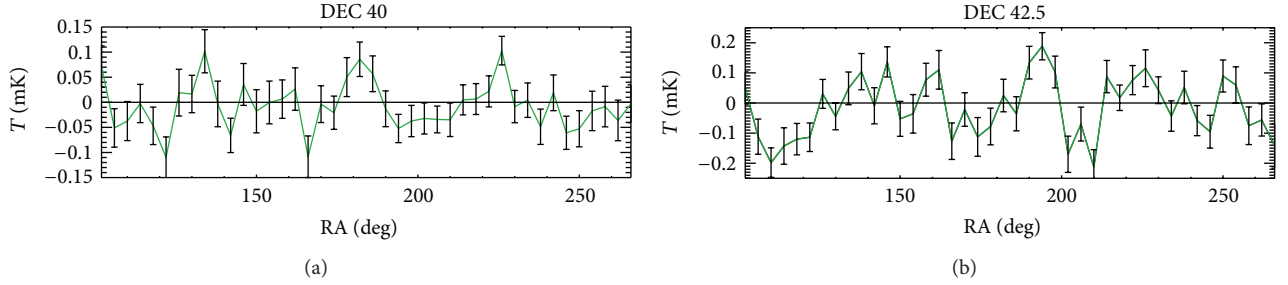


FIGURE 3: 33 GHz stacked scans. From top to bottom we plot the stacked scans for the 33 GHz radiometer in the triple beam configuration for declinations 40° to 42.5° . The data have been smoothed into 4° pixels.

increase of energy spectrum slope is expected, as the energy loss mechanism for electrons increases as the square of the energy.

Radio surveys at frequencies less than 2 GHz are dominated by synchrotron emission [52]. The only all-sky survey available at these frequencies is the 408 MHz map [53]. This survey has a resolution of 0.85° and was produced using the Parkes 64 m telescope in Australia for the southern sky and the Bonn 100 m and Jodrell Bank MK1A telescopes for the northern sky. The scanning strategy with the Bonn telescope was to fix the azimuth at the local meridian and scan up and down in elevation at a rate of about $6^\circ/\text{min}$. This technique reduced the atmospheric contribution to the map but led to a set of vertical stripes (constant RA) separated by 7° . The quoted errors in the temperature scale are of the order of 10% and ± 3 K in the absolute brightness temperature levels.

In addition, there is the 1420 MHz survey [54] which covers the declination range -19° to 90° and has a FWHM of 0.58° . Stripes are also present in this map due to the scanning strategy which consisted of azimuthal scans at constant elevation. The errors in the temperature scale are of the order of 5% and ± 0.5 K in the absolute brightness temperature.

The 408 MHz and 1420 MHz maps have been used to determine the synchrotron spectral index at radio frequencies [54, 55]. Assuming that $T_\nu \propto \nu^{-\beta}$ and after destripping and correction for zero levels, spectral indexes, β , in the range 2.8 to 3.2 were found. The spatial angular power spectrum of the synchrotron emission C_ℓ^{sync} is poorly understood but is believed to be $C_\ell^{\text{sync}} \propto \ell^{-3}$ [56]. At high galactic latitudes in the region observed by the Tenerife experiment, the synchrotron spatial angular power spectrum is slightly flatter than ℓ^{-2} [57]. In the following sections, we will use the destripped version of the 408 MHz map [55] as a template of the synchrotron emission. This map is shown in Figure 4.

3.2. Free-Free. When a charged particle is accelerated in a Coulomb field it will emit radiation which is called braking radiation or Bremsstrahlung. The galactic free-free emission is the thermal bremsstrahlung from hot electrons ($\sim 10^4$ K) produced in the interstellar gas by the UV radiation field [51]. This emission is not easily identified at radio frequencies, except near the galactic plane. At higher latitudes, it must be separated from synchrotron emission by virtue of their

different spectral indices, since the spectral index of optically thin free-free emission is $\beta^{\text{ff}} = 2.1$.

The diffuse galactic recombination radiation, H_α is a good tracer of free-free emission since both are emitted in the same Warm Ionised Medium (WIM) and both have intensities proportional to the *emission measure*,

$$\text{EM} = \int n_e n_p d\ell \approx \int n_e^2 d\ell. \quad (1)$$

The ratio of free-free brightness temperature T_b^{ff} to the H_α surface brightness I_α in R (Rayleigh) is [58]

$$\frac{T_b^{\text{ff}} [\text{mK}]}{I_\alpha [\text{R}]} = 10.4 \nu^{-2.14} T_4^{0.527} 10^{0.029/T_4} (1 + 0.08), \quad (2)$$

where ν is the observing frequency in GHz, T_4 is the temperature of the electrons in units of 10^4 K, and the last factor 0.08 corresponds to helium which is assumed completely ionised and creates free-free-emission like hydrogen but does not emit H_α light.

Recently, a full sky survey of H_α light has been released by the WHAM (Wisconsin H_α Mapper) collaboration [59]. The WHAM instrument consists of a 6 inch dual-etalon Fabry-Perot spectrometer with a narrow band filter of FWHM $\sim 20 \text{ \AA}$ which images onto a cryogenically cooled 1024×1024 CCD. The resolution of the survey is $\sim 1^\circ$. The spatial power spectrum of free-free emission C_ℓ^{ff} has not yet been determined from the WHAM map; however, analysis of H_α images of the North Celestial Pole area [60] suggests that $C_\ell^{\text{ff}} \propto \ell^{-2.27 \pm 0.07}$.

In Figure 4, we present a map of the northern sky produced by the WHAM survey. In the following sections, we will use this map as a template for the free-free emission. At intermediate Galactic latitudes (say $|b| > 30^\circ$), about 10 % of the H_α light is absorbed by dust and therefore estimates of free-free emission from H_α will be systematically lower than the true value. At latitudes below 10° , this correction becomes increasingly uncertain.

3.3. Vibrational Dust. At the higher frequency range (≥ 100 GHz) of the microwave background experiments, dust emission starts to become dominant. Dust grains are heated by interstellar radiation, absorbing optical and UV photons, and emitting energy in the far infrared.

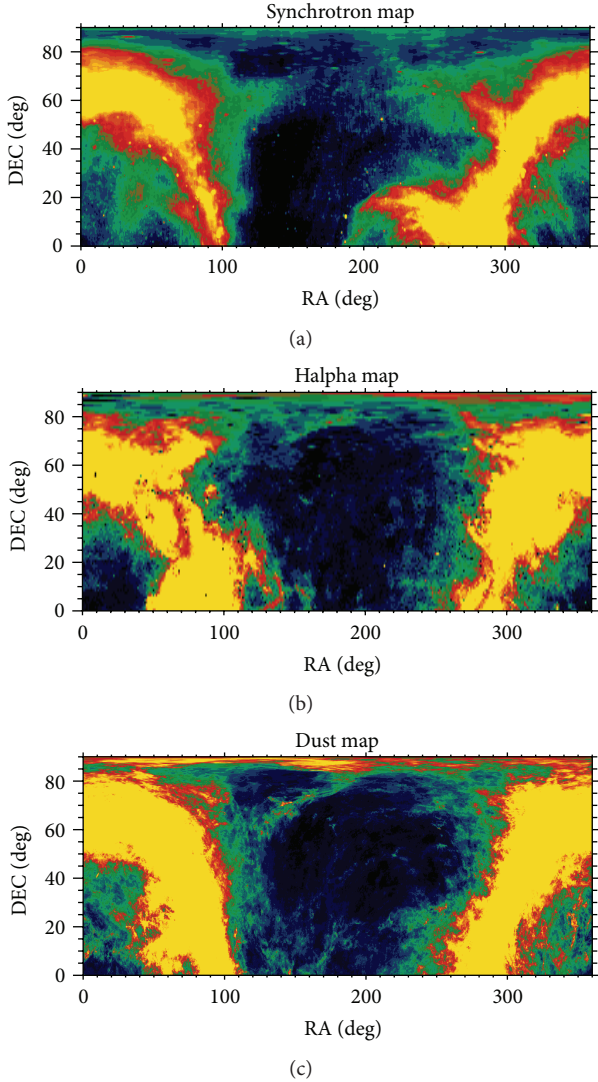


FIGURE 4: From top to bottom. 408 MHz synchrotron map. Resolution: 0.85° and pixels: 0.33° . WHAM H_α map. This map is a courtesy of the WHAM collaboration. Resolution: 1° and pixels: 1° . Combined DIRBE plus IRAS $100 \mu\text{m}$ dust map. Resolution: 6 arcmin and pixels: 0.25° .

The intensity of the emission from an ensemble of dust grains is given by

$$I(\nu) = \int \epsilon(\nu) d\ell, \quad (3)$$

where $\epsilon(\nu)$ is the emissivity at frequency ν , and the integral is along the line of sight. In the Rayleigh-Jeans regime and assuming a constant line-of-sight density of dust,

$$T_b \propto \epsilon(\nu) \nu^{-2}, \quad (4)$$

where T_b is the brightness temperature of the dust emission.

The spectrum of the dust emission has been measured at millimeter and submillimeter wavelengths by the Far Infrared Absolute Spectrophotometer (FIRAS) and can be fitted by a single greybody spectrum of temperature 17.5 K

and emissivity $\propto \nu^2$ [61] at high galactic latitudes. From IRAS observations of dust emission [62], it was found that the spatial power spectrum of the dust fluctuations is $C_\ell^{\text{dust}} \propto \ell^{-3}$. This has also been confirmed at larger angular scales by the COBE-DIRBE satellite.

In the following sections, we will use the combined IRAS-DIRBE map at $100 \mu\text{m}$ [63] as a template for the dust emission. This map has a resolution of FWHM ~ 6 arcmin and covers the full sky. Zodiacal light and point sources have been removed from the map, and the regions of the sky which were not observed by the IRAS satellite have been replaced by DIRBE data. The combined map preserves the DIRBE zero point and calibration. This map is in units of MJy/sr. In Figure 4, we present the northern sky part of the combined IRAS-DIRBE map.

3.4. Rotational Dust. Small spinning interstellar dust grains containing 10^2 – 10^3 atoms can produce detectable rotational emission in the 10–100 GHz range. This emission depends on the component of the electric dipole moment perpendicular to the angular velocity of the grain and on the physical properties of the interstellar medium [3]. For these small grains, rotational excitation is dominated by direct collisions with ions and *plasma drag*. The very smallest grains ($N \leq 150$) have their rotation damped primarily by electric dipole emission; for $150 \leq N \leq 10^3$ plasma drag dominates.

In the following sections, we show models for the spectrum of the spinning dust emission provided by Dr. Draine (private communication). These models depend on a large set of parameters such as the distribution of grain sizes, the charge of the grains, the composition of the grains, and the physical properties of the interstellar medium which were fixed by the authors. However, the normalization of the model can be assumed as a free parameter although it is related to the hydrogen column density in the interstellar medium which is of the order of a few times 10^{20} .

The spatial distribution of small dust grains is not well-known although it seems reasonable to believe that it is not different from that of larger grains but for dense regions where dust coagulation may deplete small grains. For the purpose of this work, we will use the IRAS-DIRBE $100 \mu\text{m}$ map as a template for the spinning dust grains.

4. Galactic and Extragalactic Point Sources

The contribution from resolved point sources to the Tenerife data at 10 and 15 GHz was extrapolated from data of the Michigan monitoring program (M. Aller and H. Aller 2000, private communication). The Michigan program regularly monitors point sources with fluxes above 0.5 Jy at 4.8, 8.0, and 14.5 GHz. The Michigan catalog is neither complete in flux nor time domain. Well-known strong variable sources such as 3C345 are regularly observed, and data at all observing frequencies are available. Weak sources are poorly observed, and often data are available at a single frequency of the three possible. Further, data are available up to June 1999 while the Tenerife experiment operated until September 2000. For the 33 GHz Tenerife data, we used the Metsahovi catalog

(Metsahovi group, private communication) which regularly monitors sources above 1 Jy at 22 and 37 GHz. This catalog is neither complete in flux nor time, although observations are available up to January 2000.

We have developed a software to produce time and frequency complete point source catalogs. The flux of the sources for each frequency was interpolated in time by fitting Fourier series to the data. If the number of independent observations per frequency was smaller than 10, the sources were assumed not variable, and the data was fitted to a constant with time. The extrapolation of the source fluxes into the future time was performed assuming no variability since last observed data point. Spectral indices were calculated for each source from the available data. If only observations at a single frequency were available, we assumed a flat spectrum. We constructed four point source catalogs at 10, 13, 15, and 33 GHz covering the time range from January 1984 to December 2000 with one Julian day sampling and a flux limit of about 0.5 Jy.

For each single day of observations with the Tenerife radiometers, we estimated the total contribution from point sources to the data. This contribution was calculated from the extrapolated catalog at 10, 15, and 33 GHz and the flux, S , was converted into antenna temperature, T , using [64]

$$T = \frac{S\lambda^2}{2k\Omega}, \quad (5)$$

where Ω is the beam solid angle, and λ is the wavelength. The daily point source contributions were stacked in the same manner as the Tenerife data and subtracted from the Tenerife stacks. In the left column of Figure 5, we plot the Tenerife stacked data at 15 GHz for the 10 declinations presented in this paper and overplot in green the contribution from point sources to the data. In the right column, we plot the stacks after subtraction of the point sources.

4.1. Unresolved Sources. A study of the contribution of unresolved point sources (i.e., weak point sources not detected individually) to CMB experiments has been produced by Franceschini et al. [65]. They used numerous surveys, including VLA and IRAS data, to put limits on the contribution to single beam CMB experiments by a random distribution of point sources. The contribution from unresolved point sources to the Tenerife data deduced from the previous analysis is presented in Table 4. We consider sources with flux under 1 Jy at 5 GHz and a main beam of 5° .

5. Assessment of the Galactic Contribution to the Tenerife Data

To assess galactic contribution to the Tenerife data, we correlated observations with the galactic synchrotron, dust, and H_α emission templates described in the previous sections. We convolved the foreground maps with the Tenerife beam at each of the Tenerife frequencies before the correlation was performed. The Tenerife data used in the correlation are the final stacked data presented in Section 2. At 15 GHz we used ten declination stacks in the range 25° – 47.5° ; seven

TABLE 4: Contribution from unresolved point sources to the Tenerife experiment.

ν (GHz)	$\Delta T/T$ (μK)
10	$\leq 7.5 \mu\text{K}$
15	$\leq 4.0 \mu\text{K}$
33	$\leq 0.6 \mu\text{K}$

declination stacks at 10 GHz in the range 30° – 45° ; and only two declination stacks at 33 GHz covering declinations 40° and 42.5° . The data were processed so that data at $|b| \leq 15$ were excluded from the baseline fit and therefore were neither stacked or reconstructed. The discrete point sources were subtracted from the Tenerife stacks as discussed in the previous section.

5.1. The Method. To simultaneously correlate the Tenerife data to the three galactic templates, we use a method which was first applied to this problem by Górski et al. [66] to fit galactic and extragalactic templates in Fourier space to the COBE-DMR data. This method was applied to the Tenerife data first by de Oliveira-Costa et al. [29, 30] and then by Mukherjee et al. [39] to study the possible emission of spinning dust at the Tenerife frequencies.

Assuming that the microwave data is a superposition of CMB, noise, and galactic components, we can write

$$y = aX + x_{\text{CMB}} + n, \quad (6)$$

where y is a Tenerife data vector of N pixels; X is an $N \times M$ element matrix containing $M = 3$ foreground templates convolved with the Tenerife beam; a is a vector of size M that represents the levels at which these foreground templates are present in the Tenerife data—correlation coefficients for each foreground template; n is the instrumental noise in the data; and x_{CMB} is the CMB component of the data. For this analysis, we assume the noise and CMB to be uncorrelated.

The minimum variance estimate of a is given by

$$\hat{a} = [X^T C^{-1} X]^{-1} X^T C^{-1} y \quad (7)$$

with errors given by $\sigma_{\hat{a}_i} = \sum_{ii}^{1/2}$, where \sum is given as

$$\sum = \langle \hat{a}^2 \rangle - \langle \hat{a} \rangle^2 = [X^T C^{-1} X]^{-1}. \quad (8)$$

In the before mentioned, C is the total covariance matrix, the sum of the noise covariance matrix, and the CMB covariance matrix. The noise covariance matrix of the Tenerife data is taken to be diagonal—no correlation between different pixels. The CMB covariance matrix was obtained analytically following Zaldarriaga [67].

This correlation method produces minimum variance and unbiased estimates of a if the following holds.

- (i) *The error in the Tenerife data is Gaussian and with zero mean.* To a very good approximation the instrumental noise in the Tenerife data is uncorrelated.

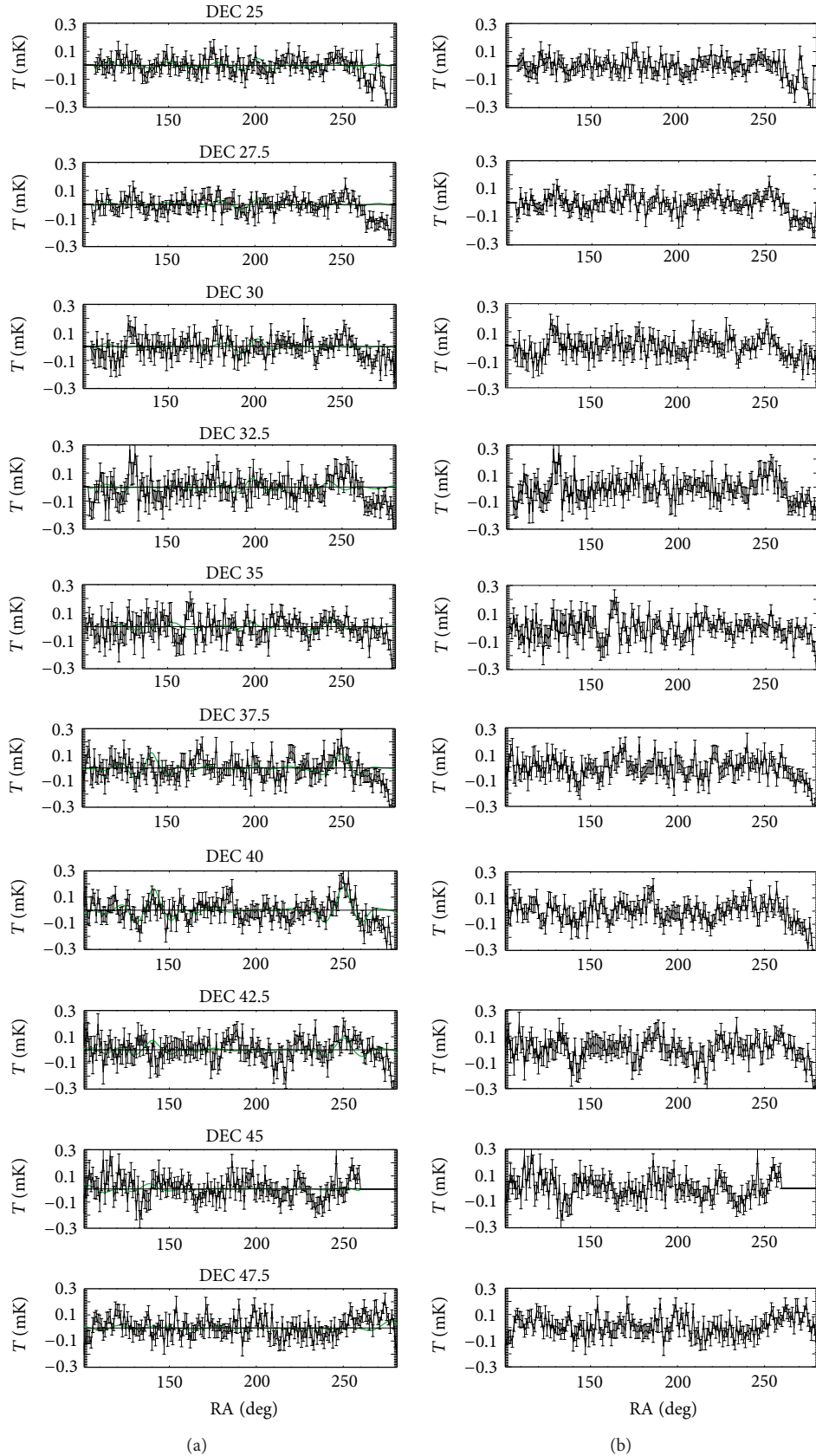


FIGURE 5: Extrapolated point source contribution to the 15 GHz Tenerife data. (a): Observed scans; (b): point source-corrected scans.

- (ii) *The templates perfectly trace the foreground emissions at microwave frequencies.* There may be components of emission present in the Tenerife data, apart from those we have identified, for which there are not obvious counterparts at other frequencies. Moreover, the templates we use do not perfectly trace the microwave emission of the galactic foreground. The latter is specially important in the case of vibrational and rotational dust for which the template comes from data at much higher frequencies. For example, Draine and Lazarian [3] proposed that a $12\ \mu\text{m}$ map would be a much better tracer of rotational dust emission because small grains will also emit at this frequency. Also, the H_α emission is absorbed at low galactic latitudes by interstellar dust and therefore does not fully trace the free-free emission at those latitudes. Moreover, the 408 MHz map has residual striping.
- (iii) *The templates are perfect—errors bars equal to zero.* The error estimated for the templates are about 5%–10 % of the signal. They are not corrected for in this analysis because they are small compared to the errors in the Tenerife data.
- (iv) *The templates are not correlated.* It there is a correlation between the different templates, the set of minimum variance correlation coefficients \hat{a} is degenerate and, therefore, we would not be able to discriminate among the different foreground components. At low galactic latitudes, the galactic plane emission dominates and Mukherjee et al. [39] have found that the foreground templates are correlated in this region.
- (v) *The correlation coefficient a is the same throughout the area of sky for which the correlation is performed.* If it is not, the error associated with a is systematically underestimated. As a double check, we divided the sky observed into independent areas and performed the same correlation test in each, calculating a mean correlation coefficient and the dispersion of the individual values which in most cases was in good agreement with the error of a calculated for the total area.

5.2. Cross-Correlation Results. The cross-correlation results are presented in Table 5. The correlation was performed for three different galactic cuts $b > 20$, $b > 30$, and $b > 40$. σ_{gal} represents the r.m.s. of the galactic maps after convolution with the Tenerife beam. \hat{a} and $\sigma_{\hat{a}}$ are the correlation coefficient and the error associated with it. They have units of $\mu\text{K}/\text{K}$, $\mu\text{K}/(\text{MJy sr}^{-1})$ and $\mu\text{K}/\text{R}$ for the correlation with the 408 MHz, $100\ \mu\text{m}$, and WHAM maps respectively. ΔT is the r.m.s. contribution from the galactic foregrounds to the Tenerife data, which was obtained as $\sigma_{\text{gal}} \times \hat{a}$. This analysis is improved with respect to previous analyses by de Oliveira-Costa et al. [29, 30] and Mukherjee et al. [39], First, because we present Tenerife data at 10 and 15 GHz for a much larger area of the sky and with improved sensitivity; and second, because we also include in the cross-correlation a template

TABLE 5: Cross-correlation results. See text for details.

Galactic cut	ν (GHz)	σ_{gal}	$\hat{a} \pm \sigma_{\hat{a}}$	ΔT (μK)		
$b > 20^\circ$	10 GHz	408 MHz	1.0217	17 ± 6	17.4 ± 6.0	
		$100\ \mu\text{m}$	0.3256	23 ± 17	7.5 ± 5.5	
		WHAM	0.2513	42 ± 20	10.5 ± 5.5	
	15 GHz	408 MHz	1.0244	9 ± 3	9.2 ± 3.0	
		$100\ \mu\text{m}$	0.3308	66 ± 8	21.8 ± 2.6	
		WHAM	0.2758	-10 ± 10	-2.7 ± 2.7	
		408 MHz	0.8904	4 ± 9	3.6 ± 8.0	
		33 GHz	$100\ \mu\text{m}$	0.3089	86 ± 27	26.0 ± 8.0
		WHAM	0.2768	21 ± 51	5.8 ± 10.0	
	$b > 30^\circ$	10 GHz	408 MHz	0.8722	15 ± 7	13.0 ± 6.0
			$100\ \mu\text{m}$	0.2028	72 ± 30	14.6 ± 6.0
			WHAM	0.1435	83 ± 42	11.9 ± 6.0
15 GHz		408 MHz	0.8544	13 ± 4	11.1 ± 3.4	
		$100\ \mu\text{m}$	0.2036	-1 ± 14	-0.2 ± 2.8	
		WHAM	0.1504	30 ± 20	4.5 ± 3.0	
		408 MHz	0.7749	7 ± 10	5.4 ± 7.7	
		33 GHz	$100\ \mu\text{m}$	0.2143	90 ± 45	19.2 ± 9.6
		WHAM	0.1473	17 ± 63	2.5 ± 9.3	
$b > 40^\circ$		10 GHz	408 MHz	0.7676	11 ± 9.5	8.4 ± 8.0
			$100\ \mu\text{m}$	0.1898	110 ± 45	20.9 ± 8.5
			WHAM	0.1292	77 ± 52	9.9 ± 6.7
	15 GHz	408 MHz	0.7412	15 ± 5	11.1 ± 3.7	
		$100\ \mu\text{m}$	0.1782	-11 ± 21	-1.9 ± 3.7	
		WHAM	0.1354	51 ± 25	6.9 ± 3.4	
		408 MHz	0.6630	4 ± 15	2.6 ± 9.9	
		33 GHz	$100\ \mu\text{m}$	0.2138	66 ± 55	14.8 ± 11.8
		WHAM	0.1499	47 ± 69	7.0 ± 10.3	

for the free-free emission. Moreover, data at 33 GHz have also been included in the analysis although the area of the sky observed is significantly smaller than at 10 and 15 GHz and consequently the error bars in the estimated cross-correlation coefficients are much larger. We have pictorially summarised the cross-correlation results in Figure 6. In the top row of the figure, we plot the r.m.s. contribution from synchrotron to the Tenerife data at the three galactic cuts analysed. In black, we overplot the expected synchrotron contribution for a spectral index of -3.0 and derived from the r.m.s. level in the 408 MHz map. The contributions are systematically lower than expected at 10 GHz, and the spectral index is much flatter such that, for example, the contribution at 15 GHz is consistent with that at 10 GHz for $b > 40^\circ$. We have derived from the Tenerife data spectral indexes of $-1.77_{-2.0}^{+1.0}$, $-0.40_{-1.9}^{+1.0}$ and $-0.40_{-1.6}^{+2.0}$ at $b > 20^\circ$, $b > 30^\circ$ and $b > 40^\circ$ respectively, and the r.m.s. contributions based on these spectral indices is overplotted in red.

In the middle row, we plot the r.m.s. contribution from free-free emission to the Tenerife data. In black, we overplot the expected free-free emission at microwave frequencies derived from (2) which are actually in very good agreement

TABLE 6: Cross-correlation results of CMB data with dust. Available cross-correlation coefficients of CMB data sets with dust templates at $100 \mu\text{m}$.

Experiment	Frequency (GHz)	$ b >$ (degrees)	$\hat{a} \pm \sigma_{\hat{a}} \mu\text{K}/(\text{MJy}\cdot\text{sr}^{-1})$	References
COBE DMR	31.5	20	18.0 ± 2.5	Kogut et al. [37]
COBE DMR	31.5	30	14.5 ± 6.0	Kogut et al. [37]
COBE DMR	53.0	20	6.8 ± 1.4	Kogut et al. [37]
COBE DMR	53.0	30	6.4 ± 3.4	Kogut et al. [37]
COBE DMR	90.0	20	2.7 ± 1.6	Kogut et al. [37]
COBE DMR	90.0	30	4.6 ± 3.9	Kogut et al. [37]
Saskatoon (Ka band)	30.0	NCP	15.0 ± 8.1	De Oliveira-Costa et al. [25, 26]
Saskatoon (Q band)	40.0	NCP	11.8 ± 10	De Oliveira-Costa et al. [25, 26]
19 GHz survey	19.0	20	38.5 ± 3.5	De Oliveira-Costa et al. [27, 28]
19 GHz survey	19.0	30	47.1 ± 9.0	De Oliveira-Costa et al. [27, 28]
OVRO	14.5	NCP	209	Leitch et al. [1, 2]
OVRO	32.0	NCP	36	Leitch et al. [1, 2]
PYTHON V	40.3		-3.0 ± 18.0	Coble et al. [38]
Tenerife	10.0	20	49.8 ± 11.0	De Oliveira-Costa et al. [29, 30]
Tenerife	10.0	30	-8.3 ± 31.0	De Oliveira-Costa et al. [29, 30]
Tenerife	10.0	40	84.0 ± 54.0	De Oliveira-Costa et al. [29, 30]
Tenerife	15.0	20	71.8 ± 4.5	De Oliveira-Costa et al. [29, 30]
Tenerife	15.0	30	94.9 ± 15.0	De Oliveira-Costa et al. [29, 30]
Tenerife	15.0	40	72.0 ± 33.0	De Oliveira-Costa et al. [29, 30]
Tenerife	10.0	20	71.0 ± 18.0	Mukherjee et al. [39]
Tenerife	10.0	30	-7.0 ± 32.0	Mukherjee et al. [39]
Tenerife	10.0	40	28.0 ± 39.0	Mukherjee et al. [39]
Tenerife	15.0	20	91.0 ± 11.0	Mukherjee et al. [39]
Tenerife	15.0	30	29.0 ± 20.0	Mukherjee et al. [39]
Tenerife	15.0	40	3.0 ± 26.0	Mukherjee et al. [39]
South Pole 94	30.0	40	20.0 ± 36.0	Hamilton and Ganga [40]
South Pole 94	40.0	40	68.1 ± 42.4	Hamilton and Ganga [40]

with the observations. In red, we plot the free-free contribution for spectral indexes of -0.5 , -2.20 , and -1.0 at $b > 20^\circ$, $b > 30^\circ$, and $b > 40^\circ$, respectively.

In the bottom row of Figure 6, we plot the r.m.s. contribution from dust emission to the Tenerife data which is significantly larger (few orders of magnitude) than expected from vibrational dust. In solid black, we overplot an r.m.s. brightness temperature expected from the CNM model of rotational dust proposed by Draine and Lazarian [3]. The models were rescaled to fit the data. The intensity spectrum for this model peaks at 50 GHz which corresponds to a peak in brightness temperature around 20 GHz of about $300 \mu\text{K}$. From the best fit model to the data, we have estimated fluctuations in the temperature of the rotational dust of $\sim 8\%$ at the angular scales of the Tenerife experiment.

The r.m.s. contributions from dust to the 15 GHz data at $b > 30^\circ$ and $b > 40^\circ$, as well as the contribution from free-free at $b > 20^\circ$ seem to be underestimated. This could be caused by correlations between the synchrotron, dust, and free-free templates which would reduce the validity of the minimum variance solution and could bias the estimates of the correlation. In Figure 7, we plot the following correlations, from top to bottom synchrotron versus dust; free-free

versus dust, and free-free versus synchrotron for $b > 20^\circ$, $b > 30^\circ$, and $b > 40^\circ$. We observe no correlation between free-free and synchrotron, moderate correlation between free-free and dust and a quite strong correlation between synchrotron and dust at low galactic latitudes weakening down at high latitudes. Note that at $b > 20^\circ$, the correlation plots show negative versus negative points which do not follow the correlation pattern of the main body of points. The former points correspond to the lowest galactic latitude data which run into a negative beam of the triple beam pattern for the galactic plane crossing. The observed correlations between templates can not justify the observed lack of dust correlation at 15 GHz data at $b > 30^\circ$ and $b > 40^\circ$. In the following, we concentrate on the $b > 20^\circ$ region for which we detect significant dust correlated signal at all Tenerife frequencies.

6. Dust-Related Emission

Hinshaw et al. [37] cross-correlated the COBE differential microwave radiometer (DMR) maps with DIRBE far infrared maps and discovered that statistically significant correlation did exist at each DMR frequency, which was inconsistent with vibrational dust alone. This extra correlation was explained

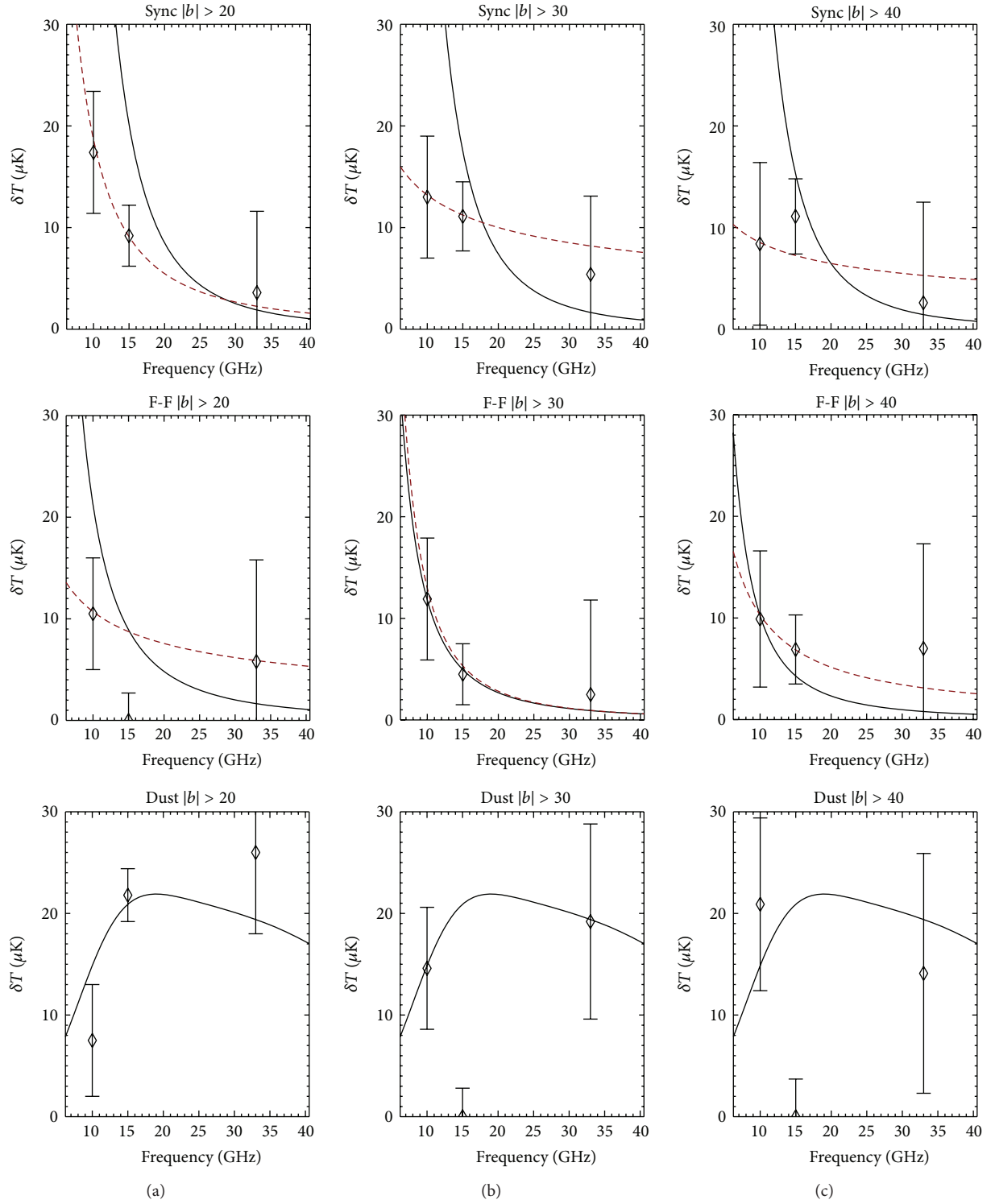


FIGURE 6: Spectra of foregrounds at the Tenerife frequencies. We represent the cross-correlation coefficients as a function of frequency for $b > 20$, $b > 30$, and $b > 40$ ((a), (b), and (c), resp.). From top to bottom, we plot the r.m.s. contribution from synchrotron, free-free, and dust to the Tenerife data. In solid black and red, we show standard and best-fit models of the electromagnetic spectrum for each galactic emission. The models for dust are rescaled to fit the data. Details on the best-fit models can be found in the text.

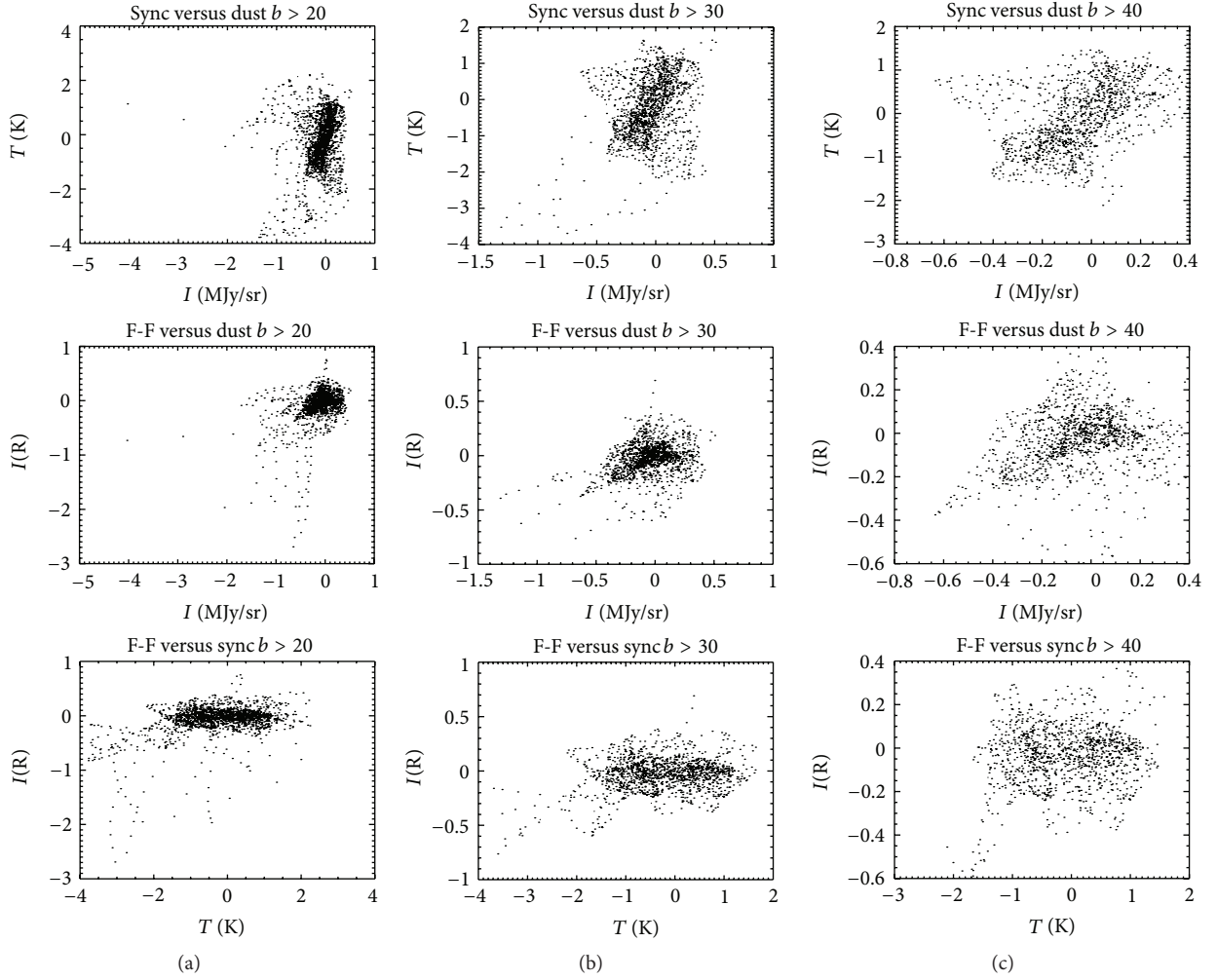


FIGURE 7: Correlation between the foreground templates. From top to bottom, we plot synchrotron versus dust, free-free versus dust and free-free versus synchrotron. The correlation is presented for $b > 20$, $b > 30$, and $b > 40$ ((a), (b), and (c), resp.).

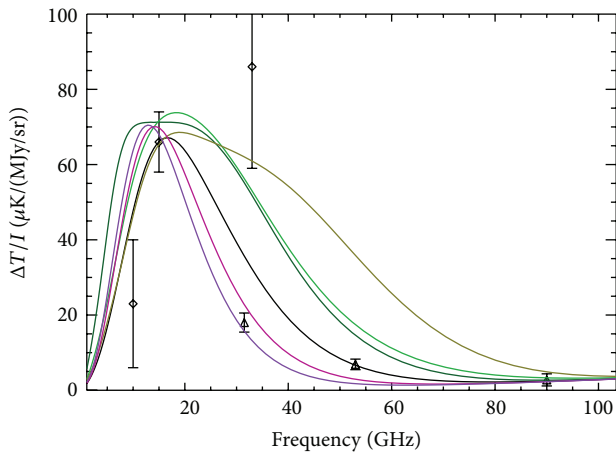


FIGURE 8: Cross-correlation coefficients for the dust-correlated emission. We plot the Tenerife data as diamonds and the COBE DMR data as triangles. The color solid curves over plotted correspond to joint vibrational and rotational dust models as described in the text.

at the time as free-free emission. Following this publication, other authors have cross-correlated CMB data sets with dust templates and found an excess of correlation which has been interpreted as free-free emission, flat-spectrum synchrotron, or emission from spinning dust. In Table 6, we present an up-to-date list of CMB data for which the correlation with dust has been performed. In all cases, a multitemplate method has been used to perform the correlation but no free-free template has been used. We have also added in this table previous analyses of the Tenerife data by de Oliveira-Costa et al. [29, 30] and Mukherjee et al. [39] which did not include the 33 GHz data and covered a much smaller area of the sky at 10 and 15 GHz.

The correlation coefficients we deduced are significantly smaller at $|b| > 20$ than those calculated by de Oliveira-Costa et al. [29, 30] and Mukherjee et al. [39]. This is probably due to 50 % larger area (localized signals are diluted) and a more careful subtraction of baselines at low galactic latitudes in our data. The inclusion of an extra free-free template seems to play a minor role on this at 10 GHz and none at 15 GHz.

The cross-correlation results for the Tenerife experiment presented in this paper confirm the existence of extra dust-correlated emission at microwave frequencies and suggest that it is not due to free-free emission. The moderate correlation found between the dust and free-free templates could confuse the results obtained but clearly cannot account for all the observed dust-correlated component. A more detailed study is needed to take into account correlations between templates in the calculation of the correlation coefficients.

In Figure 8, we plot the dust cross-correlation coefficients ($|b| > 20$) for the Tenerife (diamonds) and COBE-DMR (triangles) data. The rest of the experiments presented in Table 6 were not included in this plot because they observe at different angular scales and different areas of the sky (see table for details) and therefore no direct comparison with the Tenerife and COBE data is possible. The Tenerife data suggest a peak in the spectrum at about 30 GHz although this is mainly based on the data at 33 GHz which is significantly much noisier and cover a much smaller part of the sky. However, DMR data combined with the 10 and 15 GHz Tenerife data points prefer a peak in the range 15–20 GHz. In color, we overplot the six spinning dust models proposed by Draine and Lazarian [3] combined with the standard vibrational dust model described in the previous sections, for which the amplitude has been taken as a free parameter and fitted to the COBE and Tenerife 10 and 15 GHz data. We observe that the shape of the spectrum given by the data is similar to some of the predicted spectra although the models do not indicate a sharp rise in the range 10–15 GHz.

7. Conclusions

We have presented in this paper a reanalysis of the Tenerife data including previously published data and new data from January 1998 to December 2000. This analysis leads to evidences for an excess of dust-correlated emission at microwave frequencies in the range 10–33 GHz and at large angular scales, from 5 to 15 degrees. This correlation can not all be associated with free-free emission. A combination of the Tenerife and COBE data suggests spinning dust emission could account for the extra correlation. However, the scatter observed in the data and the discrepancy in the spectrum shape indicate other components may also be responsible for the extra correlation. Furthermore, the analysis does not take into account correlations between the galactic emission templates and this can bias the estimate of the correlation coefficients. To correct this, a more detailed analysis, which will account for the cross-correlation between templates, is needed.

Acknowledgment

The authors would like to thank the editors of this paper.

References

- [1] E. M. Leitch, A. C. S. Readhead, T. J. Pearson, and S. T. Myers, “An anomalous component of galactic emission,” *The Astrophysical Journal*, vol. 486, no. 1, pp. 23–26, 1997.
- [2] E. M. Leitch, A. C. S. Readhead, T. J. Pearson, and S. T. Myers, “An anomalous component of galactic emission,” *Astrophysical Journal Letters*, vol. 486, no. 1, pp. L23–L26, 1997.
- [3] B. T. Draine and A. Lazarian, “Diffuse Galactic emission from spinning dust grains,” *The Astrophysical Journal Letters*, vol. 494, no. 1, pp. L19–L22, 1998.
- [4] B. T. Draine and A. Lazarian, “Electric dipole radiation from spinning dust grains,” *The Astrophysical Journal*, vol. 508, no. 1, pp. 157–179, 1998.
- [5] Douglas P. Finkbeiner, “A full-sky $H\alpha$ template for microwave foreground prediction,” *The Astrophysical Journal Supplement*, vol. 146, no. 2, pp. 407–415, 2003.
- [6] A. De Oliveira-Costa, M. Tegmark, R. D. Davies et al., “The quest for microwave foreground X,” *Astrophysical Journal Letters*, vol. 606, no. 2, pp. L89–L92, 2004.
- [7] R. A. Watson, R. Rebolo, J. A. Rubiño-Martín et al. et al., “Detection of anomalous microwave emission in the perseus molecular cloud with the COSMOSOMAS experiment,” *The Astrophysical Journal Letters*, vol. 624, no. 2, pp. L89–L92, 2005.
- [8] S. Iglesias-Groth, “Electric dipole emission by fullerenes and galactic anomalous microwave emission,” *The Astrophysical Journal Letters*, vol. 632, no. 1, pp. L25–L28, 2005.
- [9] S. Casassus, G. F. Cabrera, F. Förster, T. J. Pearson, A. C. S. Readhead, and C. Dickinson, “Morphological analysis of the centimeter-wave continuum in the dark cloud LDN 1622,” *The Astrophysical Journal*, vol. 639, no. 2, pp. 951–964, 2006.
- [10] S. Casassus, C. Dickinson, K. Cleary et al. et al., “Centimetre-wave continuum radiation from the ρ Ophiuchi molecular cloud,” *Monthly Notices of the Royal Astronomical Society*, vol. 391, no. 3, pp. 1075–1090, 2008.
- [11] C. Dickinson, R. D. Davies, J. R. Allison et al. et al., “Anomalous microwave emission from the HII region RCW175,” *The Astrophysical Journal*, vol. 690, no. 2, pp. 1585–1589, 2009.
- [12] C. T. Tibbs, R. A. Watson, C. Dickinson et al., “Very small array observations of the anomalous microwave emission in the Perseus region,” *Monthly Notices of the Royal Astronomical Society*, vol. 402, no. 3, pp. 1969–1979, 2010.
- [13] Y. Ali-Haïmoud, C. M. Hirata, and C. Dickinson, “A refined model for spinning dust radiation,” *Monthly Notices of the Royal Astronomical Society*, vol. 395, no. 2, pp. 1055–1078, 2009.
- [14] T. Hoang, B. T. Draine, and A. Lazarian, “Improving the model of emission from spinning dust: effects of grain wobbling and transient spin-up,” *Astrophysical Journal Letters*, vol. 715, no. 2, pp. 1462–1485, 2010.
- [15] T. Hoang, A. Lazarian, and B. T. Draine, “Spinning dust emission: effects of irregular grain shape, transient heating and comparison with WMAP results,” *The Astrophysical Journal*, vol. 741, no. 2, p. 87, 2011.
- [16] B. T. Draine and A. Lazarian, “Magnetic dipole microwave emission from dust grains,” *Astrophysical Journal Letters*, vol. 512, no. 2, pp. 740–754, 1999.
- [17] E. S. Battistelli, R. Rebolo, J. A. Rubiño-Martín et al., “Polarization observations of the anomalous microwave emission in the perseus molecular complex with the COSMOSOMAS experiment,” *The Astrophysical Journal Letters*, vol. 645, no. 2, pp. L141–L144, 2006.
- [18] A. Kogut, J. Dunkley, C. L. Bennett et al., “Three-year wilkinson microwave anisotropy probe (WMAP) observations: foreground polarization,” *The Astrophysical Journal*, vol. 665, no. 1, pp. 335–362, 2007.

- [19] B. S. Mason, T. Robishaw, C. Heiles, D. Finkbeiner, and C. Dickinson, "A limit on the polarized anomalous microwave emission of Lynds 1622," *Astrophysical Journal Letters*, vol. 697, no. 2, pp. 1187–1193, 2009.
- [20] C. H. López-Caraballo, J. A. Rubiño-Martín, R. Rebolo, and R. Génova-Santos, "Constraints on the polarization of the anomalous microwave emission in the Perseus molecular complex from seven-year WMAP data," *The Astrophysical Journal*, vol. 729, no. 1, p. 25, 2011.
- [21] B. T. Draine and B. Hensley, "Magnetic nanoparticles in the interstellar medium: emission spectrum and polarization," *The Astrophysical Journal*, vol. 765, no. 2, p. 159, 2013.
- [22] F. X. Desert, F. Boulanger, and J. L. Puget, Eds., "Interstellar dust models for extinction and emission," *Astronomy & Astrophysics*, vol. 237, no. 1, pp. 2015–236, 1990.
- [23] A. Kogut, A. J. Banday, C. L. Bennett, K. M. Gorski, G. Hinshaw, and W. T. Reach, "High-Latitude Galactic Emission in the COBE Differential Microwave Radiometer 2 Year Sky Maps," *The Astrophysical Journal*, vol. 460, 1 pages, 1996.
- [24] A. Kogut, A. J. Banday, C. L. Bennett et al., "Microwave emission at high galactic latitudes in the four-year DMR sky maps," *The Astrophysical Journal Letters*, vol. 464, no. 1, pp. L5–L19, 1996.
- [25] M. S. Kowitt, E. S. Cheng, D. A. Cottingham et al., "A detection of bright features in the microwave background," *The Astrophysical Journal*, vol. 482, no. 1, pp. 17–21, 1997.
- [26] A. De Oliveira-Costa, A. Kogut, M. J. Devlin, C. Barth Netterfield, L. A. Page, and E. J. Wollack, "Galactic microwave emission at degree angular scales," *Astrophysical Journal Letters*, vol. 482, no. 1, pp. L17–L20, 1997.
- [27] A. de Oliveira-Costa, M. Tegmark, L. A. Page, and S. P. Boughn, "Galactic emission at 19 GHz," *Astrophysical Journal*, vol. 509, no. 1, pp. 9–12, 1998.
- [28] A. de Oliveira-Costa, M. Tegmark, L. A. Page, and S. P. Boughn, "Galactic emission at 19 GHz," *Astrophysical Journal Letters*, vol. 509, no. 1, pp. L9–L12, 1998.
- [29] A. de Oliveira-Costa, M. Tegmark, C. M. Gutierrez et al., "Cross-correlation of Tenerife data with Galactic templates—evidence for spinning dust?" *The Astrophysical Journal Letters*, vol. 527, no. 1, pp. L9–L12, 1999.
- [30] A. de Oliveira-Costa, M. Tegmark, C. M. Gutierrez et al., "Cross-correlation of Tenerife data with Galactic templates—evidence for spinning dust?" *The Astrophysical Journal*, vol. 527, no. 1, pp. 9–12, 1999.
- [31] R. Genova-Santos, R. Rebolo, J. A. Rubiño-Martín, C. H. López-Caraballo, and S. R. Hildebrandt, "Detection of anomalous microwave emission in the Pleiades reflection nebula with Wilkinson Microwave Anisotropy Probe and the COSMOSOMAS experiment," *Astrophysical Journal*, vol. 743, no. 1, p. 67, 2011.
- [32] A. M. M. Scaife, N. Hurley-Walker, D. A. Green et al., "An excess of emission in the dark cloud LDN1111 with the Arcminute Microkelvin Imager," *Monthly Notices of the Royal Astronomical Society*, vol. 394, no. 1, pp. L46–L50, 2009.
- [33] A. M. I. Consortium, A. M. M. Scaife, N. Hurley-Walker et al. et al., "AMI observations of Lynds dark nebulae: further evidence for anomalous cm-wave emission," *Monthly Notices of the Royal Astronomical Society*, vol. 400, no. 3, pp. 1394–1412, 2009.
- [34] P. Castellanos, S. Casassus, C. Dickinson et al. et al., "Dust-correlated centimetre-wave radiation from the M78 reflection nebula," *Monthly Notices of the Royal Astronomical Society*, vol. 411, no. 2, pp. 1137–1150, 2011.
- [35] Planck Collaboration, "Planck early results. XX. New light on anomalous microwave emission from spinning dust grains," *Astronomy & Astrophysics*, vol. 536, article A20, 17 pages, 2011.
- [36] C. Bot, N. Ysard, D. Paradis et al., "Submillimeter to centimeter excess emission from the Magellanic Clouds. II. On the nature of the excess," *Astronomy & Astrophysics*, vol. 523, article A20, pp. 1–7, 2010.
- [37] G. Hinshaw, A. J. Banday, C. L. Bennett et al., "Band power spectra in the COBE 1 DMR four-year anisotropy maps," *Astrophysical Journal Letters*, vol. 464, no. 1, pp. L17–L20, 1996.
- [38] K. Coble, M. Dragovan, J. Kovac et al. et al., "Anisotropy in the cosmic microwave background at degree angular scales: python V results," *The Astrophysical Journal Letters*, vol. 519, no. 1, pp. L5–L8, 1999.
- [39] P. Mukherjee, A. W. Jones, R. Kneissl, and A. N. Lasenby, "On dust-correlated Galactic emission in the Tenerife data," *Monthly Notices of the Royal Astronomical Society*, vol. 320, no. 2, pp. 224–234, 2001.
- [40] J. C. Hamilton and K. M. Ganga, "Correlation of the South Pole 94 data with 100 μm and 408 MHz maps," *Astronomy & Astrophysics*, vol. 368, no. 3, pp. 760–765, 2001.
- [41] C. L. Bennett, M. Halpern, G. Hinshaw et al. et al., "First-year Wilkinson Microwave Anisotropy Probe (WMAP) observations: preliminary maps and basic results," *The Astrophysical Journal Supplement Series*, vol. 148, no. 1, pp. 1–27, 2003.
- [42] S. Fernández-Cerezo, C. M. Gutierrez, R. Rebolo et al., "Observations of the cosmic microwave background and galactic foregrounds at 12–17 GHz with the COSMOSOMAS experiment," *Monthly Notices of the Royal Astronomical Society*, vol. 370, no. 1, pp. 15–24, 2006.
- [43] S. R. Hildebrandt, R. Rebolo, J. A. Rubiño-Martín et al., "COSMOSOMAS observations of the cosmic microwave background and Galactic foregrounds at 11 GHz: evidence for anomalous microwave emission at high Galactic latitude," *Monthly Notices of the Royal Astronomical Society*, vol. 382, no. 2, pp. 594–608, 2007.
- [44] N. Ysard, M. A. Miville-Deschênes, and L. Verstraete, "Probing the origin of the microwave anomalous foreground," *Astronomy & Astrophysics*, vol. 509, article L1, 2010.
- [45] R. D. Davies, C. Dickinson, A. J. Banday, T. R. Jaffe, K. M. Gorski, and R. J. Davis, "A determination of the spectra of Galactic components observed by the Wilkinson Microwave Anisotropy Probe," *Monthly Notices of the Royal Astronomical Society*, vol. 370, no. 3, pp. 1125–1139, 2006.
- [46] A. Kogut, D. J. Fixsen, S. M. Levin et al., "Arcade 2 observations of galactic radio emission," *The Astrophysical Journal*, vol. 734, no. 1, p. 4, 2011.
- [47] Carlos M. Gutierrez, R. Rebolo, Robert A. Watson, Rod D. Davies, Aled W. Jones, and Anthony N. Lasenby, "The Tenerife cosmic microwave background maps: observations and first analysis," *The Astrophysical Journal*, vol. 529, no. 1, pp. 47–55, 2000.
- [48] S. Hancock, R. D. Davies, A. N. Lasenby et al., "Direct observation of structure in the cosmic microwave background," *Nature*, vol. 367, no. 6461, pp. 333–338, 1994.
- [49] G. Ribicki and A. Lightman, *Radiative Processes in Astrophysics*, Wiley, New York, NY, USA, 1979.
- [50] M. Longair, *High Energy Astrophysics*, Cambridge University Press, 1994.
- [51] G. De Zotti, L. Toffolatti, F. Argüeso et al., "The Planck Surveyor mission: astrophysical prospects," *AIP Conference Proceedings*, vol. 476, pp. 204–223, 1999.

- [52] K. Lawson, C. Mayer, J. Osborn, and M. Parkinson, "Variations in the Spectral Index of the Galactic Radio Continuum Emission in the Northern Hemisphere," *Monthly Notices of the Royal Astronomical Society*, vol. 286, p. 307, 1987.
- [53] C. G. T. Haslam, U. Klein, C. J. Salter et al., "A 408 MHz all-sky continuum survey. I: observations at southern declinations and for the North Polar region," *Astronomy & Astrophysics*, vol. 100, no. 2, pp. 209–219, 1981.
- [54] P. Reich and W. Reich, "A map of spectral indices of the Galactic radio continuum emission between 408 MHz and 1420 MHz for the entire northern sky," *Astronomy & Astrophysics*, vol. 74, p. 4, 1988.
- [55] R. D. Davies, R. A. Watson, and C. M. Gutierrez, "Galactic synchrotron emission at high frequencies," *Monthly Notices of the Royal Astronomical Society*, vol. 278, no. 4, pp. 925–939, 1996.
- [56] F. R. Bouchet and R. Gispert, "Foregrounds and CMB experiments: I. Semi-analytical estimates of contamination," *New Astronomy*, vol. 4, no. 6, pp. 443–479, 1999.
- [57] A. Lasenby, "Radio frequency foreground emission and the separation of microwave anisotropies from foreground contamination," in *Proceedings of the 16th Moriond Astrophysics Meeting: Microwave Background Anisotropies*, vol. 453, 1996.
- [58] D. Valls-Gabaud, "Cosmological applications of H α surveys," *Publications of the Astronomical Society of Australia*, vol. 15, no. 1, pp. 111–117, 1998.
- [59] L. M. Haffner, R. J. Reynolds, and S. L. Tufte, "WHAM observations of H-alpha, [S II], and [N II] toward the Orion and perseus arms: probing the physical conditions of the warm ionized medium," *Astrophysical Journal Letters*, vol. 523, no. 1, pp. 223–233, 1999.
- [60] S. Veeraraghavan and R. D. Davies, "Low frequency galactic backgrounds," in *Proceedings of the Particle Physics and Early Universe Conference*, Cambridge, UK, April 1997.
- [61] F. Boulanger, A. Abergel, J. P. Bernard et al., "The dust/gas correlation at high Galactic latitude," *Astronomy & Astrophysics*, vol. 312, no. 1, pp. 256–262, 1996.
- [62] T. N. Gautier, T. Cawfield, and M. W. Werner, "IR emission from small grains in HII regions and reflection nebulae," *Bulletin of the American Astronomical Society*, vol. 24, p. 1120, 1992.
- [63] D. J. Schlegel, D. P. Finkbeiner, and M. Davis, "Maps of dust infrared emission for use in estimation of reddening and cosmic microwave background radiation foregrounds," *Astrophysical Journal Letters*, vol. 500, no. 2, pp. 525–553, 1998.
- [64] K. Rohlfs and T. Wilson, *Tools of Radio Astronomy*, Springer, 2000.
- [65] A. Franceschini, L. Toffolatti, L. Danese, and G. de Zotti, "Discrete source contributions to small-scale anisotropies of the microwave background," *Astrophysical Journal*, vol. 344, pp. 35–45, 1989.
- [66] K. M. Górski, A. J. Banday, C. L. Bennett et al., "Power spectrum of primordial inhomogeneity determined from the FOUR-Year COBE DMR sky maps," *The Astrophysical Journal Letters*, vol. 464, no. 1, pp. L11–L15, 1996.
- [67] M. Zaldarriaga, *Fluctuations in the cosmic microwave background [Ph.D. thesis]*, Massachusetts Institute of Technology, 1998.

Research Article

Investigating the Source of Planck-Detected AME: High-Resolution Observations at 15 GHz

Yvette C. Perrott,¹ Anna M. M. Scaife,²
Natasha Hurley-Walker,³ and Keith J. B. Grainge¹

¹ Astrophysics Group, Cavendish Laboratory, 19 J. J. Thomson Avenue, Cambridge CB3 0HE, UK

² School of Physics & Astronomy, University of Southampton, Highfield, Southampton SO17 1BJ, UK

³ International Centre for Radio Astronomy Research, Curtin Institute of Radio Astronomy, 1 Turner Avenue, Technology Park, Bentley, Perth, WA 6845, Australia

Correspondence should be addressed to Yvette C. Perrott; ycp21@mrao.cam.ac.uk

Received 13 August 2012; Accepted 18 January 2013

Academic Editor: Roberta Paladini

Copyright © 2013 Yvette C. Perrott et al. This is an open access article distributed under the Creative Commons Attribution License, which permits unrestricted use, distribution, and reproduction in any medium, provided the original work is properly cited.

The *Planck* 28.5 GHz maps were searched for potential Anomalous Microwave Emission (AME) regions on the scale of $\sim 3^\circ$ or smaller, and several new regions of interest were selected. Ancillary data at both lower and higher frequencies were used to construct spectral energy distributions (SEDs), which seem to confirm an excess consistent with spinning dust models. Here we present higher resolution observations of two of these new regions with the Arcminute Microkelvin Imager Small Array (AMI SA) between 14 and 18 GHz to test for the presence of a compact (~ 10 arcmin or smaller) component. For AME-G107.1+5.2, dominated by the Hii region S140, we find evidence for the characteristic rising spectrum associated with either the spinning dust mechanism for AME or an ultra-/hypercompact Hii region across the AMI frequency band; however, for AME-G173.6+208 we find no evidence for AME on scales of ~ 2 – 10 arcmin.

1. Introduction

The *Planck* satellite [1, 2] observes the sky in nine frequency bands, covering a range from 30 to 857 GHz. Its wide frequency range potentially allows the detection of AME since the high-frequency data above 100 GHz can be used to constrain the thermal emission, while the lower frequency data is close to the theoretical peak of the spinning dust emission. When combined with ancillary data at lower frequencies, the spectra of AME regions can be accurately determined and used to probe their properties on large (~ 1 degree) scales. The *Planck* maps were used to detect several new potential AME regions [3] by subtracting a spatial model of known emission mechanisms (synchrotron, free-free, and thermal dust) extrapolated from observational or theoretical predictions. Two of these regions, AME-G173.6+2.8 and AME-G107.1+5.2, were selected, and ancillary data were used at both higher and lower frequencies to construct SEDs, which contain suggestions of AME consistent with spinning dust emission.

The Arcminute Microkelvin Imager Small Array (AMI SA) is a radio interferometer situated near Cambridge, UK. Primarily an SZ survey instrument, the AMI-SA, is specifically designed to have high sensitivity to low-surface-brightness emission on scales of 2–10 arcmin. It operates between 14 and 18 GHz, close in frequency to the theoretical peak of the spinning dust emission, the position of which varies between 10–50 GHz depending on grain size, composition, and ambient conditions. The AMI SA has previously been used both to identify and to characterize spinning dust regions in multiple galactic (e.g. [4, 5]) and extragalactic [6] sources. The higher angular resolution and lower frequency coverage of the AMI SA make it a highly complementary instrument to the *Planck* satellite for studies of AME. The synthesised beam of the SA, which is an effective measure of the resolution, is ≈ 2 arcmin at FWHM, while the *Planck* maps and ancillary data were smoothed to a common resolution of $\approx 1^\circ$ for AME detection.

TABLE 1: The *Planck* AME candidates observed with the AMI SA and the sources used as phase calibrators.

<i>Planck</i> ID	Other names	RA (J2000)	δ (J2000)	Phase calibrator
AME-G173.6+2.8	S235	05 41 06.0	+35 50 00	J0555 + 3948
AME-G107.1+5.2	S140	22 19 18.1	+63 18 49	J2125 + 6423

TABLE 2: Assumed $I + Q$ flux densities of 3C286, 3C48, and 3C147.

Channel	$\bar{\nu}$ /GHz	S^{3C286} /Jy	S^{3C48} /Jy	S^{3C147} /Jy
3	13.88	3.74	1.89	2.72
4	14.63	3.60	1.78	2.58
5	15.38	3.47	1.68	2.45
6	16.13	3.35	1.60	2.34
7	16.88	3.24	1.52	2.23
8	17.63	3.14	1.45	2.13

2. Observations and Data Reduction

The AMI SA is situated at the Mullard Radio Astronomy Observatory, Cambridge, UK [7]. It consists of ten 3.7 m diameter dishes with a baseline range of ≈ 5 –20 m and observes in the band 12–18 GHz with eight 0.75-GHz bandwidth channels. In practice, the lowest two frequency channels are unused due to a low response in this frequency range and interference from geostationary satellites.

The two sources listed in Table 1 were observed from 2011 Jan 21–Feb 09, for ≈ 5 hours each.

Data reduction was performed using the local software tool REDUCE, which flags interference, shadowing, and hardware errors, and applies phase and amplitude calibrations. The correlator data is then Fourier transformed to synthesize the frequency channels, before output to disk in uv FITS format. Flux calibration was performed using short observations of 3C48, 3C286, or 3C147 near the beginning and the end of each run. The assumed flux densities for 3C286 were converted from very large array total-intensity measurements provided by Perley (private communication) and are consistent with the Rudy et al. [8] model of Mars transferred on to absolute scale, using results from the *Wilkinson Microwave Anisotropy Probe*. The assumed flux densities for 3C48 and 3C147 are based on long-term monitoring with the AMI SA using 3C286 for flux calibration (see Table 2). A correction for changing airmass is also applied using a noise-injection system, the “rain gauge.”

Bright, nearby point sources selected from the Very Long Baseline Array Calibrator Survey [9] were observed during each observation at hourly intervals for phase calibration purposes (see Table 1 for phase calibrators used for the AMI SA observations). The reduced visibility data were imaged using AIPS (<http://aips.nrao.edu/>), from the individual channel datasets (for channels 3 to 8 inclusive), as well as from the combined channels at a central frequency of 15.75 GHz. Gaussians were fitted to the sources detected at $>5\sigma$ in the maps using the AIPS task JMFIT. Errors on AMI SA flux density values were estimated by adding in quadrature the error output from JMFIT, which folds in an estimate of the

r.m.s. map noise and the error associated with the Gaussian fit, and the error on flux calibration (including rain-gauge correction) of ≈ 5 percent of the integrated flux density.

2.1. Matching Spatial Scales. Since the sources detected were extended to the AMI SA beam, flux loss corrections had to be applied. These were calculated by sampling Canadian Galactic Plane Survey (CGPS, [10]) 1.4 GHz total power maps with the uv coverage of the AMI observations, followed by mapping and fitting Gaussians to the sampled maps in the same manner as the AMI observations. Figure 2 shows the sampled visibilities compared to the AMI observed visibilities and the ratios derived from fitting elliptical Gaussians to the maps. As a consistency check, the flux loss corrections were also calculated by modeling the sources as Gaussians based on the size parameters derived from the AMI continuum maps. The channel 3 flux density was taken as the reference, and channels 4–8 and the CGPS 1.42 GHz flux density were corrected to the channel 3 scale using the fitted flux loss percentages.

Lower frequency flux densities at 0.408, 2.7, and 4.85 GHz are estimated from the lower resolution CGPS, Effelsberg, and GB6 [10] maps by convolving the CGPS 1.42 GHz maps to the appropriate resolution, measuring a flux density on the convolved CGPS and lower resolution maps, and calculating a spectral index. The lower resolution flux density is then normalised to the flux density estimated from the CGPS map sampled with AMI channel 3 uv coverage using the calculated spectral index. These fluxes are, however, considered as upper limits since the amount of extra background flux density measured by the lower resolution maps is uncertain and is not accounted for in the flux loss correction.

3. Results

AMI SA maps of both sources are shown in Figures 3 and 7. The maps displayed are not corrected for attenuation due to the primary beam; the flux densities reported have been so corrected, where spectral indices α are quoted, the convention $S \propto \nu^{-\alpha}$ is used, S is flux density, and ν is frequency. Errors quoted are 1σ .

3.1. AME-G173.6+2.8. This region is centred on the HII region S235 [11], part of the FVW 172.8+1.5 complex within Auriga. FVW 172.8+1.5 is an HII complex composed of Sharpless HII regions and OB associations in the Perseus arm with individual objects organized along a large (~ 7 –4 deg) filamentary structure, the morphology of which has been compared to a bow tie [12]. Several HII regions within this complex have been the subject of previous study (e.g. [13]). The north-eastern regions: S231, S232, S233, and S235, are known to be associated with a giant molecular cloud at an adopted distance of 1.8 kpc ([14]; individual distances determined by spectrophotometry to each of the exciting stars within the HII regions range from 1.0 to 2.3 kpc) and have systematic CO radial velocities of -18.1 to -23.0 kms $^{-1}$ [15].

It has recently been proposed that these four HII regions lie on the shell of a SNR [16]. This premise, rather than that of

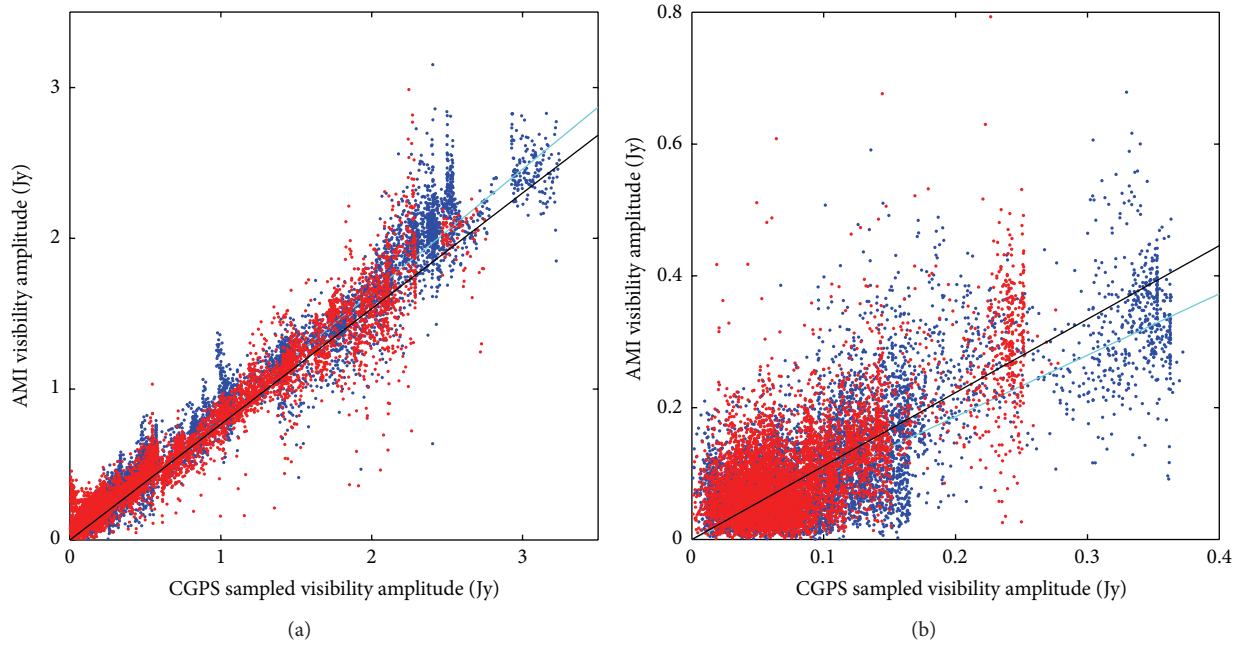


FIGURE 1: (a) S235 and (b) S140. Visibilities sampled from CGPS 1.42 GHz data are plotted on the x -axis, with the corresponding AMI observed visibilities on the y -axis for channels 3 (blue points) and 8 (red points). The solid cyan and black lines show the respective ratios derived from fitting elliptical Gaussians to the maps, for example (integrated flux density from AMI channel map)/(integrated flux density from CGPS map sampled with corresponding AMI channel uv -coverage). There is a very good correlation between the sampled and true AMI visibilities, indicating that the morphology that AMI observes is very similar to that observed by CGPS.

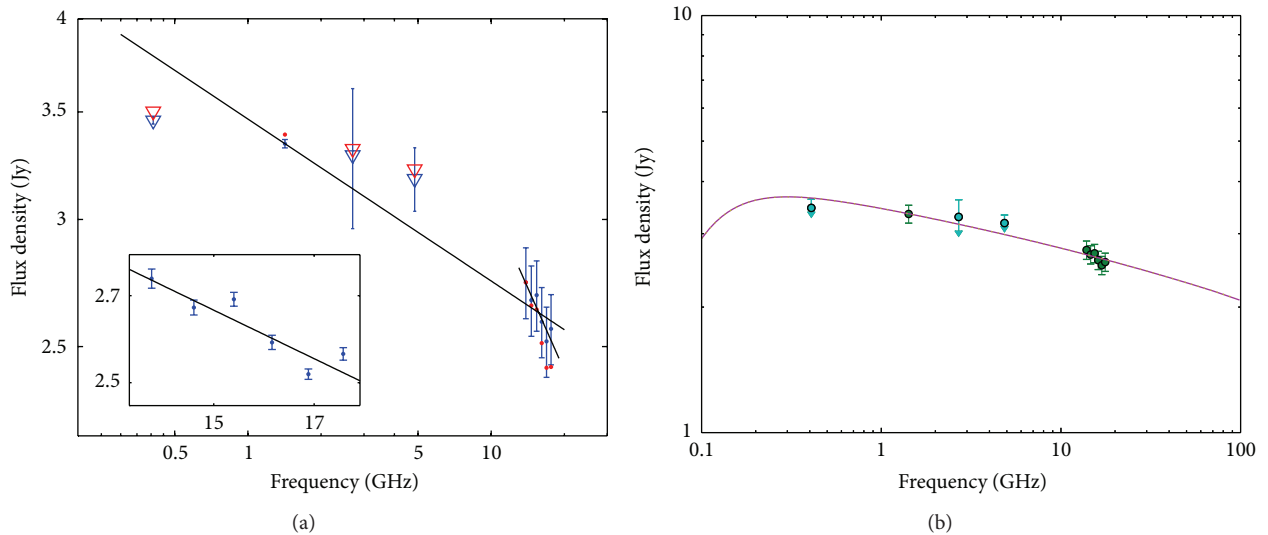


FIGURE 2: SED for AME-G173.6+2.8, including flux densities at 0.408 and 1.42 GHz from the CGPSE catalogue, 2.7 GHz from Effelsberg, and 4.85 GHz from the GB6 catalogue corrected by the flux loss percentage of the AMI channel 3 observation and the flux-loss-corrected AMI fluxes. (a) shows flux densities corrected using the sampled CGPS map (blue) and using a simulated Gaussian source as a consistency check (red). Lower resolution flux densities are shown as triangles as they are considered to be upper limits. Also shown are the spectral index fits to CGPS 1.42 GHz and AMI together and to the blue AMI points separately. The inset plot is zoomed in to the AMI flux densities; here the errors plotted are the JMFIT error estimates only (without calibration uncertainty). (b) shows a free-free spectrum fit to the flux densities (see text for details).

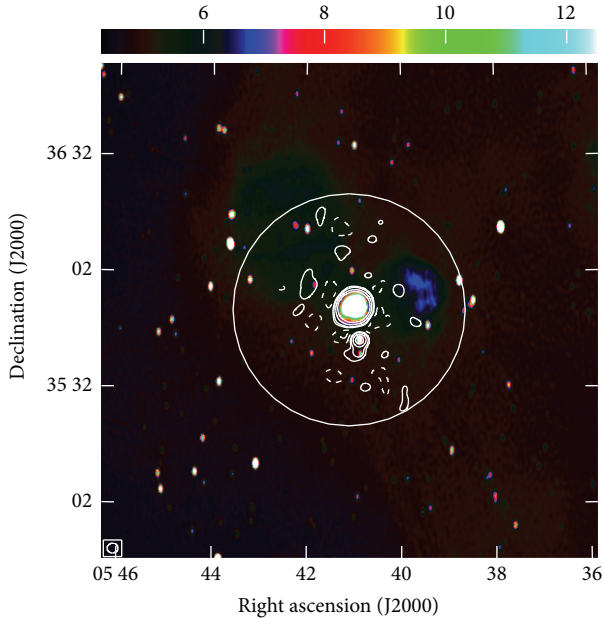


FIGURE 3: AME-G173.6+2.8: AMI SA data is shown as contours over CGPS 1.4 GHz pseudo colour, in brightness temperature. The pseudo-colour scale is truncated at 12.5K ($\approx 0.25 \times$ peak brightness of S235) to show the low-surface-brightness diffuse structures. AMI contours are at ± 5 , 10, 25, and $50 \sigma_{\text{rms}}$ on the AMI map ($1.77 \text{ mJy beam}^{-1}$). The 1° *Planck* smoothing scale is shown as the large circle, and the AMI SA synthesised beam is shown in the bottom left corner.

an expanding HII region, is supported by the fast expansion velocity of the shell and high kinetic energy associated with it. In addition the filamentary structures joining individual HII regions were shown to have nonthermal spectral contributions, inconsistent with an HII bubble.

Figure 3 shows the AMI SA channel-averaged map and the corresponding CGPS 1.4 GHz map. The 1° smoothing resolution of the *Planck* analysis is shown for comparison. It can be seen that there are many components within the smoothing radius, both diffuse and compact, which could potentially contribute to the excess emission seen by *Planck*.

A number of discrete sources are detected within the AMI SA primary beam towards this region. The field is dominated by the north-south string of HII regions: S235, S235A (BFS46), and BFS47. BFS46 (S235A) was previously part of an AME study of HII regions [17] where it was found to exhibit no excess, having a spectrum consistent with optically thin free-free emission with $\alpha = 0.09 \pm 0.03$. This provides a useful check for any systematic offsets in individual channel calibration that may affect the spectrum of S235. Although it lies away from the centre of the pointing where phase errors are expected to have greater effect, the flux densities derived from the AME-G173.6+2.8 map for BFS46 are consistent with those from the previous study.

Here we also confirm that the spectrum of S235 is consistent with optically thin free-free emission. After flux loss correction using the CGPS sampled maps, a spectral index of $\alpha = 0.34 \pm 0.03$ is fitted to the AMI channel

flux densities. Using a simulated elliptical Gaussian with the deconvolved source size and position angle from the AMI continuum map as a consistency check gives a spectral index of $\alpha = 0.57 \pm 0.03$, and it is likely that the difference indicates that this source is not well modelled by a Gaussian. Figure 1(a) shows the CGPS sampled visibilities compared to the AMI visibilities and shows the correspondence derived from fitting to the maps. It can be seen that the correlation between the visibilities is very good, indicating a good morphological correlation between 1.42 and 16 GHz.

Although a spectrum with an index of $\alpha = 0.34$ is steeper than the canonical free-free index of $\alpha = 0.1$, such indices are expected for bremsstrahlung from cooler (heavy) plasma [18]. However, it is more likely in this instance that the steeper spectrum across the AMI band arises as a consequence of inexact flux loss corrections due to differences in the structure of the source between 1.4 GHz and the frequency range covered by AMI. Fitting to the CGPS 1.42 GHz catalogue flux for S235 and the AMI channel fluxes gives a spectral index of $\alpha = 0.101 \pm 0.008$, consistent with the radio recombination line measurements of Lockman [19] who found $\Delta v = 22.3 \pm 2.4 \text{ kms}^{-1}$ for this region, indicative of optically thin plasma. Figure 2(a) shows the SED indicating the corrections for flux loss; it can be clearly seen that AMI sees no AME. Flux densities from the Effelsberg 11 cm and GB6 4.85 GHz surveys should be considered upper limits as the flux loss corrections calculated from the CGPS data fitted at a resolution of 1 arcmin cannot account for any contribution from proximal low-surface-brightness emission which has contributed to the flux density of sources fitted at resolutions of 4.3 and 3 arcmin, respectively. Indeed, when considered in conjunction with lower frequency data, Figure 2(b), we find that the AMI data is well fitted by a free-free spectrum ([20]; see Scaife 2012, this volume). Fixing the electron temperature at $T_e = 8000 \text{ K}$, we find an emission measure of $EM = 2.54 \pm 0.04 \times 10^4 \text{ cm}^{-6} \text{ pc}$, assuming a source with deconvolved size as determined from the AMI data ($\Omega_{\text{S235}} = 232.6 \times 208.9'' \text{ P.A.} = 104.5^\circ$).

3.2. *AME-G107.1+5.2*. This region is centred on the HII region S140 [11]. At a distance of 910 pc, S140 is a bright-rimmed cloud that forms the interface between an HII region and the molecular cloud L1204 [21]. S140 contains an IR cluster of at least three sources [22]. IRS1 is the progenitor of a large molecular outflow in the SE-NW direction with a reflection nebula associated with the blue-shifted SE lobe ([23]; see also [24]). The activity of this outflow has caused significant disturbance in the surrounding area where a number of sweeping feather-like structures are visible in high angular resolution K-band images [25]. Perpendicular to the outflow a disk has been detected at cm wavelengths, confirmed by K-band polarimetric imaging ([26, 27]).

The AMI observation of this region is shown in Figure 7. After flux loss correction, a spectral index of $\alpha = -0.75 \pm 0.05$ is fitted to the AMI channel fluxes. The spectral index calculated using a simulated Gaussian source with size derived from the AMI channel-averaged map for flux loss correction is $\alpha = +0.66 \pm 0.06$; however, it can be seen that the

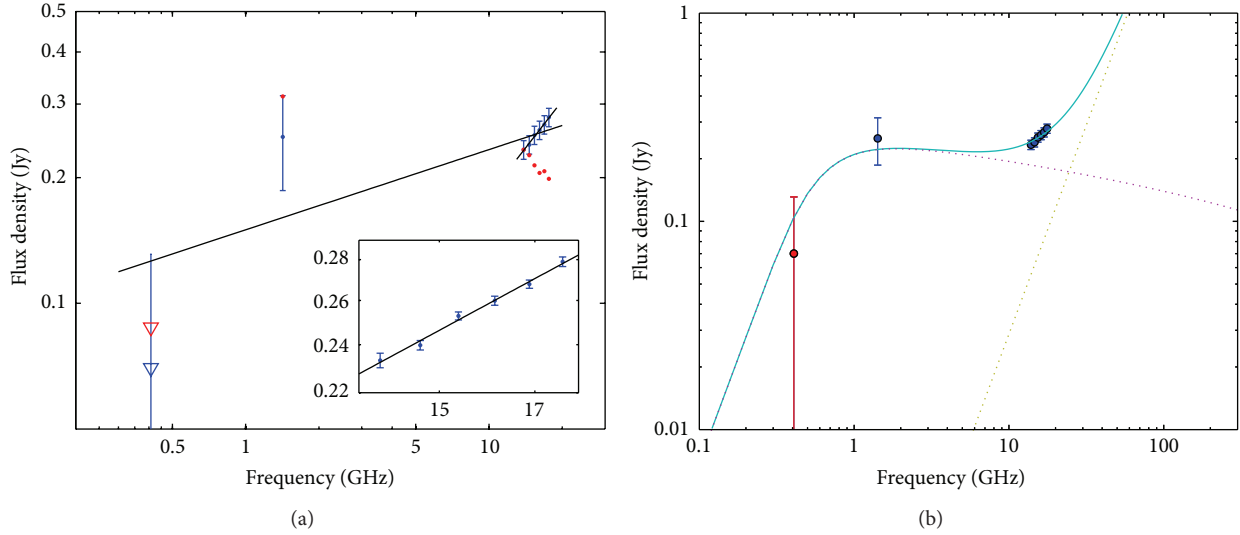


FIGURE 4: SED for AME-G107.1+5.2. (a) shows the fluxes at 0.408 and 1.42 GHz from the CGPSE catalogue normalised by the flux loss expected in AMI channel 3 and the flux-loss-corrected AMI fluxes. The markers and spectral index fits shown are in Figure 2. (b) shows a fit to the flux densities using a two-component model consisting of a classical and a hypercompact HII region.

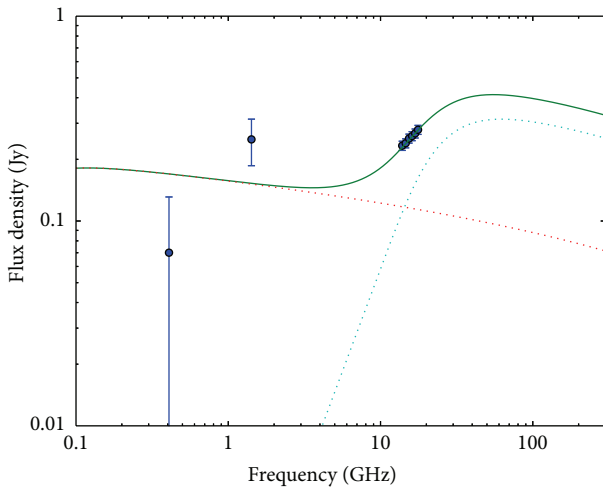


FIGURE 5: SED for AME-G107.1+5.2. The fluxes at 0.408 and 1.42 GHz are from the CGPSE catalogue normalised by the flux loss expected in AMI channel 3; the higher frequency fluxes are the flux-loss-corrected AMI fluxes. Two free-free SED components are shown using a source size for the low-frequency component fixed to that measured from the AMI SA maps.

source is highly non-Gaussian which is likely to account for the difference. Figure 1 shows the CGPS sampled visibilities compared to the AMI visibilities and the flux density ratio derived from fitting to the maps. It can be seen that the correlation between the visibilities is very good, indicating a good morphological correlation between 1.42 and 15 GHz and supporting the rising spectrum derived by using the CGPS data to correct the AMI flux densities for flux loss.

Fitting to the sampled CGPS 1.42 GHz flux density and AMI channel 3 uv coverage gives a spectral index of $\alpha = -0.02 \pm 0.2$, consistent with optically thin free-free emission.

Fluxes at lower resolution were not estimated due to the more complex background of this source; the CGPS 408 MHz catalogue flux density adjusted by the same flux loss percentage as the 1.42 GHz value is included as a reference; however, the errors are extremely large. Figure 4(a) shows the SED; it seems likely that the AMI fluxes indicate the presence of AME or an ultra-/hypercompact HII region. Figure 7 shows the AMI SA channel-averaged map and the corresponding CGPS 1.4 GHz map.

Two scenarios are possible that may explain the rising spectrum across the AMI band: scenario 1 is the presence of a hypercompact HII (HCHII) region and scenario 2 is the presence of a spinning dust component. Scenario 1 is illustrated in Figure 4(b) where the lower frequency data is dominated by free-free emission from plasma with an emission measure of $EM = 5.26 \pm 1.5 \times 10^5 \text{ cm}^{-6} \text{ pc}$ assuming an electron temperature of $T_e = 8000 \text{ K}$. This would indicate a region of classical HII; however, the relatively high-emission measure implied by the turnover frequency lying between 408 MHz and 1.4 GHz requires that the source have a much smaller angular size ($\sim 0.1 \text{ arcmin}$) than that fitted to the AMI map ($\Omega_{S140} = 242.5 \times 109.3'' \text{ P.A.} = 148.7^\circ$) to be consistent with the magnitude of the flux density. In addition the best fitting emission measure for the high-frequency component is $EM = 5.37 \times 10^1 \text{ cm}^{-6} \text{ pc}$, which is extremely high.

Fixing the source size to that measured from the AMI data produces a poorer fit to the low-frequency data, with an emission measure of $EM = 2.05 \pm 0.41 \times 10^3 \text{ cm}^{-6} \text{ pc}$, see Figure 5. The rising spectrum across the AMI band requires a second free-free component with $EM > 7 \times 10^8 \text{ cm}^{-6} \text{ pc}$, consistent with an ultra- or hypercompact HII region. In this case we find a best fitting emission measure for the high-frequency component of $2.16 \times 10^9 \text{ cm}^{-6} \text{ pc}$ with a size of $\sim 0.001 \text{ pc}$ consistent with an object on the ultra- /hypercompact border. In spite of the poorer fit to the

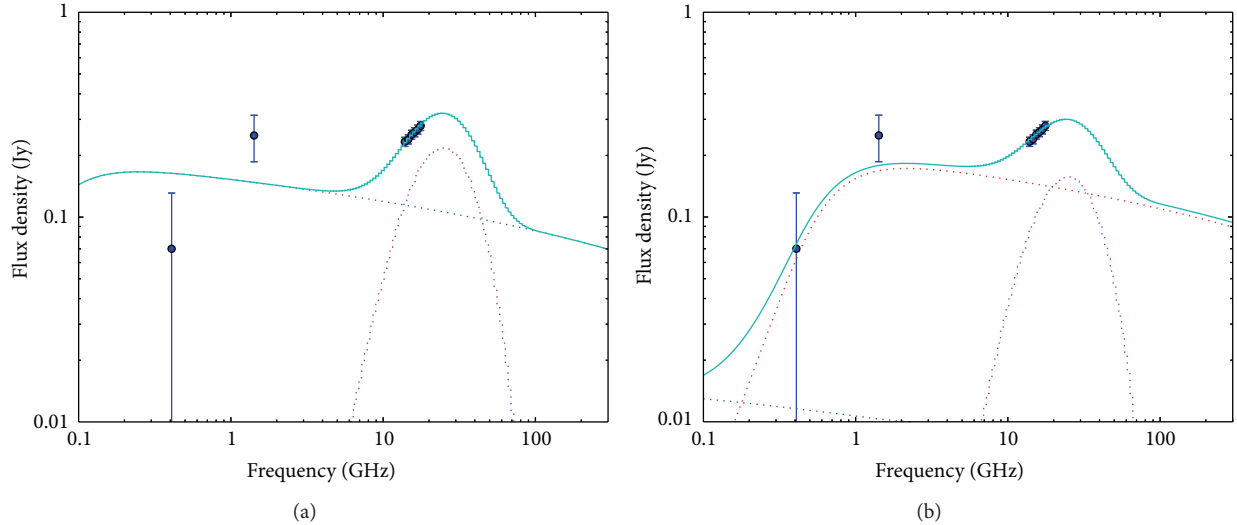


FIGURE 6: SED for AME-G107.1+5.2 including fluxes at 0.408 and 1.42 GHz from the CGPSE catalogue normalised by the flux loss expected in AMI channel 3 and the flux-loss-corrected AMI fluxes. (a) shows a single free-free component plus spinning dust contribution to the SED; (b) shows a fit to the flux densities using a two-component free-free model plus a spinning dust contribution. Please see the text for details.

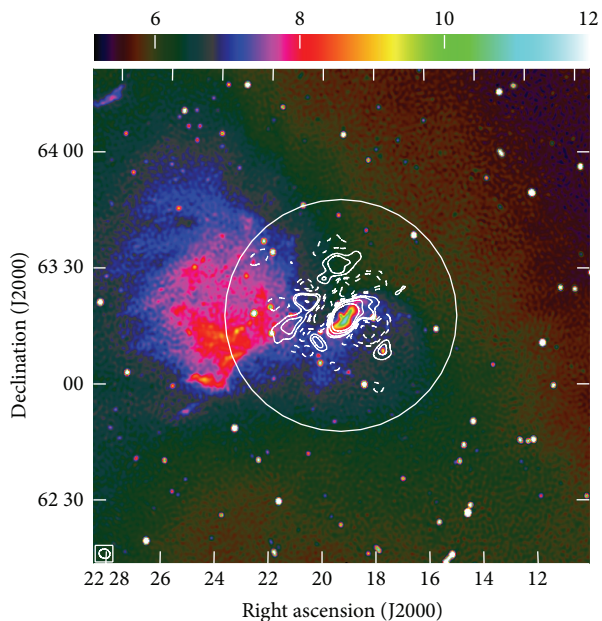


FIGURE 7: AME-G107.1+5.2: AMI SA data is shown as contours over CGPS 1.4 GHz pseudo colour, in brightness temperature. The pseudo-colour scale is truncated at 12 K (\approx the peak brightness of S140) to show the low-surface-brightness diffuse structures. AMI contours are at ± 5 , 10, 25, and $50 \sigma_{\text{rms}}$ on the AMI map ($0.34 \text{ mJy beam}^{-1}$). The 1° *Planck* smoothing scale is shown as the large circle, and the AMI SA synthesised beam is shown at the bottom left corner.

low-frequency data we consider this case more likely than the first as it is consistent with the measured source extent and predicts emission measures which are more physically feasible.

Scenario 2 is illustrated in Figure 6(a) where the rising spectrum in the AMI data is accounted for by the introduction of a spinning dust model, here taken as the Draine and Lazarian Warm Ionized Medium (WIM) model [28]. For the small angular size of the emitting region the column density of the spinning dust emitting region needs to be reasonably high at $n_H = 6.14 \pm 1.09 \times 10^{22} \text{ cm}^{-2}$. A further possibility is that the 408 MHz datum defines an optically thin free-free component, whilst the 1.4 GHz point represents a contribution from a more compact region of HII, and the rising spectrum across the AMI band indicates a *further* component arising from even more compact HII or spinning dust. This possibility is shown in Figure 6(b); interestingly the optically thin free-free component shown has a similar emission measure to that fitted to the low-frequency data on larger scales by [3], although the uncertainty on the fitted emission measure due to the large error on the 408 MHz point makes the comparison weak.

With only the upturn in the SED visible over the AMI band it is not possible to distinguish between these two scenarios using the AMI data alone. We do, however, confirm that a rising spectrum is present at frequencies above 10 GHz. However, we also note that the magnitude of the emission required to explain the rising AMI spectrum is approximately an order of magnitude, too small to explain the excess observed with *Planck* at $\approx 1^\circ$ resolution.

4. Discussion

Detections of AME from *Planck* data are based on flux densities integrated within an aperture of 1-degree radius. Such measurements will contain contributions from a variety of discrete sources, in addition to the large-scale diffuse background. The data presented here allow us to examine the population of discrete sources that contribute to these

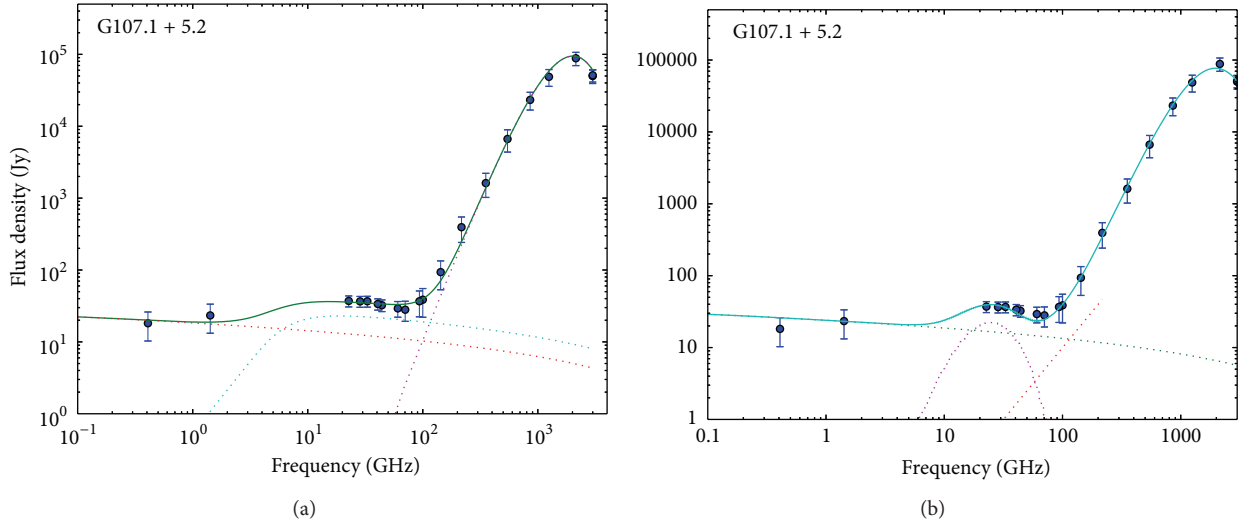


FIGURE 8: Spectrum for G107.1+5.2 at $\approx 1^\circ$ scales, from *Planck*, *WMAP*, and ancillary datasets (data points as in [3]). (a) Fitted with a two-component free-free model. The two free-free components are shown as red and blue dotted lines and the contribution from the thermal dust greybody as a purple dotted line. The combined model is shown as a solid green line. Model parameters are listed in Table 3. (b) Fitted with a free-free plus spinning dust model, the free-free component is shown as a green dotted line and the spinning dust component as a purple dotted line. The Rayleigh-Jeans tail of a CMB component is shown as a red dotted line, with the thermal dust greybody model excluded for clarity. The combined model is shown as a blue solid line.

detections and investigate the physics behind their emission over a frequency range sensitive to the proposed spinning dust mechanism, which is generally considered to provide the physical basis for AME.

The data presented here have shown that the emission from S235, the dominant source within the G173.6+2.8 region, has a spectrum consistent with optically thin free-free emission and shows no indication of a spinning dust component. For the source S140, dominant within the G107.1+5.2 region, the data presented here have shown that the spectrum of this source rises across the AMI band and is not consistent with an extrapolation of optically thin free-free from lower frequencies.

4.1. The Spectrum of G107.1+5.2. On large scales the spectrum of G107.1+5.2 [3] is ambiguous in nature. Here we examine that ambiguity by comparing different physical scenarios through their spectra (data points from Dickinson, priv. comm.). In Figure 8(a) we show a scenario where the excess emission at microwave frequencies is provided by the presence of an ultracompact HII region, and in Figure 8(b) we show a scenario where the excess emission at microwave frequencies is provided by a spinning dust component. In both cases maximum likelihood (ML) fitted models are shown. These fits were found using an MCMC-based method which calculates both ML parameters with associated uncertainties, as well as the evidence values for the specific model using a simulated annealing approach [29].

We consider models of the same form as the original *Planck* analysis with the electron temperature of the free-free emitting gas fixed to $T_e = 8000$ K but leave the emission measure free to vary. Similarly we fix the temperature of the

dust component to be $T_d = 18.96$ K [3] as this is determined largely by the peak of the dust greybody; we retain the opacity index, β , as a free parameter as well as a normalization coefficient. To these two initial components we add a second free-free component, parameterized by a second emission measure and by a size which is defined relative to the size of the first free-free emitting region. The electron temperature of this second component is also fixed at $T_e = 8000$ K.

In the second scenario we assume an identical first free-free component and similarly a dust greybody with a fixed dust temperature. To these two components we add a spinning dust component parameterized by a column density, n_H , and include a potential CMB contribution in a similar fashion to [3]. The spinning dust component that we use is the Draine and Lazarian WIM model [28]. The model parameters we obtain differ slightly from those of [3] but are consistent within errors.

In the first scenario we find that the data are well fitted by a two-component free-free model where the second component has an emission measure of $EM > 10^7 \text{ cm}^{-6} \text{ pc}$ and a source size which is greater than a factor of ~ 1200 , smaller than the size of the first emitting region. Both constraints are consistent with the presence of an ultracompact HII region as the relative source size indicates an object of $< 0.1 \text{ pc}$ at a distance of 910 pc. The lack of data in the frequency range 1.4–20 GHz makes these two parameters highly degenerate as the optical depth of such an object can reach unity anywhere over an order of magnitude in frequency. Indeed a rising spectrum over the AMI band, as observed, would indicate a turn over frequency at $\nu_t > 15$ GHz and consequently an emission measure of $EM > 7 \times 10^8 \text{ cm}^{-6} \text{ pc}$, consistent with the fitted constraints.

TABLE 3: Maximum likelihood parameters for two-component free-free model fitted to G107.1 + 5.2.

Parameter	HII	UC/HCHII [‡]	Thermal dust
T_e [K]	8000	8000	—
T_d [K]	—	—	18.96
EM [cm^{-6} pc]	147 ± 47	4.4×10^7	—
β	—	—	2.20 ± 0.18
Size [†] [arcmin]	60	0.16	60

[†]Radius of circular aperture. [‡]Listed parameters represent the best fit values, and uncertainties are highly nonsymmetric.

TABLE 4: Maximum likelihood parameters for spinning dust model fitted to G107.1+5.2.

Parameter	HII	Spinning dust	Thermal dust	CMB
T_e [K]	8000	—	—	—
T_d [K]	—	—	18.96	—
EM [cm^{-6} pc]	235 ± 48	—	—	—
β	—	—	1.91 ± 0.11	—
Size [†] [arcmin]	60	60	60	60
n_H [10^{21} cm^{-2}]	—	4.59 ± 1.13	—	—
ΔT [μK]	—	—	—	34 ± 4

[†]Radius of circular aperture.

In the second scenario we find parameter values similar to those determined by [3], with the exception of the CMB contribution where we find a maximum likelihood value of approximately half of that determined by [3]. Maximum likelihood parameters for both models are listed in Tables 3 and 4. These models are shown to be fitted to the data in Figures 8(a) and 8(b). The logarithmic difference in the evidence between the two models, as determined over a 3σ prior volume, is $\Delta \ln Z = 36.0 \pm 0.7$ in favour of the spinning dust model.

Assuming that the optically thin free-free component which dominates the *Planck* SED arises on scales which are not visible to AMI, we examine the possibility that the rising spectrum observed across the AMI band and the excess emission detected by *Planck* can both be explained by a single hypercompact HII region. If this is the case, we predict that the emission seen across the AMI band in a *Planck*-size aperture would be simply the sum of an extrapolation of the optically thin component to these frequencies plus the measured AMI flux densities. This is subject to a couple of strong assumptions: firstly, the emission from the HCHII region arises on scales which are compact to the AMI beam, and there will consequently be no flux loss relative to the *Planck* measurement; secondly, the HCHII is the dominant contribution to the AMI flux densities. The first of these assumptions is reliable as HCHII exists on scales which are highly compact to both the AMI and *Planck* beams. The second assumption is less reliable as it depends on the parameters of the HCHII model, which are not possible to constrain absolutely from the AMI data alone. Considering this to be the case it is immediately obvious that the magnitude of the AMI flux densities is insufficient to be compatible with the

excess seen by *Planck* being contributed by a single HCHII region.

By the same token it is also not possible for the *Planck* excess to be explained by the presence of a spinning dust region with angular scales entirely recovered by AMI. Since the possibility of an extended region of HCHII has no precedent in the literature, it seems likely then that the excess measured by *Planck* towards G107.1+5.2 arises from a spinning dust region, the majority of which is extended on scales larger than those measured by AMI. This conclusion is supported by the strong evidence in favour of a spinning dust component found by the model comparison.

5. Conclusions

In the case of both G173.6+2.8 (S235) and G107.1+5.2 (S140) we conclude that the bulk of the excess emission seen by *Planck* must arise on scales larger than 10 arcmin; the magnitude of the emission seen by AMI is <2% of that expected at 15 GHz at $\approx 1^\circ$ resolution. In the case of G173.6+2.8 we confirm that the dominant source within the *Planck* aperture, S235, has a spectrum on scales of 2–10 arcmin consistent with optically thin free-free emission. In the case of G107.1+5.2 we demonstrate that the dominant source, S140, has a rising spectrum across the AMI band. This spectrum is consistent with either spinning dust emission or the presence of UC/HCHII. With only the low-frequency data available on these scales it is not possible to distinguish between the two mechanisms; however, we conclude that the magnitude of the contribution causing the rising spectral index across the AMI band is not sufficient to explain the measured *Planck* excess, which must once again arise on scales larger than those probed by AMI. In this case, it is therefore possible that the rising spectrum over the AMI band is also a consequence of spinning dust emission.

Acknowledgments

The authors thank the staff of the Mullard Radio Astronomy Observatory for their invaluable assistance in the commissioning and operation of AMI, which is supported by Cambridge University and the STFC. They also thank Clive Dickinson for the data points for the large-scale spectrum of G107.1+5.2 and the referee for useful comments. This research has made use of the SIMBAD database, operated at CDS, Strasbourg, France. Y. C. Perrott acknowledges the support of a CCT/Cavendish Laboratory studentship.

References

- [1] J. A. Tauber, N. Mandolesi, J. L. Puget et al., “Planck pre-launch status: the Planck mission,” *Astronomy & Astrophysics*, vol. 520, p. A1, 2010.
- [2] P. A. R. Ade, N. Aghanim, M. Arnaud et al., “Planck early results. I. The Planck mission,” *Astronomy & Astrophysics*, vol. 536, article A1, 16 pages, 2011.
- [3] P. A. R. Ade, N. Aghanim, M. Arnaud et al., “Planck early results. XX. New light on anomalous microwave emission from

- spinning dust grains,” *Astronomy & Astrophysics*, vol. 536, article A20, 17 pages, 2011.
- [4] A. M. M. Scaife, N. Hurley-Walker, D. A. Green et al., “An excess of emission in the dark cloud LDN1111 with the Arcminute Microkelvin Imager,” *Monthly Notices of the Royal Astronomical Society*, vol. 394, no. 1, pp. L46–L50, 2009.
- [5] A. M. M. Scaife, D. A. Green, G. G. Pooley et al., “High-resolution AMI Large Array imaging of spinning dust sources: spatially correlated $8\ \mu\text{m}$ emission and evidence of a stellar wind in L675,” *Monthly Notices of the Royal Astronomical Society*, vol. 403, no. 1, pp. L46–L50, 2010.
- [6] E. J. Murphy, G. Helou, J. J. Condon et al., “The detection of anomalous dust emission in the nearby galaxy NGC 6946,” *The Astrophysical Journal*, vol. 709, no. 2, p. L108, 2010.
- [7] J. T. L. Zwart, R. W. Barker, P. Biddulph et al., “The arcminute microkelvin imager,” *Monthly Notices of the Royal Astronomical Society*, vol. 391, no. 4, pp. 1545–1558, 2008.
- [8] D. J. Rudy, D. O. Muhleman, G. L. Berge, B. M. Jakosky, and P. R. Christensen, “Mars: VLA observations of the Northern Hemisphere and the north polar region at wavelengths of 2 and 6 cm,” *Icarus*, vol. 71, no. 1, pp. 159–177, 1987.
- [9] A. B. Peck and A. J. Beasley, “A VLBA calibrator survey,” in *Radio Emission from Galactic and Extragalactic Compact Sources: Proceedings of IAU Colloquium 164, Held in Socorro, New Mexico, USA, 21–26 April 1997*, vol. 144, p. 155, 1998.
- [10] P. C. Gregory, W. K. Scott, K. Douglas, and J. J. Condon, “The GB6 catalog of radio sources,” *The Astrophysical Journal Supplement Series*, vol. 103, pp. 427–432, 1996.
- [11] S. Sharpless, “A catalogue of H II regions,” *The Astrophysical Journal Supplement Series*, vol. 4, p. 257, 1959.
- [12] C. R. Kerton, J. Murphy, and J. Patterson, “A sharper view of the outer Galaxy at 1420 and 408 MHz from the Canadian Galactic Plane Survey II: the catalogue of extended radio sources,” *Monthly Notices of the Royal Astronomical Society*, vol. 379, no. 1, pp. 289–296, 2007.
- [13] F. P. Israel and M. Felli, “Aperture synthesis observations of galactic H II regions. VIII—S106 and S235: regions of star formation,” *Astronomy and Astrophysics*, vol. 63, no. 3, pp. 325–334, 1978.
- [14] N. J. Evans II and G. N. Blair, “The energetics of molecular clouds. III—The S235 molecular cloud,” *The Astrophysical Journal*, vol. 246, pp. 394–408, 1981.
- [15] L. Blitz, M. Fich, and A. A. Stark, “Catalog of CO radial velocities toward galactic H II regions,” *The Astrophysical Journal Supplement Series*, vol. 49, pp. 183–206, 1982.
- [16] J.-H. Kang, B.-C. Koo, and C. Salter, “An old supernova remnant within an H II complex at $\ell \approx 173^\circ$: FVW 172.8+1.5,” *The Astronomical Journal*, vol. 143, no. 3, article 75, 2012.
- [17] A. M. M. Scaife, N. Hurley-Walker, M. L. Davies et al., “AMI limits on 15-GHz excess emission in northern H II regions,” *Monthly Notices of the Royal Astronomical Society*, vol. 385, no. 2, pp. 809–822, 2008.
- [18] C. Dickinson, R. D. Davies, and R. J. Davis, “Towards a free-free template for CMB foregrounds,” *Monthly Notices of the Royal Astronomical Society*, vol. 341, pp. 369–384, 2003.
- [19] F. J. Lockman, “A survey of radio H II regions in the northern sky,” *The Astrophysical Journal Supplement Series*, vol. 71, pp. 469–479, 1989.
- [20] L. Oster, “Free-free emission in the radio-frequency range,” *Astronomical Journal*, vol. 70, p. 50, 1961.
- [21] D. Crampton and W. A. Fisher, “Spectroscopic observations of stars in H II regions,” *Publications of the Dominion Astrophysical Observatory, Victoria, British Columbia*, vol. 14, no. 12, pp. 283–304, 1974.
- [22] C. A. Beichman, E. E. Becklin, and C. G. Wynn-Williams, “New multiple systems in molecular clouds,” *The Astrophysical Journal*, vol. 232, pp. L47–L51, 1979.
- [23] M. Hayashi, T. Hasegawa, T. Omodaka, S. S. Hayashi, and R. Miyawaki, “The bright-rimmed molecular cloud around S140 IRS. II—bipolar outflow from S140 IRS 1,” *The Astrophysical Journal*, vol. 312, pp. 327–336, 1987.
- [24] M. G. Hoare and J. Franco, “Massive star formation,” in *Diffuse Matter from Star Forming Regions to Active Galaxies—A Volume Honouring John Dyson*, T. W. Hartquist, J. M. Pittard, and S. A. E. G. Falle, Eds., *Astrophysics and Space Science Proceedings*, p. 61, Springer, Dordrecht, The Netherlands, 2007.
- [25] W. J. Forrest and M. A. Shure, “Unipolar bubbles in star-forming regions,” *The Astrophysical Journal*, vol. 311, pp. L81–L84, 1986.
- [26] M. G. Hoare, “An equatorial wind from the massive young stellar object S140 IRS 1,” *The Astrophysical Journal*, vol. 649, p. 856, 2006.
- [27] Z. Jiang, M. Tamura, M. G. Hoare et al., “Disks around massive young stellar objects: are they common?” *The Astrophysical Journal Letters*, vol. 673, no. 2, pp. L175–L179, 2008.
- [28] B. T. Draine and A. Lazarian, “Diffuse galactic emission from spinning dust grains,” *The Astrophysical Journal Letters*, vol. 494, no. 1, pp. L19–L22, 1998.
- [29] M. P. Hobson and J. E. Baldwin, “Markov-chain monte carlo approach to the design of multilayer thin-film optical coatings,” *Applied Optics*, vol. 43, no. 13, pp. 2651–2660, 2004.

Review Article

Observations of Anomalous Microwave Emission from HII Regions

Clive Dickinson

Jodrell Bank Centre for Astrophysics, School of Physics & Astronomy, University of Manchester, Oxford Road, Manchester M13 9PL, UK

Correspondence should be addressed to Clive Dickinson; clive.dickinson@manchester.ac.uk

Received 15 August 2012; Accepted 9 January 2013

Academic Editor: Roberta Paladini

Copyright © 2013 Clive Dickinson. This is an open access article distributed under the Creative Commons Attribution License, which permits unrestricted use, distribution, and reproduction in any medium, provided the original work is properly cited.

I give a summary of the observations of Anomalous Microwave Emission (AME) from HII regions. AME has been detected in, or in the vicinity of, HII regions. Given the difficulties in measuring accurate SEDs over a wide range of frequencies and in complex environments, many of these detections require more data to confirm them as emitting significant AME. The contribution from optically thick free-free emission from UCHII regions may be also be significant in some cases. The AME emissivity, defined as the ratio of the AME brightness to the 100 μm brightness, is comparable to the value observed in high-latitude diffuse cirrus in some regions, but is significantly lower in others. However, this value is dependent on the dust temperature. More data, both at high frequencies (>5 GHz) and high resolution ($\sim 1'$ or better) is required to disentangle the emission processes in such complex regions.

1. Introduction

HII regions refer to the environment around the most (O and B type) massive stars, which are hot enough to produce intense UV radiation that can ionize the gas around them. HII regions typically form within large molecular clouds, often in clusters (due to triggered star formation), and are therefore also associated with significant amounts of dust grains. Anomalous Microwave Emission (AME), if due to electric dipole radiation from spinning dust [1], requires a large column of dust grains (with a population of the smallest dust grains or PAHs) and a mechanism for rotationally exciting these grains, for example, plasma drag and photons. For these reasons, HII regions may be a good place to look for AME. In fact, there is evidence that photodissociation regions (PDRs) typically found around the edges of HII regions/molecular clouds might be good AME emitters [2, 3]. Counterarguments include the depletion of PAHs close in the centre of HII regions and the fact that they strongly emit in other forms of continuum emission, notably free-free (thermal bremsstrahlung) and thermal dust radiation.

In this paper, I give an overview of the the continuum radiation and current observations of AME from HII regions. I will discuss some issues with measuring AME from HII

regions, including calibration, the contribution from ultra-compact (UCHII) regions, and the definition of emissivity.

2. Observations of HII Regions

2.1. The SEDs of Classical HII Regions. The general form of HII region SEDs (radio to the far infrared continuum) is thought to be well understood. Figure 1 shows the SED of the well-known Orion nebula (M42) HII region, measured by a number of different experiments including *Planck* [4]. The spectral shape is typical of HII regions. At radio wavelengths (frequencies ~ 1 GHz to ~ 100 GHz) it is dominated by free-free emission from warm ($T_e \sim 10^4$ K) ionized gas. This is usually expressed in terms of the free-free opacity, τ_{ff} , which at radio wavelengths can be approximated by [5]

$$\tau_{\text{ff}} \approx 3.27 \times 10^{-7} \left(\frac{T_e}{10^4 \text{ K}} \right)^{-1.35} \left(\frac{\nu}{\text{GHz}} \right)^{-2.1} \left(\frac{\text{EM}}{\text{pc cm}^{-6}} \right). \quad (1)$$

The intensity is proportional to the Emission Measure, defined as $\text{EM} = \int n_e^2 dl$, the integral of the square of the electron density along the line of sight. Above a certain

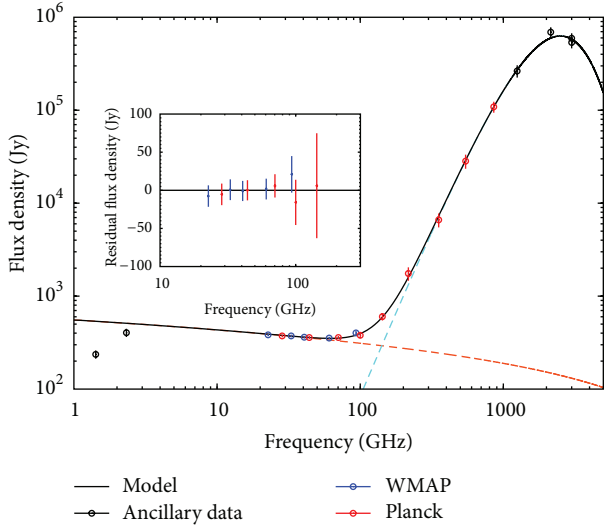


FIGURE 1: SED of the Orion Nebula (M42) HII region [4]. Free-free emission dominates at frequencies below 100 GHz while thermal dust emission dominates above 100 GHz. The free-free emission is optically thin above a few GHz. There is no evidence of significant AME.

“turnover” frequency (i.e., $\tau_{\text{ff}} < 1$; optically thin), free-free emission has an almost flat flux density spectrum of $\alpha \approx -0.1$ ($S \propto \nu^\alpha$). At lower frequencies, and particularly for more dense (young and compact HII regions) with $EM \gg 10^7 \text{ pc cm}^{-6}$, the emission becomes optically thick ($\tau_{\text{ff}} > 1$) and has a spectrum of $\alpha = +2$.

At frequencies $\geq \sim 100$ GHz, black-body emission from dust grains at $T_d \sim 10\text{--}100$ K dominates. The thermal dust spectrum is often parameterised by a modified black-body function, $S \propto \nu^{\beta+2} B(\nu, T_d)$, with typical values of the emissivity index of $\beta \sim +1.8$ in the Rayleigh-Jeans tail (corresponding to $\alpha = +3.8$) and a peak at ~ 3000 GHz ($100 \mu\text{m}$). Also, the dust temperatures around HII regions are typically warmer ($\sim 30\text{--}80$ K) compared to the diffuse cirrus ($T_d \sim 18$ K) [6].

2.2. Observations of AME in HII Regions. To search for AME, one is essentially looking for excess emission at frequencies ~ 30 GHz. AME is usually detected at frequencies in the range $\sim 10\text{--}60$ GHz where the non-AME components are weaker. Also, theoretical models of spinning dust tend to peak at frequencies near 30 GHz [1]. Table 1 summarises the observations of AME from HII regions to-date (We focus on observations that have either detected AME or have placed upper limits on AME. We do not include results from reflection nebulae or PNe. There exists many other observations at frequencies relevant to AME in the literature, most of which do not show obvious signature of AME (most of these are at relatively high angular resolution with instruments such as the GBT, VLA, and ATCA)). We list the frequency range, approximate angular scales (of the experiment or of the source, whichever is largest), the AME significance level (σ_{AME}), and the emissivity (E), defined as the AME brightness relative the $100 \mu\text{m}$ brightness, in units of $\mu\text{K}/(\text{MJy}/\text{sr})$. The

list is ordered in terms of their approximate AME detection significance level.

3. Discussion

3.1. Reliability of Detections. The measurement of AME in HII regions is clearly a difficult task. It must be remembered that measuring accurate flux densities over a wide range of frequencies, particularly for extended regions in the presence of complicated backgrounds (as is often the case for Galactic HII regions) is exceptionally difficult. For low angular resolution observations, the free-free and dust emission regions will be coincident and therefore may well be a small fraction of the total flux. To subtract free-free to say 1% precision relies on having absolute flux scales that are good to this accuracy. (Most astronomical data are accurate to a few % and many older data are good to $\sim 10\%$ or worse!) Perhaps even more problematic is the comparison of data with a wide range of angular resolutions, and especially interferometric data compared to single-dish data, where the response to different angular scales can vary and is difficult to quantify (unless a detailed model of the source is available).

Given the above issues, one must be cautious given that the majority of the detections listed in Table 1 are not hugely significant (i.e., they are $\sim 5\sigma$ or below). One of the most clear detections comes from the source G159.6–18.5 within the Perseus molecular cloud. However, this is actually a very weak HII region relative to the dust-correlated emission from the larger surrounding area (the *Planck* AME source is actually located at G160.26–18.62). The free-free emission is therefore a very small fraction ($\sim 10\%$) of the total large-scale flux. The environment is therefore somewhat different to the other HII regions and perhaps should not be compared with the other HII regions.

From the other HII regions listed in Table 1, several of them are likely to be spurious detections. LPH96 201.663 + 1.643 was one of the first claimed detections of AME [14] based on a rising spectrum from 5 to 10 GHz. However, it was later shown that this result is likely to be spurious when no AME was observed at 31 GHz with an upper limit of 24% (2σ) [15]. Indeed, private communication with Doug Finkbeiner revealed that follow-up observations of this source with the GBT did not confirm the spectral rise seen in early observations. Similarly, an analysis of the SED of W40 using WMAP 1-year data [12] suggested that W40 may have a significant AME excess at 33 GHz. However a reanalysis using WMAP 7-year data, combined with higher resolution CBI data, could not confirm any significant deviations from an optically thin free-free spectrum [13]. The detection of RCW49 [11] could be contested based on the reliability and scarcity of low frequency (1–15 GHz) data. If one were to remove the data point at 14.7 GHz, which happens to be lower than the other data, then the significance of the detection at 31 GHz is reduced to $\sim 2\sigma$. Finally, analyses involving averaging the results from a sample of HII regions (e.g., [10, 11]) can be misleading since systematics errors (e.g., calibration and background subtraction) can become dominant.

TABLE 1: Summary of observations of AME from HII regions. The entries are listed according to their approximate detection significance, σ_{AME} . The angular sizes are approximate or refer to the telescope beam. E is the AME emissivity relative to $100 \mu\text{m}$, in units $\mu\text{K}/(\text{MJy}/\text{sr})$.

Source(s)	Experiment	ν [GHz]	θ [']	σ_{AME}	E	Reference(s)	Notes
G159.6–18.5	Various	10–60	60	17	$17.8^{\pm 0.3}$	[4, 7]	Perseus MC. Low free-free
RCW175	CBI/VSA	31	10	7.9	$5.5^{\pm 0.7}$	[8, 9]	2 components
G173.6+2.8	<i>Planck</i>	30–70	60	6.4	$10.0^{\pm 3.4}$	[4]	Contains S235
9 northern HII	VSA	33	~15	5.4	$3.9^{\pm 0.8}$	[10]	Mean
G107.1+5.2	<i>Planck</i>	30–70	60	4.8	$11.3^{\pm 4.8}$	[4]	Contains S140
RCW49	CBI	31	8	3.3	$13.6^{\pm 4.2}$	[11]	G284.3–0.3
6 southern HII	CBI	31	~5–10	1.9	$3.3^{\pm 1.7}$	[11]	Mean includes RCW49
W40	WMAP/CBI	31–33	60/8	5*	$< 0.2^a$	[12]	*No excess detected by [13]
LPH96 201.6+1.6	GBT/CBI	5–30	~10	10*	$5.8^{\pm 2.3}$	[14, 15]	*Spurious; AME < 24% [15]
16 compact HII	AMI	15	<1	~0	<5	[16]	Upper limits only

^aEmissivity for W40 estimate is based on a $100 \mu\text{m}$ flux density of 10^5 Jy and a 2σ upper limit at 33 GHz of 5 Jy.

Clearly, more data at a range of frequencies and angular resolution are required to confirm and improve the accuracy for the quantification of AME.

3.2. Compact versus Extended Regions and the Contribution from UCHII. The SED of an evolved diffuse HII region ($\text{EM} \ll 10^6 \text{ pc cm}^{-6}$) will typically be optically thin above $\sim 1 \text{ GHz}$. However, very compact HII regions, with $\text{EM} > 10^7 \text{ cm pc}^{-6}$ (ultracompact (UCHII) and hypercompact (HCHII)) can have turnover frequencies of $\sim 15 \text{ GHz}$ and higher. These would be difficult to detect at lower frequencies. A nearby ionized region at $T_e \sim 10000 \text{ K}$ with angular size $\sim 1''$ could have a maximum flux density of up to $\sim 10 \text{ Jy}$ at 30 GHz although most are at $< 1 \text{ Jy}$ [17]. It is therefore possible that AME (or a portion of it) from HII regions could be produced by UCHII regions that turnover at $\sim 15\text{--}40 \text{ GHz}$.

Estimating the contribution from UCHII is somewhat difficult. Methods include using high-resolution radio data to extrapolate flux densities of point sources assuming a given EM and angular size (e.g., Perrott et al., this issue) or the use of $\text{H}\alpha$ [5] and/or Radio Recombination Line(s) data [18]. Another way is to use an empirical relation between the ratio of $100 \mu\text{m}$ flux density, $S_{100 \mu\text{m}}$, and 2 cm (15 GHz) radio flux density, $S_{2 \text{ cm}}$, from [7] who measured $S_{100 \mu\text{m}}/S_{2 \text{ cm}}$ values between 1000 and 360000, with no UCHII regions below 1000; the median value was $\sim 3000\text{--}5000$. We apply this method for the Perseus, S140 and S235 AME regions to estimate the maximum UCHII flux density, S_{max} , assuming $S_{100 \mu\text{m}}/S_{2 \text{ cm}} = 1000$.

To identify UCHII candidates within the vicinity of these HII regions, we use the colour-colour relation of [19] who found that UCHII regions tend to have IRAS colour ratios of $\log_{10}(S_{60}/S_{12}) \geq 1.30$ and $\log_{10}(S_{25}/S_{12}) \geq 0.57$. Although this method was found to be very useful for finding the majority of UCHII regions, it also selects a large fraction of non-UCHII regions, such as cloud cores with lower mass stars [20]. This therefore serves to be a very conservative upper limit to the contribution of UCHII and is more likely to be a significant overestimate by factors of several.

Figure 2 shows the colours of matched IRAS Point Source Catalogue (PSC v2.1) for the three AME regions. UCHII candidates have ratios $\log_{10}(S_{60}/S_{12}) \geq 1.30$ and $\log_{10}(S_{25}/S_{12}) \geq 0.57$, corresponding to the top-right hand corner of this plot (marked with a dashed line). We have ignored sources that are categorised as extragalactic (IRAS IDTYPE 1) or only have upper limits at 25 or $60 \mu\text{m}$. There are a few UCHII candidates within each of the three regions with a wide range of $100 \mu\text{m}$ flux densities. Summing these up for each region, and assuming $S_{100 \mu\text{m}}/S_{2 \text{ cm}} = 1000$ gives 0.52, 14.3, and 7.9 Jy for Perseus, S140 and S235, respectively. This corresponds to upper limits of the fraction of the AME that could be due to UCHII at frequencies $\sim 15\text{--}30 \text{ GHz}$ of $< 4\%$ (Perseus), $< 102\%$ (S140), and $< 122\%$. In the Perseus source, the contribution of UCHII is negligible. But for the AME detected in the two bright HII regions (S140 and S235), it could potentially all be due to UCHII. However, this is a very conservative upper limit. High resolution observations (e.g., with AMI at 15 GHz; see Perrott et al., this issue) shows that the majority of the AME is in fact diffuse and therefore is unlikely to be dominated by UCHII. Nevertheless, the possible contribution from UCHII regions should not be overlooked.

3.3. AME Emissivity of HII Regions. The first detections of dust-correlated AME originate from CMB experiments measuring the sky at high Galactic latitudes, and thus authors have often calculated the dust ‘‘emissivity’’ in terms of the radio brightness relative to a dust template map. This has led to the use of the IRAS $100 \mu\text{m}$ map being used as a predictor of the AME amplitude with the emissivity defined in these terms, specifically, in units of $\mu\text{K}/(\text{MJy}/\text{sr})$. Typical values for diffuse cirrus at high Galactic latitudes are $\sim 10 \mu\text{K}/(\text{MJy}/\text{sr})$ with variations of a factor of ~ 2 [21]; this corresponds to approximately 1 Jy at 33 GHz for every 3000 Jy at $100 \mu\text{m}$.

Table 1 lists the AME dust emissivities, E , in terms of the AME brightness temperature relative to the $100 \mu\text{m}$ brightness, converted to units $\mu\text{K}/(\text{MJy}/\text{sr})$. Although the uncertainties are large, it appears that the AME emissivity are comparable to the high latitude value, but on average are lower compared to the high latitude value (and lower still than the Perseus AME region). More strikingly, upper limits from

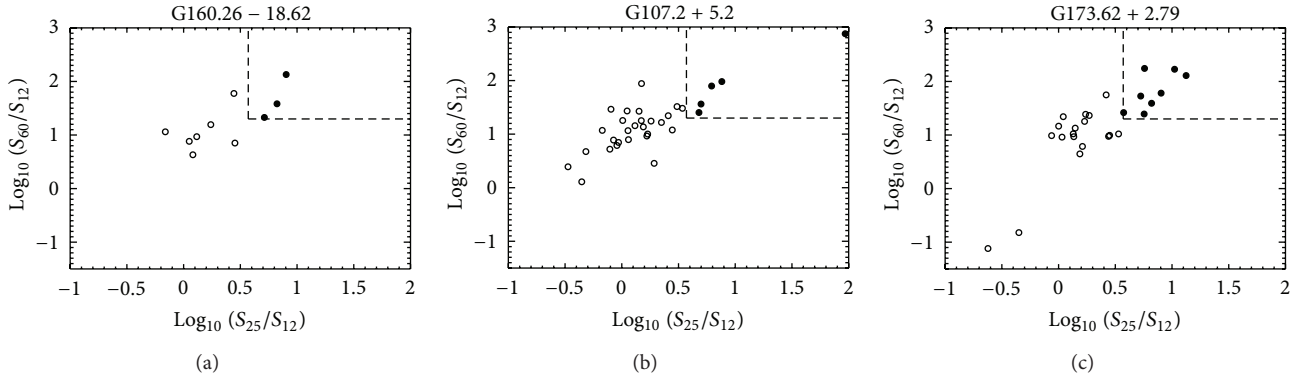


FIGURE 2: Colour–Colour plots of IRAS sources in the vicinity of Perseus (a), G107.2+5.2 (b), and G173.6 + 2.79 (c) AME regions. The colours are calculated for sources within 1° of the central source positions using the IRAS PSC. UCHII region candidates, shown as solid-filled circles, have ratios $\log_{10}(S_{60}/S_{12}) \geq 1.30$ and $\log_{10}(S_{25}/S_{12}) \geq 0.57$, corresponding to the top-right hand corner of this plot (marked with a dashed line).

the compact sample observed by AMI [16] and also upper limits from W40 suggest the AME emissivities are at least an order of magnitude lower still.

This surprising result can be understood in terms of the different environments in the vicinity of HII regions. The most important is the lack of smallest dust grains (PAHs) which are known to be depleted inside HII regions (e.g., [22]). If AME is due to spinning dust grains this would severely reduce the AME brightness since the very smallest grains produce most of the spinning dust flux. Other factors may also be contributing such as the interstellar radiation field and distribution of ions.

Finally, we point out that although the $100 \mu\text{m}$ emissivity is a convenient quantity, it can be significantly biased in regions with a higher than average dust temperature. The $100 \mu\text{m}$ intensity is very sensitive to the dust temperature. For example, compared to an average dust temperature of 18.1 K, for a value of 22 K the $100 \mu\text{m}$ intensity is a factor of 4 times higher, while for 30 K it is a factor of 23 times higher (see Tibbs et al., this issue). HII regions are known to have warmer dust, typically 30–80 K, and thus the AME emissivity will naturally be lower. This may explain the apparently lower values observed in more compact regions where this will be pronounced. A better definition of emissivity would be to use the column density or, equivalently, the thermal dust optical depth [12].

4. Conclusions

HII regions are an interesting place to look for AME. So far, there have been a number of detections from HII regions (or in the vicinity of HII regions). However, measuring accurate SEDs over a wide frequency range, in addition to the complex environment and the presence of bright continuum (e.g., free-free, thermal dust) emission makes this a very difficult task. Furthermore, the presence of optically thick free-free emission from UCHII regions may be contributing to a portion of the AME for some regions. Nevertheless, the AME emissivity is comparable to the more robust detections on

molecular clouds and diffuse cirrus, although on average it is lower; in some HII regions there are only upper limits on AME. More data, particularly at higher resolutions and high frequencies (>5 GHz) are needed.

Acknowledgments

C. Dickinson acknowledges an STFC Advanced Fellowship, an EC Marie-Curie IRG grant under the FP7, and an ERC Starting Grant no. 307209.

References

- [1] B. T. Draine and A. Lazarian, “Diffuse galactic emission from spinning dust grains,” *The Astrophysical Journal Letters*, vol. 494, no. 1, p. L19, 1998.
- [2] S. Casassus, C. Dickinson, K. Cleary et al., “Centimetre-wave continuum radiation from the ρ Ophiuchi molecular cloud,” *Monthly Notices of the Royal Astronomical Society*, vol. 391, no. 3, pp. 1075–1090, 2008.
- [3] A. Abergel, P. A. R. Ade, N. Aghanim et al., “*Planck* early results. XXI. Properties of the interstellar medium in the Galactic plane,” *Astronomy & Astrophysics*, vol. 536, article A21, 18 pages, 2011.
- [4] P. A. R. Ade, N. Aghanim, M. Arnaud et al., “*Planck* early results. XX. New light on anomalous microwave emission from spinning dust grains,” *Astronomy & Astrophysics*, vol. 536, article A20, 17 pages, 2011.
- [5] C. Dickinson, R. D. Davies, and R. J. Davis, “Towards a free-free template for CMB foregrounds,” *Monthly Notices of the Royal Astronomical Society*, vol. 341, no. 2, pp. 369–384, 2003.
- [6] X. Dupac, J. P. Bernard, N. Boudet et al., “Inverse temperature dependence of the dust submillimeter spectral index,” *Astronomy and Astrophysics*, vol. 404, no. 1, pp. L11–L15, 2003.
- [7] S. Kurtz, E. Churchwell, and D. O. S. Wood, “Ultracompact HII regions. II. New high-resolution radio images,” *Astrophysical Journal, Supplement Series*, vol. 91, no. 2, pp. 659–712, 1994.
- [8] C. Dickinson, R. D. Davies, J. R. Allison et al., “Anomalous microwave emission from the HII region RCW175,” *The Astrophysical Journal*, vol. 690, no. 2, p. 1585, 2009.

- [9] C. T. Tibbs, R. Paladini, M. Compiègne et al., “A multi-wavelength investigation of RCW175: an HII region harboring spinning dust emission,” *The Astrophysical Journal*, vol. 754, article 94, 2012.
- [10] M. Todorović, R. D. Davies, C. Dickinson et al., “A 33-GHz very small array survey of the galactic plane from $l = 27^\circ$ to 46° ,” *Monthly Notices of the Royal Astronomical Society*, vol. 406, p. 1629, 2010.
- [11] C. Dickinson, R. D. Davies, L. Bronfman et al., “CBI limits on 31 GHz excess emission in southern HII regions,” *Monthly Notices of the Royal Astronomical Society*, vol. 379, no. 1, pp. 297–307, 2007.
- [12] D. P. Finkbeiner, G. I. Langston, and A. H. Minter, “Microwave interstellar medium emission in the green bank galactic plane survey: evidence for spinning dust,” *Astrophysical Journal*, vol. 617, no. 1, pp. 350–359, 2004.
- [13] D. Stamadianos, *Microwave observations of W40 [M.Sc. thesis]*, University of Manchester, Manchester, UK, 2010.
- [14] D. P. Finkbeiner, D. J. Schlegel, C. Frank, and C. Heiles, “Tentative detection of electric dipole emission from rapidly rotating dust grains,” *Astrophysical Journal Letters*, vol. 566, no. 2, pp. 898–904, 2002.
- [15] C. Dickinson, S. Casassus, J. L. Pineda, T. J. Pearson, A. C. S. Readhead, and R. D. Davies, “An upper limit on anomalous dust emission at 31 GHz in the diffuse cloud [LPH96] 201.663+1.643,” *Astrophysical Journal*, vol. 643, no. 2, pp. L111–L114, 2006.
- [16] A. M. M. Scaife, N. Hurley-Walker, M. L. Davies et al., “AMI limits on 15-GHz excess emission in northern HII region,” *Monthly Notices of the Royal Astronomical Society*, vol. 385, no. 2, pp. 809–822, 2008.
- [17] D. O. S. Wood, T. Handa, Y. Fukui et al., “Flux densities of ultracompact HII regions at 7 millimeters,” *The Astrophysical Journal*, vol. 326, pp. 884–888, 1988.
- [18] M. I. R. Alves, R. D. Davies, C. Dickinson et al., “A derivation of the free-free emission on the Galactic plane between $l = 20^\circ$ and 44° ,” *Monthly Notices of the Royal Astronomical Society*, vol. 422, no. 3, pp. 2429–2443, 2012.
- [19] D. O. S. Wood and E. Churchwell, “Massive stars embedded in molecular clouds—their population and distribution in the galaxy,” *Astrophysical Journal*, vol. 340, pp. 265–272, 1989.
- [20] B. Ramesh and T. K. Sridharan, “Reliable galaxy-wide identification of ultracompact HII regions,” *Monthly Notices of the Royal Astronomical Society*, vol. 284, p. 1001, 1997.
- [21] R. D. Davies, C. Dickinson, A. J. Banday, T. R. Jaffe, K. M. Górski, and R. J. Davis, “A determination of the spectra of Galactic components observed by the *Wilkinson Microwave Anisotropy Probe*,” *Monthly Notices of the Royal Astronomical Society*, vol. 370, no. 3, pp. 1125–1139, 2006.
- [22] M. S. Povich, J. M. Stone, E. Churchwell et al., “A multiwavelength study of M17: the spectral energy distribution and PAH emission morphology of a massive star formation region,” *Astrophysical Journal*, vol. 660, no. 1, pp. 346–362, 2007.

Review Article

Spinning Dust Radiation: A Review of the Theory

Yacine Ali-Haïmoud

Institute for Advanced Study, Einstein Drive, Princeton, NJ 08540, USA

Correspondence should be addressed to Yacine Ali-Haïmoud; yacine@ias.edu

Received 29 August 2012; Accepted 8 November 2012

Academic Editor: Laurent Verstraete

Copyright © 2013 Yacine Ali-Haïmoud. This is an open access article distributed under the Creative Commons Attribution License, which permits unrestricted use, distribution, and reproduction in any medium, provided the original work is properly cited.

This paper reviews the current status of theoretical modeling of electric dipole radiation from spinning dust grains. The fundamentally simple problem of dust grain rotation appeals to a rich set of concepts of classical and quantum physics, owing to the diversity of processes involved. Rotational excitation and damping rates through various mechanisms are discussed, as well as methods of computing the grain angular momentum distribution function. Assumptions on grain properties are reviewed. The robustness of theoretical predictions now seems mostly limited by the uncertainties regarding the grains themselves, namely, their abundance, dipole moments, and size and shape distribution.

1. Introduction

Rotational radiation from small grains in the interstellar medium (ISM) has been suggested as a source of radio emission several decades ago already. The basic idea was first introduced by Erickson (1957) [1] and then revisited by Hoyle and Wickramasinghe (1970) [2] and Ferrara and Dettmar (1994) [3]. Rouan et al. (1992) [4] were the first to provide a thorough description of the physics of rotation of polycyclic aromatic hydrocarbons (PAHs), although not including all gas processes.

Shortly after the discovery of the anomalous dust-correlated microwave emission (AME) in the galaxy by Leitch et al. (1997) [5], Draine and Lazarian (1998, hereafter DL98) [6, 7] suggested that spinning dust radiation might be responsible for the AME and provided an in-depth theoretical description of the process.

Understanding the spinning dust spectrum in as much detail as possible is important. First, the AME constitutes a foreground emission to cosmic microwave background (CMB) radiation. Second, it provides a window into the properties of small grains, which play crucial roles for the physics and chemistry of the ISM.

Motivated by these considerations and the accumulating observational evidence for diffuse and localized AME, several groups have since then revisited and refined the DL98

model [8–12]. New physical processes were accounted for, which can significantly affect the predicted spectrum. A publicly available code to evaluate spinning dust emissivities (SPDUST) is now available, including most (but not all thus far) processes recently investigated (SPDUST is available at <http://www.sns.ias.edu/yacine/spdust/spdust.html>).

The purpose of this paper is to provide an overview of the physics involved in modeling spinning dust spectra. We attempt to provide a comprehensive description of the problem at the formal level, and let the interested reader learn about the details in the various works that deal with the subject.

This paper is organized as follows: Section 2 reviews the basic process of electric dipole radiation and the resulting emissivity. We then describe the assumed properties of the small grains, which are believed to be the source of the spinning dust radiation in Section 3. Section 4 discusses the rotational configuration of small grains stochastically heated by ultraviolet (UV) photons. Section 5 describes the methods to obtain the distribution of grain angular momentum, as well as the various physical processes that affect it. We conclude and mention potential future research directions in Section 6.

2. Basic Process

2.1. Electric Dipole Radiation of a Spinning Grain. Consider a grain with permanent electric dipole moment $\mu(t)$ rotating

classically, such that its angular momentum is much larger than \hbar (this was shown to be indeed the case even for the smallest grains, for which $J = L/\hbar \sim 70$ [7]). The instantaneous power radiated is given by

$$P(t) = \frac{2}{3c^3} \ddot{\boldsymbol{\mu}}^2. \quad (1)$$

Averaging this power over many rotation cycles, we get

$$\begin{aligned} \langle P \rangle &= \frac{2}{3c^3} \langle \dot{\boldsymbol{\mu}}^2 \rangle = \frac{2}{3c^3} \sum_i \langle \dot{\mu}_i^2 \rangle = \frac{2}{3c^3} \sum_i \int d\nu S_{\mu_i}(\nu) \\ &= \int d\nu \frac{2}{3c^3} (2\pi\nu)^4 \sum_i S_{\mu_i}(\nu), \end{aligned} \quad (2)$$

where $S_{\mu_i}(\nu)$ is the power spectrum of the i th cartesian component of $\boldsymbol{\mu}$. From (2) we can directly read off the power radiated per unit frequency:

$$\frac{dP}{d\nu}(\nu | \mathbf{L}, \boldsymbol{\omega}) = \frac{2}{3c^3} (2\pi\nu)^4 \sum_i S_{\mu_i}(\nu). \quad (3)$$

In general, the power spectrum of the electric dipole moment depends not only on the total angular momentum of the grain \mathbf{L} but also on the the orientation of the grain axes and dipole moment with respect to \mathbf{L} , which we formally represent by the set of angles $\boldsymbol{\omega}$.

2.1.1. Spherical Grain. We first consider the simplest case of a freely rotating spherical grain, with isotropic moment of inertia tensor $I_{ij} = I\delta_{ij}$. In that case, the angular velocity $\boldsymbol{\omega}_0 = \mathbf{L}/I$ is a constant vector, which we take along the z -axis, and the power spectra of the components of the dipole moment are

$$S_{\mu_z} = 0, \quad S_{\mu_x} = S_{\mu_y} = \frac{1}{2} \mu_{\perp}^2 \delta(\nu - \nu_0), \quad (4)$$

where μ_{\perp} is the component of $\boldsymbol{\mu}$ perpendicular to $\boldsymbol{\omega}_0$ and $\nu_0 = \omega_0/(2\pi) = L/(2\pi I)$ is the frequency of rotation. The power radiated in this simple case is then

$$\frac{dP}{d\nu} = \frac{2\mu_{\perp}^2}{3c^3} (2\pi\nu)^4 \delta\left(\nu - \frac{L}{2\pi I}\right). \quad (5)$$

2.1.2. Axisymmetric Grain. Here we consider an oblate axisymmetric grain with moments of inertia $I_3 > I_2 = I_1$. We describe the orientation of the grain principal axes with respect to its angular momentum \mathbf{L} with the three Euler angles ϕ, θ, ψ pictured in Figure 1.

Between two discrete events that change its angular momentum, the grain can be considered as freely rotating. During these periods, the Euler angles change according to

$$\begin{aligned} \theta &= \text{constant}, \\ \dot{\phi} &= \frac{L}{I_1}, \\ \dot{\psi} &= -\left(\frac{L}{I_1} - \frac{L}{I_3}\right) \cos \theta. \end{aligned} \quad (6)$$

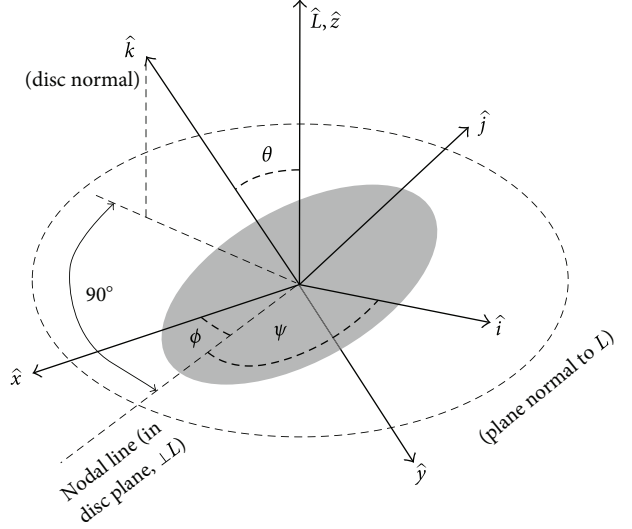


FIGURE 1: Euler angles used for the description of an axisymmetric grain. The figure was reproduced from [9].

Electromagnetic radiation is now emitted at the four frequencies $\dot{\phi}/(2\pi)$, $|\dot{\psi}|/(2\pi)$, $(\dot{\phi} \pm \dot{\psi})/(2\pi)$ [9, 10]:

$$\begin{aligned} \frac{dP}{d\nu} &= \frac{2\mu_{\parallel}^2}{3c^3} \dot{\phi}^4 \sin^2 \theta \delta\left(\nu - \frac{\dot{\phi}}{2\pi}\right) + \frac{\mu_{\perp}^2}{3c^3} \dot{\psi}^4 \sin^2 \theta \delta\left(\nu - \frac{|\dot{\psi}|}{2\pi}\right) \\ &+ \sum_{\pm} \frac{\mu_{\perp}^2}{6c^3} (\dot{\phi} \pm \dot{\psi})^4 (1 \pm \cos \theta)^2 \delta\left(\nu - \frac{(\dot{\phi} \pm \dot{\psi})}{2\pi}\right). \end{aligned} \quad (7)$$

2.1.3. Triaxial Grain. The case of a triaxial grain is unfortunately not analytic. In that case, power is radiated at a countably infinite number of frequencies. Hoang et al. (2011) [11] obtained the power spectrum of a freely rotating grain numerically. They show that for a classically rotating grain, only a few modes are dominant.

2.2. Emissivity. The quantity of interest to us is the emissivity j_{ν} (with units of power per frequency interval per unit volume per steradian), which we obtain from integrating the power over grain size and shape distribution $dn_{gr}/d\mathbf{a}$ (where \mathbf{a} is meant to formally represent the characteristic size and three-dimensional shape of a grain), as well as the electric dipole distribution, $f(\boldsymbol{\mu} | \mathbf{a})$ convolved with the probability distribution for the angular momentum and rotational configuration $f(\mathbf{L}, \boldsymbol{\omega} | \mathbf{a}; \boldsymbol{\mu})$ (We use repeatedly the letter f to denote probability distribution functions. The arguments of f should always make its meaning unambiguous: $f(X, Y | \alpha, \beta, \dots)$ denotes the differential probability distribution for the variables X, Y given the values α, β, \dots of some other variables.) In the absence of any preferred direction, the dependence on \mathbf{L} is in fact only through its magnitude L . This is the case if there are no magnetic fields and anisotropic radiation fields, or if none of them are efficient at aligning

the grains. In what follows, we will assume perfect *isotropy* of space. The emissivity is then given by

$$j_\nu = \frac{1}{4\pi} \int d\mathbf{a} \frac{dn_{gr}}{d\mathbf{a}} \int d^3\mu f(\mu | \mathbf{a}) \times \int d^3\mathbf{L} d\boldsymbol{\omega} f(L, \boldsymbol{\omega} | \mathbf{a}, \mu) \frac{dP}{d\nu}(\nu | L, \boldsymbol{\omega}, \mathbf{a}, \mu). \quad (8)$$

Finally, we note that the actual *observable* is the radio intensity, given by the emissivity integrated along the line of sight,

$$I_\nu(\hat{\mathbf{n}}) = \int j_\nu(s\hat{\mathbf{n}}) ds. \quad (9)$$

At each point in space, the emissivity depends on the local environmental conditions (density, temperature, ionization degree, and ambient radiation field, as well as grain abundance), as we shall see below. Therefore, predicting the spinning dust spectrum along a line of sight requires modeling the ISM properties (see e.g., [13]). Reference [11] evaluates the effect of turbulence on the spinning dust spectrum and finds that the effective emissivity (averaged over the probability distribution for the compression factor along the line of sight) can be shifted to larger frequencies and enhanced by several tens of percent.

We do not deal with this aspect in this paper as it does not belong, *per se*, to the field of spinning dust theory, but rather to the larger field of ISM modeling. It is, however, crucial to accurately model the environmental spatial variations in order to get precise predictions.

3. Grain Properties

3.1. Abundance and Size Distribution. The small grain abundance is determined primarily from observations of the wavelength-dependent extinction and the 3–25 μm emission, attributed to various vibrational modes of PAHs (for a review on interstellar PAHs and their properties, see e.g., Tielens (2008) [14]). Note that the UV extinction indicates the presence of nanodust but does not give any detailed information on grain sizes. Only the IR emission allows to constrain the small grain size distribution, as discussed in Li and Mann (2012) [15]. Observations require a few percent of the interstellar carbon to be locked in PAHs, and a significant population of very small grains (less than ~ 1 nm in size) to reproduce the strength of the 3–12 μm bands, which are emitted by small grains stochastically heated to large temperatures [16]. Following DL98, Li and Draine (2001) [17] and Weingartner and Draine (2001) [18] have adopted a log-normal distribution in grain radius, starting and centered at $a_{\min} = a = 3.5 \text{ \AA}$ (corresponding roughly to a coronene molecule with formula $\text{C}_{24}\text{H}_{12}$) and variance $\sigma = 0.4$ in $\log a$ and showed that such a distribution reproduced the infrared emission well. Observations tend to indicate that PAHs are less abundant in dense clouds than in the diffuse ISM.

Note that we assume the smallest grains in the ISM being mostly PAHs, but a population of ultrasmall silicate grains is not completely ruled out by observations [19].

3.2. Shapes. PAHs may take a variety of shapes, from disk-like to nearly linear. They are not necessarily planar: for example, if one of the hexagonal carbon rings is replaced by a pentagonal ring, they are bent and become three dimensional. Above a certain size, PAHs may form irregular clusters and eventually, large three-dimensional grains.

The exact distribution of shapes is largely unknown. The lowest-frequency IR emission bands in principle carry information about the individual grains and seem to indicate that PAHs may be dominated by a few well-defined molecular structures, although not conclusively [14].

The smallest grains dominate the spinning dust spectrum (they can be spun up to larger frequencies and hence emit more power). It is commonly assumed that these grains are nearly planar up to a spherical-equivalent radius $a = 6 \text{ \AA}$, corresponding to 100 carbon atoms. The peak of the spinning dust spectrum is not very sensitive to the exact cut-off between planar and spherical grains.

3.3. Permanent Dipole Moments. In principle a consistent prescription should be given for small grains, which gives the precise nature of the grain, hence its shape (or rotational constants) and permanent electric dipole moment, which can be computed quantum-mechanically for small enough molecules. Such computations were carried out by Hudgins et al. (2005) [20] for nitrogen-substituted PAHs. They found typical permanent dipole moments of a few Debyes, depending on the precise position of the substituted nitrogen atom.

Eventually, observations will hopefully allow for a more precise determination of the population of PAHs and their properties. We are currently far from having a definite handle on such refined properties of small grains, and an empirical distribution of dipole moments is required. Following DL98, more recent models assume a three-dimensional Gaussian distribution of dipole moments, with variance

$$\langle \mu^2 \rangle = N_{\text{at}} \beta^2 + (\epsilon a e Z)^2, \quad (10)$$

where $\beta \approx 0.4$ Debye and $\epsilon \approx 0.01$. The first term, largely dominant, accounts for the permanent dipole moment and the second term accounts for charge displacement in ionized grains. We repeat that this distribution is largely *ad hoc* and may be far from reflecting reality, except (hopefully) for the characteristic permanent dipole moment.

4. Rotational Configuration

4.1. Fast Vibration-Rotation Energy Transfer. In principle, one should solve for the distribution of angular momentum *and* rotational configuration $f(L, \boldsymbol{\omega})$ at once. Indeed, a priori, the same processes that change the angular momentum may also change the relative orientation of the grain at a similar rate. Grains can exchange angular momentum with several “baths,” all characterized by different characteristic “temperatures,” and the resulting overall distribution function cannot easily be factored into a pure angular momentum part and a pure rotational configuration part (one can always formally write the factorization, $f(L, \boldsymbol{\omega}) = f(L)f(\boldsymbol{\omega} | L)$, but one cannot in principle compute the two factors independently).

The situation is much simplified if one single process is very efficient at changing the rotational configuration, on timescales much shorter than the overall timescale to change the angular momentum. If this process is characterized by an equilibrium temperature $T_{\boldsymbol{\omega}}$, then one can indeed compute the probability distribution $f(\boldsymbol{\omega} | L)$ *independently*:

$$f(\boldsymbol{\omega} | L) \propto \exp\left[-\frac{E_{\text{rot}}(L, \boldsymbol{\omega})}{kT_{\boldsymbol{\omega}}}\right], \quad (11)$$

where the rotational energy is most easily written using the projections of the angular momentum on the grain's principal axes with principal moments of inertia I_i ,

$$E_{\text{rot}}(L, \boldsymbol{\omega}) = \sum_i \frac{L_i^2}{2I_i} = L^2 \sum_i \frac{l_i^2}{2I_i}, \quad (12)$$

where we have defined $l_i \equiv L_i/L$, the normalized projection of the angular momentum along the axis i . One can formally identify $\boldsymbol{\omega} \leftrightarrow \{l_i\}$ (at least in some time-averaged sense), and (11) then uniquely determines the probability distribution for the rotational configuration, given a value for the total angular momentum L . The angular momentum distribution $f(L)$ can then be obtained from transition rates averaged over the rotational configuration with the known distribution $f(\boldsymbol{\omega} | L)$.

Luckily Nature does provide us with such an efficient process to change $\boldsymbol{\omega}$ at constant L : *internal vibrational-rotational energy transfer* (IVRET) (see e.g., [9, 11, 21–23] for application to spinning dust modeling). The first detailed studies of how internal relaxation may affect grain alignment were carried in [24, 25].

Following the absorption of an ultraviolet (UV) photon, small grains get heated up to large vibrational temperatures T_{vib} (the notion of temperature is not well defined for the smallest grains, so we mean temperature as a characteristic energy per degree of freedom). IVRET leads to a rapid energy exchange between vibrational and rotational degrees of freedom, at constant angular momentum, so that during a thermal spike, the distribution $f(\boldsymbol{\omega} | L)$ is given by (11) with $T_{\boldsymbol{\omega}} = T_{\text{vib}}$. As the grain cools down by emitting infrared photons, its vibrational temperature decreases, until the grain reaches its fundamental vibrational mode, with typical energy $E_0/k \sim 100$ K for the smallest grains. IVRET is only active as long as the density of vibrational states is large enough that there exist transitions at frequencies near the rotation frequency. Therefore, energy exchange *freezes* at a characteristic temperature $T_{\boldsymbol{\omega}} = T_{\text{fr}} > E_0/k$, probably of at least a couple hundred Kelvins, and this temperature characterizes the final rotational configuration following a thermal spike. For this distribution to remain valid at all times, it is necessary that the rate of absorption of UV photons is larger than the rate of change of angular momentum. This is indeed the case in diffuse environments (see Table 1 of [9]), where absorption of UV photons is a few times faster than angular momentum changes; this difference of timescales gets more pronounced as the ambient radiation field increases. In dense and underilluminated clouds, however, the rate of absorption of photons is not large enough to maintain the distribution

(11), and the rotational configuration needs in principle to be computed from the full $f(L, \boldsymbol{\omega})$.

Let us now discuss the implications of (11). The angular momentum itself has a characteristic value L_{peak} , and therefore the rotational energy is of order $E_{\text{rot}} \sim L_{\text{peak}}^2/I \equiv kT_L$. If $T_{\boldsymbol{\omega}} \ll T_L$, the most probable rotational configuration will be the one minimizing the energy, that is, where the grain rotates about its axis of greatest inertia. In the opposite case where $T_{\boldsymbol{\omega}} \gg T_L$, all rotational configurations become equiprobable (of course when converting to actual angles one needs to be careful of using the appropriate phase-space volume $d\boldsymbol{\omega}$).

For example, an axisymmetric oblate grain with $I_3 > I_2 = I_1$ has a rotational energy

$$E_{\text{rot}}(L, \theta) = \frac{L^2}{2I_1} \left[1 - \left(1 - \frac{I_1}{I_3} \right) \cos^2 \theta \right], \quad (13)$$

where θ is the angle between \mathbf{L} and the axis of greatest inertia. If $T_{\boldsymbol{\omega}} \ll T_L$, the most probable configurations are $\theta = 0$ or π . In the case where $T_{\boldsymbol{\omega}} \gg T_L$, we obtain that $f(\theta | L) \propto \sin \theta$ (here we used $d\boldsymbol{\omega} = d\phi \sin \theta d\theta$ in the usual spherical polar coordinates).

SPDUST only allows for the two limiting regimes $T_{\boldsymbol{\omega}} \rightarrow 0$ and $T_{\boldsymbol{\omega}} \rightarrow \infty$, bracketing the range of possibilities. The authors of [11] explore the effect of continuously varying $T_{\boldsymbol{\omega}}$, interpolating continuously between the two extreme regimes. In general, there will be a different temperature $T_{\boldsymbol{\omega}}$ for each grain size and depending on the environment, but the precise modeling of this parameter has not been addressed in the literature yet. In what follows, we shall only discuss the two limiting regimes.

4.2. Implication for the Emitted Power at Fixed Angular Momentum. The last integral in (8) can be rewritten as

$$\int d^3\mathbf{L} d\boldsymbol{\omega} f(L, \boldsymbol{\omega}) \frac{dP}{d\nu}(L, \boldsymbol{\omega}) = \int d^3\mathbf{L} f(L) \left\langle \frac{dP}{d\nu} \right\rangle(L), \quad (14)$$

where the power averaged over the rotational configuration is

$$\left\langle \frac{dP}{d\nu} \right\rangle(L) \equiv \int d\boldsymbol{\omega} f(\boldsymbol{\omega} | L) \frac{dP}{d\nu}(L, \boldsymbol{\omega}). \quad (15)$$

In the case of a grain rotating about its axis of the greatest inertia I_3 , the averaged power collapses to

$$\left\langle \frac{dP}{d\nu} \right\rangle = \frac{2}{3c^3} (2\pi\nu)^4 \mu_1^2 \delta\left(\nu - \frac{L}{2\pi I_3}\right), \quad T_{\boldsymbol{\omega}} \rightarrow 0, \quad (16)$$

which is identical to the case of a spherical grain. If we now consider an oblate axisymmetric grain with $T_{\boldsymbol{\omega}} \rightarrow \infty$, we

obtain, using the results of Section 2.1.2 and averaging over isotropically distributed nutation angles θ ,

$$\begin{aligned} \left\langle \frac{dP}{d\nu} \right\rangle &= \frac{4\mu_{\parallel}^2}{9c^3} (2\pi\nu_1)^4 \delta(\nu - \nu_1) + \frac{\mu_{\perp}^2}{3c^3} (2\pi\nu)^4 \\ &\times \left[1 - \left(\frac{\nu}{\nu_{13}} \right)^2 \right] \frac{\mathbf{1}_{\nu < \nu_{13}}}{\nu_{13}} + \frac{\mu_{\perp}^2}{3c^3} (2\pi\nu)^4 \\ &\times \left(\frac{\nu_1 + \nu_{13} - \nu}{\nu_{13}} \right)^2 \frac{\mathbf{1}_{\nu_3 < \nu < \nu_1 + \nu_{13}}}{2\nu_{13}}, \quad T_{\omega} \longrightarrow \infty, \end{aligned} \quad (17)$$

where the function $\mathbf{1}$ is unity where its subscript is valid and zero elsewhere, and we have defined the two frequencies

$$\begin{aligned} \nu_1 &\equiv \frac{L}{2\pi I_1}, \\ \nu_{13} &\equiv \frac{L}{2\pi I_1} - \frac{L}{2\pi I_3}. \end{aligned} \quad (18)$$

In the case of a planar grain with $I_3 = 2I_1$ and $\nu_1 = 2\nu_3 = 2\nu_{13}$, the power radiated by a wobbling grain is emitted at characteristic frequencies about twice as large as in the case of a grain rotating primarily about its axis of greatest inertia. The integrated power is, in the former case (and assuming $\nu_3 = \nu_{13}$),

$$P(T_{\omega} \longrightarrow \infty) = \frac{4\mu_{\parallel}^2}{9c^3} (2\pi\nu_1)^4 + 10 \frac{\mu_{\perp}^2}{3c^3} (2\pi\nu_3)^4, \quad (19)$$

which is about 10 times larger, *at equal angular momentum*, than the power radiated by a grain rotating mostly about its axis of greatest inertia if $\mu_{\perp}^2 = 2\mu_{\parallel}^2$.

One must not forget, however, that the angular momentum distribution itself depends upon the rotational configuration $f(\boldsymbol{\omega} \mid L)$, since one must use this distribution to average transition rates. We shall see in the next section that the effect of randomized rotational configuration is to lower the characteristic angular momentum L .

5. Angular Momentum Distribution

To determine the angular momentum distribution, we need to evaluate the differential transition rates $\Gamma(L \rightarrow L')$ between different values of the angular momentum magnitude, defined such that $\Gamma(L \rightarrow L')\Delta L'$ is the rate of transition from an initial angular momentum L to a final angular momentum in the interval $[L', L' + \Delta L']$. These rates are averaged over the rotational configuration for $\boldsymbol{\omega}$ discussed above. The steady-state distribution function $f(L)$ should then in principle be obtained from the integral master equation

$$\begin{aligned} \frac{\partial \tilde{f}(L)}{\partial t} &= \int \left[\tilde{f}(L') \Gamma(L' \rightarrow L) - \tilde{f}(L) \Gamma(L \rightarrow L') \right] dL' \\ &= 0, \quad \forall L, \end{aligned} \quad (20)$$

where we have defined $\tilde{f}(L) \equiv 4\pi L^2 f(L)$ so that $\tilde{f}(L)$ is the distribution function for the magnitude of \mathbf{L} (whereas $f(\mathbf{L}) = f(L)$ is the distribution function for the *vector* angular momentum, even if it only depends on its magnitude due to isotropy). This equation is, clearly, rather cumbersome to solve and below we present a simpler (if approximate) method of solution, based on the Fokker-Planck equation. Section 5.1 provides a formal introduction to the problem, and actual physical mechanisms are discussed in Section 5.2.

5.1. The Fokker-Planck Equation

5.1.1. Derivation. In general, transition rates are not significant for arbitrarily large values of $\Delta L \equiv L' - L$: there always exists some characteristic ΔL_0 such that $\Gamma(L \rightarrow L + \Delta L)$ decreases rapidly for $|\Delta L| \gtrsim \Delta L_0$. An important simplification can be made if the scale ΔL_0 is much smaller than the characteristic scale over which both the distribution function varies and the rates themselves vary—the distribution function being unknown a priori, the validity this assumption has in principle to be checked a posteriori. If this is the case, we may expand the first term in the integral of (20), setting $L' = L + \Delta L$:

$$\begin{aligned} \tilde{f}(L + \Delta L) \Gamma(L + \Delta L \rightarrow L) &\approx \tilde{f}(L) \Gamma(L \rightarrow L - \Delta L) \\ &+ \Delta L \frac{\partial}{\partial L} \left[\tilde{f}(L) \Gamma(L \rightarrow L - \Delta L) \right] \\ &+ \frac{1}{2} (\Delta L)^2 \frac{\partial^2}{\partial L^2} \\ &\times \left[\tilde{f}(L) \Gamma(L \rightarrow L - \Delta L) \right]. \end{aligned} \quad (21)$$

Plugging this expansion back into (20), we see that the term linear in $\tilde{f}(L)$ cancels out with the second term of the integral (the integrand being an odd function of ΔL). Recalling that $\tilde{f}(L) = 4\pi L^2 f(L)$, we finally obtain

$$\begin{aligned} 4\pi L^2 \frac{\partial f(L)}{\partial t} &= - \frac{\partial}{\partial L} \left[\frac{d \langle \Delta L \rangle}{dt} 4\pi L^2 f(L) \right] \\ &+ \frac{1}{2} \frac{\partial^2}{\partial L^2} \left[\frac{d \langle (\Delta L)^2 \rangle}{dt} 4\pi L^2 f(L) \right] = 0, \end{aligned} \quad (22)$$

where we have defined the rate of angular momentum *drift* (the opposite of which is the rate of angular momentum *dissipation* or *damping*),

$$\frac{d \langle \Delta L \rangle}{dt} \equiv \int \Delta L \Gamma(L \rightarrow L + \Delta L) d(\Delta L), \quad (23)$$

and the rate of angular momentum *diffusion* (also termed *fluctuation* or *excitation*),

$$\frac{d \langle (\Delta L)^2 \rangle}{dt} \equiv \int (\Delta L)^2 \Gamma(L \rightarrow L + \Delta L) d(\Delta L). \quad (24)$$

Equation (22) is known as the *Fokker-Planck equation* and has a broad range of applications in physics (see e.g., Chapter 6 of the book [26] by Blandford and Thorne). In the context of grain rotation, this approach was used in [1, 8, 9, 27] and is the basic equation solved in SPDUST. Solving this equation is much simpler than solving the full master equation, and it may even have a simple analytic solution if the excitation and damping rates are simple enough.

5.1.2. General Form of the Rates and Solution

General Processes besides Electric Dipole Radiation Damping. Most processes through which grains may change angular momentum (except for electric dipole radiation itself, to which we shall come back later on) are characterized by a damping timescale τ such that

$$\frac{d\langle\Delta\mathbf{L}\rangle}{dt} = -\frac{\mathbf{L}}{\tau} \quad (25)$$

and have an isotropic and constant diffusion rate of the form

$$\frac{d\langle\Delta L_i\Delta L_j\rangle}{dt} = \frac{1}{3}\frac{\sigma_L^2}{\tau}\delta_{ij}. \quad (26)$$

Taylor-expanding ΔL to second order in $\Delta\mathbf{L}$, we obtain

$$\Delta L = |\mathbf{L} + \Delta\mathbf{L}| - L \approx \Delta\mathbf{L} \cdot \hat{\mathbf{L}} + \frac{(\Delta\mathbf{L})^2 - (\Delta\mathbf{L} \cdot \hat{\mathbf{L}})^2}{2L}. \quad (27)$$

The excitation and damping rates for the *magnitude* of the angular momentum are therefore

$$\frac{d\langle\Delta L\rangle}{dt} = \frac{\sigma_L^2/3 - L^2}{L\tau}, \quad (28)$$

$$\frac{d\langle(\Delta L)^2\rangle}{dt} = \frac{\sigma_L^2}{3\tau}. \quad (29)$$

The form of these coefficients stems from the fact that only longitudinal excitation generates a true diffusion in the magnitude of \mathbf{L} , whereas excitations perpendicular to \mathbf{L} lead to a systematic increase of the magnitude of the angular momentum and hence appear as a positive drift rate in (28).

If only one single process was interacting with the grains, their steady-state distribution would then be the Maxwellian with three-dimensional variance $\langle L^2 \rangle = (1/2)\sigma_L^2$,

$$f(L) \propto \exp\left[-\frac{3L^2}{\sigma_L^2}\right], \quad (30)$$

as can be seen from inserting the rates (28) and (29) into the Fokker-Planck equation (22).

Often, however, there is not a single process that dominates both excitation and damping. Since transition rates add up linearly for independent processes, so do excitation and damping rates. If all rates are of the form (25), (26), then the final distribution is still Maxwellian, with a variance weighted

by the characteristic rates of the various processes indexed by α

$$f(L) \propto \exp\left[-\frac{3L^2}{\sigma_L^2}\right], \quad \sigma_L^2 \equiv \frac{\sum_{\alpha} \tau_{\alpha}^{-1} \sigma_{L,\alpha}^2}{\tau^{-1}}, \quad \tau^{-1} \equiv \sum_{\alpha} \tau_{\alpha}^{-1}. \quad (31)$$

Damping through Electric Dipole Radiation. One process behaves differently from (25), (26): the damping of angular momentum through electric dipole radiation itself. Since the rotational energy is proportional to L^2 and the radiated power is proportional to L^4 , the rate of angular momentum damping scales as L^3 . We may write it in the form

$$\frac{d\langle\Delta\mathbf{L}\rangle}{dt}\Big|_{\text{ed}} = -\frac{L^2\mathbf{L}}{\sigma_L^2\tau_{\text{ed}}}, \quad (32)$$

where we may take the variance σ_L^2 to be that given by (31). This defines τ_{ed} as the characteristic timescale to damp an angular momentum of order σ_L through electric dipole radiation (note that this definition of τ_{ed} is different from the ones adopted in [7, 8], where $\sigma_L^2 = 3IkT_{\text{gas}}$ was specifically used in (32) to define τ_{ed}). Every damping process has in general an associated excitation process, and *vice versa*. In the case of electric dipole radiation, the associated fluctuation in angular momentum is due to absorption of and decays stimulated by microwave photons (dominated by Cosmic Microwave Background (CMB) photons in the diffuse ISM). To our knowledge, this process was only considered in [28] and we shall get back to it in the next section.

Accounting for the damping only for now and including this additional damping into the Fokker-Planck equation, we obtain the solution

$$f(L) \propto \exp\left[-3\frac{L^2}{\sigma_L^2} - \frac{3}{2}\frac{\tau}{\tau_{\text{ed}}}\frac{L^4}{\sigma_L^4}\right]. \quad (33)$$

The most likely angular momentum for this distribution is such that the net drift rate vanishes

$$L_{\text{peak}}^2 = \frac{\sigma_L^2}{3} \frac{2}{1 + \sqrt{1 + (4/3)(\tau/\tau_{\text{ed}})}}. \quad (34)$$

For $\tau_{\text{ed}} \ll \tau$, which is often the case for the smallest grains, the most likely angular momentum results from equilibrium between damping through electric dipole radiation and excitations through other mechanisms and is approximately

$$L_{\text{peak}}^2 \approx \sqrt{\frac{\tau_{\text{ed}}}{\tau}} \sigma_L^2, \quad \tau_{\text{ed}} \ll \tau. \quad (35)$$

In that case, the characteristic damping time at the peak is $\tau_{\text{rot}} = \sqrt{\tau\tau_{\text{ed}}}$. In general, one can define a characteristic damping time as

$$\tau_{\text{rot}} \approx \min[\tau, \sqrt{\tau\tau_{\text{ed}}}] . \quad (36)$$

We can rewrite the peak angular momentum in terms of τ_{rot} as

$$L_{\text{peak}}^2 \approx \frac{\tau_{\text{rot}}}{\tau} \sigma_L^2. \quad (37)$$

5.1.3. Limitation of the Fokker-Planck Approach: Impulsive Torques. The Fokker-Planck equation is a diffusion equation, and its validity is limited to processes that change the angular momentum by small increments. In this section, we formally discuss in which cases it may break down.

Let us now consider some stochastic interaction process α (in practice, collisions with passing ions [10]) with rate τ_{coll}^{-1} , such that the characteristic angular momentum exchanged with a grain at each interaction has variance

$$\langle \Delta L_i \Delta L_j \rangle_\alpha = \frac{\tau_{\text{coll}} \sigma_{L,\alpha}^2}{\tau_\alpha} \delta_{ij}. \quad (38)$$

The diffusion rate for such an interaction is, indeed, formally equal to that of (26). However, this process can only be considered as diffusive if $\langle (\Delta L)^2 \rangle_\alpha \ll L_{\text{peak}}^2$. This translates to the condition

$$\tau_{\text{coll}} \ll \tau_{\text{rot}} \frac{\tau_{\text{coll}}^{-1} \sigma_L^2}{\tau_\alpha^{-1} \sigma_{L,\alpha}^2}. \quad (39)$$

If the process α is the dominant excitation mechanism, $\tau_{\text{coll}}^{-1} \sigma_L^2 = \tau_\alpha^{-1} \sigma_{L,\alpha}^2$ and the condition for the validity of the diffusion approximation is that $\tau_{\text{coll}} \ll \tau_{\text{rot}}$, the characteristic time to change the angular momentum.

The issue of impulsive torques was addressed by Hoang et al. [10]. Instead of solving a Fokker-Planck equation, Hoang et al. start with the *Langevin equation*, of the form

$$dL = \frac{d \langle \Delta L \rangle}{dt} dt + \sqrt{\frac{d \langle (\Delta L)^2 \rangle}{dt}} dq, \quad (40)$$

where dq is a random variable with variance $\langle (dq)^2 \rangle = dt$. They then solve it numerically to obtain $L(t_i)$ at a set of discrete time steps t_i . The distribution function $f(L)$ is then obtained from the histogram of values of L_i after a long enough evolution. In the form (40), the Langevin equation is exactly equivalent to the Fokker-Planck equation, in the sense that it assumes infinitesimal torques. However, it is simple to generalize this treatment to include impulsive torques. First, one draws the interval between two collisions from the Poisson distribution with mean τ_{coll} . Second, an angular momentum $\Delta \mathbf{L}$ is drawn from an isotropic distribution with variance $\langle (\Delta L)^2_{\text{coll}} \rangle$. This method allows to include random impulsive torques in addition to the quasicontinuous torques. We defer the discussion of Hoang et al.'s results to Section 5.4.

5.2. Excitation and Damping Rates for Various Mechanisms.

In this section, we describe the principal mechanisms that excite and damp the grains' rotation. Since the detailed calculations are already worked out in various papers [4, 7–9], here we limit ourselves to giving a semiquantitative description of each process and order of magnitude estimates for the relevant rates. Since the smallest grains are producing the peak of the spinning dust spectrum, all numerical evaluations are normalized to the characteristic radius of coronene, $a \approx 3.5 \text{ \AA}$.

5.2.1. Collisions. Collisional interactions of grains with gas atoms, molecules, or ions are perhaps the most intuitive of angular momentum transfer processes, even though the microphysical details could be very complex (see e.g., the discussion in Section 4.2 of [4]). Impactors with density n_{imp} reach the grain with a rate

$$\tau_{\text{coll}}^{-1} \approx n_{\text{imp}} \pi b_{\text{max}}^2 \bar{v}_{\text{in}}, \quad (41)$$

where πb_{max}^2 is the effective collisional cross-section (b_{max} being the maximal impact parameter for which a collision occurs) and \bar{v}_{in} is the characteristic velocity of the impactors at infinity. As they impact the grain, they stick to its surface, providing there are available adsorption sites. The random angular momentum transferred to the grain has variance

$$\langle (\Delta L)^2 \rangle_{\text{in}} \sim (m_{\text{imp}} b_{\text{max}} \bar{v}_{\text{in}})^2, \quad (42)$$

where m_{imp} is the mass of the impactor.

The attached impactors are ejected from the grain's surface following the absorption of UV photons that heat up small grains to large temperatures (this is the process of *photoevaporation*). Because ions are in general more electronegative than large molecules, they leave the grain surface as neutral species. Here again, they give a random recoil to the grain, leading to

$$\langle (\Delta L)^2 \rangle_{\text{out}} \sim (m_{\text{imp}} a \bar{v}_{\text{out}})^2, \quad (43)$$

where \bar{v}_{out} is the characteristic velocity of ejection, related to the dust grain temperature T_{vib} following thermal spikes by $m_{\text{imp}} \bar{v}_{\text{out}}^2 \sim kT_{\text{vib}}$.

In addition to a random component, ejected particles systematically decrease the angular momentum of the grain: if their ejection velocity is random in the rotating grain's frame, they carry on average an angular momentum

$$\Delta L_{\text{out}} = m_{\text{imp}} a^2 \omega \sim \frac{m_{\text{imp}} a^2}{I} L \sim \frac{m_{\text{imp}}}{m_{\text{grain}}} L, \quad (44)$$

where ω is the rotation rate of the grain and $I \sim m_{\text{grain}} a^2$ is its characteristic moment of inertia. In steady-state, the rate of ejections equals the rate of collisions and therefore

$$\frac{d \langle \Delta L \rangle}{dt} \sim -\tau_{\text{coll}}^{-1} \frac{m_{\text{imp}}}{m_{\text{grain}}} L. \quad (45)$$

From this expression, we see that the characteristic timescale for damping the angular momentum through ejection of colliding gas particles is

$$\tau \sim \frac{m_{\text{grain}}}{m_{\text{imp}}} \tau_{\text{coll}}. \quad (46)$$

Using the definition (29), we see that the characteristic variance in angular momentum that would stem from collisions alone is

$$\begin{aligned} \sigma_L^2 \sim \frac{\tau}{\tau_{\text{coll}}} \langle (\Delta L)^2 \rangle &\sim \frac{I}{m_{\text{imp}} a^2} \left[(m_{\text{imp}} b_{\text{max}} \bar{v}_{\text{in}})^2 \right. \\ &\left. + (m_{\text{imp}} a \bar{v}_{\text{out}})^2 \right] \sim I \left[\frac{b_{\text{max}}^2}{a^2} kT_{\text{in}} + kT_{\text{out}} \right]. \end{aligned} \quad (47)$$

We see that collisions tend to drive the angular momentum distribution to a thermal distribution with temperature

$$T_{L,\text{coll}} \approx \frac{1}{2} \left[\frac{b_{\text{max}}^2}{a^2} T_{\text{in}} + T_{\text{out}} \right]. \quad (48)$$

The maximum impact parameter (or effective cross-section) for incoming particles depends upon the charge state of the grain and impactor. It can easily be determined at an order-of magnitude for a spherically symmetric interaction potential $V(r)$. Requiring energy and angular momentum conservation, we find

$$\left(\frac{b_{\text{max}}}{a} \right)^2 \sim 1 - \frac{V(a)}{E_{\text{in}}} \sim 1 - \frac{V(a)}{kT_{\text{in}}}. \quad (49)$$

In the case of a repulsive interaction $V > 0$, this should be understood as $b_{\text{max}} \approx a$ if $V(a) \ll kT_{\text{in}}$ and 0 in the opposite case.

- (i) For neutral impactors and neutral grains, $b_{\text{max}} = a$.
- (ii) For neutral impactors and charged grains (with charge $Z_g e$), the collisional cross-section can be determined from equating the kinetic energy of the incoming particle to the potential energy of the attractive induced-dipole interaction,

$$V(r) = -\frac{1}{2} \alpha \frac{Z_g^2 e^2}{r^4}, \quad (50)$$

where α is the polarizability of the impactor. Typically, $\alpha \approx 1 \text{ \AA}^3$ so the focusing factor $(b_{\text{max}}/a)^2$ is of order $\sim 1 + (T/10^3 \text{ K})^{-1}$ for $a \approx 3.5 \text{ \AA}$. This potential must also be accounted for when evaluating the escape probability of neutral particles ejected from ionized grains.

- (i) For positively charged impacting ions, the dominant interaction is the attractive Coulomb attraction with negatively charged grains (whenever collisions with ions are relevant, a significant fraction of grains are negatively charged by colliding electrons, so the cation-PAH⁻ collisions are in general dominant over cation-PAH⁰ and cation-PAH⁺)

$$V(r) = -\frac{|Z_i Z_g| e^2}{r}, \quad (51)$$

corresponding to a large focusing factor

$$\left(\frac{b_{\text{max}}}{a} \right)^2 \approx \frac{|Z_i Z_g| e^2}{akT} \approx 50 \left(\frac{a}{3.5 \text{ \AA}} \right)^{-1} \left(\frac{T}{10^3 \text{ K}} \right)^{-1}. \quad (52)$$

Therefore, we see that collisions with ions may overcome collisions with neutrals even for relatively small ionization degrees.

5.2.2. *Plasma Excitation and Drag.* Ions can exchange angular momentum with the grains at a distance, without necessarily colliding with them, by exerting a torque on their permanent electric dipole moment,

$$\frac{d\mathbf{L}}{dt} = \boldsymbol{\mu} \times \mathbf{E} \sim \mu \frac{Z_i e}{r^2}. \quad (53)$$

With the characteristic interaction timescale being $\Delta t \sim b/v$, the variance of the angular momentum change for each interaction event is

$$\langle (\Delta L)^2 \rangle \sim \left(\frac{\mu Z_i e}{bv} \right)^2. \quad (54)$$

Integrating over impact parameters b and velocities of ions v , one obtains the rate of angular momentum diffusion

$$\frac{\langle (\Delta L)^2 \rangle}{dt} \sim n_i (\mu Z_i e)^2 \sqrt{\frac{m_i}{kT}} \ln \Lambda, \quad (55)$$

where the order-unity Coulomb logarithm $\ln \Lambda = \ln(b_{\text{hi}}/b_{\text{lo}})$ appears because of the logarithmic divergence of the integral over impact parameters. In practice, the lower cut-off must be set to the maximal impact parameter leading to a collision (denoted b_{max} in the previous section), in order not to double-count the angular momentum transfer in collisions. The upper cut-off comes from the fact that when the interaction timescale b/v is much larger than the rotation timescale ω^{-1} , the torque along the angular momentum vector averages out to zero [8].

To obtain the damping rate from first principles would require accurate evaluations of the back-reaction of the grain on the ions' trajectories, leading to a small asymmetry between trajectories increasing the magnitude of \mathbf{L} and those decreasing it. However, a powerful theorem, the *fluctuation-dissipation theorem* [26, 29], allows us to very simply evaluate the dissipation rate from the fluctuation rate if the interaction is with a thermal bath. Put simply, excitation and damping must balance in such a way that, if only the thermal process considered was at play, the resulting distribution would also be thermal, of the form $f(L) \propto \exp[-E(L)/kT]$ with the same temperature T as the bath.

In the case of a grain rotating about its axis of greatest inertia, and using the notation of Section 5.1.2, the damping timescale for plasma drag τ_p must therefore be such that

$$3\tau_p \frac{\langle (\Delta L)^2 \rangle}{dt} = \sigma_{L,p}^2 = 6IkT_{\text{gas}}. \quad (56)$$

The case of a wobbling grain is a little more complex, since the temperature for the rotational configuration is set by the internal relaxation process and is in general different from the gas temperature. However, one can use a closely related principle, that of *detailed balance*, to compute the proper damping rate given the tensorial excitation rate. Details can be found in [9].

5.2.3. *Emission of Infrared Photons.* Every time a small dust grain absorbs a UV photon, it gets into a highly excited

vibrational state from which it decays by emitting a cascade of infrared (IR) photons, typically about a hundred per absorbed UV photon. Each one of the emitted IR photons carries one quantum of angular momentum, so its angular momentum squared is $L_\nu^2 = 2\hbar^2$. If photons are emitted isotropically with a energy flux F_ν , the rate of diffusion of angular momentum is then

$$\frac{d\langle(\Delta L)^2\rangle}{dt} = \frac{1}{3}2\hbar^2 \int d\nu \frac{F_\nu}{h\nu}. \quad (57)$$

A ro-vibrational transition from the excited state (ν, J) [ν denoting the vibrational configuration and J the rotational quantum number] to another state $(\nu', J + \Delta J)$ has a transition frequency

$$\nu = \nu_0 - \frac{\omega}{2\pi}\Delta J, \quad (58)$$

where ν_0 is the transition frequency for $(\nu, J) \rightarrow (\nu', J)$ and $\omega = \hbar J/I$ is the angular rotation frequency. Quantum-mechanical transition rates are proportional to the transition frequency cubed. Summing over the three allowed transitions $\Delta J = 0, \pm 1$ (and assuming they have nearly the same matrix elements), the net rate of angular momentum drift relates to the rate of photon emission \dot{N}_ν through

$$\dot{J} = -3\frac{\omega}{2\pi\nu_0} \frac{2}{3}\dot{N}_\nu, \quad (59)$$

which implies, in the case of a grain rotating about its axis of greatest inertia,

$$\frac{d\langle\mathbf{L}\rangle}{dt} = -2\frac{\mathbf{L}}{(2\pi)^2 I} \int d\nu \frac{F_\nu}{\nu^2}. \quad (60)$$

A classical calculation can be found in [7] (with missing factors of two for both damping and excitation rates), [8] (with a missing factor of two for the excitation rate), and [9]. A fully rigorous quantum-mechanical treatment can be found in [4, 8, 12, 28]. They are perfectly equivalent since ISM grains are classical rotators.

The main difficulty in correctly evaluating (57) and (60) is that one must be able to compute the infrared spectrum with high accuracy, especially at long wavelengths (where it is not well constrained by observations).

5.2.4. Electric Dipole Radiation and Absorption of CMB Photons

Damping Rate. A grain emitting electric dipole radiation also radiates away angular momentum. Classically, the radiation reaction torque is given by

$$\frac{d\langle\Delta\mathbf{L}\rangle}{dt}\Big|_{\text{ed}} = -\frac{2}{3c^3}\langle\dot{\boldsymbol{\mu}} \times \ddot{\boldsymbol{\mu}}\rangle, \quad (61)$$

where the averaging is over the quasiperiodic rotation of the grain. For a grain rotating about its axis of greatest inertia, the result is

$$\frac{d\langle\Delta\mathbf{L}\rangle}{dt}\Big|_{\text{ed}} = -\frac{2\mu_\perp^2}{3c^3}\left(\frac{L}{I_3}\right)^3\hat{\mathbf{L}}, \quad T_\omega \rightarrow 0. \quad (62)$$

In the case of a wobbling disk-like grain with completely randomized nutation state, the corresponding damping rate is (assuming $I_3 = 2I_1$ for simplicity) [9]:

$$\frac{d\langle\Delta\mathbf{L}\rangle}{dt}\Big|_{\text{ed}} = -\left[\frac{82\mu_\perp^2}{45c^3} + \frac{32\mu_\parallel^2}{9c^3}\right]\left(\frac{L}{I_3}\right)^3\hat{\mathbf{L}}, \quad T_\omega \rightarrow \infty. \quad (63)$$

The characteristic timescale to damp an angular momentum $L = \sigma_L$ [defined in (32)] is therefore such that

$$\begin{aligned} \tau_{\text{ed}}^{-1} &= \frac{2\mu_\perp^2}{3c^3} \frac{\sigma_L^2}{I_3^3}, \quad T_\omega \rightarrow 0, \\ &= \left[\frac{82\mu_\perp^2}{45c^3} + \frac{32\mu_\parallel^2}{9c^3}\right] \frac{\sigma_L^2}{I_3^3}, \quad T_\omega \rightarrow \infty. \end{aligned} \quad (64)$$

We see that the electric dipole radiation damping timescale is typically about 5 times shorter if the grain is wobbling than when it is rotating primarily about its axis of greatest inertia.

Excitation Rate. The associated excitation mechanism comes from the absorption of CMB photons [28]. For simplicity, here we only consider the case of a grain rotating about its axis of greatest inertia.

Quantum mechanically, the damping of the angular momentum is due to spontaneous decays $J \rightarrow J - 1$, with rate $A_{J,J-1}$, so we may rewrite

$$\frac{d\langle\Delta\mathbf{L}\rangle}{dt}\Big|_{\text{ed}} = -\hbar A_{J,J-1}\hat{\mathbf{L}}. \quad (65)$$

In addition to these spontaneous decays, stimulated decays take place, as well as absorptions of CMB photons. For large J , the net angular momentum change due to these transition nearly cancel out (so the drift is essentially due to spontaneous decays). However, the rate of excitation parallel to the angular momentum axis is (in the limit that $J \gg 1$),

$$\frac{d\langle(\Delta L_\parallel)^2\rangle}{dt}\Big|_{\text{ed}} \approx 2\hbar^2 n_\nu(\nu) A_{J,J-1} = 2\hbar n_\nu(\nu) \left| \frac{d\langle\Delta\mathbf{L}\rangle}{dt}\Big|_{\text{ed}} \right|, \quad (66)$$

where $\nu = L/(2\pi I_3)$ is the transition frequency and

$$n_\nu(\nu) \equiv \frac{1}{e^{h\nu/kT_\nu} - 1} \quad (67)$$

is the photon occupation number at the transition frequency. The CMB temperature is $T_\nu \approx 2.73$ K, corresponding to a frequency $kT_\nu/h \approx 57$ GHz, so the photon occupation number is of order unity at characteristic grain rotation frequencies of a few tens of GHz.

For a characteristic angular momentum $L_{\text{peak}} \sim \sigma_L(\tau_{\text{ed}}/\tau)^{1/4}$ (see discussion in Section 5.1.2), the ratio of excitations by CMB photons to other excitations is of order

$$\frac{d\langle(\Delta L)^2\rangle/dt\Big|_{\text{ed}}}{d\langle(\Delta L)^2\rangle/dt\Big|_{\text{tot}}} \sim \left(\frac{L}{L_{\text{peak}}}\right)^4 \frac{\hbar}{L} n_\nu(\nu). \quad (68)$$

For a coronene grain rotating at 30 GHz, the rotational quantum number is typically $J = L/\hbar \approx 70$. We therefore conclude that excitations by absorptions of and decays stimulated by CMB photons are subdominant, having an effect of the order of a few percent, with a greater importance in regions where grains are slowly rotating.

5.2.5. H_2 Formation and Photoelectric Ejection. Draine and Lazarian [7] considered the random torques exerted on grains as molecular hydrogen is formed on their surface and subsequently ejected and found that this effect was subdominant.

Similarly, the rotational excitation due to photoejection of electrons following UV photon absorption is a subdominant excitation mechanism.

5.3. Dominant Excitation and Damping Mechanisms as a Function of Environment. The relative importance of the various mechanisms described above depends upon the precise environmental conditions, that is, the gas density, temperature, ionization state, and ambient radiation field. Note that these parameters also affect the rotational transition rates through their dependence on *grain charge*. Since the timescale for grains to change charge is in general shorter than the timescale to change the grain angular momentum (though they are in fact comparable for the smallest grains, see Figure 3 of [7]), excitation and damping rates must be averaged over the grain charge distribution function. As a consequence, the electric dipole radiation should not be correlated with indicators of grain charge, such as IR line strength ratios. However, since charging time and rotational decay time are comparable for the smallest grains, in practice there could be some level of correlation. Quantifying this would require solving for $f(L, Z)$ simultaneously, a problem not addressed in the literature.

We list in Table 1 the dominant excitation and damping mechanisms for the smallest grains in the various idealized environments defined in Table 1 of Draine and Lazarian [7]. It can be seen that every mechanism discussed above can be dominant under some conditions, and several may be of comparable importance in some regions. In diffuse ISM phases, electric dipole radiation torque is systematically the dominant damping mechanism, and collisions (in general with ions) are almost always the dominant excitation mechanism.

5.4. Effect of Impulsive Torques. We discussed in Section 5.1.3 how to characterize the importance of impulsive torques. In this section, we discuss specifically the case of the warm ionized medium (WIM), where collisions with ions are frequent and the rotational damping time is short.

The WIM is characterized by a large gas temperature $T \approx 8000$ K and a fully ionized gas at low density, $n_{H^+} \approx 0.1 \text{ cm}^{-3}$. Collisions with ions provide the dominant excitation mechanism. Grains are mostly negatively charged due to the high rate of sticking collisions with high-velocity electrons. For a coronene molecule, the characteristic time between ion collisions and the characteristic rotational damping time at

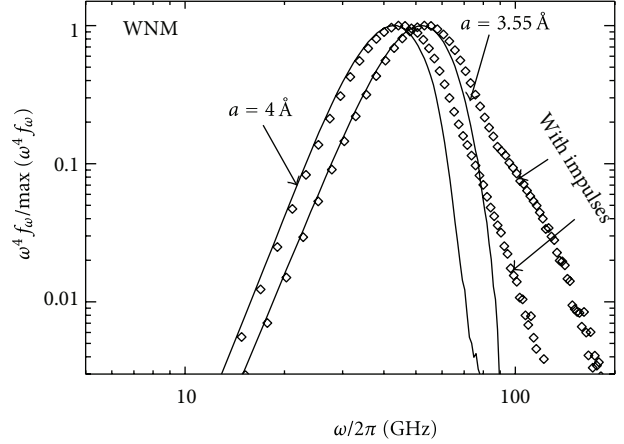


FIGURE 2: Effect of impulsive torques due to collisions with ions in the WIM. Figure reproduced from [10].

the peak angular momentum $\tau_{\text{rot}} = \sqrt{\tau \tau_{\text{ed}}}$ turn out to be comparable, (of order a few years). This indicates that the diffusion approximation is not strictly correct, and impulsive torques may affect the rotational distribution function. Note that Hoang et al. [10] compare τ_{coll} to τ_{ed} (which is the rotational damping time at $L = \sqrt{3IkT} \gg L_{\text{peak}}$ and in this specific case turns out to be equal to our τ_{ed} within a factor of a few), and find $\tau_{\text{ed}} \ll \tau_{\text{coll}}$, by more than two orders of magnitude. The correct comparison should be with τ_{rot} (the actual rotational damping near L_{peak}), which is in fact comparable to τ_{coll} , explaining the marginal importance of the effect near the peak of the distribution function.

Hoang et al. [10] provided a detailed calculation for the effect of impulsive torques by solving a generalized Langevin equation. We reproduce the angular momentum distribution function they obtain in Figure 2. We see that impulsive torques significantly enhance the high-frequency tail of the distribution function, due to grains rotating near the peak frequency being impulsively spun up to larger rotation rates. This enhancement is mostly unobservable because the vibrational emission from large grains dominate at these frequencies. More importantly, Hoang et al. found that the peak emissivity is enhanced by about 23% for the WIM [and only 11% for the warm neutral medium (WNM)], although the peak frequency remains unchanged. This effect is therefore marginally important for the WIM and should be included in precise modeling tools (this effect is not, as yet, included into SPDUST).

5.5. Effect of Grain Wobbling. A more important effect on the spectrum is that of increasing the characteristic internal temperature T_{w} , which makes the grains wobble rather than simply spin about their axis of greatest inertia. It is instructive to make a basic estimate of the effect from simple considerations.

The rotational energy of an axisymmetric grain is given by (13). Depending on the value of T_{w} , the relation between mean rotation energy (averaged over the distribution of

TABLE 1: Dominant excitation and damping mechanisms for the smallest grains considered ($a = 3.5 \text{ \AA}$), as a function of idealized environment (see definitions in Table 1 of [7]). Two or more mechanisms are written down if they are of comparable importance, by decreasing order of importance. “e.d” stands for electric dipole radiation torque.

Phase	DC	MC	RN	PDR
Excitation	coll. (neutrals, ions)	coll. (ions)	IR	coll. (neutrals)
Damping	e.d., coll. (neutrals)	plasma drag	e.d., IR	e.d., IR, coll. (neutrals)
Phase	CNM	WNM	WIM	
Excitation	coll. (ions, neutrals)	coll. (ions, neutrals), IR	coll. (ions)	
Damping	e.d.	e.d	e.d	

nutration angles) and total angular momentum is (assuming $I_3 = 2I_1$)

$$\begin{aligned} L^2 &= 2I_3 \langle E_{\text{rot}} \rangle, \quad T_{\varpi} \longrightarrow 0, \\ L^2 &= \frac{3}{5} \times 2I_3 \langle E_{\text{rot}} \rangle, \quad T_{\varpi} \longrightarrow \infty. \end{aligned} \quad (69)$$

If interacting with a bath of characteristic temperature T_{bath} , grains tend to have a characteristic rotational energy

$$\langle E_{\text{rot}} \rangle \approx kT_{\text{bath}}, \quad (70)$$

regardless of their internal temperature T_{ϖ} . Therefore, the characteristic angular momentum variance (defined in (29)) is

$$\sigma_L^2(T_{\varpi} \longrightarrow \infty) \approx \frac{3}{5} \sigma_L^2(T_{\varpi} \longrightarrow 0). \quad (71)$$

With the excitation rate being roughly independent of the actual angular momentum, we deduce that the damping timescale must scale in a similar fashion as σ_L^2 , that is,

$$\tau(T_{\varpi} \longrightarrow \infty) \approx \frac{3}{5} \tau(T_{\varpi} \longrightarrow 0). \quad (72)$$

We saw previously that the rate of electric dipole damping is about 5 times larger in the wobbling case, at equal angular momentum. The characteristic electric dipole damping timescale defined in (32) is therefore

$$\tau_{\text{ed}}(T_{\varpi} \longrightarrow \infty) \approx \frac{1}{3} \tau_{\text{ed}}(T_{\varpi} \longrightarrow 0). \quad (73)$$

Finally, the most likely angular momentum, in the case $\tau_{\text{ed}} \ll \tau$, was given in (35) and is therefore such that

$$L_{\text{peak}}^4(T_{\varpi} \longrightarrow \infty) \approx \frac{1}{5} L_{\text{peak}}^4(T_{\varpi} \longrightarrow 0). \quad (74)$$

The peak frequency is linear in the peak angular momentum, and at equal angular momentum it is \sim twice as large in the case of a wobbling grain, hence we get

$$\begin{aligned} \nu_{\text{peak}}(T_{\varpi} \longrightarrow \infty) &\approx \frac{2}{5^{1/4}} \nu_{\text{peak}}(T_{\varpi} \longrightarrow 0) \\ &\approx 1.34 \nu_{\text{peak}}(T_{\varpi} \longrightarrow 0). \end{aligned} \quad (75)$$

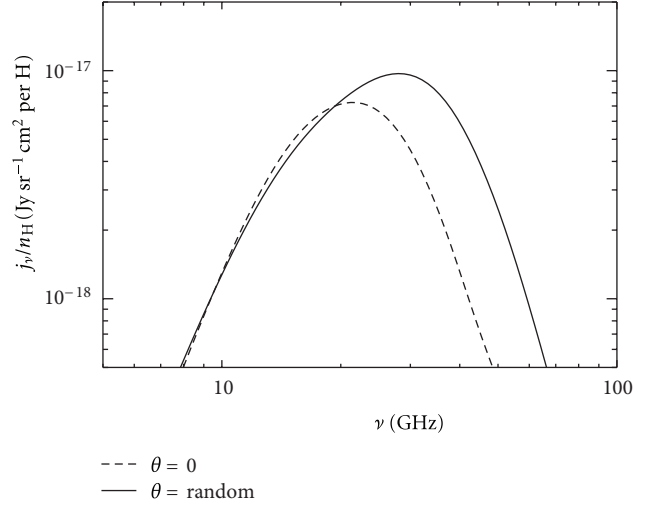


FIGURE 3: Effect of wobbling of axisymmetric grains on the spinning dust emissivity in the WIM environment. The spectra were produced with SPDUST.

The total power radiated scales as the fourth power of the angular momentum and at equal angular momentum are \sim ten as large in the case of a wobbling grain, and therefore the total power radiated is roughly twice as large in the case of wobbling grains.

This heuristic argument is in excellent agreement with results from detailed calculations. We show in Figure 3 the difference in emissivity in the WIM environment. The peak frequency is enhanced by a factor of 1.33 and the total power by a factor of 1.9 for wobbling grains. Hoang et al. [10] studied the intermediate case where the internal relaxation temperature T_{ϖ} is set to a finite value, and obtain similar results as they vary it from low values to large values. A similar heuristic argument could be made to estimate the peak frequency and total radiated power as a function of T_{ϖ} .

Hoang et al. [11] also studied the effect of triaxiality. They found an *additional* enhancement of the peak frequency and total power by up to the same factors (\sim 30% and 2, resp.) for a large internal relaxation temperature and highly elliptical grains.

One cannot therefore neglect the fact that small PAHs are likely to be somewhat triaxial. The difficulty in properly

accounting for this is that the exact distribution of ellipticities is largely unknown.

6. Concluding Remarks

In this paper we have reviewed the current status of spinning dust modeling, and tried to summarize the recent advances in this field since the seminal papers of Draine and Lazarian [8–12]. In addition to refined calculations, the most important new effect accounted for recently is grain wobbling following frequent absorption of UV photons. The rotational dynamics of small grains of various shapes is now believed to be well understood, even if there remain uncertainties and simplifications in the implemented models.

The accuracy of theoretical predictions remains mostly limited by our poor knowledge of the properties of small grains, namely, their dipole moments, shapes and sizes, and their overall abundance, about which other observations give little information. This uncertainty can be turned into an asset, as one could potentially use the observed spinning dust emission (assuming it is the dominant AME process at tens of GHz frequencies) to constrain properties of small grains.

Such a procedure can, however, only be accomplished if environmental parameters are very well known. Indeed, the gas density, temperature, and ionization state as well as the ambient radiation field all affect the rotational distribution function of small grains in nontrivial ways. In addition, the actual observable, the emissivity, depends upon the properties of the medium along the line of sight, and an accurate modeling of the spatial properties of the environment is also required. Unless the properties of the environment are well understood, it seems very difficult to extract dust grain parameters from observed spectra, due to the important degeneracies that are bound to be present for such a large parameter space.

The view of the author is that significant advances in the field would be possible if several regions of the ISM were put under the scrutiny, not only of radio telescopes, but also of instruments at other wavelengths, in order to determine their detailed properties as much as possible and get rid of the uncertainties related to environmental dependencies.

Finally, let us mention another potentially interesting avenue to probe the properties of emitting grains, namely, the high-resolution *spectral properties* of the spinning dust spectrum. Indeed, even if the PAHs are classical rotators with large rotational quantum numbers, the line spacing remains relatively large for the smallest molecules (for coronene, e.g., rotational lines are spaced by about 0.33 GHz). A large number of different grains are probably present in the ISM, which results in a dense, quasismooth forest of lines. However, grains with a few tens of atoms might only be present in a limited number of stable configurations, or there might only be a fraction of possible grain configurations that lead to a significant electric dipole moment. If this were the case, radio observations with a narrow bandwidth should allow to detect some amount of bumpiness on top of a smooth spectrum. Even upper limits on the variability of the spectrum in the frequency domain should allow one to get some handle on

the properties of small grains. A quantitative analysis of this issue will be the subject of future work.

Acknowledgments

The author thanks Bruce Draine and Alexander Lazarian for providing detailed comments on this paper, as well as Rashid Sunyaev for his hospitality and generous financial support at the Max Planck Institute for Astrophysics during the part of summer 2012, where and when this paper was written. The author is supported by the National Science Foundation Grant no. AST-080744 and the Frank and Peggy Taplin Membership at the Institute for Advanced Study.

References

- [1] W. C. Erickson, “A Mechanism of non-thermal radio-noise origin,” *Astrophysical Journal*, vol. 126, article 480, 1957.
- [2] F. Hoyle and N. C. Wickramasinghe, “Radio waves from grains in HII regions,” *Nature*, vol. 227, no. 5257, pp. 473–474, 1970.
- [3] A. Ferrara and R. J. Dettmar, “Radio-emitting dust in the free electron layer of spiral galaxies: testing the disk/halo interface,” *Astrophysical Journal Letters*, vol. 427, no. 1, pp. 155–159, 1994.
- [4] D. Rouan, A. Leger, A. Omont, and M. Giard, “Physics of the rotation of a PAH molecule in interstellar environments,” *Astronomy & Astrophysics*, vol. 253, pp. 498–514, 1992.
- [5] E. M. Leitch, A. C. S. Readhead, T. J. Pearson, and S. T. Myers, “An anomalous component of galactic emission,” *Astrophysical Journal Letters*, vol. 486, no. 1, pp. L23–L26, 1997.
- [6] B. T. Draine and A. Lazarian, “Diffuse galactic emission from spinning dust grains,” *Astrophysical Journal Letters*, vol. 494, no. 1, pp. L19–L22, 1998.
- [7] B. T. Draine and A. Lazarian, “Electric dipole radiation from spinning dust grains,” *Astrophysical Journal Letters*, vol. 508, no. 1, pp. 157–179, 1998.
- [8] Y. Ali-Haïmoud, C. M. Hirata, and C. Dickinson, “A refined model for spinning dust radiation,” *Monthly Notices of the Royal Astronomical Society*, vol. 395, no. 2, pp. 1055–1078, 2009.
- [9] K. Silsbee, Y. Ali-Haïmoud, and C. M. Hirata, “Spinning dust emission: the effect of rotation around a non-principal axis,” *Monthly Notices of the Royal Astronomical Society*, vol. 411, no. 4, pp. 2750–2769, 2011.
- [10] T. Hoang, B. T. Draine, and A. Lazarian, “Improving the model of emission from spinning dust: effects of grain wobbling and transient spin-up,” *Astrophysical Journal Letters*, vol. 715, no. 2, pp. 1462–1485, 2010.
- [11] T. Hoang, A. Lazarian, and B. T. Draine, “Spinning dust emission: effects of irregular grain shape, transient heating, and comparison with wilkinson microwave anisotropy probe results,” *Astrophysical Journal*, vol. 741, article 87, 2011.
- [12] N. Ysard and L. Verstraete, “The long-wavelength emission of interstellar PAHs: characterizing the spinning dust contribution,” *Astronomy and Astrophysics*, vol. 509, no. 1, article A12, 2010.
- [13] N. Ysard, M. Juvela, and L. Verstraete, “Modelling the spinning dust emission from dense interstellar clouds,” *Astronomy & Astrophysics*, vol. 535, article A89, 2011.
- [14] A. G. G. M. Tielens, “Interstellar polycyclic aromatic hydrocarbon molecules,” *Annual Review of Astronomy and Astrophysics*, vol. 46, pp. 289–337, 2008.

- [15] A. Li and I. Mann, “Nanodust in the interstellar medium in comparison to the solar system,” in *Astrophysics and Space Science Library*, I. Mann, N. Meyer-Vernet, and A. Czechowski, Eds., vol. 385 of *Astrophysics and Space Science Library*, p. 5, 2012.
- [16] B. T. Draine and A. Li, “Infrared emission from interstellar dust. I. Stochastic heating of small grains,” *Astrophysical Journal Letters*, vol. 551, no. 2, pp. 807–824, 2001.
- [17] A. Li and B. T. Draine, “Infrared emission from interstellar dust. II. The diffuse interstellar medium,” *Astrophysical Journal Letters*, vol. 554, no. 2, pp. 778–802, 2001.
- [18] J. C. Weingartner and B. T. Draine, “Dust grain-size distributions and extinction in the Milky Way, large Magellanic Cloud, and small Magellanic Cloud,” *Astrophysical Journal Letters*, vol. 548, no. 1, pp. 296–309, 2001.
- [19] A. Li and B. T. Draine, “On ultrasmall silicate grains in the diffuse interstellar medium,” *Astrophysical Journal Letters*, vol. 550, no. 2, pp. L213–L217, 2001.
- [20] D. M. Hudgins, C. W. Bauschlicher, and L. J. Allamandola, “Variations in the peak position of the $6.2\ \mu\text{m}$ interstellar emission feature: a tracer of N in the interstellar polycyclic aromatic hydrocarbon population,” *Astrophysical Journal*, vol. 632, no. 1 I, pp. 316–332, 2005.
- [21] E. M. Purcell, “Suprathermal rotation of interstellar grains,” *Astrophysical Journal*, vol. 231, pp. 404–416.
- [22] A. Lazarian and M. Efroimsky, “Inelastic dissipation in a freely rotating body: application to cosmic dust alignment,” *Monthly Notices of the Royal Astronomical Society*, vol. 303, no. 4, pp. 673–684, 1999.
- [23] L. Sironi and B. T. Draine, “Polarized infrared emission by polycyclic aromatic hydrocarbons resulting from anisotropic illumination,” *Astrophysical Journal Letters*, vol. 698, no. 2, pp. 1292–1300, 2009.
- [24] A. Lazarian, “Gold-type mechanisms of grain alignment,” *Monthly Notices of the Royal Astronomical Society*, vol. 268, no. 3, article 713, 1994.
- [25] A. Lazarian and W. G. Roberge, “Barnett relaxation in thermally rotating grains,” *Astrophysical Journal Letters*, vol. 484, no. 1, pp. 230–237, 1997.
- [26] R. D. Blandford and K. S. Thorne, Applications of Classical-Physics (unpublished).
- [27] R. V. Jones and L. Spitzer Jr., “Magnetic alignment of interstellar grains,” *Astrophysical Journal*, vol. 147, article 943.
- [28] Y. Ali-Haimoud, *A new spin on primordial hydrogen recombination and a refined model for spinning dust radiation [Ph.D. thesis]*, California Institute of Technology, 2011.
- [29] H. B. Callen and T. A. Welton, “Irreversibility and generalized noise,” *Physical Review*, vol. 83, no. 1, pp. 34–40, 1951.

Research Article

Spectrum of the Anomalous Microwave Emission in the North Celestial Pole with *WMAP* 7-Year Data

Anna Bonaldi¹ and Sara Ricciardi²

¹Jodrell Bank Centre for Astrophysics, School of Physics and Astronomy, the University of Manchester, Alan Turing Building, Oxford Road, Manchester M13 9PL, UK

²INAF-IASF Bologna, Via Gobetti 101, Bologna, Italy

Correspondence should be addressed to Anna Bonaldi, anna.bonaldi@manchester.ac.uk

Received 30 July 2012; Accepted 3 December 2012

Academic Editor: Clive Dickinson

Copyright © 2012 A. Bonaldi and S. Ricciardi. This is an open access article distributed under the Creative Commons Attribution License, which permits unrestricted use, distribution, and reproduction in any medium, provided the original work is properly cited.

We estimate the frequency spectrum of the diffuse anomalous microwave emission (AME) on the North Celestial Pole (NCP) region of the sky with the Correlated Component Analysis (CCA) component separation method applied to *WMAP* 7-yr data. The NCP is a suitable region for this analysis because the AME is weakly contaminated by synchrotron and free-free emission. By modeling the AME component as a peaked spectrum we estimate the peak frequency to be 21.7 ± 0.8 GHz, in agreement with previous analyses which favored $\nu_p < 23$ GHz. The ability of our method to correctly recover the position of the peak is verified through simulations. We compare the estimated AME spectrum with theoretical spinning dust models to constrain the hydrogen density n_{H} . The best results are obtained with densities around $0.2\text{--}0.3\text{ cm}^{-3}$, typical of warm ionised medium (WIM) to warm neutral medium (WNM) conditions. The degeneracy with the gas temperature prevents an accurate determination of n_{H} , especially for low hydrogen ionization fractions, where densities of a few cm^{-3} are also allowed.

1. Introduction

The anomalous microwave emission (AME) component is highly correlated with the far infrared dust emission [1–10] and is believed to be the electric dipole radiation from small spinning dust grains [11]. Spinning dust models predict a peaked spectrum ranging 10–150 GHz depending on the local physical conditions [12, 13]. Probing the peak of the emission enables us to compare models with observations and is the best way to distinguish the AME from synchrotron emission and free-free emission, both having a power-law spectrum.

The AME has been studied in individual dust clouds associated with reflection nebulae, molecular clouds, photo-dissociation regions, and HII regions [14, 15]. The best examples of peaked AME spectra are probably the Perseus and ρ Ophiuchi molecular clouds, which have been probed with high accuracy thanks to the availability of many different datasets. In these regions the derived peak is at ~ 30 GHz [14].

The study of the AME in more diffuse regions essentially becomes a component separation problem, which is often complicated by the lack of low-frequency data covering large sky areas. Diffuse dust-correlated emission has been detected with COBE-DMR [2] and *WMAP* data [4, 7, 16–18]; however the details of the spectrum are still unclear. Template-fitting analyses show that the dust-correlated emission between 20 and 60 GHz is well described by a power-law [2, 4, 7, 18]. Given the error bars, a peaked spectrum is not ruled out, but a low peak frequency (< 23 GHz) is favored. Alternatively, the observed spectrum could result from the superposition of multiple peaked components. The component separation analysis done by [17] found that a peaked AME model gives better results in terms of CMB cleaning, however no estimation of the AME peak frequency was attempted.

In this work we address the estimation of the peak frequency of the diffuse AME on *WMAP* 7-yr data complemented by ancillary data with the Correlated Component Analysis (CCA, [19]) component separation method. We

consider the North Celestial Pole (NCP) region of the sky, centered on Galactic coordinates $(l, b) \sim (125^\circ, 25^\circ)$. As already noted by [4], this region of the sky is particularly suited for this analysis since there is significant thermal and anomalous dust emission, while synchrotron emission and free-free emission (traced by the 408 MHz from [20] and the H α map from [21]) are faint.

2. Description of the Method

In the following we describe the principles of operation of the harmonic-domain CCA; for further details we refer the reader to [19]. The CCA [19, 22] exploits second-order statistics to estimate the frequency scaling of the components from the statistics of data and noise. For each position on the sky (each pixel) we write our data model as

$$\mathbf{x}(r) = [\mathbf{B} * \mathbf{H}\mathbf{s}](r) + \mathbf{n}(r), \quad (1)$$

where \mathbf{s} is a vector whose elements contain the different components (CMB, free-free emission, synchrotron emission, thermal dust emission, AME); \mathbf{x} and \mathbf{n} are vectors too, each element containing, respectively, the data and the instrumental noise for each frequency. The diagonal matrix \mathbf{B} contains the instrumental beams for all frequency channels and $*$ denotes convolution. The matrix \mathbf{H} is called the mixing matrix and it contains the frequency scaling of the components for all the considered frequencies.

By translating (1) in the harmonic domain, the convolution becomes a multiplication and the data model becomes a linear mixture. For each transformed mode (ℓ) we can write

$$\mathbf{X}(\ell) = \tilde{\mathbf{B}}(\ell)\mathbf{H}\mathbf{S}(\ell) + \mathbf{N}(\ell), \quad (2)$$

where \mathbf{X} , \mathbf{S} , and \mathbf{N} are the transforms of \mathbf{x} , \mathbf{s} , and \mathbf{n} , respectively, and $\tilde{\mathbf{B}}$ is the transform of the matrix \mathbf{B} . The cross-spectra of the data $\tilde{\mathbf{C}}_{\mathbf{x}}(\ell)$, sources $\tilde{\mathbf{C}}_{\mathbf{s}}(\ell)$ and noise, $\tilde{\mathbf{C}}_{\mathbf{n}}(\ell)$, are related by

$$\tilde{\mathbf{C}}_{\mathbf{x}}(\ell) - \tilde{\mathbf{C}}_{\mathbf{n}}(\ell) = \tilde{\mathbf{B}}(\ell)\mathbf{H}\tilde{\mathbf{C}}_{\mathbf{s}}(\ell)\mathbf{H}^T\tilde{\mathbf{B}}^\dagger(\ell), \quad (3)$$

where the dagger superscript denotes the adjoint matrix.

The left-hand side of (3) can be estimated from the data for a suitable set of spectral bins $\hat{\ell}$; this is used by CCA to estimate the mixing matrix and the source cross-spectra on the right-hand side of the equation. Due to the scaling ambiguity of the problem, the mixing matrix is normalized at a reference frequency. To reduce the number of unknowns, the mixing matrix is parametrized through a parameter vector \mathbf{p} (such that $\mathbf{H} = \mathbf{H}(\mathbf{p})$), by adopting suitable fitting relations for the spectra of the astrophysical components (as detailed in the next section).

By using two-dimensional discrete Fourier transforms it is possible to apply the harmonic-domain CCA to square sky patches. This approach is advisable as the mixing matrix varies on the sky. The HEALPix ([24]) data on the sphere are projected on the plane tangential to the center of the patch and re-gridded with a suitable number of bins in order to correctly sample the original resolution. The patch

size is obtained as a trade-off between the need of having uniform spectral properties of the foregrounds and enough statistics for a robust computation of the auto- and cross-spectra of the data. In the present analysis we use a patch size of $30^\circ \times 30^\circ$. By using higher resolution data (e.g., *Planck* data) it is possible to reduce the patch size by carrying the analysis up to a larger multipole. We analyzed the sky patch centered on $(l, b) = (124^\circ, 26^\circ)$ (shown in Figure 1) and verified the stability of the results for a sample of patches shifted in latitude and longitude up to 10° .

3. Description of the Analysis

We used the following datasets:

- (i) *WMAP* 7-yr K, Ka, Q, V, and W bands [25]. All maps have been used at the original resolution except the K band, which has been smoothed to 1° resolution to reduce the effect of beam asymmetry;
- (ii) 408 MHz map [20] to trace the synchrotron component;
- (iii) predicted free-free emission at 23 GHz based on the H α map by [21] corrected for dust absorption with the E(B-V) map by [26] assuming $f_d = 0.3$;
- (iv) predicted dust emission at 94 GHz by [23].

The different resolution of the data maps is accounted for with the beam matrix $\tilde{\mathbf{B}}$ in (3). In particular, the beams are deconvolved for the mixing matrix estimation. The noise properties for the *WMAP* maps have been computed by simulating different noise realizations starting from the input N_{obs} maps and σ_0 values. For the maps used as foreground templates (408 MHz map, 23 GHz free-free map, and 94 GHz dust prediction) we assumed a Gaussian noise at the 10% level, which is much higher than the instrumental noise. This extra noise mimics the error on the template as a tracer of the true component, the 10% level being indicative. We verified, however, that the results are not sensitive to the exact value assumed. We modeled the data as a mixture of five components: CMB, synchrotron emission, thermal dust emission, free-free emission, and AME. Each frequency map contributes five elements to the mixing matrix, one for each component. The synchrotron, free-free and dust templates are used as frequency channels having only one mixing matrix entry, that of the corresponding component, different from zero.

It is worth noting that, compared with previous work, we are not assuming correlation between the AME and thermal dust emission and we are not exploiting any template for the AME. Though the AME and the thermal dust emission are significantly correlated, the correlation is not supposed to be perfect, as, according to spinning dust models, the AME traces the distribution of smaller dust grains (PAHs). Indeed, the intensity ratio of AME and thermal dust is found to vary in the sky by a factor of ~ 2 (e.g., [4]).

We estimated the frequency spectrum of the AME while assuming the spectra of the other components to be known. For CMB we used the usual black-body law with temperature

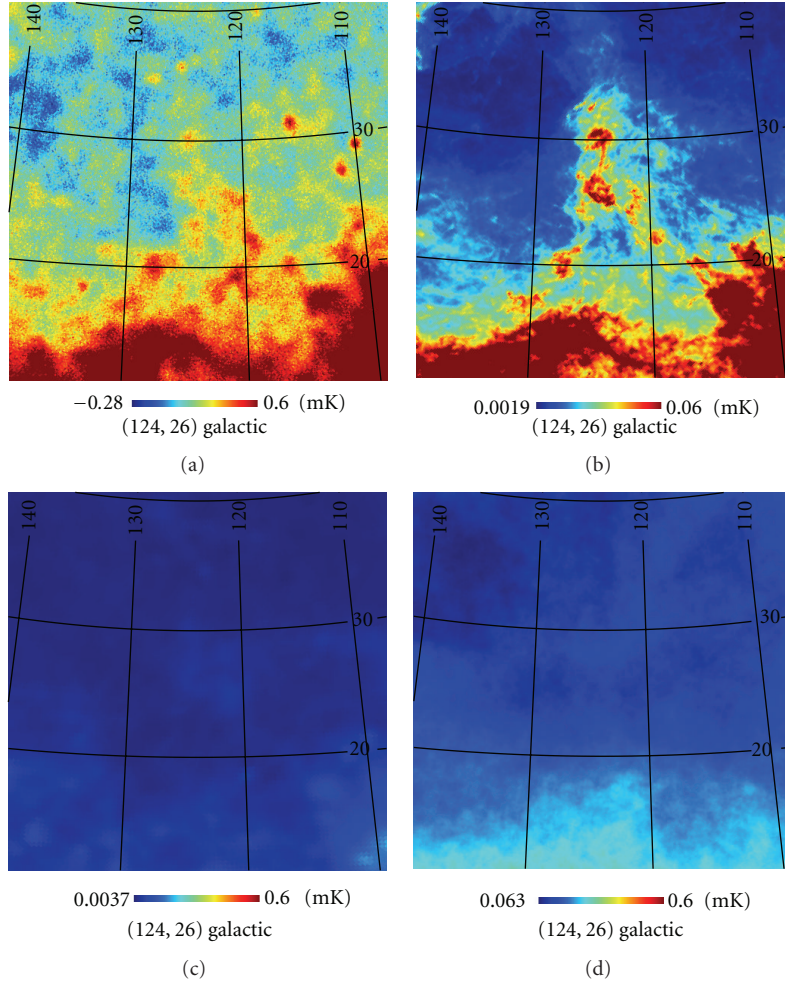


FIGURE 1: Maps of the region of interest. *WMAP* K band (a), 94 GHz dust prediction (b, [23]). free-free (c) and synchrotron (d) predictions at 23 GHz based on the $H\alpha$ map ([21]) and the 408 MHz map ([20]) assuming a spectral index $\beta_s = -2.9$.

of 2.726 K ([27]); for free-free we used the model $T_{\text{RJ,ff}}(\nu) \propto G \times (\nu/10)^{-2}$ where $G = 3.96 (T_4)^{0.21} (\nu/40)^{-0.14}$ is the Gaunt factor, which is responsible for the departure from a pure power-law behavior, and $T_4 = 0.7$ is the electron temperature T_e in units of 10^4 K. The thermal dust emission has been modeled as a grey-body with temperature $T_d = 18$ K and spectral index $\beta_d = 1.7$. This is consistent with the 1-component dust model by [23]; *Planck* data, extending the observations up to 857 GHz, will allow a refinement of this model. For synchrotron we assumed a power-law scaling with spectral index $\beta_s = -2.9$.

For the AME we used the parametric relation proposed by [17]

$$\log T_{\text{RJ,ame}}(\nu) \propto \left(\frac{m_{60} \log \nu_p}{\log(\nu_p/60)} + 2 \right) \log \nu + \frac{m_{60} (\log \nu)^2}{2 \log(\nu_p/60)}, \quad (4)$$

which is a parabola in the $\log(\nu) - \log(S)$ plane parametrized in terms of peak frequency ν_p and slope at 60 GHz m_{60} . The CCA solves for the two parameters m_{60} and ν_p , so the accuracy of the estimation of the AME peak frequency ν_p is

related to the ability of the parametric relation to reproduce the true spectrum. We verified, however, that this parametric model can fit a wide range of spinning dust spectra. This is shown in Figure 2, comparing spinning dust spectra produced with the SpDust [12, 28] code with the results of the fit of (4) obtained by minimizing the χ^2 for the set of frequencies considered in this work. The physical models that we consider are: warm neutral medium (WNM), cold neutral medium (CNM), warm ionised medium (WIM), and molecular cloud (MC). In general, the fits are accurate up to 61 GHz, while at 94 GHz the parametric relation may not be able to reproduce the input spectra in detail. This is a consequence of fitting complex spectra with only a few parameters, the fit being less accurate where the AME is weaker. The best-fit parameters that we obtain, reported in Table 1, vary significantly from one input model to another.

4. Test on Simulated Data

We simulated *WMAP* 7-yr data by assuming monochromatic band-passes centered at the central frequency of the realistic

TABLE 1: Parameters for the spectra in Figure 2. The SpDust input parameters are as follows: the total hydrogen number density n_{H} , the gas temperature T , the intensity of the radiation field relative to the average interstellar radiation field χ , the hydrogen ionization fraction $x_{\text{H}} = n_{\text{H}^+}/n_{\text{H}}$, and the ionized carbon fractional abundance $x_{\text{C}} = n_{\text{C}^+}/n_{\text{H}}$. We also report the CCA spectral parameters ν_p , m_{60} (4).

Model name	n_{H} [cm^{-3}]	T [K]	χ	x_{H}	x_{C}	ν_p	m_{60}
WNM	0.4	6000	1.00	0.10	0.0003	24.34	7.64
CNM	30.0	100	1.00	0.0012	0.0003	29.26	5.31
WIM	0.1	8000	1.00	0.99	0.001	27.64	5.99
MC	300	20	0.01	0.0	0.0001	38.13	2.23

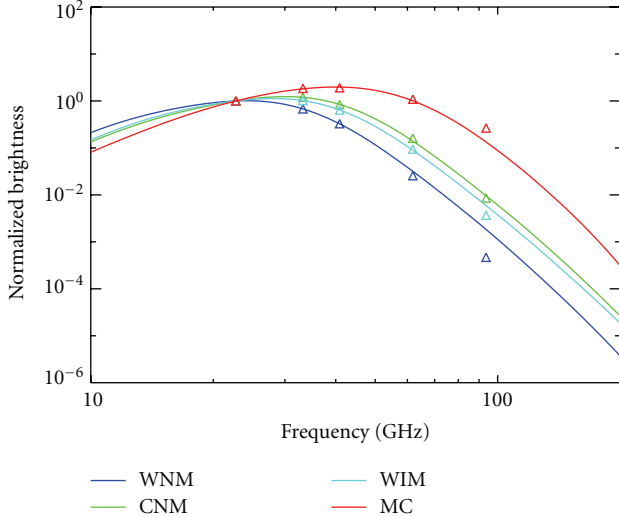


FIGURE 2: Theoretical spinning dust models produced with SpDust (solid lines) and fitted with CCA parametric model (triangles, same color of the model). Input SpDust parameters and best-fit parameters for the CCA model are provided in Table 1.

bands, Gaussian beams at the nominal values, Gaussian noise generated according to realistic (spatially varying) RMS. Our model of the sky consists of the following components:

- (i) CMB emission constrained by the best-fit power spectrum model to *WMAP* 7-yr;
- (ii) synchrotron emission given by [20] scaled in frequency with a power-law model with a spatially varying synchrotron spectral index β_s as modeled by [29];
- (iii) free-free component modeled by the $\text{H}\alpha$ map of [21] corrected for dust absorption with the E(B-V) map from [26] with $f_d = 0.3$ and scaled in frequency with a power-law with fixed spectral index of -2.14 ;
- (iv) thermal dust emission modeled with the $100 \mu\text{m}$ map from [26] scaled in frequency with the best-fit model by [23] which consists of two grey-body laws having different temperatures and emissivity indices;
- (v) AME emission modeled by the E(B-V) map from [26] with intensity at 23 GHz calibrated on the results by [4] for average intermediate-latitude conditions and scaled according to SpDust models.

It is worth noting that this sky model is more complex than the spectral model assumed in the component separation. The synchrotron spectral index is spatially varying and both the thermal dust AME spectra, though spatially constant, are not generated with the CCA parametric models. This has been done purposely, to reflect a more realistic situation. To test the ability of our pipeline to recover the AME spectrum in different situations, we adopted two SpDust models for the AME: one peaking at 26 GHz and the other peaking at 19 GHz.

We performed an estimate of the AME spectrum on the simulated data following the same procedure applied to the real data. The results are presented in Figure 3. For AME peaking at 26 GHz the recovery of the spectrum is very accurate; the result on the peak frequency is $\nu_p = 26.5 \pm 0.5$. The accuracy of the estimation is helped by the weak synchrotron and free-free contamination in this region of the sky (in a more general case the error on ν_p would be of a few GHz). With the AME peaking at 19 GHz the errors increase, but the recovery of the spectrum is still satisfactory; we obtain $\nu_p = 18.5 \pm 1.5$. Our pipeline is able to distinguish very clearly between the two input models and to correctly estimate the peak frequency of the AME in both cases.

5. Results

The results for the AME spectrum on the NCP are shown in Figure 4; the estimated peak frequency is $\nu_p = 21.7 \pm 0.8$. The diamonds with error bars are the AME mixing matrix elements at *WMAP* frequencies and related uncertainties derived from the results on ν_p and m_{60} .

By comparing these data points with theoretical models produced with SpDust we can constrain the physical properties of the medium with the hypothesis of spinning dust emission. Some relevant parameters of the SpDust code are: hydrogen number density n_{H} (cm^{-3}); gas temperature T (K); intensity of the radiation field with respect to average Galactic conditions, χ , and hydrogen ionization fraction, x_{H} . Advanced parameters describe the dust grains and define the abundance of other elements.

The hydrogen density n_{H} is sensitive to the position of the peak and in general to the shape of the spectrum in the considered frequency range. It is also degenerate with other parameters, in particular the gas temperature T . We investigated this degeneracy by sampling the 2-dimensional $n_{\text{H}}-T$ space with a grid approach while conditioning the remaining parameters. For each point in the parameter space we computed the likelihood as $\Lambda = \exp(-\chi^2/2)$ where χ^2

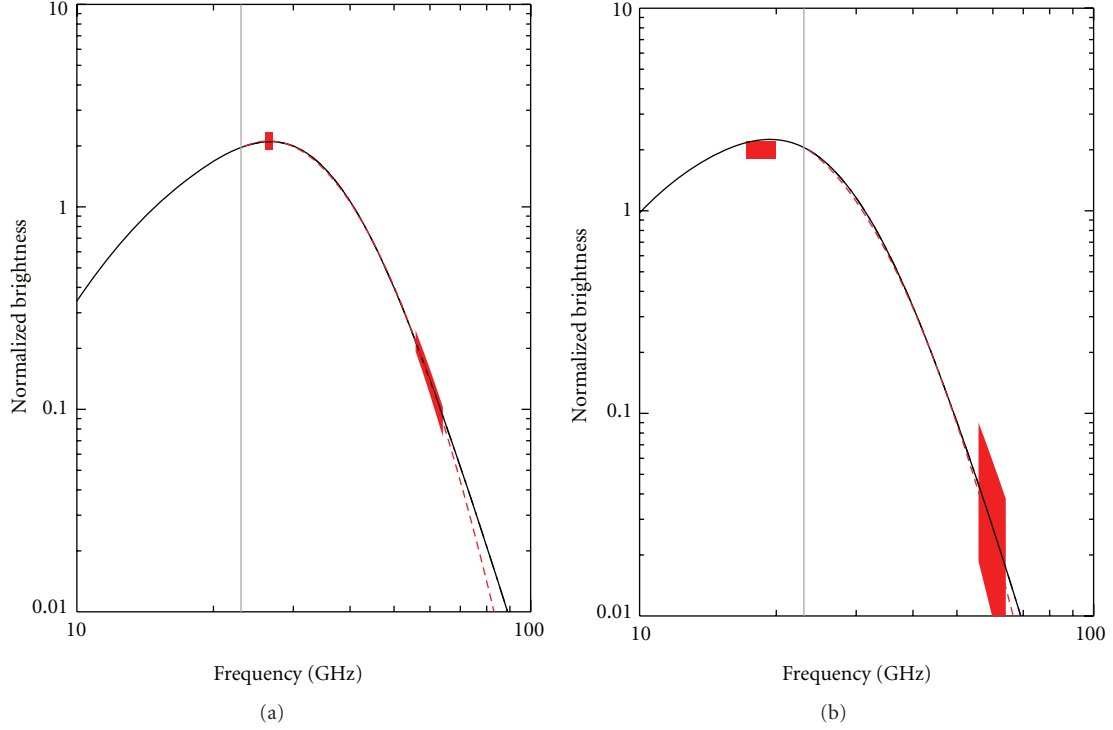


FIGURE 3: Comparison of true input AME spectra (black solid lines) with CCA estimates (red dashed lines) for two AME models, one peaking at 26 GHz (a) and one at 19 GHz (b). The red shaded areas show the recovered ν_p and m_{60} with 1σ error bar. The results for the peak frequency are $\nu_p = 26.5 \pm 0.5$ and $\nu_p = 18.5 \pm 1.5$ for (a) and (b), respectively. The grey vertical lines indicate the frequency of 23 GHz which sets the limit of our data.

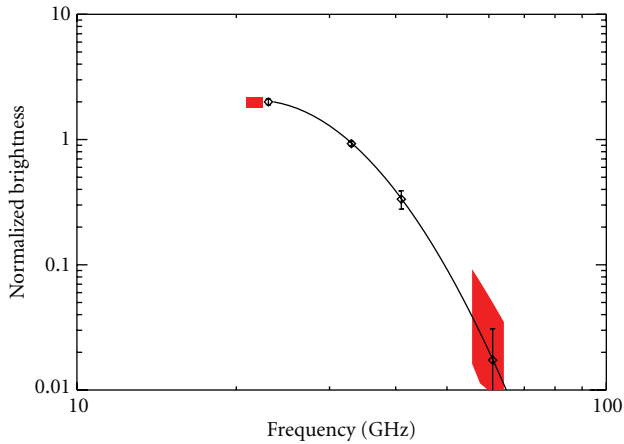


FIGURE 4: Best-fit AME model (black line) and results in terms of ν_p and m_{60} considering 1σ uncertainties (red areas). The peak frequency results $\nu_p = 21.7 \pm 0.8$. Diamonds with error bars are the results in terms of normalized intensity at WMAP bands and related uncertainties.

is the standard chi-square. In computing the χ^2 we did not consider the 94 GHz data point, which could be biased, as verified through simulations (see Section 4). We repeated the likelihood estimation for different choices of the parameters x_H and χ (varying all those parameters simultaneously would be computationally too demanding). As the CCA outputs are

TABLE 2: Statistics for n_H marginalized over T corresponding to the results of Figure 5.

x_H	χ	n_H	Δn_H^-	Δn_H^+
0.001	1	0.3	0.1	0.9
0.01	1	0.3	0.1	0.7
0.1	1	0.25	0.09	0.07
0.001	0.1	0.4	0.1	1.2

in normalized units, we compared both the model and the data after scaling each of them by the sum of the intensities at 23, 33, 41 and 61 GHz.

The results of the n_H - T parameter estimation are shown in Figure 5. The colored lines show the likelihoods for n_H for different values of T as detailed in the legend, while the black lines show the likelihood for n_H marginalized over T in the range 100–10000 K. Different panels correspond to different choices for the other parameters: $x_H = 0.001$, $\chi = 1$, on the top left; $x_H = 0.001$, $\chi = 0.1$, on the top right; $x_H = 0.01$, $\chi = 1$, on the bottom left; and $x_H = 0.1$, $\chi = 1$ on the bottom right. The marginalized statistics for n_H are reported in Table 2 (Δn_H^- and Δn_H^+ being the lower and upper 1σ error on n_H). The n_H - T degeneracy weakens the constraint on n_H in particular on the high-density side of the distribution. The degeneracy decreases with increasing hydrogen ionization fraction.

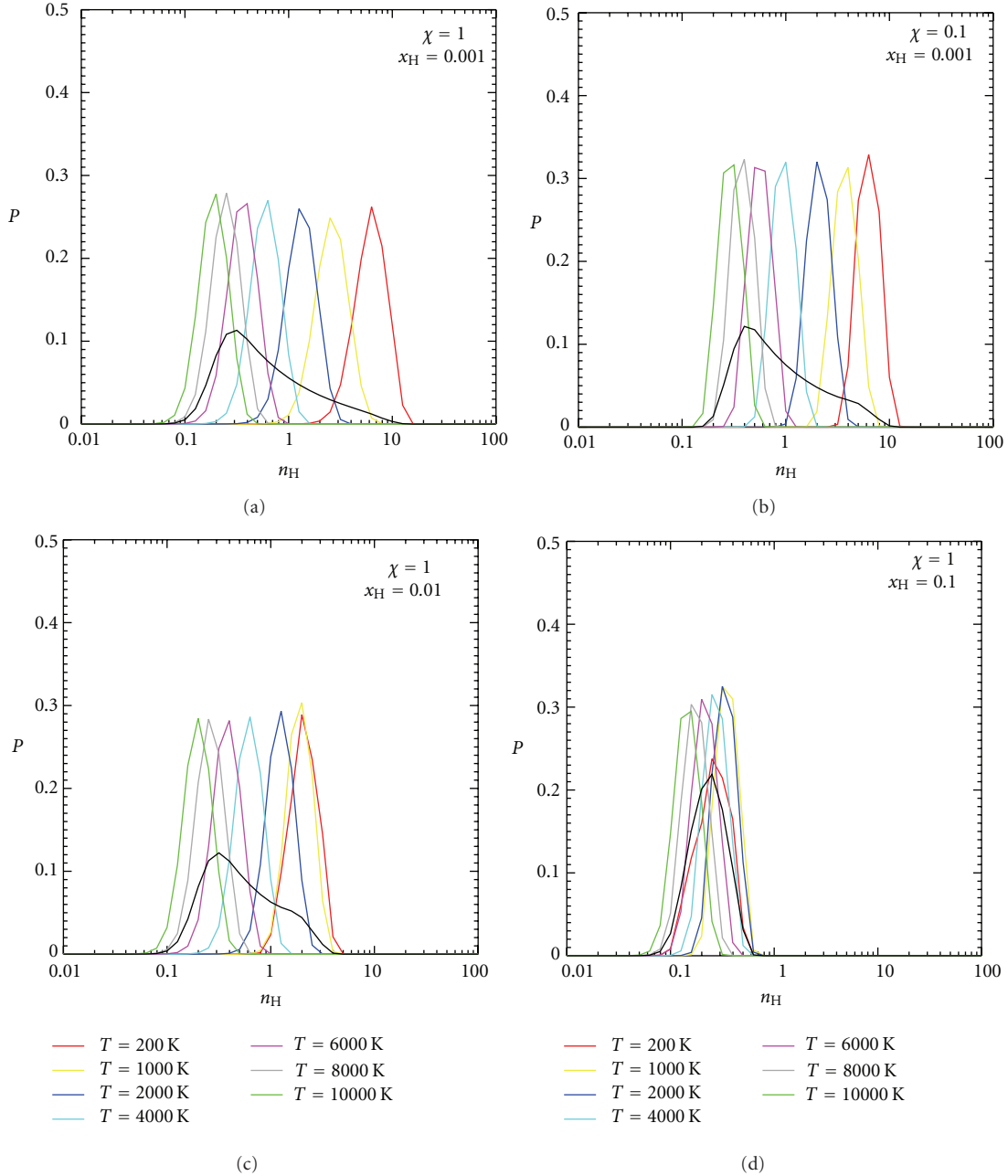


FIGURE 5: Colored lines: likelihoods for n_{H} for different values of T as detailed in the legend; black line: likelihood for n_{H} marginalized over T . (a) $x_{\text{H}} = 0.001$, $\chi = 1$; (b) same as (a) with $\chi = 0.1$; (c, d): same as (a) with $x_{\text{H}} = 0.01$ (c) and $x_{\text{H}} = 0.1$ (d).

The best results are obtained for densities of $0.2\text{--}0.4\text{ cm}^{-3}$, typical of WIM/WNM conditions. In Figure 6 we show the data compared to some SpDust models to exemplify the quality of the fit. The comparison of the red ($n_{\text{H}} = 0.25\text{ cm}^{-3}$, $T = 6000\text{ K}$, $x_{\text{H}} = 0.1$, $\chi = 1$) and magenta ($n_{\text{H}} = 0.25\text{ cm}^{-3}$, $T = 6000\text{ K}$, $x_{\text{H}} = 0.01$, $\chi = 1$) lines illustrates the effect of x_{H} . The blue line corresponds to $n_{\text{H}} = 0.3\text{ cm}^{-3}$, $T = 6000\text{ K}$, $x_{\text{H}} = 0.31$, $\chi = 1$; compared to the magenta line, it illustrates the effect of increasing n_{H} . Finally, the cyan ($n_{\text{H}} = 0.40\text{ cm}^{-3}$, $T = 6000\text{ K}$, $x_{\text{H}} = 0.001$, $\chi = 0.1$) and green ($n_{\text{H}} = 0.40\text{ cm}^{-3}$, $T = 6000\text{ K}$, $x_{\text{H}} = 0.001$, $\chi = 1$) lines show the effect of χ . The availability of data at frequencies of

a few GHz will be very valuable to improve the constraints on such parameters.

To complement the physical description of the medium we computed the hydrogen column density N_{H} (cm^{-2}) from the brightness at $100\text{ }\mu\text{m}$, I_{100} , through $I_{100} [\text{MJy sr}^{-1}] = (0.69 \pm 0.03) \times N_{\text{H}} [10^{20}\text{ cm}^{-2}]$ [30]. We used the IRIS [31] band 4 ($100\text{ }\mu\text{m}$) data and integrated the emission inside a 1° beam centered in $l = 25^\circ$, $b = 125^\circ$, corresponding to bright dust emission (see Figure 1), to compute a representative value for I_{100} . This analysis yields $N_{\text{H}} = (2.9 \pm 0.2) \times 10^{20}\text{ cm}^{-2}$, which is a plausible value for the diffuse ISM environment at intermediate latitudes.

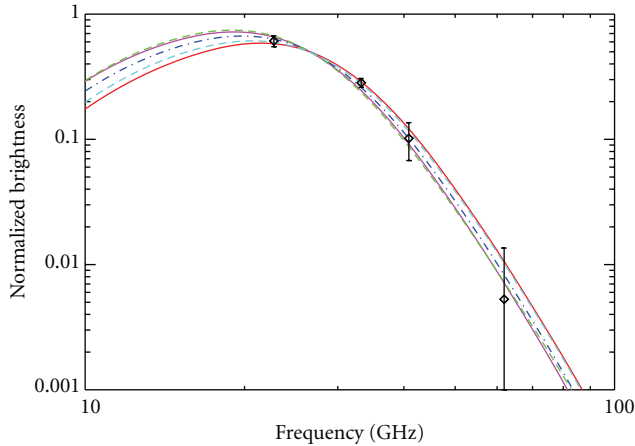


FIGURE 6: Comparison between data (diamonds and error bars) and different SpDust models. Red: $n_{\text{H}} = 0.25 \text{ cm}^{-3}$, $T = 6000 \text{ K}$, $x_{\text{H}} = 0.1$, $\chi = 1$; magenta: same as red with $x_{\text{H}} = 0.01$; blue: $n_{\text{H}} = 0.30 \text{ cm}^{-3}$, $T = 6000 \text{ K}$, $x_{\text{H}} = 0.01$, $\chi = 1$; green: $n_{\text{H}} = 0.40 \text{ cm}^{-3}$, $T = 6000 \text{ K}$, $x_{\text{H}} = 0.001$, $\chi = 1$; cyan: same as blue with $\chi = 0.1$.

6. Conclusions

We have studied the spectrum of the diffuse AME with *WMAP* 7-yr and ancillary data in the North Celestial Pole (NCP) region of the sky. In this region the AME dominates the low-frequency emission, as both synchrotron and free-free are faint. Previous template-fitting analysis by [4] found that the AME spectrum in this region is consistent with a power-law above 23 GHz; the same would apply to most diffuse AME at intermediate latitudes [2, 4, 7, 16–18]. This favors a low peak frequency ($\nu_p < 23 \text{ GHz}$).

For our analysis we rely on the CCA component separation method, which exploits the data auto- and cross-spectra to estimate the frequency spectra of the components in terms of a set of spectral parameters. Our method models the AME as a peaked spectrum and fits for the peak frequency, ν_p , and the slope at 60 GHz, m_{60} . We verified with simulations that we are able to correctly recover the AME spectrum and more specifically the peak frequency, even when it is below 23 GHz. We get $\nu_p = 21.7 \pm 0.8 \text{ GHz}$, which is both a confirmation and an improvement of the previous results. This result relies on the assumption that our parametric model for the AME is a good representation of the true spectrum, which has been verified for a wide range of theoretical spinning dust models.

Using the SpDust code, we linked the estimated spectrum to the local physical conditions with the hypothesis of spinning dust emission. We investigated in particular the hydrogen density ($n_{\text{H}} [\text{cm}^{-3}]$), which is sensitive to the position of the peak, and its degeneracy with the gas temperature T [K]. The densities that we get are those typical of WIM/WNM conditions ($0.2\text{--}0.4 \text{ cm}^{-3}$). For a low hydrogen ionization fraction ($n_{\text{H}} \leq 10^{-2}$), densities up to a few cm^{-3} are allowed by the $n_{\text{H}}\text{--}T$ degeneracy. Lower radiation fields (χ) require slightly lower n_{H} . By considering $100 \mu\text{m}$ data for our region we obtain a hydrogen column density $N_{\text{H}} \sim 10^{20} \text{ cm}^{-2}$. Overall, the recovered AME

spectrum is found to be consistent with that predicted by spinning dust models for plausible physical conditions.

Acknowledgments

S. Ricciardi acknowledges support by MIUR through PRIN 2009 Grant no. 2009XZ54H2.

References

- [1] G. Lagache, “The large-scale anomalous microwave emission revisited by *WMAP*,” *Astronomy and Astrophysics*, vol. 405, no. 3, pp. 813–819, 2003.
- [2] A. J. Banday, C. Dickinson, R. D. Davies, R. J. Davis, and K. M. Górski, “Reappraising foreground contamination in the COBE-DMR data,” *Monthly Notices of the Royal Astronomical Society*, vol. 345, no. 3, pp. 897–911, 2003.
- [3] A. Kogut, “Spatial correlation between dust and diffuse ionized gas,” in *American Astronomical Society Meeting Abstracts*, vol. 28 of *Bulletin of the American Astronomical Society*, p. 1295, 1996.
- [4] R. D. Davies, C. Dickinson, A. J. Banday, T. R. Jaffe, K. M. Górski, and R. J. Davis, “A determination of the spectra of Galactic components observed by the Wilkinson Microwave Anisotropy Probe,” *Monthly Notices of the Royal Astronomical Society*, vol. 370, no. 3, pp. 1125–1139, 2006.
- [5] N. Ysard, M. A. Miville-Deschênes, and L. Verstraete, “Probing the origin of the microwave anomalous foreground,” *Astronomy and Astrophysics*, vol. 509, no. 1, 4 pages, 2010.
- [6] B. Gold, N. Odegard, J. L. Weiland et al., “Seven-year wilkinson microwave anisotropy probe (*WMAP*) observations: galactic foreground emission,” *Astrophysical Journal*, vol. 192, no. 2, 2011.
- [7] G. Dobler and D. P. Finkbeiner, “Extended anomalous foreground emission in the *WMAP* three-year data,” *Astrophysical Journal Letters*, vol. 680, no. 2, pp. 1222–1234, 2008.
- [8] A. De Oliveira-Costa, M. Tegmark, R. D. Davies et al., “The quest for microwave foreground X,” *Astrophysical Journal*, vol. 606, no. 2, pp. L89–L92, 2004.
- [9] D. P. Finkbeiner, G. I. Langston, and A. H. Minter, “Microwave interstellar medium emission in the green bank galactic plane survey: evidence for spinning dust,” *Astrophysical Journal*, vol. 617, no. 1, pp. 350–359, 2004.
- [10] E. M. Leitch, A. C. S. Readhead, T. J. Pearson, and S. T. Myers, “An anomalous component of galactic emission,” *Astrophysical Journal Letters*, vol. 486, no. 1, pp. L23–L26, 1997.
- [11] B. T. Draine and A. Lazarian, “Electric dipole radiation from spinning dust grains,” *Astrophysical Journal Letters*, vol. 508, no. 1, pp. 157–179, 1998.
- [12] Y. Ali-Haïmoud, C. M. Hirata, and C. Dickinson, “A refined model for spinning dust radiation,” *Monthly Notices of the Royal Astronomical Society*, vol. 395, pp. 1055–1078, 2009.
- [13] N. Ysard and L. Verstraete, “The long-wavelength emission of interstellar PAHs: characterizing the spinning dust contribution,” *Astronomy and Astrophysics*, vol. 509, no. A12, 13 pages, 2010.
- [14] Planck Collaboration, “Planck early results 20: new light on anomalous microwave emission from spinning dust grains,” *Astronomy & Astrophysics*, vol. 536, no. A20, 17 pages, 2011.
- [15] R. Génova-Santos, R. Rebolo, J. A. Rubiño-Martín, C. H.

- López-Caraballo, and S. R. Hildebrandt, “Detection of anomalous microwave emission in the pleiades reflection nebula with wilkinson microwave anisotropy probe and the COSMOSOMAS experiment,” *Astrophysical Journal Letters*, vol. 743, p. 67, 2011.
- [16] M. A. Miville-Deschênes, N. Ysard, A. Lavabre et al., “Separation of anomalous and synchrotron emissions using WMAP polarization data,” *Astronomy and Astrophysics*, vol. 490, no. 3, pp. 1093–1102, 2008.
- [17] A. Bonaldi, S. Ricciardi, S. Leach, F. Stivoli, C. Baccigalupi, and G. De Zotti, “WMAP 3-yr data with correlated component analysis: anomalous emission and impact of component separation on the CMB power spectrum,” *Monthly Notices of the Royal Astronomical Society*, vol. 382, no. 4, pp. 1791–1803, 2007.
- [18] T. Ghosh, A. J. Banday, T. Jaffe et al., “Foreground analysis using cross-correlation of external templates on the 7-year Wilkinson Microwave Anisotropy Probe data,” *Monthly Notices of the Royal Astronomical Society*, vol. 422, no. 4, pp. 3617–3642, 2012.
- [19] S. Ricciardi, A. Bonaldi, P. Natoli et al., “Correlated component analysis for diffuse component separation with error estimation on simulated Planck polarization data,” *Monthly Notices of the Royal Astronomical Society*, vol. 406, no. 3, pp. 1644–1658, 2010.
- [20] C. G. T. Haslam, C. J. Salter, H. Stoffel, and W. E. Wilson, “A 408 MHz all-sky continuum survey. II—the atlas of contour maps,” *Astronomy and Astrophysics*, vol. 47, p. 1, 1982.
- [21] C. Dickinson, R. D. Davies, and R. J. Davis, “Towards a free-free template for CMB foregrounds,” *Monthly Notices of the Royal Astronomical Society*, vol. 341, no. 2, pp. 369–384, 2003.
- [22] A. Bonaldi, L. Bedini, E. Salerno, C. Baccigalupi, and G. De Zotti, “Estimating the spectral indices of correlated astrophysical foregrounds by a second-order statistical approach,” *Monthly Notices of the Royal Astronomical Society*, vol. 373, no. 1, pp. 271–279, 2006.
- [23] D. P. Finkbeiner, M. Davis, and D. J. Schlegel, “Extrapolation of galactic dust emission at 100 microns to cosmic microwave background radiation frequencies using FIRAS,” *Astrophysical Journal Letters*, vol. 524, no. 2, pp. 867–886, 1999.
- [24] M. Górski, E. Hivon, A. J. Banday et al., “HEALPix: a framework for high-resolution discretization and fast analysis of data distributed on the sphere,” *Astrophysical Journal*, vol. 622, no. 2, pp. 759–771, 2005.
- [25] N. Jarosik, C. L. Bennett, J. Dunkley et al., “Seven-year wilkinson microwave anisotropy probe (WMAP) observations: sky maps, systematic errors, and basic results,” *Astrophysical Journal*, vol. 192, no. 2, 2011.
- [26] D. J. Schlegel, D. P. Finkbeiner, and M. Davis, “Maps of dust infrared emission for use in estimation of reddening and cosmic microwave background radiation foregrounds,” *Astrophysical Journal Letters*, vol. 500, no. 2, pp. 525–553, 1998.
- [27] D. J. Fixsen, J. L. Weiland, S. Brodd et al., “Comparison of the COBE FIRAS and DIRBE calibrations,” *Astrophysical Journal Letters*, vol. 490, no. 2, pp. 482–487, 1997.
- [28] K. Silsbee, Y. Ali-Haïmoud, and C. M. Hirata, “Spinning dust emission: the effect of rotation around a non-principal axis,” *Monthly Notices of the Royal Astronomical Society*, vol. 411, pp. 2750–2769, 2011.
- [29] G. Giardino, A. J. Banday, K. M. Górski, K. Bennett, J. L. Jonas, and J. Tauber, “Towards a model of full-sky galactic synchrotron intensity and linear polarisation: a re-analysis of the Parkes data,” *Astronomy and Astrophysics*, vol. 387, no. 1, pp. 82–97, 2002.
- [30] F. Boulanger, A. Abergel, J. P. Bernard et al., “The dust/gas correlation at high Galactic latitude,” *Astronomy and Astrophysics*, vol. 312, no. 1, pp. 256–262, 1996.
- [31] M. A. Miville-Deschênes and G. Lagache, “IRIS: a new generation of IRAS maps,” in *Astronomical Society of the Pacific Conference Series*, L. Armus and W. T. Reach, Eds., vol. 357 of *Astronomical Society of the Pacific Conference Series*, p. 167, 2006.

Review Article

Spinning Dust Emission from Wobbling Grains: Important Physical Effects and Implications

Thiem Hoang¹ and A. Lazarian²

¹Canadian Institute for Theoretical Astrophysics, University of Toronto, 60 St. George Street, Toronto, ON, Canada M5S 3H8

²Department of Astronomy, University of Wisconsin-Madison, Madison, WI 53705, USA

Correspondence should be addressed to Thiem Hoang, hoang@cita.utoronto.ca

Received 14 August 2012; Accepted 24 October 2012

Academic Editor: Laurent Verstraete

Copyright © 2012 T. Hoang and A. Lazarian. This is an open access article distributed under the Creative Commons Attribution License, which permits unrestricted use, distribution, and reproduction in any medium, provided the original work is properly cited.

We review the major progress on the modeling of electric dipole emission from rapidly spinning tiny dust grains, including polycyclic aromatic hydrocarbons (PAHs). We begin by summarizing the original model of spinning dust proposed by Draine and Lazarian and recent theoretical results improving the Draine and Lazarian model. The paper is focused on important physical effects that were disregarded in earlier studies for the sake of simplicity and recently accounted for by us, including grain wobbling due to internal relaxation, impulsive excitation by single-ion collisions, the triaxiality of grain shape, charge fluctuations, and the turbulent nature of astrophysical environments. Implications of the spinning dust for constraining the physical properties of ultrasmall dust grains and environmental conditions are discussed. We discuss the alignment of tiny dust grains and the possibility of polarized spinning dust emission. Suggestions for constraining the alignment of tiny grains and polarization of spinning dust are also discussed.

1. Introduction

Diffuse Galactic microwave emission carries important information on the fundamental properties of the interstellar medium, but it also interferes with cosmic microwave background (CMB) experiments (see Bouchet et al. [1] and Tegmark et al. [2]). Precision cosmology with *Wilkinson Microwave Anisotropy Probe* (WMAP) and Planck satellite requires a good model of the microwave foreground emission to allow for reliable subtraction of Galactic contamination from the CMB radiation.

The discovery of an anomalous microwave emission (hereafter AME) in the range from 10–100 GHz illustrates well the treacherous nature of dust. Until very recently, it has been thought that there are three major components of the diffuse Galactic foreground: synchrotron emission, free-free radiation from plasma (thermal bremsstrahlung), and thermal emission from dust. In the microwave range, the latter is subdominant, leaving essentially two components. However, it is exactly in this range that an anomalous

emission component was reported (Kogut et al. [3, 4]). In the paper by De Oliveira-Costa et al. [5], this emission was nicknamed “Foreground X,” which properly reflects its mysterious nature. This component is spatially correlated with 100 μm thermal dust emission, but its intensity is much higher than one would expect by directly extrapolating the thermal dust emission spectrum to the microwave range.

An early explanation for AME was proposed by Draine and Lazarian model [6, 7] (hereafter DL98 model), where it was identified as electric dipole emission from very small grains (mostly containing polycyclic aromatic hydrocarbons—PAHs) that spin rapidly due to several processes, including gas-grain interactions and dust infrared emission. Although spinning dust emission had been discussed previously (see Erickson [8] and Ferrara and Dettmar [9]), Draine and Lazarian were the first to include the variety of excitation and damping processes that are relevant for very small grains.

While the DL98 model appears to be in general agreement with observations (see [10, 11]), it did not account for

some important effects, namely, the nonsphericity of grain shapes, the internal relaxation within grain, and the transient spinup due to ion collisions.

This induced more recent work in order to improve the original DL98 model. The recent papers include Ali-Haïmoud et al. [12], Hoang et al. [13], Ysard and Verstraete [14], Hoang et al. [15], Silsbee et al. [16]. In this paper, we review both the original DL98 model and the ways that it has been improved recently. We focus on the improvement of the dynamics of PAHs and the important physical effects associated with these ultrasmall grains. Recent reviews of the subject include Draine and Lazarian [17], Lazarian and Prunet [18], and Lazarian and Finkbeiner [10].

In Section 2, we briefly present the history of AME and discuss the original DL98 model including their basic assumptions. Section 3 presents our principal results improving the DL98 model from Hoang et al. [13, 15]. From Section 4 to Section 6, we review the grain rotational dynamics and discuss our general approach to calculate power spectrum of spinning dust emission, grain angular momentum distribution, and emissivity for PAHs of arbitrary shapes. In Section 7, we discuss the implications of spinning dust for constraining physical parameters of PAHs as well as environmental conditions. The possibility of polarization of spinning dust and its constraint is discussed in Section 8. A summary of the present paper is given in Section 9.

2. The Original DL98 Model

2.1. Anomalous Microwave Emission and PAHs. The emission spectrum of diffuse interstellar dust was mostly obtained by the *Infrared Astronomy Satellite* (IRAS) and infrared spectrometers on the *Cosmic Background Explorer* (COBE) and on the *Infrared Telescope in Space* (IRTS). The emission at short wavelength ($\lambda < 50 \mu\text{m}$) arises from transiently heated ultrasmall grains (e.g., PAHs). These grains have such a small heat capacity that the absorption of a single ultraviolet (UV) starlight photon ($\sim 6 \text{ eV}$) raises their temperature to $T_{\text{vib}} > 200 \text{ K}$. Typically, these grains have less than 300 atoms and can be viewed as large molecules rather than dust particles. They are, however, sufficiently numerous to account for most of the prominent 2175 \AA absorption features and for $\sim 35\%$ of the total starlight absorption (see, e.g., Li and Draine [19]).

The thermal (vibrational) emissivity of these grains is thought to be negligible at low frequency, because they spend most of their time cold and only emit most of their energy when they are hot. These ultrasmall grains (PAHs) are invoked in the DL98 model to account for the anomalous microwave emission (AME) that was measured in observations.

The first detection of anomalous dust-correlated emission by COBE (Kogut et al. [3, 4]) was quickly followed by detections in the data sets from Saskatoon (de Oliveira-Costa et al. [20]), OVRO (Leitch et al. [21]), the 19 GHz survey (De Oliveira-Costa et al. [22]), de Oliveira-Costa et al. ([23]). Initially, AME was identified as thermal bremsstrahlung from ionized gas correlated with dust (Kogut et al. [3])

and was presumably produced by photoionized cloud rims (McCullough et al. [24]). This idea was scrutinized in Draine and Lazarian [6] and criticized on energetic grounds. Poor correlation of $\text{H}\alpha$ with $100 \mu\text{m}$ emission also argued against the free-free explanation (McCullough et al. [24]). These arguments are summarized in [17]. Later, [25] used Wisconsin H-Alpha Mapper (WHAM) survey data and established that the free-free emission “is about an order of magnitude below Foreground X over the entire range of frequencies and latitudes where it is detected.” The authors concluded that the Foreground X cannot be explained as the free-free emission. Additional evidence supporting this conclusion has come from a study at 5, 8, and 10 GHz by Finkbeiner et al. [26] of several dark clouds and HII regions, two of which show a significantly rising spectrum from 5 to 10 GHz.

The recent Wilkinson Microwave Anisotropy Probe (WMAP) data were used to claim a lower limit of 5% for the spinning dust fraction at 23 GHz (Bennett et al. [27]). However, other models of spinning dust are not ruled out by the WMAP data and in fact fit reasonably well. Finkbeiner [11] performed a fit to WMAP data using a CMB template, a free-free template (based on $\text{H}\alpha$ -correlated emission plus hot gas emission near the Galactic center), a soft synchrotron template traced by the 408 MHz map, a thermal dust extrapolation (Finkbeiner et al. [28]), and a spinning dust template consisting of dust column density times T_d^3 . This fit results in excellent χ^2/dof values of 1.6, 1.09, 1.08, 1.05, and 1.08 at 23, 33, 41, 61, and 94 GHz and a reasonable spectral shape for the average spinning dust spectrum.

This WMAP analysis alone does not rule out the Bennett et al. [27] hypothesis of hard synchrotron emission, but when it is combined with the Green Bank Galactic Plane survey data (Langston et al. [29]) at 8 and 14 GHz, spinning dust appears to provide a much better fit than hard synchrotron (Finkbeiner et al. [30]).

Spinning dust emission has recently been reported in a wide range of astrophysical environments, including general ISM (Gold et al. [31, 32] and Collaboration et al. [33]), star-forming regions in the nearby galaxy NGC 6946 (Scaife et al. [34, 35]), and Perseus and Ophiuchus clouds (Casassus et al. [36] and Tibbs et al. [37]). Early Planck results have been interpreted as showing a microwave emission excess from the spinning dust in the Magellanic Clouds (Bot et al. [38]; Collaboration et al. [33]).

2.2. Basic Assumptions

- (i) The smallest PAH particles of a few Angstroms are expected to be planar. The grain size a is defined as the radius of an equivalent sphere of the same mass. PAHs are assumed to be planar, disklike with height L and radius R for $a < a_2$, and spherical for $a \geq a_2$. The value $a_2 = 6 \text{ \AA}$ is adopted.
- (ii) PAHs usually have electric dipole moment μ arising from asymmetric polar molecules or substructures (*intrinsic dipole moment*) and from the asymmetric

distribution of grain charge. The latter is shown to be less important.

- (iii) The grain spins around its symmetry axis \mathbf{a}_1 with angular momentum \mathbf{J} parallel to \mathbf{a}_1 , and \mathbf{J} is isotropically oriented in space.
- (iv) For a fixed angular momentum, the spinning grain emits electric dipole radiation at a *unique* frequency mode ν , which is equal to the rotational frequency, that is, $\nu = \omega/2\pi$.
- (v) A grain in the gas experiences collisions with neutral atoms and ions, interacts with passing ions (plasma-grain interactions), emits infrared photons following UV absorption, and emits electric dipole radiation. All these processes result in the damping and excitation of grain rotation, that is, they change grain angular momentum J and velocity ω .
- (vi) Due to the excitation of various aforementioned processes, the grain angular velocity randomly fluctuates and its distribution can be approximated as the Maxwellian distribution function $f_{Mw}(\omega)$.
- (vii) The total emissivity per H atom of the electric dipole radiation from spinning dust at the frequency ν is given by

$$\frac{j_\nu}{n_H} = \frac{1}{4\pi} \frac{1}{n_H} \int_{a_{\min}}^{a_{\max}} da \frac{dn}{da} 4\pi\omega^2 f_{Mw}(\omega) 2\pi \left(\frac{2\mu_\perp^2 \omega^4}{3c^3} \right), \quad (1)$$

where n_H is the density of H nuclei, μ_\perp is the electric dipole moment perpendicular to the rotation axis, and dn/da is the grain size distribution function with a in the range from a_{\min} to a_{\max} .

3. Improved Model of Spinning Dust Emission

Ali-Haïmoud et al. [12] revisited the spinning dust model and presented an analytic solution of the Fokker-Planck (FP) equation that describes the rotational excitation of a spherical grain if the discrete nature of impulses from single-ion collisions can be neglected.

Hoang et al. [13] (hereafter HDL10) improved the DL98 model by accounting for a number of physical effects. The main modifications in their improved model of spinning dust emission are as follows.

- (i) Disk-like grains rotate with their grain symmetry axis \mathbf{a}_1 that is not perfectly aligned with angular momentum \mathbf{J} . The disaligned rotation of \mathbf{J} with \mathbf{a}_1 causes the wobbling of the grain principal axes with respect to \mathbf{J} due to internal thermal fluctuations.
- (ii) The power spectrum of a freely spinning grain is obtained using Fourier transform.
- (iii) Distribution function of grain angular momentum, J , and velocity, ω , is obtained exactly using the Langevin equation (LE) for the evolution of \mathbf{J} in an inertial coordinate system.

- (iv) The limiting cases of fast internal relaxation and no internal relaxation are both considered for calculations of the angular momentum distribution and emissivity of spinning dust.
- (v) Infrequent collisions of single ions which deposit an angular momentum larger than the grain angular momentum prior to the collision are treated as Poisson-distributed events.

The wobbling disk-like grain has anisotropic rotational damping and excitation. Such an anisotropy can increase the peak emissivity by a factor ~ 2 and increases the peak frequency by a factor 1.4–1.8, compared to the results from the DL98 model.

The effects of grain wobbling on electric dipole emission were independently studied in Silsbee et al. [16] using the FP equation approach, but they disregarded the transient spinup by infrequent single-ion collisions and considered two limiting cases of dust grain temperature, $T_d \rightarrow 0$ and $T_d \rightarrow \infty$.

Further improvements of the DL98 model were performed in Hoang et al. [15], where a couple of additional effects were taken into account:

- (i) emission from very small grains of triaxial ellipsoid (*irregular*) shape with the principal moments of inertia $I_1 \geq I_2 \geq I_3$,
- (ii) effects of the orientation of dipole moment $\boldsymbol{\mu}$ within grain body for different regimes of internal thermal fluctuations,
- (iii) effects of compressible turbulence on the spinning dust emission.

The work found that a freely rotating irregular grain with a given angular momentum radiates at multiple frequency modes. The resulting spinning dust spectrum has peak frequency and emissivity increasing with the degree of grain shape irregularity, which is defined by $I_1 : I_2 : I_3$. Considering the transient heating of grains by UV photons, the study found that the spinning dust emissivity in the case of strong thermal fluctuations is less sensitive to the orientation of $\boldsymbol{\mu}$ than in the case of weak thermal fluctuations. In addition, the emission in a turbulent medium increases by a factor from 1.2–1.4 relative to that in a uniform medium, as sonic Mach number M_s increases from 2–7. The latter Mach numbers are relevant to cold phases of the ISM (see Hoang et al. [15] for more details).

4. Grain Rotational Configuration and Power Spectrum

A discussion of the basic physical processes involved in spinning dust can be found in the review by Yacine Ali-Haïmoud, which can be found in the same volume. There, the use of Fokker-Planck equation for describing grain dynamics is discussed. Here, we discuss our numerical approach based on Fourier transform and the Langevin equation, which exhibits a number of advantages to the FP equation when numerical studies of grain dynamics are

performed and arbitrary shape of PAHs is considered. We summarize a general approach to find the spinning dust emissivity from grains of triaxial ellipsoid shape with $I_1 > I_2 > I_3$ subject to fast internal relaxation.

4.1. Torque-Free Motion and Internal Relaxation. The dynamics of a triaxial (*irregular*) grain is more complicated than that of a disk-like grain with $I_2 = I_3$. Indeed, in addition to the precession of the axis of major inertia \mathbf{a}_1 around \mathbf{J} as in the disk-like grain, the axis \mathbf{a}_1 wobbles rapidly, resulting in the variation of the angle θ between \mathbf{a}_1 and \mathbf{J} (see Figure 1).

To describe the torque-free motion of an irregular grain having a rotational energy E_{rot} , the conserved quantities are taken, including the angular momentum \mathbf{J} , and a dimensionless parameter that characterizes the deviation of the grain rotational energy from its minimum value

$$q = \frac{2I_1 E_{\text{rot}}}{J^2}. \quad (2)$$

The orientation of the triaxial grain in the lab system is completely described by three Euler angles ψ , ϕ , and θ (see, e.g., Hoang et al. [15]). Following [39], we define the total number of states s in phase space for q ranging from 1 to q as

$$s \equiv 1 - \frac{2}{\pi} \int_0^{\psi_1} d\psi \left[\frac{I_3(I_1 - I_2q) + I_1(I_2 - I_3)\cos^2\psi}{I_3(I_1 - I_2) + I_1(I_2 - I_3)\cos^2\psi} \right]^{1/2}, \quad (3)$$

where

$$\psi_1 = \cos^{-1} \left[\frac{I_3(I_2q - I_1)}{I_1(I_2 - I_3)} \right]^{1/2}, \quad (4)$$

for $q > q_{\text{sp}}$ and $\psi_1 = \pi/2$ for $q \leq q_{\text{sp}}$, with $q_{\text{sp}} \equiv I_1/I_2$ being the separatrix between the two regimes.

The intramolecular vibrational-rotational energy transfer process (IVRET) due to imperfect elasticity occurs on a timescale 10^{-2} s, for a grain of a few angstroms (Purcell [40]), which is shorter than the IR emission time. So, when the vibrational energy decreases due to IR emission, as long as the vibrational-rotational (V-R) energy exchange exists, interactions between vibrational and rotational systems maintain a thermal equilibrium, that is, $T_{\text{rot}} \approx T_{\text{vib}}$. As a result, the LTE distribution function of rotational energy reads (hereafter VRE regime; see Lazarian and Roberge [41])

$$f_{\text{VRE}}(s, J) \propto \exp\left(-\frac{E_{\text{rot}}}{k_B T_{\text{rot}}}\right) \approx \exp\left(-\frac{E_{\text{rot}}}{k_B T_{\text{vib}}}\right). \quad (5)$$

Substituting E_{rot} as a function of J and q from (2) into (5), the distribution function for the rotational energy becomes

$$f_{\text{VRE}}(s, J) = A \exp\left(-\frac{q(s)J^2}{2I_1 k_B T_{\text{vib}}}\right), \quad (6)$$

where A is a normalization constant such that $\int_0^1 f_{\text{VRE}}(s, J) ds = 1$.

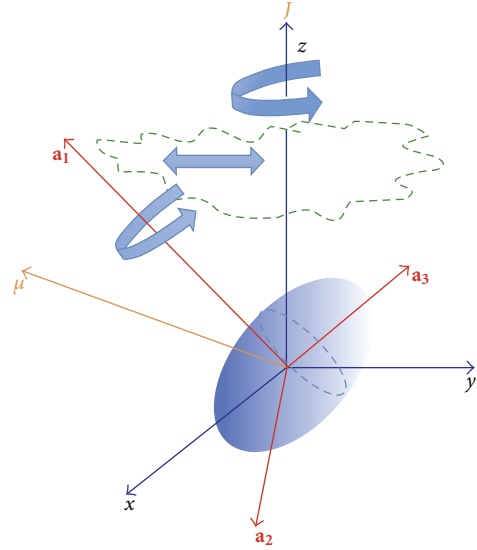


FIGURE 1: Rotational configuration of a triaxial ellipsoid characterized by three principal axes: \mathbf{a}_1 , \mathbf{a}_2 , and \mathbf{a}_3 in the inertial coordinate system xyz . Grain angular momentum \mathbf{J} is conserved in the absence of external torques and directed along z -axis. The torque-free motion of the triaxial grain comprises the rotation around the axis of major inertia \mathbf{a}_1 , the precession of \mathbf{a}_1 around \mathbf{J} , and the wobbling of \mathbf{a}_1 with respect to \mathbf{J} . The dipole moment $\boldsymbol{\mu}$, which is fixed to grain body, moves together with the grain and thus radiates electric dipole emission.

4.2. Power Spectrum of a Freely Spinning Grain. Consider a grain with a dipole moment $\boldsymbol{\mu}$ fixed in the grain body rotating with an angular momentum \mathbf{J} . If the grain only spins around its symmetry axis, then the rotating dipole moment emits radiation at a unique frequency ν equal to the rotational frequency, that is, $\nu = \omega/2\pi$ (see DL98). The power spectrum for this case is simply a delta function $\delta(\nu - \omega/2\pi)$ with a unique frequency mode.

For an irregular grain of triaxial ellipsoid shape, the grain rotational dynamics is more complicated. In general, one can also obtain analytical expressions for power spectrum, but it is rather tedious. To find the power spectrum of a freely rotating irregular grain, Hoang et al. [13, 15] have employed a more simple brute force approach based on the Fourier transform approach. First, they represent the dipole moment $\boldsymbol{\mu}$ in an inertial coordinate system, and then they compute its second derivative. We obtain

$$\ddot{\boldsymbol{\mu}} = \sum_{i=1}^3 \mu_i \ddot{\mathbf{a}}_i, \quad (7)$$

where μ_i are components of $\boldsymbol{\mu}$ along principal axes \mathbf{a}_i , $\ddot{\mathbf{a}}_i$ are second derivatives of \mathbf{a}_i with respect to time, and $i = 1, 2, \text{ and } 3$.

The instantaneous emission power by the rotating dipole moment is equal to

$$P_{\text{ed}}(J, q, t) = \frac{2}{3c^3} \ddot{\boldsymbol{\mu}}^2. \quad (8)$$

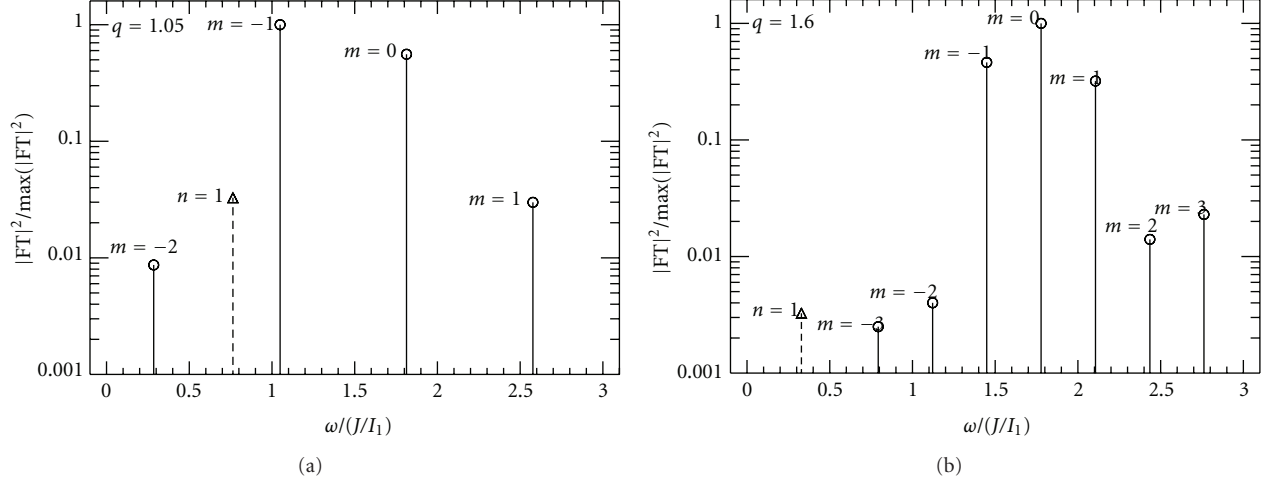


FIGURE 2: Normalized power spectrum of a torque-free rotating irregular grain with $I_1 : I_2 : I_3 = 1 : 0.6 : 0.5$ for the different values of $q = 1.05, 1.60$ (i.e., $q < q_{sp} \equiv I_1/I_2$) and $q = 1.81 > q_{sp}$. The components of $|\text{FT}(\ddot{\mu}_x)|^2/\max(|\text{FT}(\ddot{\mu}_x)|^2)$ (or $|\text{FT}(\ddot{\mu}_y)|^2/\max(|\text{FT}(\ddot{\mu}_x)|^2)$) are indicated by circles, while the components of $|\text{FT}(\ddot{\mu}_z)|^2/\max(|\text{FT}(\ddot{\mu}_x)|^2)$ are indicated by triangles. Orders of in-plane modes m and out-of-plane modes n are indicated, and case 1 ($\mu_1 = \mu/\sqrt{3}$) of $\boldsymbol{\mu}$ orientation is assumed. The figure is reproduced from Hoang et al. [15].

The power spectrum is then obtained from the Fourier transform (FT) for the components of $\ddot{\boldsymbol{\mu}}$. For example, the amplitude of $\ddot{\mu}_x$ at the frequency ν_k is defined as

$$\ddot{\mu}_{x,k} = \int_{-\infty}^{+\infty} \ddot{\mu}_x(t) \exp(-i2\pi\nu_k t) dt, \quad (9)$$

where k denotes the frequency mode. The emission power at the positive frequency ν_k is given by

$$P_{\text{ed},k}(J, q) = \frac{4}{3c^3} (\dot{\mu}_{x,k}^2 + \dot{\mu}_{z,k}^2 + \dot{\mu}_{y,k}^2), \quad (10)$$

where the factor 2 arises from the positive/negative frequency symmetry of the Fourier spectrum. To reduce the spectral leakage in the FT, we convolve the time-dependent function $\ddot{\boldsymbol{\mu}}$ with the Blackman-Harris window function (see Harris, 1978). The power spectrum then needs to be corrected for the power loss due to the window function.

The total emission power from all frequency modes for a given J and q then becomes

$$P_{\text{ed}}(J, q) = \sum_k P_{\text{ed},k}(J, q) \equiv \frac{1}{T} \int_0^T dt \left(\frac{2}{3c^3} \dot{\boldsymbol{\mu}}^2 \right), \quad (11)$$

where T is the integration time. (this is the result of Parseval's theorem).

Figure 2 presents normalized power spectra (squared amplitude of Fourier transforms), $|\text{FT}(\mu_{x,y})|^2/\max(|\text{FT}(\mu_{x,y})|^2)$ and $|\text{FT}(\mu_z)|^2/\max(|\text{FT}(\mu_x)|^2)$, for the components $\ddot{\mu}_x$ (or $\ddot{\mu}_y$) and $\ddot{\mu}_z$ for a freely rotating irregular grain having the ratio of moments of inertia $I_1 : I_2 : I_3 = 1 : 0.6 : 0.5$ and for various q . Circles and triangles indicated with m and n denote peaks of the power spectrum for oscillating components of $\ddot{\mu}_x$ (or $\ddot{\mu}_y$) and $\ddot{\mu}_z$, respectively. The horizontal axis is the angular frequency of emission modes normalized over the frequency of emission when the grain spins around its shortest axis.

Multiple frequency modes are observed in the power spectra of the irregular grain, but in Figure 2, we show only the modes with power no less than 10^{-3} the maximum value. One can see that in the case with large $q = 1.6$, the modes with $\omega/(J/I_1) > 1$ have increasing power, while the modes with $\omega/(J/I_1) < 1$ have decreasing power. It indicates that if grain rotational energy is increased so that the grain spends a significant fraction of time rotating with large q , then the grain should radiate larger rotational emission.

Although one should not expect the analytical expression of power spectrum for the triaxial grain, the frequency modes can be approximately found. Indeed, for $q < I_1/I_2$, we found that power spectra for $\ddot{\mu}_x$ (or $\ddot{\mu}_y$) have angular frequency modes

$$\omega_m \approx \langle \dot{\phi} \rangle + m \langle |\dot{\psi}| \rangle, \quad (12)$$

where the bracket denotes the averaging value over time, and $m = 0, \pm 1, \pm 2, \dots$ denote the order of the mode. The frequency modes for $\ddot{\mu}_z$ are given by

$$\omega_n = n \langle |\dot{\psi}| \rangle, \quad (13)$$

where n is integer and $n \geq 1$.

In the following, the emission modes induced by the oscillation of μ_x or μ_y , which lie in the $\hat{\mathbf{x}}\hat{\mathbf{y}}$ plane, perpendicular to \mathbf{J} , are called *in-plane* modes, and those induced by the oscillation of μ_z in the direction perpendicular to the $\hat{\mathbf{x}}\hat{\mathbf{y}}$ plane, are called *out-of-plane* modes. The order of mode is denoted by m and n , respectively. Figure 2 also shows that the emission power for out-of-plane modes ω_n is negligible compared to the power emitted by in-plane modes ω_m .

Emission power spectra are numerically calculated to find ω_k and $P_{\text{ed},k}$, as functions of J and q , for the various ratio of moments of inertia $I_1 : I_2 : I_3$. The obtained data will be used later to compute spinning dust emissivity.

5. Grain Angular Momentum Distribution: Langevin Equation

5.1. Langevin Equation. To find the exact distribution function for grain angular momentum \mathbf{J} , Hoang et al. [13] and Hoang et al. [15] proposed a numerical approach based on the Langevin equation. Basically, they numerically solved the Langevin equation describing the evolution of three components of \mathbf{J} in an inertial coordinate system. They read

$$dJ_i = A_i dt + \sqrt{B_{ii}} dq_i, \quad \text{for } i = x, y, z, \quad (14)$$

where dq_i are random Gaussian variables with $\langle dq_i^2 \rangle = dt$, and $A_i = \langle \Delta J_i / \Delta t \rangle$ and $B_{ii} = \langle (\Delta J_i)^2 / \Delta t \rangle$ are damping and diffusion coefficients defined in the inertial coordinate system. Detailed expressions of these coefficients can be found in Hoang et al. [13] and Hoang et al. [15].

For an irregular grain, and to simplify calculations, we adopt the A_i and B_{ii} for a disk-like grain obtained in HDL10. Following DL98b and HDL10, the disk-like grain has the radius R and thickness $L = 3.35 \text{ \AA}$, and the ratio of moments of inertia is along and perpendicular to the grain symmetry axis $h = I_{\parallel} / I_{\perp}$. Thereby, the effect of nonaxisymmetry on A_i and B_{ii} is ignored, and we only examine the effect of grain wobbling resulting from the grain triaxiality.

In dimensionless units, $\mathbf{J}' \equiv \mathbf{J} / I_{\parallel} \omega_{T,\parallel}$ with $\omega_{T,\parallel} \equiv (2k_B T_{\text{gas}} / I_{\parallel})^{1/2}$ being the thermal angular velocity of the grain along the grain symmetry axis and $t' \equiv t / \tau_{H,\parallel}$; (14) becomes

$$dJ'_i = A'_i dt' + \sqrt{B'_{ii}} dq'_i, \quad (15)$$

where $\langle dq_i'^2 \rangle = dt'$,

$$A'_i = -\frac{J'_i}{\tau'_{\text{gas,eff}}} - \frac{2}{3} \frac{J_i'^3}{\tau'_{\text{ed,eff}}}, \quad (16)$$

$$B'_{ii} = \frac{B_{ii}}{2I_{\parallel} k_B T_{\text{gas}}} \tau_{H,\parallel},$$

where

$$\tau'_{\text{gas,eff}} = \frac{\tau_{\text{gas,eff}}}{\tau_{H,\parallel}} = \frac{F_{\text{tot},\parallel}^{-1}}{\cos^2 \theta + \gamma_H \sin^2 \theta}, \quad (17)$$

$$\gamma_H = \frac{F_{\text{tot},\perp} \tau_{H,\parallel}}{F_{\text{tot},\parallel} \tau_{H,\perp}}, \quad \tau'_{\text{ed,eff}} = \frac{\tau_{\text{ed,eff}}}{\tau_{H,\parallel}},$$

where $\tau_{H,\parallel}$ and $\tau_{H,\perp}$ are rotational damping times due to gas of purely hydrogen atom for rotation along parallel and perpendicular direction to the grain symmetry axis \mathbf{a}_1 , $\tau_{\text{ed,eff}}$ is the effective damping time due to electric dipole emission (see HDL10, HLD11), θ is the angle between \mathbf{a}_1 and \mathbf{J} , and $F_{\text{tot},\parallel}$ and $F_{\text{tot},\perp}$ are total damping coefficients parallel and perpendicular to \mathbf{a}_1 (see HDL10). In the case of fast internal relaxation, the diffusion coefficients A and B are averaged over the distribution function f_{VRE} .

The Langevin equation (15) is solved using the numerical integration with a constant timestep. At each timestep, the angular momentum J_i obtained from LEs is recorded and later used to find the distribution function f_J with normalization $\int_0^\infty f_J dJ = 1$.

5.2. Advantages of the Langevin Equation Approach. There are two apparent advantages of the LE approach. First, it allows us to treat the spinning dust emission from grains with an arbitrary grain vibrational temperature. Second, the impulsive excitation by single-ion collisions, which can deposit an amount of angular momentum greater than the grain angular momentum prior the collision, is easily included in (14) (see [15]). Next, we briefly discuss the effect of impulsive excitations arising from single-ion collisions.

DL98b showed that for grains smaller than 7 \AA , the angular impulse due to an individual ion-grain collision may be comparable to the grain angular momentum prior the collision. Thus, infrequent hits of ions can result in the transient rotational excitation for very small grains.

Let τ_{icoll}^{-1} be the mean rate of ion collisions with the grain given by

$$\tau_{\text{icoll}}^{-1} = f(Z_g = 0) n_i \pi a^2 \left(\frac{8k_B T_{\text{gas}}}{m_i \pi} \right)^{1/2} \left[1 + \frac{\sqrt{\pi}}{2} \Phi \right] + \sum_{Z_g \neq 0} f(Z_g) n_i \pi a^2 \left(\frac{8k_B T_{\text{gas}}}{m_i \pi} \right)^{1/2} g \left(\frac{Z_g Z_i e^2}{ak_B T_{\text{gas}}} \right), \quad (18)$$

where $\Phi = (2Z_i^2 e^2 / ak_B T_{\text{gas}})^{1/2}$, $g(x) = 1 - x$ for $x < 0$ and $g(x) = e^{-x}$ for $x > 0$, and $f(Z_g)$ is the grain charge distribution function. The probability of the next collision occurring in $[t, t + dt]$ is

$$dP = \tau_{\text{icoll}}^{-1} \exp\left(-\frac{t}{\tau_{\text{icoll}}}\right) dt. \quad (19)$$

The rms angular momentum per ion collision $\langle \delta J^2 \rangle$ is inferred by dividing the total rms angular momentum by the collision rate, and its final formula is given in Hoang et al. [13].

Provided that the random moment of a single-ion collision is obtained from (19), the angular momentum that the grain acquires through each single-ion collision can easily be incorporated into the Langevin equation (14). Hoang et al. [13] found that the impulsive excitations of ions extend the distribution of grain angular momentum to the region of high angular momentum (see next section for its effect on spinning dust emission).

6. Spinning Dust Emissivity

6.1. Spinning Grain of Triaxial Ellipsoid Shape. An irregular grain rotating with a given angular momentum J radiates at frequency modes $\omega_k \equiv \omega_m$ with $m = 0, \pm 1, \pm 2, \dots$ and $\omega_k \equiv \omega_n$ with $n = 1, 2, 3, \dots$ (see (12) and (13)). For simplicity, let ω_{m_i} denote the former and ω_{n_i} denote the latter where i indicates the value for m and n . These frequency modes depend on the parameter $q(s)$, which is determined by the internal thermal fluctuations within the grain.

To find the spinning dust emissivity by a grain at an observational frequency ν , first we need to know how much emission that is contributed by each mode ω_k .

Consider an irregular grain rotating with the angular momentum J ; the probability of finding the emission at the angular frequency ω depends on the probability of finding the value ω such that

$$pdf(\omega | J)d\omega = f_{\text{VRE}}(s, J)ds = A \exp\left(-\frac{q(s)J^2}{2I_1 k_B T_{\text{vib}}}\right) ds, \quad (20)$$

where we assumed the VRE regime with f_{VRE} given by (6).

For the mode $\omega \equiv \omega_k(s)$, from (20) we can derive

$$pdf_k(\omega | J) = \left(\frac{\partial \omega_k}{\partial s}\right)^{-1} f_{\text{VRE}}(s, J). \quad (21)$$

The emissivity from the mode k is calculated as

$$j_{\nu, k}^a = \frac{1}{4\pi} \int_{J_l}^{J_u} P_{\text{ed}, k}(J, q_{\leq}) f_J(J) pdf_k(\omega | J) 2\pi dJ \\ + \frac{1}{4\pi} \int_{J_l}^{J_u} P_{\text{ed}, k}(J, q_{>}) f_J(J) pdf_k(\omega | J) 2\pi dJ, \quad (22)$$

where q_{\leq} and $q_{>}$ denote $q \leq q_{\text{sp}}$ and $q > q_{\text{sp}}$, respectively, J_l and J_u are lower and upper limits for J corresponding to a given angular frequency $\omega_k(J, q) = \omega$, and 2π appears due to the change of variable from ν to ω .

Emissivity by a grain of size a at the observation frequency ν arising from all emission modes is then

$$j_{\nu}^a \equiv \sum_k j_{\nu, k}^a. \quad (23)$$

Consider, for example, the emission mode $k \equiv m_0$. For the case I_2 which is slightly larger than I_3 , this mode has the angular frequency $\omega_{m_0} = \langle \dot{\phi} \rangle = (J/I_1) q_0$ with q_0 obtained from calculation of ω_{m_0} , which is independent of q for $q < q_{\text{sp}}$ (q_0 approaches I_1/I_2 as $I_3 \rightarrow I_2$, i.e., when irregular shape becomes spheroid). As a result,

$$pdf_{m_0}(\omega | J) = \delta\left(\omega - \left(\frac{J}{I_1}\right) q_0\right). \quad (24)$$

Thus, the first term of (22), denoted by $j_{\nu, m_0, \leq}^a$, is rewritten as

$$j_{\nu, m_0, \leq}^a = \frac{1}{2} \int_{J_l}^{J_u} P_{\text{ed}, m_0}(J, q_{\leq}) f_J(J) \delta\left(\omega - \left(\frac{J}{I_1}\right) q_0\right) dJ \\ = \frac{1}{2} \frac{I_1 f_J(J_0)}{q_0} P_{\text{ed}, m_0}(J_0, q(s)), \quad (25)$$

where $J_0 = I_1 \omega / q_0$, and the value of $q(s)$ remains to be determined.

For $q > q_{\text{sp}}$, $\langle \dot{\phi} \rangle$ is a function of q . Hence, the emissivity (22) for the mode $k \equiv m_0$ becomes

$$j_{\nu, m_0}^a = \frac{1}{2} \frac{I_1 f_J(J_0)}{q_0} \int_0^{s_{\text{sp}}} ds P_{\text{ed}, m_0}(J_0, q(s)) f_{\text{VRE}}(J_0, s) \\ + \frac{1}{2} \int_{J_l}^{J_u} P_{\text{ed}, m_0}(J, q_{>}) f_J(J) pdf_{m_0}(\omega | J) dJ, \quad (26)$$

where s_{sp} is the value of s corresponding to $q = q_{\text{sp}}$, and the term $P_{\text{ed}, m_0}(J_0, q(s))$ in (25) has been replaced by its average value over the internal thermal distribution f_{VRE} .

The emissivity per H is obtained by integrating j_{ν}^a over the grain size distribution

$$\frac{j_{\nu}}{n_H} = \frac{1}{n_H} \int_{a_{\text{min}}}^{a_{\text{max}}} da \frac{dn}{da} j_{\nu}^a, \quad (27)$$

where j_{ν}^a is given by (23).

6.2. A Degenerate Case: Grains of Disk-Like Shape. The spinning dust emissivity from disk-like grains (e.g., $I_2 = I_3$) is a degenerate case of triaxial grains. Basically, a disk-like grain with an angular momentum \mathbf{J} radiates at four frequency modes as follows:

$$\omega_{m_i} \equiv \dot{\phi} + i\dot{\psi} = \frac{J}{I_{\parallel}} [h + i(1-h) \cos \theta], \quad (28)$$

$$\omega_{n_1} \equiv \dot{\psi} = \frac{J}{I_{\parallel}} (1-h) \cos \theta,$$

where $i = 0$ and ± 1 (see HDL10 and [12]).

The emission power of these modes are given by the following analytical forms (HDL10 and [16]):

$$P_{\omega_{m_0}} = \frac{2\mu_{\parallel}^2}{3c^3} \omega_{m_0}^4 \sin^2 \theta, \\ P_{\omega_{m_{\pm 1}}} = \frac{\mu_{\pm}^2}{6c^3} \omega_{m_{\pm 1}}^4 (1 \pm \cos \theta)^2, \quad (29) \\ P_{\omega_{n_1}} = \frac{2\mu_{\perp}^2}{3c^3} \omega_{n_1}^4 \sin^2 \theta.$$

For the disk-like grain, from (3), the number of states in phase space s for q spanning from $1 - q$ becomes

$$s = 1 - \left(\frac{h-q}{h-1}\right)^{1/2} = 1 - \cos \theta, \quad (30)$$

where $q = 1 + (h-1)\sin^2 \theta$ has been used. Thus, for an arbitrary mode with frequency ω_k , we obtain

$$pdf_k(\omega | J) d\omega = f_{\text{VRE}}(s, J) ds = f_{\text{VRE}}(\theta, J) \sin \theta d\theta. \quad (31)$$

Taking use of $\omega = \omega_k(J, \theta)$, we derive

$$pdf_k(\omega | J) = f_{\text{VRE}}(\theta, J) \left(\frac{\partial \omega_k}{\partial \theta}\right)^{-1} \sin \theta. \quad (32)$$

Therefore, by substituting (29) in (22), the emissivity at the observation frequency $\nu = \omega/(2\pi)$ from a disk-like grain of size a is now given by

$$j_{\nu}^a \equiv \frac{1}{2} \frac{f_J(I_{\parallel} \omega / h)}{h} \frac{2\mu_{\parallel}^2}{3c^3} \omega^4 \langle \sin^2 \theta \rangle \\ + \frac{1}{2} \frac{\mu_{\perp}^2}{6c^3} \omega^4 \int_{J_l}^{J_u} pdf_{m_1}(\omega | J) f_J(J) dJ \\ + \frac{1}{2} \frac{\mu_{\perp}^2}{6c^3} \omega^4 \int_{J_l}^{J_u} pdf_{m_{-1}}(\omega | J) f_J(J) dJ \\ + \frac{1}{2} \frac{\mu_{\perp}^2}{3c^3} \omega^4 \int_{J_l}^{J_u} pdf_{n_1}(\omega | J) f_J(J) dJ, \quad (33)$$

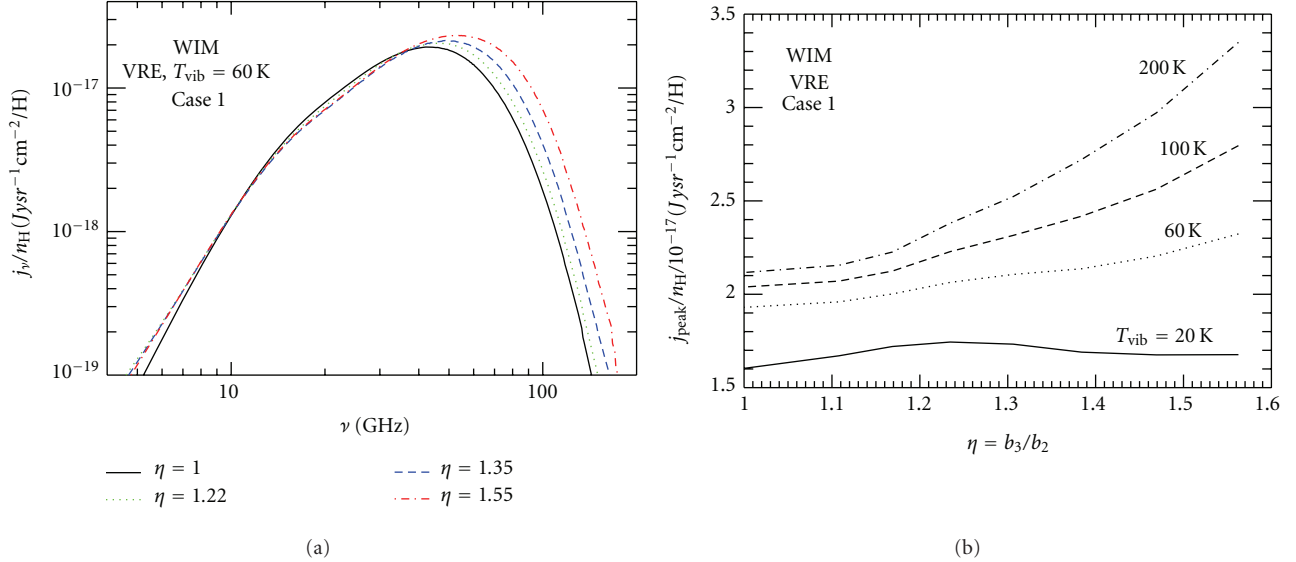


FIGURE 3: Emissivity per H from irregular grains of different degrees of irregularity $\eta = b_3/b_2$ with $T_{\text{vib}} = 60$ and 200 K in the WIM for the case in which the electric dipole moment is isotropically oriented in the grain body (i.e., case 1 with $\mu_1 = \mu/\sqrt{3}$). The emission spectrum shifts to higher frequency as η decreases (i.e., grain becomes more irregular). Here, the grain mass is held fixed as η changes. The figure is reproduced from Hoang et al. [15].

where $pdf_{m_{\pm 1}}$ and pdf_{n_1} are easily derived by using (32) for $\omega_{m_{\pm 1}}$ and ω_{n_1} , and $J_l = I_{\parallel}\omega/(2h-1)$ and $J_u = I_{\parallel}\omega$ for $m_{\pm 1}$ mode, $J_l = I_{\parallel}\omega/(h-1)$ and $J_u = \infty$ for n_1 mode.

6.3. Emissivity. Hoang et al. [15] assumed that the smallest grains of size $a \leq a_2 = 6 \text{ \AA}$ have irregular shape and larger grains are spherical. To compare the emissivity from an irregular grain with that from a disk-like grain, they considered the simplest case of the irregular shape in which the circular cross section of the disk-like grain is adjusted to the elliptical cross section. The emission by two grains of different shapes with the same mass M and thickness L is under interest; therefore, the semiaxes of the elliptical disk are constrained by the grain mass

$$M = \pi R^2 L = \pi b_2 b_3 L, \quad (34)$$

where $R = (4a^3/3L)^{1/2}$ is the radius of the disk-like grain, b_2 and b_3 are the length of semiaxes \mathbf{a}_2 and \mathbf{a}_3 , and $b_1 = L$ is kept constant. Assuming that the circular disk is compressed by a factor $\alpha \leq 1$ along \mathbf{a}_2 , then (34) yields

$$b_2 = \alpha R, \quad b_3 = \alpha^{-1} R. \quad (35)$$

Denote the parameter by $\eta \equiv b_3/b_2 = \alpha^{-2}$, then the degree of grain shape irregularity is completely characterized by η .

For each grain size a , the parameter η is increased from $\eta = 1$ to $\eta = \eta_{\text{max}}$. However, η_{max} is constrained by the fact that the shortest axis \mathbf{a}_2 should not be shorter than the grain thickness L . The value $\eta_{\text{max}} \sim 3/2$ is conservatively chosen.

Although the irregular grain can radiate at a large number of frequency modes, only the modes with the order $|m| \leq 2$ are important. The higher-order modes contribute

less than $\sim 0.5\%$ to the total emission, and thus they are neglected. Hoang et al. [15] assumed that grains smaller than a_2 have a fixed vibrational temperature T_{vib} (see Hoang et al. [15] for the detailed treatment of T_{vib} distribution), and that for the instantaneous value of J , the rotational energy has a probability distribution f_{VRE} (i.e., VRE regime, see (6)).

The grain size distribution dn/da from Draine and Li [42] is adopted with the total to selective extinction $R_V = 3.1$ and the total carbon abundance per hydrogen nucleus $b_C = 5.5 \times 10^{-5}$ in carbonaceous grains with $a_{\text{min}} = 3.55 \text{ \AA}$ and $a_{\text{max}} = 100 \text{ \AA}$.

The spinning dust emissivity is calculated for a so-called model A (similar to DL98b; HDL10), in which 25% of grains have the electric dipole moment parameter $\beta = 2\beta_0$, 50% have $\beta = \beta_0$, and 25% have $\beta = 0.5\beta_0$ with $\beta_0 = 0.4$ D. In the rest of the paper, the notation model A is omitted, unless stated otherwise.

The left panel in Figure 3 shows the spinning dust emissivity for different degrees of irregularity η and with a dust temperature $T_{\text{vib}} = 60$ K in the WIM. The emission spectrum for a given T_{vib} shifts to higher frequency as η decreases (i.e., the degree of grain irregularity increases), but their spectral profiles remain similar. The right panel shows the increase of peak emissivity J_{peak} with increasing η .

One particular feature in Figure 3(b) is that for axisymmetric grains ($\eta = 1$), the emissivity increases by a factor of 1.3 with T_{vib} increasing from 20 to 200 K. However, for the irregular grain with high triaxiality $\eta = 1.5$, the emissivity increases by a factor of 2. The peak frequency is increased by a factor of 1.4.

This feature is easy to understand because the irregular grain radiate at more frequency modes than the axisymmetric grain. As a result, for the grain temperature to increase to

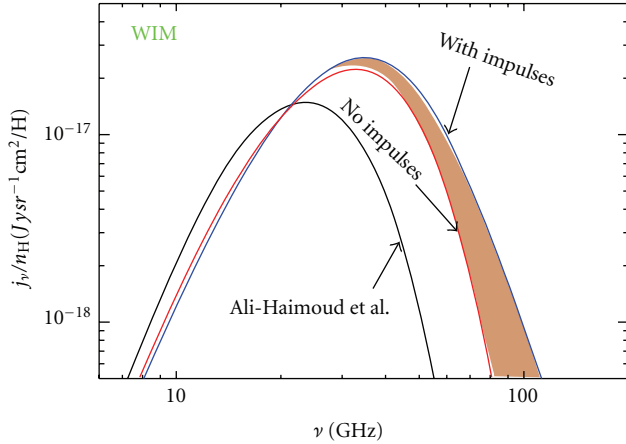


FIGURE 4: Emissivity per H obtained for WIM without ionic impulses using the Fokker-Planck equation from Ali-Haimoud et al. [12] and with impulses using our LE simulations for grain wobbling. The spectra are efficiently broadened as a result of impulses (see blue line). The figure is reproduced from Hoang et al. [13].

a sufficiently high value, it results in the uniform distribution of the angle between grain symmetry axis and angular momentum, so that the spinning dust emissivity becomes saturated. On the other hand, for the triaxial grain, as T_{vib} increases, it allows the grain to rotate about its axis of minimum inertia (smallest moment of inertia). As a result, the grain radiates at frequency modes with higher frequency and power.

In the case of efficient IVRET, vibrational energy is converted to rotational emission, which results in the increase of both emissivity and peak frequency. As shown, the energy transfer is more efficient for the more irregular grain. The reason for this is that the more irregular grain allows the grain to spend a larger fraction of time rotating along the axis of minor inertia.

The effect of impulsive excitations by single-ion collisions is shown in Figure 4. One can see that the impulses from ions can increase the emissivity by $\sim 23\%$ and slightly increase the peak frequency (see Figure 4). The tail of high frequency part is obviously extended due to the contribution from ionic impulses with large angular momentum.

7. Constraining Spinning Dust Parameters and Implications

Spinning dust emission involves a number of parameters, including grain physical parameters and environmental parameters. Among them, the grain dipole moment and gas density are two most important parameters, but they can be constrained using theoretical modeling combined with observation data (see, e.g., Dobler et al. [43] and Hoang et al. [15]). In the following, we discuss a number of parameters, which are shown to be important but more difficult to constrain through observation.

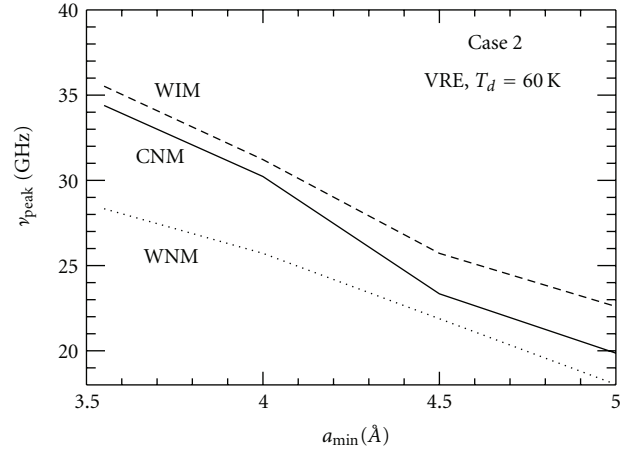


FIGURE 5: Decrease of the peak frequency ν_{peak} of spinning dust spectrum with the lower cutoff of grain size distribution a_{min} for various environmental conditions. The figure is reproduced from Hoang et al. [15].

7.1. Lower Cutoff of Grain Size Distribution a_{min} . The spinning dust emission spectrum is sensitive to the population of tiny dust grains, and its peak frequency is mostly determined by the smallest PAHs. Let a_{min} be the size of the smallest PAHs. When a_{min} is increased, the peak frequency ν_{peak} decreases accordingly.

Figure 5 shows the variation of ν_{peak} as a function of a_{min} for various environments for the case in which the grain dipole moment lies in the grain plane (Case 2) with $\mu_1 = 0$ and with the VRE regime ($T_d = 60$ K). As expected, ν_{peak} decreases generically with a_{min} increasing. Thus, in addition to grain dipole moment, the lower cutoff of grain size also plays an important role.

7.2. Constraining the Shape of Very Small Grains. Very small grains and PAHs are expected to be nonspherical. However, constraining grain triaxiality using spinning dust appears rather challenging. In the simplest case where the grain shape can be approximated as a triaxial ellipsoid, the possibility is still low because there are many parameters involved in the spinning dust.

7.3. Can Compressible Turbulence Be Observed through Spinning Dust Emission? The discussion of interstellar conditions adopted in DL98 and other works on spinning dust was limited by idealized interstellar phases. It is now recognized that turbulence plays an important role in shaping the interstellar medium.

For spinning dust, the turbulence can increase the emissivity due to its nonlinear dependence on material density. Indeed, in a medium with density fluctuations, the effective emissivity is

$$\langle j_\nu \rangle = \int_0^1 f(x) j_\nu(x \langle \rho \rangle) dx, \quad (36)$$

where $f(x)dx$ is the fraction of the mass with $\rho/\langle \rho \rangle \in (x, x+dx)$. We use compression distributions $f(x)$ obtained from

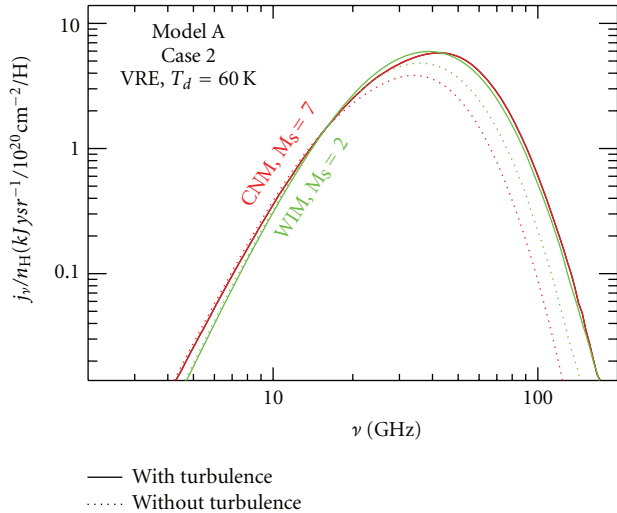


FIGURE 6: Spinning dust emissivity per H in the presence of compressible turbulence with sonic Mach number $M_s = 2$ and 7 , compared to that from uniform medium with $n_H = \bar{n}_H$ for the CNM (red) and WIM (green). The peak emissivity is increased, and the spectrum is shifted to higher frequency due to compressible turbulence. Case 2 ($\mu_1 = 0$) of μ orientation is considered. Figure reproduced from Hoang et al. [15].

MHD simulations for $M_s = 2$ and 7 to evaluate $\langle j_\nu \rangle$ for the WIM and CNM, respectively.

We assume the case 2 ($\mu_1 = 0$) of μ orientation. The resulting effective emissivity is compared with the emissivity from the uniform medium in Figure 6. It can be seen that the turbulent compression increases the emissivity and shifts the peak to higher ν_{peak} . The increase of emissivity is significant for strong turbulent medium.

The distribution of phases, for instance, CNM and WNM of the ISM at high latitudes, can be obtained from absorption lines. Similarly, by studying fluctuations of emission, it is possible to constrain parameters of turbulence. In an idealized case of a single-phase medium with fluctuations of density with a given characteristic size, one can estimate the value of the 3D fluctuation by studying the 2D fluctuations of column density. More sophisticated techniques for obtaining sonic Mach numbers have been developed recently (see Kowal et al. [44], Esquivel and Lazarian [45] and Burkhart et al. [46]). (It may be seen that Alfvén Mach numbers have subdominant effect on the distribution of densities (see Kowal et al. [44]). Thus, in our study we did not vary the Alfvén Mach number.) In particular, Burkhart et al. [47], using just column density fluctuations of the SMC, obtained a distribution of Mach numbers corresponding to the independent measurements obtained using Doppler shifts and absorption data. With such an input, it is feasible to quantify the effect of turbulence in actual observational studies of spinning dust emission.

7.4. Effect of Dust Acceleration on Spinning Dust Emission. Collisions of ultrasmall grains with ions and neutrals in plasma appear to be a dominant mechanism of rotational

excitations for spinning dust emission, particularly, in dark clouds where UV photons are blocked out. Current spinning dust models assume Brownian motion of grains relative to gas, but it is known that grains may move with suprathermal velocities due to acceleration by turbulence (see, e.g., [48], Yan and Lazarian [49, 50], and Hoang et al. [51]) and random charge fluctuations (Ivlev et al. [52] and Hoang and Lazarian [53]). The latter mechanism, namely, random charge fluctuations-induced acceleration, is found to be efficient for tiny grains (Hoang and Lazarian [53]).

The resonant acceleration by fast modes of MHD turbulence, which occurs when the grain gyroradius is comparable to the scale of turbulence eddy (i.e., $r_g \sim k^{-1}$), is considered a dominant mechanism for large grains ($>10^{-5}$ cm), whereas it is negligible for ultrasmall grains because the grain gyroradius falls below the cutoff scale of the turbulence due to viscous damping (see Yan et al. [50] and Hoang et al. [51]).

In highly ionized media (e.g., WIM, HII regions), the resonant acceleration by MHD turbulence may become important for ultrasmall grains because the damping cutoff of MHD turbulence is suppressed due to the decrease of viscous neutral damping. We also note that recent observations by Paladini et al. [54]) revealed that PAHs and ultrasmall grains may be present in HII regions, as shown through their $8 \mu\text{m}$ and $24 \mu\text{m}$ emission features, respectively.

Thus, assuming that grain rotational kinetic energy is equal to its translational energy, the acceleration by these aforementioned processes is expected to increase the spinning dust emission. Further studies should take this issue into account.

8. Polarization of Spinning Dust Emission and Alignment of Ultrasmall Grains

8.1. Polarization of Anomalous Microwave Emission. Spinning dust emission is an important foreground component that contaminates with the CMB radiation in the frequency 10–90 GHz. An understanding of how much is this emission component polarized is becoming a pressing question for future CMB B-mode missions.

Recent observational studies (Dickinson et al. [55], López-Caraballo et al. [56], and Macellari et al. [57]) showed that the average polarization of AME is between 2 and 5%. In the last years, significant progress has been made in understanding spinning dust emission, both in theory and observation, but the principal mechanism of alignment of ultrasmall grains is not well understood.

8.2. Alignment of Ultrasmall Dust Grains. Grain alignment is an exciting problem (see Lazarian [58] for a review). The most promising mechanism for the grain alignment is based on radiative torques. Proposed originally by Dolginov and Mytrophanov [59], it is related to the interaction of unpolarized radiation with *irregular* grains. The numerical studies in Draine and Weingartner [60, 61] showed the efficiency and promise of the radiative torques (which later were termed RATs). The physical picture of the RAT

alignment and a detailed study of important relevant effects are presented in Lazarian and Hoang [62, 63] and Hoang and Lazarian [64–66]. However, the efficiency of RATs plummets as the size of grains gets much smaller than the radiation wavelength. Therefore, this mechanism, which seems to provide a good correspondence with the optical and infrared data (see Lazarian [58] and Whittet et al. [67]), cannot be applicable to ultrasmall spinning dust.

Microwave emission from spinning grains is expected to be polarized if grains are aligned. Alignment of ultrasmall grains (essentially PAHs) is likely to be different from alignment of large (i.e., $a > 10^{-6}$ cm) grains as discussed previously. One of the mechanisms that might produce the alignment of the ultrasmall grains is the paramagnetic dissipation mechanism proposed by Davis and Greenstein [68]. The Davis-Greenstein alignment mechanism (Davis and Greenstein [68] and Roberge and Lazarian [69]) is straightforward; for a spinning grain, the component of the interstellar magnetic field perpendicular to the grain angular velocity varies in grain coordinates, resulting in time-dependent magnetization, associated energy dissipation, and a torque acting on the grain [68]. As a result, grains tend to rotate with angular momenta parallel to the interstellar magnetic field.

Lazarian and Draine [70] (henceforth LD00) found that the traditional picture of paramagnetic relaxation is incomplete, since it disregards the so-called “Barnett magnetization” (Landau and Lifshitz [71]). The Barnett effect, the inverse of the Einstein-de Haas effect, consists of the spontaneous magnetization of a paramagnetic body rotating in field-free space. This effect can be understood in terms of the lattice-sharing part of its angular momentum with the spin system. Therefore, the implicit assumption in Davis and Greenstein [68] that the magnetization within a *rotating grain* in a *static* magnetic field is equivalent to the magnetization within a *stationary grain* in a *rotating* magnetic field is clearly not exact.

LD00 accounted for the “Barnett magnetization” and termed the effect of enhanced paramagnetic relaxation arising from grain magnetization “resonance paramagnetic relaxation.” It is clear from Figure 7 that resonance paramagnetic relaxation persists at the frequencies when the Davis-Greenstein relaxation vanishes. However, the polarization is marginal for $\nu > 35$ GHz anyhow. The discontinuity at ~ 20 GHz is due to the assumption that smaller grains are planar and larger grains are spherical. The microwave emission will be polarized in the plane perpendicular to the magnetic field because the angular momentum is partially aligned with the magnetic field.

8.3. Constraining the Alignment of Ultrasmall Grains

8.3.1. Can We Constrain the Alignment of Ultrasmall Grains through Polarization of Midinfrared (2–12 μm) Emission Features? The answer to this question is “probably not.” Indeed, as discussed earlier, midinfrared emission from ultrasmall grains takes place as they absorb UV photons. These photons raise grain vibrational temperature, randomizing grain axes

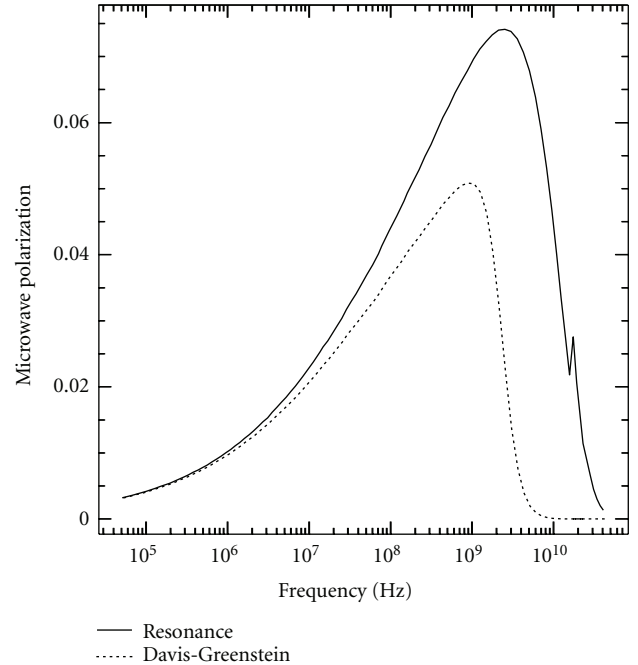


FIGURE 7: Polarization for both resonance paramagnetic relaxation and Davis-Greenstein relaxation for grains in the cold interstellar medium as a function of frequency (from LD00). For resonance relaxation the saturation effects are neglected, which means that the upper curves correspond to the *maximal* values allowed by the resonant paramagnetic mechanism.

in relation to its angular momentum (see Lazarian and Roberge [72]). Taking values for Barnett relaxation from Lazarian and Draine [73], we estimate the randomization time of the 10^{-7} cm grain to be 2×10^{-6} s, which is less than the grain cooling time due to IR emission. As a result, the emanating infrared emission will be polarized very marginally. If, however, Barnett relaxation is suppressed, the randomization time will be determined by inelastic relaxation (Lazarian and Efreimsky [74]) and will be ~ 0.1 s, which would entail a partial polarization of infrared emission.

8.3.2. Can We Constrain the Alignment of Ultrasmall Grains via the Ultraviolet Polarization? PAHs and ultrasmall grains that produce spinning dust emission are likely the same particles that produce the prominent UV absorption feature at 2175 \AA (see, e.g., Draine and Li [42]). The lack of polarization excess at 2175 \AA is consistent with the expectation that the PAHs are poorly aligned. However, the small degree of polarization (see Wolff et al. [75]) indicates that there must be some residual alignment of ultrasmall grains. The constraint for such a residual alignment can be obtained by fitting the theoretical model with the UV polarization of starlight (Martin [76]). When the residual alignment is available, one can predict the polarization level of spinning dust.

Apart from the emission from spinning dust, another new type of emission from dust is possible. Draine and

Lazarian [77] noticed that the strongly magnetized material is capable of producing much more microwave thermal emission compared with nonmagnetic grains. They suggested this as a possible alternative to spinning dust emission, which can be responsible for a part or even most of the anomalous microwave emission. Such an emission can be strongly polarized, making anomalous emission an important contaminant in terms of CMB polarization studies.

Further research showed that at the frequencies 20–90 GHz, the spinning dust dominates. However, Draine and Hensley [78] performed new calculations of microwave response of strongly magnetic grains. At higher frequencies, this new extensive study of evaluating microwave emissivity of strongly magnetic grains showed that magnetic dipole response of interstellar dust may be extremely important.

9. Summary

The principal points discussed previously are as follows.

- (i) The model of spinning dust emission proposed by DL98 proved to be capable of explaining anomalous microwave emission, and its predictions were confirmed by numerous observations since the introduction of the model.
- (ii) The DL98 spinning dust model has been improved recently by including the effects of thermal fluctuations within dust grains, impulsive excitations with single ions, transient heating by UV photons, triaxiality of grain shape, and compressible turbulence, which made the spinning dust model more realistic.
- (iii) Spinning dust emission involves a number of grain physical parameters and environmental parameters. With the latest progress on theoretical modeling and observations, the possibility of using spinning dust as a diagnostic tool for physical parameters of ultrasmall dust is open.
- (iv) The spinning dust emission is expected to be partially polarized, but further studies on alignment of ultrasmall grains and modeling of spinning dust polarization are vitally required.

Acknowledgments

A. Lazarian acknowledges the support of the Center for Magnetic Self-Organization and the NASA Grant no. NNX11AD32G. T. Hoang is grateful for fruitful discussions with Peter Martin on constraining the alignment of ultrasmall grains and polarization of anomalous microwave emission.

References

- [1] F. R. Bouchet, S. Prunet, and S. K. Sethi, “Multifrequency Wiener filtering of cosmic microwave background data with polarization,” *Monthly Notices of the Royal Astronomical Society*, vol. 302, no. 4, pp. 663–676, 1999.
- [2] M. Tegmark, D. J. Eisenstein, W. Hu, and A. de Oliveira-Costa, “Foregrounds and forecasts for the cosmic microwave background,” *The Astrophysical Journal*, vol. 530, no. 1, pp. 133–165, 2000.
- [3] A. Kogut, A. J. Banday, C. L. Bennett, K. M. Górski, G. Hinshaw, and W. T. Reach, “High-latitude galactic emission in the COBE differential microwave radiometer 2 year sky maps,” *The Astrophysical Journal*, vol. 460, no. 1, pp. 1–9, 1996.
- [4] A. Kogut, A. J. Banday, C. L. Bennett et al., “Microwave emission at high galactic latitudes in the four-year DMR sky maps,” *The Astrophysical Journal*, vol. 464, no. 1, pp. L5–L9, 1996.
- [5] A. De Oliveira-Costa, M. Tegmark, D. P. Finkbeiner et al., “A new spin on galactic dust,” *The Astrophysical Journal*, vol. 567, no. 1, pp. 363–369, 2002.
- [6] B. T. Draine and A. Lazarian, “Electric dipole radiation from spinning dust grains,” *The Astrophysical Journal*, vol. 508, no. 1, pp. 157–179, 1998.
- [7] B. T. Draine and A. Lazarian, “Diffuse galactic emission from spinning dust grains,” *The Astrophysical Journal*, vol. 494, no. 1, pp. L19–L22, 1998.
- [8] W. C. Erickson, “A mechanism of non-thermal radio-noise origin,” *The Astrophysical Journal*, vol. 126, p. 480, 1957.
- [9] A. Ferrara and R. J. Dettmar, “Radio-emitting dust in the free electron layer of spiral galaxies: testing the disk/halo interface,” *The Astrophysical Journal*, vol. 427, no. 1, pp. 155–159, 1994.
- [10] A. Lazarian and D. Finkbeiner, “Microwave emission from aligned dust,” *New Astronomy Reviews*, vol. 47, no. 11–12, pp. 1107–1116, 2003.
- [11] D. P. Finkbeiner, “Microwave interstellar medium emission observed by the Wilkinson Microwave Anisotropy Probe,” *The Astrophysical Journal*, vol. 614, no. 1, pp. 186–193, 2004.
- [12] Y. Ali-Haïmoud, C. M. Hirata, and C. Dickinson, “A refined model for spinning dust radiation,” *Monthly Notices of the Royal Astronomical Society*, vol. 395, no. 2, pp. 1055–1078, 2009.
- [13] T. Hoang, B. T. Draine, and A. Lazarian, “Improving the model of emission from spinning dust: effects of grain wobbling and transient spin-up,” *The Astrophysical Journal*, vol. 715, no. 2, pp. 1462–1485, 2010.
- [14] N. Ysard and L. Verstraete, “The long-wavelength emission of interstellar PAHs: characterizing the spinning dust contribution,” *Astronomy and Astrophysics*, vol. 509, article A12, 2010.
- [15] T. Hoang, A. Lazarian, and B. T. Draine, “Spinning dust emission: effects of irregular grain shape, transient heating, and comparison with wilkinson microwave anisotropy probe results,” *The Astrophysical Journal*, vol. 741, p. 87, 2011.
- [16] K. Silsbee, Y. Ali-Haïmoud, and C. M. Hirata, “Spinning dust emission: the effect of rotation around a non-principal axis,” *Monthly Notices of the Royal Astronomical Society*, vol. 411, no. 4, pp. 2750–2769, 2011.
- [17] B. T. Draine and A. Lazarian, “Microwave emission from galactic dust grains,” *Microwave Foregrounds*, vol. 181, p. 133, 1999.
- [18] A. Lazarian and S. Prunet, “Polarized microwave emission from dust,” in *Proceedings of the Workshop on Astrophysical Polarized Backgrounds*, vol. 609, pp. 32–43, March 2002.
- [19] A. Li and B. T. Draine, “Infrared emission from interstellar dust. II. The diffuse interstellar medium,” *The Astrophysical Journal*, vol. 554, no. 2, pp. 778–802, 2001.
- [20] A. de Oliveira-Costa, A. Kogut, M. J. Devlin, C. Barth Netterfield, L. A. Page, and E. J. Wollack, “Galactic microwave emission at degree angular scales,” *The Astrophysical Journal*, vol. 482, no. 1, pp. L17–L20, 1997.

- [21] E. M. Leitch, A. C. S. Readhead, T. J. Pearson, and S. T. Myers, "An anomalous component of galactic emission," *The Astrophysical Journal*, vol. 486, no. 1, pp. L23–L26, 1997.
- [22] A. De Oliveira-Costa, M. Tegmark, L. A. Page, and S. P. Boughn, "Galactic emission at 19 GHz," *The Astrophysical Journal*, vol. 509, no. 1, pp. L9–L12, 1998.
- [23] A. de Oliveira-Costa, M. Tegmark, C. M. Gutiérrez et al., "Cross-correlation of tenerife data with galactic templates-evidence for spinning dust?" *The Astrophysical Journal*, vol. 527, no. 1, pp. L9–L12, 1999.
- [24] P. R. McCullough, J. E. Gaustad, W. Rosing, and D. van Buren, "Implications of H observations for studies of the CMB," *Microwave Foregrounds*, vol. 181, p. 253, 1999.
- [25] A. de Oliveira-Costa, M. Tegmark, M. J. Devlin et al., "Galactic contamination in the qmap experiment," *The Astrophysical Journal*, vol. 542, no. 1, pp. L5–L8, 2000.
- [26] D. P. Finkbeiner, D. J. Schlegel, C. Frank, and C. Heiles, "Tentative detection of electric dipole emission from rapidly rotating dust grains," *The Astrophysical Journal*, vol. 566, no. 2, pp. 898–904, 2002.
- [27] C. L. Bennett, R. S. Hill, G. Hinshaw et al., "First-year Wilkinson Microwave Anisotropy Probe (WMAP) observations: foreground emission," *The Astrophysical Journal*, vol. 148, no. 1, pp. 97–117, 2003.
- [28] D. P. Finkbeiner, M. Davis, and D. J. Schlegel, "Extrapolation of galactic dust emission at 100 microns to cosmic microwave background radiation frequencies using FIRAS," *The Astrophysical Journal*, vol. 524, no. 2, pp. 867–886, 1999.
- [29] G. Langston, A. Minter, L. D'Addario, K. Eberhardt, K. Koski, and J. Zuber, "The first Galactic plane survey at 8.35 and 14.35 GHz," *The Astronomical Journal*, vol. 119, no. 6, pp. 2801–2827, 2000.
- [30] D. P. Finkbeiner, G. I. Langston, and A. H. Minter, "Microwave interstellar medium emission in the green bank galactic plane survey: evidence for spinning dust," *The Astrophysical Journal*, vol. 617, no. 1, pp. 350–359, 2004.
- [31] B. Gold, C. L. Bennett, R. S. Hill et al., "Five-year wilkinson microwave anisotropy probe observations: galactic foreground emission," *The Astrophysical Journal*, vol. 180, no. 2, pp. 265–282, 2009.
- [32] B. Gold, N. Odegard, J. L. Weiland et al., "Seven-year wilkinson microwave anisotropy probe (WMAP*) observations: galactic foreground emission," *The Astrophysical Journal*, vol. 192, no. 2, article 15, 2011.
- [33] P. Collaboration, P. A. R. Ade, N. Aghanim et al., "Planck early results. xx. new light on anomalous microwave emission from spinning dust grains," *Astronomy and Astrophysics*, vol. 536, article A20, 2011.
- [34] A. M. M. Scaife, B. Nikolic, D. A. Green et al., "Microwave observations of spinning dust emission in NGC 6946," *Monthly Notices of the Royal Astronomical Society*, vol. 406, no. 1, pp. L45–L49, 2010.
- [35] C. T. Tibbs, R. Paladini, M. Compiègne et al., "A multi-wavelength investigation of RCW175: an H II region harboring spinning dust emission," *The Astrophysical Journal*, vol. 754, no. 2, p. 94, 2012.
- [36] S. Casassus, C. Dickinson, K. Cleary et al., "Centimetre-wave continuum radiation from the ρ Ophiuchi molecular cloud," *Monthly Notices of the Royal Astronomical Society*, vol. 391, no. 3, pp. 1075–1090, 2008.
- [37] C. T. Tibbs, N. Flagey, R. Paladini et al., "Spitzer characterization of dust in an anomalous emission region: the Perseus cloud," *Monthly Notices of the Royal Astronomical Society*, vol. 418, no. 3, pp. 1889–1900, 2011.
- [38] C. Bot, N. Ysard, D. Paradis et al., "Submillimeter to centimeter excess emission from the magellanic clouds. II. on the nature of the excess," *Astronomy and Astrophysics*, vol. 523, p. 20, 2010.
- [39] J. C. Weingartner and B. T. Draine, "Radiative torques on interstellar grains. III. Dynamics with thermal relaxation," *The Astrophysical Journal*, vol. 589, no. 1, pp. 289–318, 2003.
- [40] E. M. Purcell, "Suprathermal rotation of interstellar grains," *The Astrophysical Journal*, vol. 231, pp. 404–416, 1979.
- [41] A. Lazarian and W. G. Roberge, "Barnett relaxation in thermally rotating grains," *The Astrophysical Journal*, vol. 484, no. 1, pp. 230–237, 1997.
- [42] B. T. Draine and A. Li, "Infrared emission from interstellar dust. IV. The silicate-graphite-PAH model in the post-Spitzer ERA," *The Astrophysical Journal*, vol. 657, no. 2, pp. 810–837, 2007.
- [43] G. Dobler, B. Draine, and D. P. Finkbeiner, "Constraining spinning dust parameters with the wmap five-year data," *The Astrophysical Journal*, vol. 699, no. 2, pp. 1374–1388, 2009.
- [44] G. Kowal, A. Lazarian, and A. Beresnyak, "Density fluctuations in MHD turbulence: spectra, intermittency, and topology," *The Astrophysical Journal*, vol. 658, no. 1, pp. 423–445, 2007.
- [45] A. Esquivel and A. Lazarian, "Tsallis statistics as a tool for studying interstellar turbulence," *The Astrophysical Journal*, vol. 710, no. 1, pp. 125–132, 2010.
- [46] B. Burkhart, D. Falceta-Gonçalves, G. Kowal, and A. Lazarian, "Density studies of mhd interstellar turbulence: statistical moments, correlations and bispectrum," *The Astrophysical Journal*, vol. 693, p. 250, 2009.
- [47] B. Burkhart, S. Stanimirović, A. Lazarian, and G. Kowal, "Characterizing magnetohydrodynamic turbulence in the small magellanic cloud," *The Astrophysical Journal*, vol. 708, no. 2, pp. 1204–1220, 2010.
- [48] B. T. Draine, "Grain evolution in dark clouds," in *Protostars and Planets II*, pp. 621–640, University of Arizona Press, Tucson, Ariz, USA, 1985.
- [49] H. Yan and A. Lazarian, "Grain acceleration by magnetohydrodynamic turbulence: gyroresonance mechanism," *The Astrophysical Journal*, vol. 592, no. 1, pp. L33–L36, 2003.
- [50] T. Hoang and A. Lazarian, "Acceleration of very small dust grains due to random charge fluctuations," *The Astrophysical Journal*, vol. 761, no. 2, p. 96, 2012.
- [51] T. Hoang, A. Lazarian, and R. Schlickeiser, "Revisiting acceleration of charged grains in magnetohydrodynamic turbulence," *The Astrophysical Journal*, vol. 747, no. 1, p. 54, 2012.
- [52] A. V. Ivlev, A. Lazarian, V. N. Tsytovich, U. de Angelis, T. Hoang, and G. E. Morfill, "Acceleration of small astrophysical grains due to charge fluctuations," *The Astrophysical Journal*, vol. 723, no. 1, pp. 612–619, 2010.
- [53] T. Hoang and A. Lazarian, "Acceleration of small dust grains due to charge fluctuations," arXiv, 1112.3409, 2011.
- [54] R. Paladini, G. Umana, M. Veneziani et al., "Spitzer and Herschel multiwavelength characterization of the dust content of evolved HII regions," *The Astrophysical Journal*, vol. 760, no. 2, 2012.
- [55] C. Dickinson, M. Peel, and M. Vidal, "New constraints on the polarization of anomalous microwave emission in nearby molecular clouds," *Monthly Notices of the Royal Astronomical Society*, vol. 418, no. 1, pp. L35–L39, 2011.
- [56] C. H. López-Caraballo, J. A. Rubiño-Martín, R. Rebolo, and R. Génova-Santos, "Constraints on the polarization of the anomalous microwave emission in the perseus molecular complex from seven-year wmap data," *The Astrophysical Journal*, vol. 729, no. 1, article 25, 2011.

- [57] N. Macellari, E. Pierpaoli, C. Dickinson, and J. E. Vaillancourt, "Galactic foreground contributions to the 5-year Wilkinson Microwave Anisotropy Probe maps," *Monthly Notices of the Royal Astronomical Society*, vol. 418, no. 2, pp. 888–905, 2011.
- [58] A. Lazarian, "Tracing magnetic fields with aligned grains," *Journal of Quantitative Spectroscopy and Radiative Transfer*, vol. 106, no. 1–3, pp. 225–256, 2007.
- [59] A. Z. Dolginov and I. G. Mytrophanov, "Orientation of cosmic dust grains," *Astrophysics and Space Science*, vol. 43, no. 2, pp. 291–317, 1976.
- [60] B. T. Draine and J. C. Weingartner, "Radiative torques on interstellar grains. I. Superthermal spin-up," *The Astrophysical Journal*, vol. 470, no. 1, pp. 551–565, 1996.
- [61] B. T. Draine and J. C. Weingartner, "Radiative torques on interstellar grains. II. Grain alignment," *The Astrophysical Journal*, vol. 480, no. 2, pp. 633–646, 1997.
- [62] A. Lazarian and T. Hoang, "Radiative torques: analytical model and basic properties," *Monthly Notices of the Royal Astronomical Society*, vol. 378, no. 3, pp. 910–946, 2007.
- [63] A. Lazarian and T. Hoang, "Alignment of dust with magnetic inclusions: radiative torques and superparamagnetic barnett and nuclear relaxation," *The Astrophysical Journal*, vol. 676, no. 1, pp. L25–L28, 2008.
- [64] T. Hoang and A. Lazarian, "Radiative torque alignment: essential physical processes," *Monthly Notices of the Royal Astronomical Society*, vol. 388, no. 1, pp. 117–143, 2008.
- [65] T. Hoang and A. Lazarian, "Grain alignment induced by radiative torques: effects of internal relaxation of energy and complex radiation field," *The Astrophysical Journal*, vol. 697, no. 2, pp. 1316–1333, 2009.
- [66] T. Hoang and A. Lazarian, "Radiative torques alignment in the presence of pinwheel torques," *The Astrophysical Journal*, vol. 695, pp. 1457–1476, 2009.
- [67] D. C. B. Whittet, J. H. Hough, A. Lazarian, and T. Hoang, "The efficiency of grain alignment in dense interstellar clouds: a reassessment of constraints from near-infrared polarization," *The Astrophysical Journal*, vol. 674, no. 1, pp. 304–315, 2008.
- [68] L. Davis and J. L. Greenstein, "The polarization of starlight by aligned dust grains," *The Astrophysical Journal*, vol. 114, p. 206, 1951.
- [69] W. G. Roberge and A. Lazarian, "Davis-Greenstein alignment of oblate spheroidal grains," *Monthly Notices of the Royal Astronomical Society*, vol. 305, pp. 615–630, 1999.
- [70] A. Lazarian and B. T. Draine, "Resonance paramagnetic relaxation and alignment of small grains," *The Astrophysical Journal*, vol. 536, no. 1, pp. L15–L18, 2000.
- [71] L. D. Landau and E. M. Lifshitz, *Electrodynamics of Continuous Media*, Addison-Wesley, Reading, Mass, USA, 1960.
- [72] A. Lazarian and W. G. Roberge, "Cosmic rays and grain alignment," *Monthly Notices of the Royal Astronomical Society*, vol. 287, no. 4, pp. 941–946, 1997.
- [73] A. Lazarian and B. T. Draine, "Nuclear spin relaxation within interstellar grains," *The Astrophysical Journal*, vol. 520, no. 1, pp. L67–L70, 1999.
- [74] A. Lazarian and M. Efroimsky, "Inelastic dissipation in a freely rotating body: application to cosmic dust alignment," *Monthly Notices of the Royal Astronomical Society*, vol. 303, no. 4, pp. 673–684, 1999.
- [75] M. J. Wolff, G. C. Clayton, S. H. Kim, P. G. Martin, and C. M. Anderson, "Ultraviolet interstellar linear polarization. III. Features," *The Astrophysical Journal*, vol. 478, no. 1, pp. 395–402, 1997.
- [76] P. G. Martin, "On predicting the polarization of low frequency emission by diffuse interstellar terstellar dust," in *Sky Polarisation at Far-infrared to Radio Wavelengths: The Galactic Screen Before the Cosmic Microwave Background*, M. -A. Miville-Deschênes and F. Boulanger, Eds., vol. 23 of *EAS Publications Series*, pp. 165–188, 2007.
- [77] B. T. Draine and A. Lazarian, "Magnetic dipole microwave emission from dust grains," *The Astrophysical Journal*, vol. 512, no. 2, pp. 740–754, 1999.
- [78] B. T. Draine and B. Hensley, "Magnetic nanoparticles in the interstellar medium: emission spectrum and polarization," arXiv, astro-ph.GA, 2012.

Research Article

On the Limitations of the Anomalous Microwave Emission Emissivity

Christopher T. Tibbs,¹ Roberta Paladini,² and Clive Dickinson³

¹Spitzer Science Center, Infrared Processing and Analysis Center, California Institute of Technology, Pasadena, CA 91125, USA

²NASA Herschel Science Center, Infrared Processing and Analysis Center, California Institute of Technology, Pasadena, CA 91125, USA

³Jodrell Bank Centre for Astrophysics, School of Physics and Astronomy, The University of Manchester, Manchester, M13 9PL, UK

Correspondence should be addressed to Christopher T. Tibbs, ctibbs@ipac.caltech.edu

Received 13 August 2012; Revised 12 October 2012; Accepted 7 November 2012

Academic Editor: Laurent Verstraete

Copyright © 2012 Christopher T. Tibbs et al. This is an open access article distributed under the Creative Commons Attribution License, which permits unrestricted use, distribution, and reproduction in any medium, provided the original work is properly cited.

Many studies of anomalous microwave emission (AME) have computed an AME emissivity to compare the strength of the AME detected in different regions. Such a value is usually defined as the ratio between the intensity of the AME at 1 cm and the thermal dust emission at 100 μm . However, as studies of Galactic dust emission have shown, the intensity of the thermal dust emission at 100 μm is strongly dependent on the dust temperature, which has severe implications for the AME emissivity defined in this way. In this work, we illustrate and quantify this effect and find that the AME emissivity decreases by a factor of 11.1 between dust temperatures of 20 and 30 K. We, therefore, conclude that computing the AME emissivity relative to the 100 μm emission does not allow for accurate comparisons between the AME observed in different environments. With this in mind, we investigate the use of other tracers of the dust emission with which to compute the AME emissivity and we ultimately conclude that, despite the difficulty in deriving its value, the column density of the dust would be the most suitable quantity with which to compute the AME emissivity.

1. Introduction

In recent years there has been growing evidence for the existence of a new component of microwave emission present in the interstellar medium (ISM). This emission appears to be spatially correlated with the dust in the ISM, although it produces an excess of emission with respect to the predicted thermal, vibrational dust emission at these frequencies (e.g., [1]), and as such this component is often described as anomalous. There have been only a handful of detections of this anomalous microwave emission (AME) component originating from both the diffuse ISM at mid-to-high latitudes (e.g., [2–4]) and specific Galactic sources such as the Perseus and ρ Oph molecular clouds [5–9], the dark clouds LDN1622 [10, 11], LDN1621 [12], and LDN1111 [13], and a variety of HII regions [14–16]. Additionally, the first detection of AME in a star forming region in the external galaxy, NGC6946, was reported [17, 18], confirming that this emission mechanism is truly ubiquitous.

Observations have shown that the AME occurs in the frequency range ~ 10 –100 GHz and is highly correlated with the mid-infrared (IR) dust emission. It is this correlation with the mid-IR emission that led Draine and Lazarian [19] to postulate their model of spinning dust emission. In this model, the observed excess emission is produced by the very smallest dust grains (very small grains, VSGs or polycyclic aromatic hydrocarbons, PAHs), characterised by an electric dipole moment, rotating rapidly, resulting in the production of electric dipole radiation. The model predicts a well-defined peaked spectrum, rising below ~ 20 –30 GHz and then falling off at higher frequencies as expected from a Boltzmann cutoff in grain rotation frequencies. The Draine and Lazarian [19] spinning dust model has been refined and updated [20–24], and current spinning dust models incorporate a variety of grain rotational excitation and damping processes: collisions with neutral and ionised gas particles, plasma drag (the interaction between the electric field of ions and the electric dipole moment of the dust grains),

TABLE 1: Sample of AME emissivity values for AME detections in a variety of different environments computed relative to the intensity of the 100 μm emission.

Source	AME emissivity ($\mu\text{K} (\text{MJy sr}^{-1})^{-1}$)	Reference
HII regions		
6 southern HII regions	3.3 ± 1.7	Dickinson et al. [14]
9 northern HII regions	3.9 ± 0.8	Todorović et al. [15]
Pleiades	2.01 ± 0.09	Génova-Santos et al. [25]
RCW49	13.6 ± 4.2	Dickinson et al. [14]
RCW175	14.2 ± 2.7	Tibbs et al. [16]
High latitudes		
15 regions WMAP	11.2 ± 1.5	Davies et al. [3]
All-sky WMAP	10.9 ± 1.1	Davies et al. [3]
Molecular clouds		
Perseus	15.7 ± 0.3	Watson et al. [5]
Perseus A1	2.8 ± 0.7	Tibbs et al. [7]
Perseus A2	16.4 ± 4.1	Tibbs et al. [7]
Perseus A3	12.8 ± 6.1	Tibbs et al. [7]
Perseus B	13.2 ± 3.6	Tibbs et al. [7]
Perseus C	13.0 ± 3.2	Tibbs et al. [7]
Dark clouds		
LDN1621	18.1 ± 4.4	Dickinson et al. [12]
LDN1622	21.3 ± 0.6	Casassus et al. [11]

absorption and emission of a photon, the photoelectric effect, microwave emission, and the formation of H_2 on the grain surface. Some of the more recent models incorporate additional features including dust grains that are not only spinning about their axis of greatest inertia [21, 24] and dust grains of irregular shape [23].

Understanding how the AME varies between different phases of the ISM is extremely important in improving our understanding of the AME. To help compare the strength of AME detected in one region to another, some authors have computed an AME emissivity. Given the strong association between the AME and the dust grains in the ISM, the AME emissivity is usually defined as the ratio between the antenna temperature of the AME at wavelengths of 1 cm and the surface brightness of the thermal dust emission at 100 μm . This quantity, first calculated as a cross-correlation coefficient over large areas of sky (e.g., [28, 29]), has now been computed for a variety of individual regions in which AME has been detected (see Table 1). However, the AME emissivity defined in this manner is a highly biased method for making these comparisons because the surface brightness at 100 μm is significantly dependent on the dust temperature.

In this work, we aim to (1) illustrate the weakness of such a definition and (2) present and discuss possible alternatives. In Section 2, we point out why the commonly used AME emissivity definition is flawed and estimate the amplitude of

the bias it introduces when comparing regions with different dust temperatures. In Section 3, we discuss more suitable definitions of the AME emissivity including the use of gas and dust column densities. Finally, we present our conclusions in Section 4.

2. The AME Emissivity Defined Relative to the 100 μm Emission

The concept of an AME emissivity is particularly useful as it provides a normalisation of the strength of the AME detected in a variety of regions, and hence it facilitates a comparison between such AME detections. In Table 1, we list AME emissivities defined relative to the 100 μm emission from the literature for a variety of different phases of the ISM, including HII regions, molecular clouds, dark clouds, and diffuse emission at intermediate latitudes. Looking at the values in Table 1, it is possible to identify the observed range of values of the AME emissivity. A typical value for the AME emissivity is of the order $10 \mu\text{K} (\text{MJy sr}^{-1})^{-1}$ with a range from ~ 3 to $25 \mu\text{K} (\text{MJy sr}^{-1})^{-1}$ [2, 3]. In terms of flux density, this corresponds to approximately 1 Jy of AME at 1 cm for every 3000 Jy at 100 μm .

Observations at far-IR and submillimeter wavelengths (e.g., [30, 31]) have revealed that the spectrum of the thermal dust emission is well represented by a modified black body function of the form

$$S_\nu \propto \frac{2h\nu^{3+\beta}}{c^2} \frac{1}{\exp(h\nu/kT_{\text{dust}}) - 1}, \quad (1)$$

where β is the dust emissivity spectral index and T_{dust} is the equilibrium temperature of the big dust grains. The thermal dust emission observed at such far-IR and submillimeter wavelengths is produced by big dust grains absorbing ultraviolet photons from the exciting radiation field of the environment and reradiating this emission thermally. It is this balance between absorption and emission that produces the well-defined spectrum of thermal dust emission (see Figure 1) and keeps the big grains in thermal equilibrium. In the ISM, the dust temperature is known to vary from one environment to another [32] with dust temperatures ranging from ~ 15 K in dense molecular clouds to 25–30 K in HII regions. Additionally, the dust temperature has been observed to vary on small angular scales and within regions in which AME has been detected (e.g., between 15 and 25 K in the Perseus molecular cloud [33]). Since β is dependent on the physical properties of the dust grains, it is also expected to vary between different environments; Dupac et al. [34] found β to vary from 0.8 to 2.4 in a range of Galactic environments with dust temperatures between 11 and 80 K. Therefore, given that the emission at 100 μm is an observed quantity that depends strongly on T_{dust} and β , and since both T_{dust} and β are known to vary in the different phases of the ISM, the 100 μm emission is not a suitable quantity with which to estimate the AME emissivity.

To quantify the effect of dust temperature variations on the AME emissivity, we consider a dust emissivity spectral index of 1.8, which is the value derived for the Galactic solar

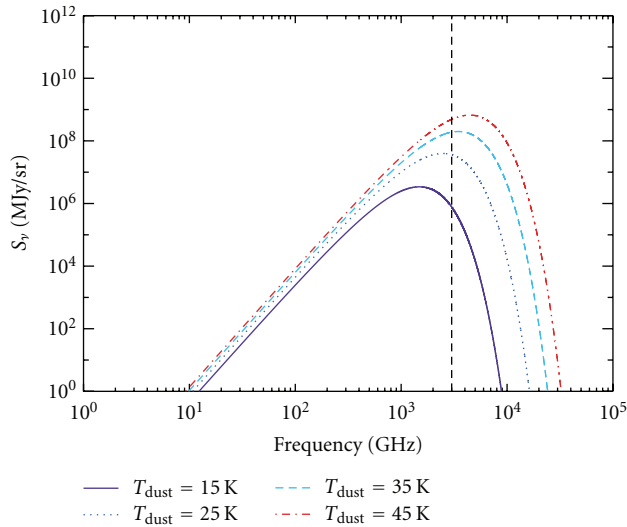


FIGURE 1: The modified black body spectrum representing the thermal dust emission for a range of dust temperatures from 15 to 45 K with a fixed dust emissivity spectral index of 1.8. This illustrates how the $100\ \mu\text{m}$ emission (vertical dashed line) increases with increasing dust temperature, and hence how the AME emissivity defined relative to the $100\ \mu\text{m}$ emission is biased by changes in dust temperature.

neighbourhood [32], and two dust temperatures (20 and 30 K). We then calculate that for a given intensity at 1 cm, the AME emissivity at 20 K is 11.1 times higher than at 30 K. This effect is substantial and could by itself, without any intrinsic variation of the AME intensity, explain the variations of the AME emissivities listed in Table 1. This clearly demonstrates the bias in the AME emissivity when computed relative to the $100\ \mu\text{m}$ emission. With this in mind, we can now revisit the AME emissivity values listed in Table 1. For example, we focus on the five regions of AME detected in the Perseus molecular cloud (A1, A2, A3, B, and C) by Tibbs et al. [7]. It is apparent that region A1 is much less emissive (by a factor of ~ 4 -5) than the other four regions. However, as discussed by Tibbs et al. [7, 33], the physical environment of region A1, which corresponds to the open cluster IC348, is very different from the other four regions. In fact, simply because of the difference in dust temperature between IC348 (~ 22 K) and the other regions (~ 18 K), we estimate that the AME emissivity is reduced by a factor of 4.3 in region A1 relative to the other regions. Therefore, the inconsistency between region A1 and the other regions can be solely accounted for by dust temperature variations, illustrating the impact of the dust temperature in biasing the AME emissivity computed using the $100\ \mu\text{m}$ emission.

3. Redefining the AME Emissivity

In Section 2, we have shown that the commonly used definition of the AME emissivity computed relative to the $100\ \mu\text{m}$ emission is flawed. Therefore, an unbiased definition of the AME emissivity is required to help quantify the AME variations.

As part of their investigation of the diffuse emission at intermediate latitudes, Davies et al. [3] computed the AME emissivity relative to the dust emission at 94 GHz rather than $100\ \mu\text{m}$. Since 94 GHz is further from the peak of the thermal dust emission (see Figure 1), the emission at 94 GHz is much less dependent on the dust temperature than the emission at $100\ \mu\text{m}$. However, even using the intensity of the 94 GHz emission, there is still an effect due to the dust temperature, as the AME emissivity decreases by a factor of 1.6 when the dust temperature increases from 20 to 30 K.

Rather than using the intensity of the dust emission to compute an AME emissivity, other authors (e.g., [10, 26]) have computed an AME emissivity relative to the hydrogen column density, N_{H} . This definition has several advantages. First, it results in an AME emissivity that is more directly suited to comparing with the theoretical values as the current spinning dust theories compute an emissivity in units of $\text{Jy sr}^{-1} \text{cm}^2$ per H atom. Using N_{H} also mitigates the effects of dust temperature, hence allowing a much more impartial comparison between measurements of AME in different environments. To illustrate this, we use the N_{H} map of the Perseus molecular cloud from Tibbs et al. [33], which is based on a visual extinction map, and compute the AME emissivity for the five regions of AME in the Perseus molecular cloud (see Table 2). When computing the AME emissivity relative to N_{H} , we find that region A1 is now consistent (within 2 - 3σ) with the four other regions in the Perseus molecular cloud, which leads to a completely different interpretation. We now want to explore how this new definition can help us to perform a less biased comparison between AME detections in different environments. Vidal et al. [26] compared the AME emissivity of six regions covering a range of column densities from Galactic cirrus to dense dark clouds (see Table 2). Adding these six measurements to the five we computed for the Perseus molecular cloud gives a sample of 11 AME emissivities based on N_{H} . It is apparent that the AME emissivities for the Perseus molecular cloud are consistent with the values computed for other AME detections. It is also noticeable that there is less scatter in the AME emissivities listed in Table 2 compared to those listed in Table 1.

Following the example of Vidal et al. [26], we plotted the AME emissivities listed in Table 2 as a function of N_{H} . This plot is displayed in Figure 2. We fitted the data with a power-law and found that the best fitting spectral index is -0.31 ± 0.03 . Although there is some scatter in the data, the results hint that the AME emissivity is decreasing with increasing N_{H} , suggesting that the AME becomes less emissive as the column density increases. This is consistent with the AME being due to the smallest dust grains, as it is known that as N_{H} increases, the abundance of the smallest dust grains decreases due to dust grain coagulation (e.g., [35, 36]). The idea of the AME being associated with the smallest dust grains is additional support for the AME being due to spinning dust.

Although we have shown that defining the AME emissivity using N_{H} removes the bias introduced by the dust temperature and allows for a much more impartial comparison of AME between different environments, estimating N_{H} , including molecular, atomic and ionised forms, is technically

TABLE 2: AME emissivity values for a variety of phases of the ISM computed relative to the hydrogen column density.

Source	N_{H} (10^{22} H cm^{-2})	AME emissivity (10^{-18} Jy sr^{-1} cm^2/H)	Reference
Perseus A1	0.82 ± 0.19	2.2 ± 0.5	This work
Perseus A2	1.19 ± 0.27	2.7 ± 0.6	This work
Perseus A3	1.28 ± 0.29	1.2 ± 0.3	This work
Perseus B	0.79 ± 0.18	3.4 ± 0.8	This work
Perseus C	0.74 ± 0.17	3.6 ± 0.8	This work
Cirrus	0.15 ± 0.07	4.6 ± 2.0	Leitch et al. [1]
ζ Oph	0.22 ± 0.02	4.1 ± 0.6	Vidal et al. [26]
LDN1780	0.45 ± 0.04	3.5 ± 0.4	Vidal et al. [26]
LDN1622	1.50 ± 0.15	2.0 ± 0.2	Casassus et al. [11]
ρ Oph	5.00 ± 0.50	3.2 ± 0.5	Casassus et al. [6]
M78	22.80 ± 0.23	0.9 ± 0.1	Castellanos et al. [27]

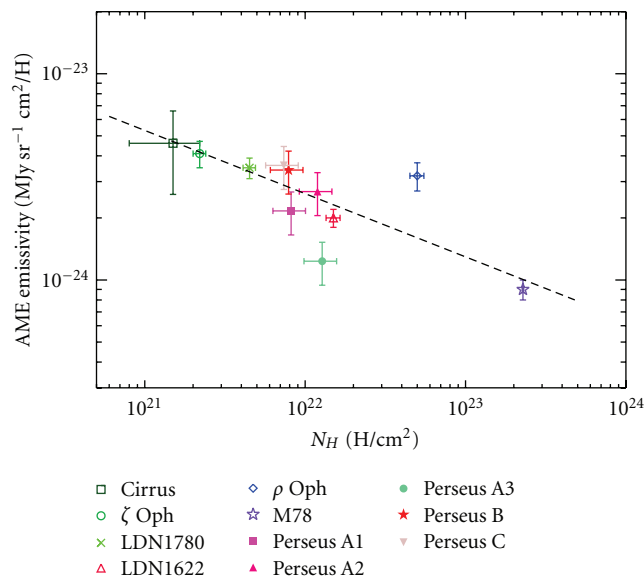


FIGURE 2: AME emissivity computed using N_{H} for the AME detections listed in Table 2 plotted as a function of N_{H} . Also plotted is the fit to the data (dashed line), which we estimate to have a spectral index of -0.31 ± 0.03 .

challenging. There are three methods used to estimate N_{H} : near-IR extinction mapping; far-IR thermal dust emission, and the use of gas tracers. However, each method has its limitations. For example, near-IR extinction is only reliable if there are a sufficient number of background sources available, thermal dust emission estimates are affected by variations in the dust opacity, while observations of gas tracers, although they do provide kinematical information, are limited by the critical density of the observed molecule. A detailed analysis performed by Goodman et al. [37] clearly illustrates the various uncertainties and limitations in estimating N_{H} using the three separate methods.

In addition to the difficulties in measuring N_{H} , the AME is believed to be associated with interstellar dust grains, and hence it would make more sense to normalise the strength of

the AME with a physical property of the dust. For example, the column density of dust, N_{dust} , would be a useful quantity as it has the same advantages as using N_{H} with the addition that it is a direct tracer of the dust. However, N_{dust} is even more difficult to estimate than N_{H} . It is possible to assume a given $M_{\text{dust}}/M_{\text{H}}$ and convert from N_{H} to N_{dust} ; however, this assumes that we know $M_{\text{dust}}/M_{\text{H}}$. Globally, within our own Galaxy, it is known that $M_{\text{dust}}/M_{\text{H}}$ is ~ 0.01 (e.g., [38]), but AME has recently been observed in external galaxies (e.g., [17, 39]) where it is known that the metallicity, and hence $M_{\text{dust}}/M_{\text{H}}$, differs from our own Galaxy (e.g., [40]). To mitigate the effects introduced by variations in $M_{\text{dust}}/M_{\text{H}}$, N_{dust} may be computed by fitting the far-IR SED with a dust model which incorporates the physical properties of the dust grains. However, to date, no such modelling has yet been performed systematically for the environments in which AME has been detected.

4. Conclusions

Having discussed various definitions of the AME emissivity, it is clear that using the $100 \mu\text{m}$ emission introduces a bias due to the effect of dust temperature, and that using N_{H} allows for more accurate comparisons. However, given the association between the AME and the interstellar dust, an intrinsic property of the dust such as N_{dust} , would represent the best quantity with which to compute the AME emissivity. Therefore, until such a time as a new AME emissivity is defined, we stress that care should be taken before using it to directly compare the strength of AME in different environments.

Acknowledgments

The authors thank the referee for useful comments which helped improve the content of the paper. This work has been performed within the framework of a NASA/ADP ROSES-2009 Grant no. 09-ADP09-0059. C. Dickinson acknowledges the support from an SFTC Advanced Fellowship and an EU Marie-Curie IRG Grant under the FP7.

References

- [1] E. M. Leitch, A. C. S. Readhead, T. J. Pearson, and S. T. Myers, "An anomalous component of Galactic emission," *Astrophysical Journal Letters*, vol. 486, no. 1, pp. L23–L26, 1997.
- [2] A. J. Banday, C. Dickinson, R. D. Davies, R. J. Davis, and K. M. Górski, "Reappraising foreground contamination in the COBE-DMR data," *Monthly Notices of the Royal Astronomical Society*, vol. 345, no. 3, pp. 897–911, 2003.
- [3] R. D. Davies, C. Dickinson, A. J. Banday, T. R. Jaffe, K. M. Górski, and R. J. Davis, "A determination of the spectra of Galactic components observed by the *Wilkinson Microwave Anisotropy Probe*," *Monthly Notices of the Royal Astronomical Society*, vol. 370, no. 3, pp. 1125–1139, 2006.
- [4] T. Ghosh, A. J. Banday, T. Jaffe et al., "Foreground analysis using cross-correlations of external templates on the 7-year *Wilkinson Microwave Anisotropy Probe* data," *Monthly Notices of the Royal Astronomical Society*, vol. 422, no. 4, pp. 3617–3642, 2012.
- [5] R. A. Watson, R. Rebolo, J. A. Rubiño-Martín et al., "Detection of anomalous microwave emission in the Perseus molecular cloud with the COSMOSOMAS experiment," *Astrophysical Journal Letters*, vol. 624, no. 2, pp. L89–L92, 2005.
- [6] S. Casassus, C. Dickinson, K. Cleary et al., "Centimetre-wave continuum radiation from the ρ Ophiuchi molecular cloud," *Monthly Notices of the Royal Astronomical Society*, vol. 391, no. 3, pp. 1075–1090, 2008.
- [7] C. T. Tibbs, R. A. Watson, C. Dickinson et al., "Very Small Array observations of the anomalous microwave emission in the Perseus region," *Monthly Notices of the Royal Astronomical Society*, vol. 402, no. 3, pp. 1969–1979, 2010.
- [8] Planck Collaboration, "Planck early results. XX. New light on anomalous microwave emission from spinning dust grains," *Astronomy & Astrophysics*, vol. 536, A20, 2011.
- [9] C. T. Tibbs, A. M. M. Scaife, C. Dickinson et al., "AMI Observations of the Anomalous Microwave Emission in the Perseus Molecular Cloud," *The Astrophysical Journal*. submitted to.
- [10] D. P. Finkbeiner, D. J. Schlegel, C. Frank, and C. Heiles, "Tentative detection of electric dipole emission from rapidly rotating dust grains," *Astrophysical Journal Letters*, vol. 566, no. 2, pp. 898–904, 2002.
- [11] S. Casassus, G. F. Cabrera, F. Förster, T. J. Pearson, A. C. S. Readhead, and C. Dickinson, "Morphological analysis of the centimeter-wave continuum in the dark cloud LDN 1622," *Astrophysical Journal*, vol. 639, no. 2 I, pp. 951–964, 2006.
- [12] C. Dickinson, S. Casassus, R. D. Davies et al., "Infrared-correlated 31-GHz radio emission from Orion East," *Monthly Notices of the Royal Astronomical Society*, vol. 407, no. 4, pp. 2223–2229, 2010.
- [13] A. M. M. Scaife, N. Hurley-Walker, D. A. Green et al., "An excess of emission in the dark cloud LDN 1111 with the Arcminute Microkelvin Imager," *Monthly Notices of the Royal Astronomical Society: Letters*, vol. 394, no. 1, pp. L46–L50, 2009.
- [14] C. Dickinson, R. D. Davies, L. Bronfman et al., "CBI limits on 31 GHz excess emission in southern HII regions," *Monthly Notices of the Royal Astronomical Society*, vol. 379, no. 1, pp. 297–307, 2007.
- [15] M. Todorović, R. D. Davies, C. Dickinson et al., "A 33-GHz Very Small Array survey of the Galactic plane from $\ell = 27^\circ$ to 46° ," *Monthly Notices of the Royal Astronomical Society*, vol. 406, no. 3, pp. 1629–1643, 2010.
- [16] C. T. Tibbs, R. Paladini, M. Compiègne et al., "A multi-wavelength investigation of RCW175: An H II region harboring spinning dust emission," *Astrophysical Journal*, vol. 754, no. 2, article no. 94, 2012.
- [17] E. J. Murphy, G. Helou, J. J. Condon et al., "The detection of anomalous dust emission in the nearby galaxy NGC 6946," *Astrophysical Journal Letters*, vol. 709, no. 2, pp. L108–L113, 2010.
- [18] A. M. M. Scaife, B. Nikolic, D. A. Green et al., "Microwave observations of spinning dust emission in NGC 6946," *Monthly Notices of the Royal Astronomical Society: Letters*, vol. 406, no. 1, pp. L45–L49, 2010.
- [19] B. T. Draine and A. Lazarian, "Electric dipole radiation from spinning dust grains," *Astrophysical Journal Letters*, vol. 508, no. 1, pp. 157–179, 1998.
- [20] Y. Ali-Haïmoud, C. M. Hirata, and C. Dickinson, "A refined model for spinning dust radiation," *Monthly Notices of the Royal Astronomical Society*, vol. 395, no. 2, pp. 1055–1078, 2009.
- [21] T. Hoang, B. T. Draine, and A. Lazarian, "Improving the model of emission from spinning dust: effects of grain wobbling and transient spin-up," *Astrophysical Journal Letters*, vol. 715, no. 2, pp. 1462–1485, 2010.
- [22] N. Ysard and L. Verstraete, "The long-wavelength emission of interstellar PAHs: characterizing the spinning dust contribution," *Astronomy and Astrophysics*, vol. 509, no. 1, article no. A12, 2010.
- [23] T. Hoang, A. Lazarian, and B. T. Draine, "Spinning dust emission: effects of irregular grain shape, transient heating, and comparison with *Wilkinson Microwave Anisotropy Probe* results," *Astrophysical Journal*, vol. 741, no. 2, article no. 87, 2011.
- [24] K. Silsbee, Y. Ali-Haïmoud, and C. M. Hirata, "Spinning dust emission: the effect of rotation around a non-principal axis," *Monthly Notices of the Royal Astronomical Society*, vol. 411, no. 4, pp. 2750–2769, 2011.
- [25] R. Génova-Santos, R. Rebolo, J. A. Rubiño-Martín, C. H. López-Caraballo, and S. R. Hildebrandt, "Detection of anomalous microwave emission in the Pleiades reflection nebula with *Wilkinson Microwave Anisotropy Probe* and the COSMOSOMAS experiment," *Astrophysical Journal*, vol. 743, no. 1, article no. 67, 2011.
- [26] M. Vidal, S. Casassus, C. Dickinson et al., "Dust-correlated cm wavelength continuum emission from translucent clouds ζ Oph and LDN 1780," *Monthly Notices of the Royal Astronomical Society*, vol. 414, no. 3, pp. 2424–2435, 2011.
- [27] P. Castellanos, S. Casassus, C. Dickinson et al., "Dust-correlated centimetre-wave radiation from the M78 reflection nebula," *Monthly Notices of the Royal Astronomical Society*, vol. 411, no. 2, pp. 1137–1150, 2011.
- [28] A. Kogut, A. J. Banday, C. L. Bennett et al., "Microwave emission at high Galactic latitudes in the four-year DMR sky maps," *Astrophysical Journal Letters*, vol. 464, no. 1, pp. L5–L9, 1996.
- [29] A. De Oliveira-Costa, A. Kogut, M. J. Devilin, C. B. Netterfield, L. A. Page, and E. J. Wollack, "Galactic microwave emission at degree angular scales," *Astrophysical Journal Letters*, vol. 482, no. 1, part 2, pp. L17–L20, 1997.
- [30] W. T. Reach, E. Dwek, D. J. Fixsen et al., "Far-infrared spectral observations of the Galaxy by COBE," *Astrophysical Journal Letters*, vol. 451, no. 1, pp. 188–199, 1995.
- [31] F. Boulanger, A. Abergel, J. P. Bernard et al., "The dust/gas correlation at high Galactic latitude," *Astronomy and Astrophysics*, vol. 312, no. 1, pp. 256–262, 1996.

- [32] Planck Collaboration, “Planck early results. XIX. All-sky temperature and dust optical depth from Planck and IRAS. Constraints on the “dark gas” in our Galaxy,” *Astronomy & Astrophysics*, vol. 536, article A19, 2011.
- [33] C. T. Tibbs, N. Flagey, R. Paladini et al., “*Spitzer* characterization of dust in an anomalous emission region: the Perseus cloud,” *Monthly Notices of the Royal Astronomical Society*, vol. 418, no. 3, pp. 1889–1900, 2011.
- [34] X. Dupac, J.-P. Bernard, N. Boudet et al., “Inverse temperature dependence of the dust submillimeter spectral index,” *Astronomy and Astrophysics*, vol. 404, no. 1, pp. L11–L15, 2003.
- [35] B. Stepnik, A. Abergel, J.-P. Bernard et al., “Evolution of dust properties in an interstellar filament,” *Astronomy and Astrophysics*, vol. 398, no. 2, pp. 551–563, 2003.
- [36] N. Flagey, A. Noriega-Crespo, F. Boulanger et al., “Evidence for dust evolution within the Taurus complex from *Spitzer* images,” *Astrophysical Journal Letters*, vol. 701, no. 2, pp. 1450–1463, 2009.
- [37] A. A. Goodman, J. E. Pineda, and S. L. Schnee, “The “True” column density distribution in star-forming molecular clouds,” *The Astrophysical Journal*, vol. 692, article 91, 2009.
- [38] B. T. Draine and A. Li, “Infrared emission from interstellar dust. IV. The silicate-graphite-PAH model in the post-*Spitzer* era,” *Astrophysical Journal Letters*, vol. 657, no. 2, pp. 810–837, 2007.
- [39] Planck Collaboration, “Planck early results. XVII. Origin of the submillimetre excess dust emission in the Magellanic Clouds,” *Astronomy & Astrophysics*, vol. 536, A17, 2011.
- [40] B. T. Draine, D. A. Dale, G. Bendo et al., “Dust masses, PAH abundances, and starlight intensities in the SINGS galaxy sample,” *Astrophysical Journal Letters*, vol. 663, no. 2 I, pp. 866–894, 2007.

Review Article

Large Radio Telescopes for Anomalous Microwave Emission Observations

E. S. Battistelli,¹ E. Carretti,² P. de Bernardis,¹ and S. Masi¹

¹ Physics Department, Sapienza University of Rome, Piazzale Aldo Moro 5, 00185 Rome, Italy

² CSIRO, Astronomy and Space Science, P.O. Box 276, Parkes, NSW 2870, Australia

Correspondence should be addressed to E. S. Battistelli, elia.battistelli@roma1.infn.it

Received 3 August 2012; Accepted 19 October 2012

Academic Editor: Clive Dickinson

Copyright © 2012 E. S. Battistelli et al. This is an open access article distributed under the Creative Commons Attribution License, which permits unrestricted use, distribution, and reproduction in any medium, provided the original work is properly cited.

We discuss in this paper the problem of the Anomalous Microwave Emission (AME) in the light of ongoing or future observations to be performed with the largest fully steerable radio telescope in the world. High angular resolution observations of the AME will enable astronomers to drastically improve the knowledge of the AME mechanisms as well as the interplay between the different constituents of the interstellar medium in our galaxy. Extragalactic observations of the AME have started as well, and high resolution is even more important in this kind of observations. When cross-correlating with IR-dust emission, high angular resolution is also of fundamental importance in order to obtain unbiased results. The choice of the observational frequency is also of key importance in continuum observation. We calculate a merit function that accounts for the signal-to-noise ratio (SNR) in AME observation given the current state-of-the-art knowledge and technology. We also include in our merit functions the frequency dependence in the case of multifrequency observations. We briefly mention and compare the performance of four of the largest radiotelescopes in the world and hope the observational programs in each of them will be as intense as possible.

1. Introduction

The interest of the scientific community in the Anomalous Microwave Emission (AME) is growing. This emission was first detected by the Cosmic Background Explorer (COBE) as diffuse emission excess at 30 GHz [1], and significant effort has been spent to understand its nature and properties since then. What is puzzling about it is that it is correlated with the brightness of thermal dust but peaks at 20–30 GHz where the thermal dust contribution is negligible and the emission budget is supposed to be dominated by free-free and synchrotron. It is thus a new type of emission, whose nature is still unknown. Its investigation is thus crucial for understanding the composition of the interstellar medium (ISM).

Statistical evidence of this emission has been found in observations of the diffuse Galactic background by several authors (see, e.g., [2–5]), while AME has been detected directly in individual regions in a limited number of cases (see Table 1), which still makes to derive its properties hard.

The AME regions typically emit 10%–30% more than expected from synchrotron and free-free, in the range 8–30 GHz (e.g., [6, 7], see Figure 1). Most of the published results relate to galactic objects, with some exceptions. The galactic sources are typically several arc minutes wide and are associated to HII regions, supernova remnants (SNRs) or dark clouds. Among them, only in one case, a significant polarization degree has been detected [8], while upper limits have been set for other cases [9–11]. Several models have been proposed to explain AME, the most popular of which are by Draine and Lazarian.

- (i) Spinning dust (electric dipole): Draine and Lazarian [12, 13] (hereafter DL98a and DL98b) have proposed that the AME is due to electric dipole emission from rapidly rotating small dust grains in the ISM (i.e., spinning dust). They find that the emission spectrum produced by such grains fits well the observed signal and could be responsible for the AME. Lazarian and Draine [14] also found that paramagnetic relaxation

TABLE 1: Individual galactic and extragalactic regions with reported detections of AME. The frequency and the resolution refer to the observations discovering the AME even when the same regions have been observed by other experiments at different frequency and angular resolution. Planck detections relate to the early release. Several other regions have already been announced in the intermediate release.

Region	RA (J2000)	DEC (J2000)	Frequency (GHz)	Resolution	Experiment	Reference
NCP loop		+88°	14.5, 32	7'.35	OVRO	Leitch et al. [38]
LDN1622	05 h 54 m 23 s	+01°46'54"	5, 8–10	6'	GBT	Finkbeiner et al. [34]
Perseus	03 h 41 m 36 s	+31°48'	11–17	0°8 × 1°1	COSMOSOMAS	Watson et al. [6]
3C396	19 h 04 m 04 s	+05°27'12"	33	9'.1 × 7'.7	VSA	Scaife et al. [39]
RCW49	10 h 24 m 20 s	−57°44'57"	31	6'	CBI	Dickinson et al. [10]
LDN1688	16 h 25 m 57 s	−24°20'50"	31	6'	CBI	Casassus et al. [11]
RCW175	18 h 46 m 40 s	−03°46'00"	31	4'	CBI	Dickinson et al. [7]
LDN1111	21 h 40 m 30 s	+57°48'00"	14–18	2'.4 × 2'.1	AMI	Ami Consortium [40]
LDN675	19 h 23 m 53 s	+11°07'39"	14–18	2'.4 × 2'.1	AMI	Scaife et al. [41]
LDN1621	05 h 55 m 22 s	+02°11'33"	31	6'.1 × 4'.8	CBI	Dickinson et al. [42]
LMC/SMC	00 h 52 m/05 h 23 m	−72°48' / −69°45'	23–94	1°	WMAP	Bot et al. [26]
NGC 6946	20 h 34 m 52 s	+60°09'14"	26–40	25"	GBT	Murphy et al. [25]
rho Oph	16 h 37 m 9 s	−10°34'01"	31	8'	CBI	Vidal et al. [22]
LDN1780	15 h 40 m 30 s	−07°14'18"	31	8'	CBI	Vidal et al. [22]
Pleiades	03 h 47 m	+24°07'	11–17, 23–94	1°	COSMOS./WMAP	Génova-Santos et al. [43]
AME-G173.6 + 2.8	05 h 41 m	+35°51'	28–857	30'	Planck	Planck Collaboration [27]
AME-G107.1 + 5.2	22 h 22 m	+63°23'	28–857	30'	Planck	Planck Collaboration [27]

resonance may be efficient at producing an alignment of grains rotating faster than 1 GHz. This may result in an observable polarization degree up to 5% at 10 GHz, decreasing at higher frequencies. Spinning dust models have then been refined since then [15–18].

- (ii) Dust grain magnetic dipole: Draine and Lazarian [19] show that magnetic dipole emission from dust grains made of strongly magnetic materials can have a spectrum accounting for the observed AME. For this model, ferromagnetic relaxation may efficiently align dust grains and produce strongly frequency and shape-dependent polarized emission, that could be as high as 30% at 10 GHz. This is further studied by Draine and Hensley [20].

Polarization level of the AME is a key point to select among models. Stokes I multiband observations in the range 8–30 GHz are instead essential to separate the AME from the other components and to confirm the rising spectrum of the AME. High angular resolution measurements, both in intensity and in polarization, are essential to understand the physics beyond the AME and to limit confusion arisen by the difficulty to disentangle different component emissions within the same region in poor angular resolution observations.

Recent models seem to predict that the AME is dominated by electric dipole emission from the smallest grains, possibly polycyclic aromatic hydrocarbons (PAHs) [21]. However, currently no observation has had sufficient sensitivity, resolution, and frequency coverage to disentangle the candidate mechanisms. This calls for further investigation of the properties of known anomalously emitting regions

and to search for new regions with higher sensitivity, frequency coverage, and polarization measurements, to further increase our understanding of the physical process producing the AME. High angular resolution (arc minute level) observations are thus crucial to disentangle different contributions within the same region. These are starting to reveal surprising effects as the vanishing of the dust-to-radio correlation when we go to fine angular scales [22, 23]. This effect is explained by Ysard et al. [24] who explain how, in dense molecular clouds, the AME is stronger towards the center of the cloud due to the higher gas density, whereas the intense surrounding radiation field boosts the dust emission in the outskirts of the cloud, where the AME is lower due to the decrease on the gas density. This makes 50–100 m class telescopes ideal instruments for such observations.

2. Localized AME Measurements

High angular resolution measurements of anomalous emitters are important to distinguish different regions within HII regions or dark clouds, in order to separate the various components and understand the physics behind these mechanism isolating single emitters. In fact, the wide majority of the detected sources are within the galactic plane. In this case, arc minute level angular resolution would be efficient at disentangling the AME in the presence of galactic emission arising from magnetic fields where the different amount of dust, free electrons, and distributed magnetic field may act at mimicking rising spectra consistent with AME. Since AME is identified by means of SED measurements, high angular resolution measurements are essential for selecting, at the different frequencies, the same physical volume of emitter in the ISM. The same applies to the comparison of radio

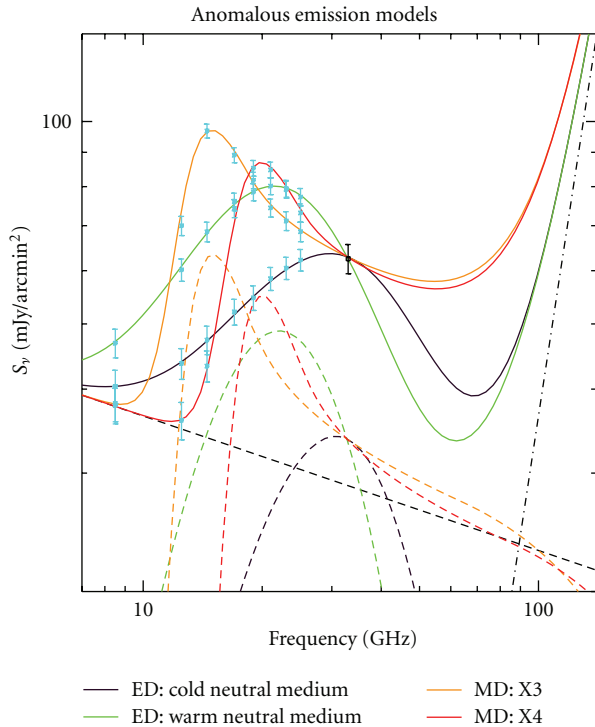


FIGURE 1: Hypothetical anomalously emitting region. The 33 GHz signal shown in the figure is inconsistent with the combination of free-free emission (dashed line) plus thermal dust emission (dot-dashed line), so an additional contribution is required to reach the measured flux. This is provided by different models of AME for electric dipole (ED, [13]) and magnetic dipole (MD, [19]). All plotted models are consistent at 33 GHz but are different at lower frequencies. Microwave measurements with high SNR will be able to select the correct model. The shown error bars correspond to the expected nominal sensitivity of the Parkes receivers.

and IR-dust emission, essential to monitor small dust grains. To match the resolution of IR surveys, the largest radio telescopes must be used. When cross-correlating high- and low- frequency (and resolution) maps, one has to degrade the highly resolved map to the worst ones losing information about the morphology of the emitting regions. It is useful and efficient to perform pixel-by-pixel correlation in order to extract emissivity information (see, e.g., [22]). In Figure 2, we show the effect of a loss of resolution in the MIPS 24-micron SPITZER maps of the Perseus complex when degrading it at 10 arc min resolution. Even more important is the angular resolution for extragalactic observations. Mapping the high star formation regions of near-by galaxies may improve our knowledge of the mechanisms as well as the comparison between ours and other galaxies. Individual regions observed so far to be anomalously emitters include HII regions, dark clouds, supernova remnants and high star formation rate regions in nearby galaxies. With the exception of NGC 6946, none of the measured regions have been observed, in the microwave range, at angular resolution beyond a few arcminutes. We report in Table 1 a list of published sources.

All the reported cases are galactic objects with the noticeable exception of the nearby galaxy NGC 6946, which shows evidence of AME from an outer-disk star-forming region [25], and the tentative detection towards the Magellanic Clouds [26, 27]. Among them, only Perseus has been detected in polarization [8], while upper limits have been set for LDN1622, RCW49, and LDN1688 [9–11] as well as for the Perseus molecular cloud [28].

The Perseus molecular cloud is the most studied region: after the first detection by the COSMOSOMAS experiment [6], it has been observed by other experiments like VSA [29, 30] and Planck Collaboration [27]. Another very well-studied region is RCW175 [31] which seems to be a source of important information not only for its integrated spectral energy density (SED), but also of its complex morphology [32]. Angular resolution down to the 1 arc min level may be enough to separate the different contributions within the same region.

Measurements at frequencies sensitive to AME (10–40 GHz) in localized regions have to be compared to lower frequency measurements, typically up to 10 GHz in order to monitor the presence of synchrotron and free-free and to assess the excess of emission. Comparing total power continuum observations, often arising from different experiments, is both crucial and difficult. Different calibration schemes, observational strategies, map-making algorithms, and background removal techniques may result in biased results when comparing between the free-free and synchrotron signals to the AME. Multifrequency measurements are thus advisable and when performed with the same receiver would then be useful in order to control common systematic effects. In particular the choice of the observational frequency is of fundamental importance and has to be chosen trading off incoming power, detector sensitivity, observational contamination, and, when multifrequency measurements are undertaken, the steepness of the frequency spectrum together with the capability of disentangling power law decreasing spectra from the typical rising spectrum of AME.

In Figure 3(a), we plot the SNR in a typical ground-based observation build accounting for the atmosphere and receiver contribution to the system temperature (as a function of the frequency) as well as the signal intensity and spectrum. This can be considered a merit function for single frequency observation. For multifrequency measurements (Figure 3(b)), we built a similar merit function with the additional ingredient of aiming at disentangling AME and power-law emission like free-free or synchrotron. The combination of the two (Figure 3(c)) accounts for both the AME power as well as its spectrum.

3. Radio Telescopes for AME Observations

Continuum broadband measurements at radiofrequency (RF) with total power receivers are affected by systematic effects such as $1/f$ noise and gain fluctuations, stripes in maps, spikes in data, variation in the transmission, and emission of the atmosphere (all resulting in striping of the maps) [33]. Ambient environment condition changes

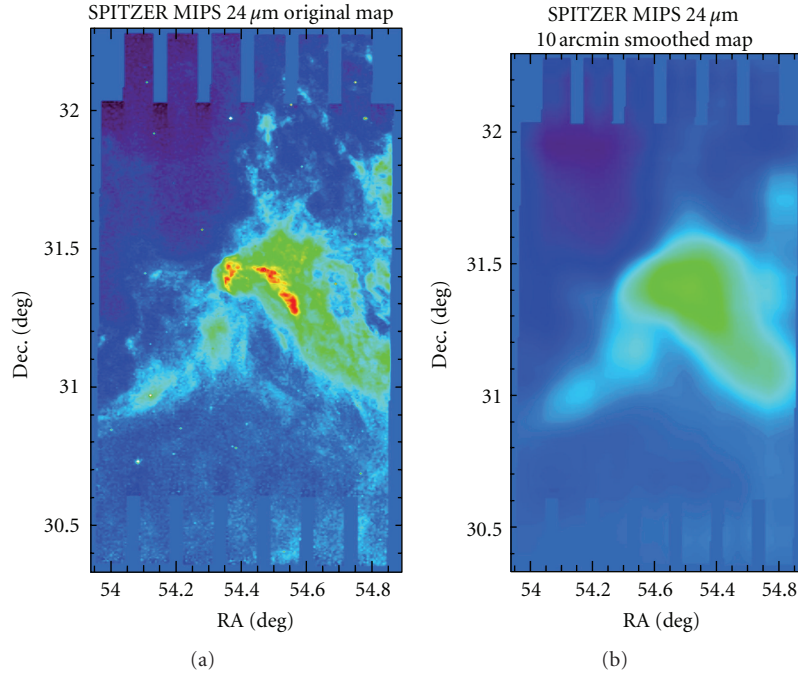


FIGURE 2: We report in this figure a $24\ \mu\text{m}$ -MIPS SPITZER map of the Perseus molecular complex. In (a), the structures detected by the high angular resolution of SPITZER are evident. In (b), we see a degraded angular resolution map to 10 arc min in order to match current microwave resolution of typical AME regions. It is evident that the lower angular resolution introduces a shift in the emission centroid for nonspherical emitters. This results in a difficult interpretation in the comparison between microwave and IR maps detected at such different angular resolution.

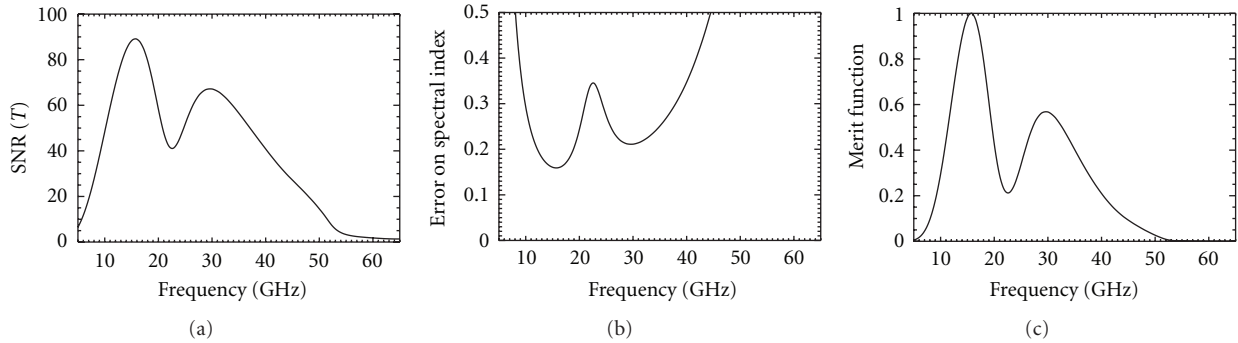


FIGURE 3: (a) SNR in ground-based observation of the SED of an AME cloud. The calculation includes the contributions of typical atmospheric and system noise and a typical spectrum of a warm ionized medium region. The dips in the SNR are due to atmospheric water (around 22 GHz) and oxygen (near 60 GHz). High SNR can be achieved with a long integration time and a large (50 m class) telescope. (b) Error in the estimate of the spectral index of the AME SED above, assuming that the same receiver is used at two frequencies 10% apart. This measurement is important if one wants to discriminate between AME and other contaminants (synchrotron or free-free or thermal dust). (c) Merit function computed as the ratio between the SNR and the error in the determination of the spectral index, normalized to the maximum. This indicates which is the optimal frequency to measure both the brightness of the AME and its spectral index.

as well as instrumental instability obviously influence the measurements. The final sensitivity clearly depends on the receiver sensitivity as well as its stability and the astronomical confusion.

Specific observational techniques are needed to mitigate the effect and include position switching (typically observing the sky a few beams apart), frequency switching (typically for spectral line observations, where the interested line is compared with the continuum baseline), Dicke switching

(comparing the observed sky with an internal reference), IF switching (comparing 2 IFs), polarization switching (comparing different polarizations), cross-link scanning strategy (in which each sky region is observed at least twice with almost orthogonal scan directions), diodes illumination (used as reference signal to overcome drifts), detailed noise filtering, and 2/3 fields beam switching observations. Low latitude observatories may also take advantage, when performing maps, of the constant elevation scan strategy.

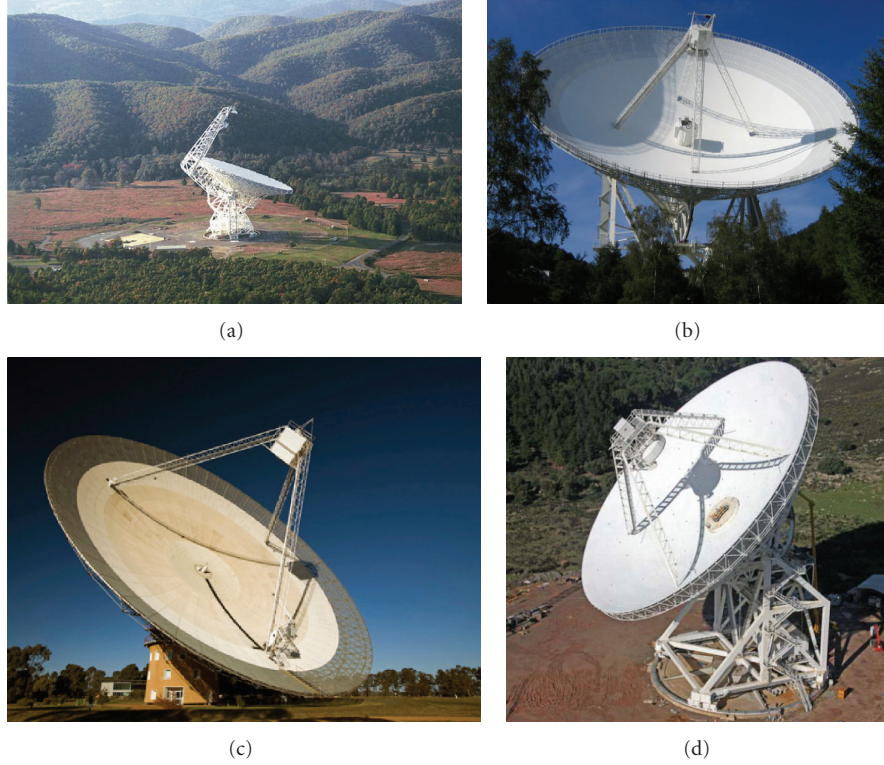


FIGURE 4: Radio telescopes appropriate for AME observations. From top left, clockwise, we see the Green Bank Telescope (<https://science.nrao.edu/facilities/gbt/>), Effelsberg (<http://www.mpifr-bonn.mpg.de/8964/effelsberg/>), Sardinia Radio Telescope (<http://www.srt.inaf.it/>), and Parkes (<http://www.parkes.atnf.csiro.au/>).

TABLE 2: Characteristics of the 3 radio telescopes able to perform continuum observations at 13 GHz and 23 GHz. Sensitivities are taken from the online sensitivity calculators assuming the same observation conditions.

		Parkes	Green Bank Telescope	Sardinia Radio Telescope
13 GHz	Frequency	0.7 GHz–26 GHz	0.1 GHz–116 GHz	0.3 GHz–100 GHz
	Sensitivity	3.7 mJy \sqrt{s} /beam	0.8 mJy \sqrt{s} /beam	0.6 mJy \sqrt{s} /beam
	T_{sys}	150 K	28 K	29 K
	Polarization capability	Yes	Yes	Yes
	Angular resolution	1.9 arc min	0.95 arc min	1.5 arc min
23 GHz	Sensitivity	3.2 mJy \sqrt{s} /beam	1.7 mJy \sqrt{s} /beam	2.0 mJy \sqrt{s} /beam
	T_{sys}	95 K	51 K	81 K
	Polarization capability	Yes	Yes	Yes
	Angular resolution	1.1 arc min	0.54 arc min	0.9 arc min

The atmospheric emission tends, in constant elevation scan, to be dominated by the atmosphere small fluctuations rather than by large air-mass dependence. In order to remove stripes in the map, one can then use a cross-link strategy observing the same region when it rises and when it sets.

Among the instruments that we believe could drastically push ahead the knowledge of the AME mechanisms, we mention the 100 m Green Bank Telescope (<http://science.nrao.edu/facilities/gbt/>) in US, the German 100 m Effelberg telescope (<http://www.mpifr-bonn.mpg.de/8964/effelsberg/>), the Australian 64 m Parkes telescope (<http://www.parkes.atnf.csiro.au/>), and the new upcoming Sardinia Radio Telescope

(<http://www.srt.inaf.it/>) in Italy. The telescopes are shown in Figure 4 and some general characteristics are reported in Table 2.

3.1. Green Bank Telescope. The Green Bank Telescope (GBT) is the largest fully steerable single-dish telescope in the world. Its off-axis design makes the GBT aperture to incoming radiation totally unblocked although increases the design complexity and the polarization interpretation due to the lack of circular symmetry. The active surface makes the GBT a suitable instrument up to 50 GHz as well as in the 80–100 GHz bands. It is located in a radio quite

zone which makes it particularly free from interference. At the frequencies of interest for AME measurements, the GBT is equipped with X, K, Ku, and Ka band receivers covering the spectral range between 8 and 40 GHz, with angular resolution of ranging from 0.3' to 1'.5 FWHM, with polarization capability and very competitive sensitivity. The GBT has already undertaken observational projects related to AME. For instance, Mason et al. [9] placed tight upper limits on the polarization of the anomalous source L1622 (previously observed by Finkbeiner et al. [34] with the 140-foot GBT) and Murphy et al. [25] used the GBT for the first extragalactic evidence of AME. The NGC 6946 result was obtained using the Caltech Continuum Backend (CCB) on the (GBT). Observations were obtained demodulating the beam-switched signal to remove atmospheric fluctuation and receiver gain variations [35]. Average beam in the 26–40 GHz with the GBT is 25". Observational pressure on the GBT is strong, so not many large programs are usually accepted [36]. However, single source of known or unknown AME usually fits the observational management of the GBT.

3.2. Effelsberg. The 100 m Effelsberg telescope is the largest European telescope. No active surface is implemented on the primary mirror, while eight actuators are installed on the secondary mirror. Its nominal observational frequencies are between 408 MHz and 86 GHz thanks to the special compensating support structure used. Its fleet covers the frequency of interest for AME measurements, but continuum observations are possible only at 1.3–1.7 GHz, 2.6 GHz, 4.85 GHz, 8.35 GHz, 10.5 GHz, and 32 GHz. To our knowledge no observational program has been undertaken in the field of AME. Due to its location, radio frequency interference may be an issue. The very efficient beam-switching receivers may however be particularly adequate for high-resolution observations of AME regions.

3.3. Parkes. One very scientifically successful single-dish telescope is the Parkes 64 m telescope. Among the reasons of its success are the availability of a state-of-the-art L-band 13-beam receiver, digital backends, and its particular radio quiet and geographical location. Parkes is equipped with a consistent receivers fleet, from the MARS to the 13 mm receiver, which allows to cover the spectral range of interest for the AME. Parkes has recently undergone a program for observing AME sources (Cruciani et al. in preparation) [32, 37] and is particularly adequate for such a program.

3.4. Sardinia Radio Telescope. The new upcoming giant single-dish steerable radio telescope is the Sardinia Radio Telescope (SRT). SRT is a new 64 m state-of-the-art radio-telescope. The most important feature of SRT is the active surface which enables the SRT to observe the sky up to 100 GHz. It is located in Sardinia in a particularly radio quiet zone. One of the special characteristics of the SRT is the availability of three different focal positions allowing to efficiently manage different kind of receivers. The spectral range of interest for AME observation is covered

by several Ku, K, and Ka receivers with 2×2000 MHz bandwidth each, and $mJy\sqrt{s}$ -level sensitivity, all positionable in the Gregorian focus. The modern design and used technology make the SRT among the most competitive Giant Radio Telescope ever built. Different observational techniques can be implemented like position switching, beam switching, frequency switching, and the secondary mirror wobbling thanks to the 6 electromechanic actuators enabling fast tilting. Mapping techniques scanning and on the fly are also possible. Continuum observations are planned with the multibeam receiver in the K band. 7 beams in the 18–26 GHz range will enable the observer to track the AME where its spectrum shows considerable different features for the other well-known dominant emission mechanisms in the microwave band like free-free or synchrotron.

In order to estimate the observing time to achieve maps of microwave emitting regions with the different telescopes, we have estimated the nominal observing time required to map a $30' \times 30'$ region with *rms* noise down to the mJy/beam level, enough for typical anomalous emitting regions of several mJy/arc min². Assuming 1-minute long scans to keep a typical 30 s overhead between consecutive scans within an acceptable fraction, and assuming 1/3 FWHM spaced scans and one full coverage along each of two orthogonal directions (RA and DEC) to make basket-weaving map-making effective, we find that, for the 13 GHz measurements, 1 full scan of 2.5 hours allows to reach the 1.8 mJy/beam level for the Parkes telescope, 1 full scan of 5 hours allows to reach the 0.6 mJy/beam level for the GBT, and 1 full scan of 3 hours allows to reach the 0.35 mJy/beam level for the SRT. As for the 23 GHz measurements, we find that, with similar scanning procedures, we have a 4-hour scan allows to reach the 2 mJy/beam level for the Parkes telescope, a 3-hour scan would allow to reach the 0.3 mJy/beam level for the GBT, and a 5-hour scan allows to reach the 1.5 mJy/beam for the SRT. Different scan lengths reflect the difference in the observing beams and the necessity to perform different number of single scans in order to uniformly cover the observed region. We stress, however, that the real integration time and the final flux *rms* level depend also on several other factors such as system instabilities, $1/f$ noise, and details of map-making. The specified times, while certainly promising for these observations, should thus be interpreted as optimistic.

4. Conclusions

We have investigated the role that high angular resolution measurements of the AME will have in the near future. Comparing the instantaneous sensitivity among the cited four instruments [36] shows that all of them would be incredibly useful for AME measurements. In particular, the GBT obviously shows the best performance in terms of angular resolution thanks to its size and the SRT is competitive with all the other instrument often overtaking them all. Several projects to the mentioned instruments are advisable in order to unveil the AME mechanisms.

Acknowledgments

The authors acknowledge the use of the MIPS 24-micron data from the NASA/IPAC Infrared Science Archive. They thank Ricardo Génova-Santos for comments and suggestions. We thank the anonymous referee for useful comments that improved the paper.

References

- [1] A. Kogut, A. J. Banday, C. L. Bennett et al., “Microwave emission at high galactic latitudes in the four-year DMR sky maps,” *Astrophysical Journal Letters*, vol. 464, no. 1, part 2, pp. L5–L9, 1996.
- [2] A. de Oliveira-Costa, A. Kogut, M. J. Devlin, C. Barth Netterfield, L. A. Page, and E. J. Wollack, “Galactic microwave emission at degree angular scales,” *Astrophysical Journal Letters*, vol. 482, no. 1, part 2, pp. L17–L20, 1997.
- [3] D. P. Finkbeiner, G. I. Langston, and A. H. Minter, “Microwave interstellar medium emission in the green bank galactic plane survey: evidence for spinning dust,” *Astrophysical Journal Letters*, vol. 617, no. 1, pp. 350–359, 2004.
- [4] S. R. Hildebrandt, R. Rebolo, J. A. Rubiño-Martín et al., “COSMOSOMAS observations of the cosmic microwave background and Galactic foregrounds at 11 GHz: evidence for anomalous microwave emission at high Galactic latitude,” *Monthly Notices of the Royal Astronomical Society*, vol. 382, no. 2, pp. 594–608, 2007.
- [5] M. Lu, J. Dunkley, and L. Page, “Evidence for anomalous dust-correlated emission at 8 GHz,” *Astrophysical Journal*, vol. 749, no. 2, article 165, 2012.
- [6] R. A. Watson, R. Rebolo, J. A. Rubiño-Martín et al., “Detection of anomalous microwave emission in the perseus molecular cloud with the cosmosomas experiment,” *Astrophysical Journal Letters*, vol. 624, no. 2, pp. L89–L92, 2005.
- [7] C. Dickinson, R. D. Davies, J. R. Allison et al., “Anomalous microwave emission from the H II region RCW175,” *Astrophysical Journal Letters*, vol. 690, no. 2, pp. 1585–1589, 2009.
- [8] E. S. Battistelli, R. Rebolo, J. A. Rubiño-Martín et al., “Polarization observations of the anomalous microwave emission in the Perseus molecular complex with the cosmosomas experiment,” *Astrophysical Journal Letters*, vol. 645, no. 2, pp. L141–L144, 2006.
- [9] B. S. Mason, T. Robishaw, C. Heiles, D. Finkbeiner, and C. Dickinson, “A limit on the polarized anomalous microwave emission of linds 1622,” *Astrophysical Journal Letters*, vol. 697, no. 2, pp. 1187–1193, 2009.
- [10] C. Dickinson, R. D. Davies, L. Bronfman et al., “CBI limits on 31 GHz excess emission in southern H II regions,” *Monthly Notices of the Royal Astronomical Society*, vol. 379, no. 1, pp. 297–307, 2007.
- [11] S. Casassus, C. Dickinson, K. Cleary et al., “Centimetre-wave continuum radiation from the ρ Ophiuchi molecular cloud,” *Monthly Notices of the Royal Astronomical Society*, vol. 391, no. 3, pp. 1075–1090, 2008.
- [12] B. T. Draine and A. Lazarian, “Diffuse galactic emission from spinning dust grains,” *Astrophysical Journal Letters*, vol. 494, no. 1, part 2, pp. L19–L22, 1998.
- [13] B. T. Draine and A. Lazarian, “Electric dipole radiation from spinning dust grains,” *Astrophysical Journal Letters*, vol. 508, no. 1, part 1, pp. 157–179, 1998.
- [14] A. Lazarian and B. T. Draine, “Resonance paramagnetic relaxation and alignment of small grains,” *Astrophysical Journal*, vol. 536, no. 1, pp. L15–L18, 2000.
- [15] Y. Ali-Haïmoud, C. M. Hirata, and C. Dickinson, “A refined model for spinning dust radiation,” *Monthly Notices of the Royal Astronomical Society*, vol. 395, no. 2, pp. 1055–1078, 2009.
- [16] N. Ysard and L. Verstraete, “The long-wavelength emission of interstellar PAHs: characterizing the spinning dust contribution,” *Astronomy and Astrophysics*, vol. 509, no. 1, article A12, 2010.
- [17] T. Hoang, B. T. Draine, and A. Lazarian, “Improving the model of emission from spinning dust: effects of grain wobbling and transient spin-up,” *Astrophysical Journal Letters*, vol. 715, no. 2, pp. 1462–1485, 2010.
- [18] K. Silsbee, Y. Ali-Haïmoud, and C. M. Hirata, “Spinning dust emission: the effect of rotation around a non-principal axis,” *MNRAS*, vol. 411, p. 2750.
- [19] B. T. Draine and A. Lazarian, “Magnetic dipole microwave emission from dust grains,” *Astrophysical Journal Letters*, vol. 512, no. 2, pp. 740–754, 1999.
- [20] B. T. Draine and B. Hensley, “The submillimeter and millimeter excess of the small magellanic cloud: magnetic dipole emission from magnetic nanoparticles?” *Astrophysical Journal*, vol. 757, no. 1, article 103, 2012.
- [21] N. Ysard, M. A. Miville-Deschênes, and L. Verstraete, “Probing the origin of the microwave anomalous foreground,” *Astronomy and Astrophysics*, vol. 509, no. 1, article L1, 2010.
- [22] M. Vidal, S. Casassus, C. Dickinson et al., “Dust-correlated cm wavelength continuum emission from translucent clouds ζ Oph and LDN 1780,” *Monthly Notices of the Royal Astronomical Society*, vol. 414, no. 3, pp. 2424–2435, 2011.
- [23] P. Castellanos, S. Casassus, C. Dickinson et al., “Dust-correlated centimetre-wave radiation from the M78 reflection nebula,” *Monthly Notices of the Royal Astronomical Society*, vol. 411, no. 2, pp. 1137–1150, 2011.
- [24] N. Ysard, M. Juvella, and L. Verstraete, “Modelling the spinning dust emission from dense interstellar clouds,” *Astronomy and Astrophysics*, vol. 535, article A89, 2011.
- [25] E. J. Murphy, G. Helou, J. J. Condon et al., “The detection of anomalous dust emission in the nearby galaxy NGC 6946,” *Astrophysical Journal Letters*, vol. 709, no. 2, part 2, pp. L108–L113, 2010.
- [26] C. Bot, N. Ysard, D. Paradis et al., “Submillimeter to centimeter excess emission from the Magellanic Clouds II. On the nature of the excess,” *Astronomy and Astrophysics*, vol. 523, article A20, 2010.
- [27] P. A. R. Ade, N. Aghanim, and M. Arnaud, “Planck early results. XX. New light on anomalous microwave emission from spinning dust grains,” *Astronomy and Astrophysics*, vol. 536, article A20, 2011.
- [28] C. H. López-Caraballo, J. A. Rubiño-Martín, R. Rebolo, and R. Génova-Santos, “Constraints on the polarization of the anomalous microwave emission in the perseus molecular complex from seven-year WMAP data,” *Astrophysical Journal Letters*, vol. 729, no. 1, article 25, 2011.
- [29] C. T. Tibbs, R. A. Watson, C. Dickinson et al., “Very small array observations of the anomalous microwave emission in the perseus region,” *Monthly Notices of the Royal Astronomical Society*, vol. 402, no. 3, pp. 1969–1979, 2010.
- [30] C. T. Tibbs, N. Flagey, R. Paladini et al., “Spitzer characterization of dust in an anomalous emission region: the Perseus cloud,” *Monthly Notices of the Royal Astronomical Society*, vol. 418, no. 3, pp. 1889–1900, 2011.

- [31] C. T. Tibbs, R. Paladini, M. Compiègne et al., “A multi-wavelength investigation of RCW175: AN H II region harboring spinning dust emission,” *Astrophysical Journal*, vol. 754, no. 2, article 94, 2012.
- [32] E. S. Battistelli et al., in preparation.
- [33] J. D. Kraus, *Radio Astronomy*, Cygnus-Quasar Books, Powell, Ohio, USA, 1986.
- [34] D. P. Finkbeiner, D. J. Schlegel, C. Frank, and C. Heiles, “Tentative detection of electric dipole emission from rapidly rotating dust grains,” *Astrophysical Journal Letters*, vol. 566, no. 2, pp. 898–904, 2002.
- [35] B. S. Mason, L. Weintraub, J. Sievers et al., “A 31 GHz survey of low-frequency selected radio sources,” *Astrophysical Journal Letters*, vol. 704, no. 2, pp. 1433–1447, 2009.
- [36] A. Possenti, “The SRT & (br)other single-dish telescopes,” *Memorie della SAI*, vol. 10, p. 198, 2006.
- [37] A. Cruciani et al., in preparation.
- [38] E. M. Leitch, A. C. S. Readhead, T. J. Pearson, and S. T. Myers, “An anomalous component of galactic emission,” *Astrophysical Journal Letters*, vol. 486, no. 1, pp. L23–L26, 1997.
- [39] A. Scaife, D. A. Green, R. A. Battye et al., “Constraints on spinning dust towards Galactic targets with the Very Small Array: a tentative detection of excess microwave emission towards 3C396,” *Monthly Notices of the Royal Astronomical Society*, vol. 377, no. 1, pp. L69–L73, 2007.
- [40] A. M. M. Scaife, N. Hurley-Walker, D. A. Green et al., “An excess of emission in the dark cloud LDN 1111 with the arcminute microkelvin imager,” *Monthly Notices of the Royal Astronomical Society*, vol. 394, no. 1, pp. L46–L50, 2009.
- [41] A. M. M. Scaife, N. Hurley-Walker, D. A. Green et al., “AMI observations of Lynds dark nebulae: further evidence for anomalous cm-wave emission,” *Monthly Notices of the Royal Astronomical Society*, vol. 400, no. 3, pp. 1394–1412, 2009.
- [42] C. Dickinson, S. Casassus, R. D. Davies et al., “Infrared-correlated 31-GHz radio emission from Orion East,” *Monthly Notices of the Royal Astronomical Society*, vol. 407, no. 4, pp. 2223–2229, 2010.
- [43] R. Génova-Santos, R. Rebolo, J. A. Rubiño-Martín, C. H. López-Caraballo, and S. R. Hildebrandt, “Detection of anomalous microwave emission in the pleiades reflection nebula with Wilkinson Microwave Anisotropy Probe and the COSMOS-MAS experiment,” *Astrophysical Journal*, vol. 743, no. 1, article 67, 2011.

Review Article

Observations of the Polarisation of the Anomalous Microwave Emission: A Review

J. A. Rubiño-Martín,^{1,2} C. H. López-Caraballo,^{1,2} R. Génova-Santos,^{1,2} and R. Rebolo^{1,2}

¹*Instituto de Astrofísica de Canarias (IAC), C/Vía Láctea s/n, 38200 La Laguna, Tenerife, Spain*

²*Departamento de Astrofísica, Universidad de La Laguna, 38206 La Laguna, Tenerife, Spain*

Correspondence should be addressed to J. A. Rubiño-Martín, jose.alberto.rubino@iac.es

Received 13 August 2012; Accepted 10 October 2012

Academic Editor: Clive Dickinson

Copyright © 2012 J. A. Rubiño-Martín et al. This is an open access article distributed under the Creative Commons Attribution License, which permits unrestricted use, distribution, and reproduction in any medium, provided the original work is properly cited.

The observational status of the polarisation of the anomalous microwave emission (AME) is reviewed, both for individual compact Galactic regions as well as for the large-scale Galactic emission. There are six Galactic regions with existing polarisation constraints in the relevant range of 10–40 GHz: four dust clouds (Perseus, ρ Ophiuchi, LDN1622, and Pleiades) and two HII regions (LPH96 and the Helix nebula). These constraints are discussed in detail and are complemented by deriving upper limits on the polarisation of the AME for those objects without published WMAP constraints. For the case of large-scale emission, two recent works, based on WMAP data, are reviewed. Currently, the best constraints on the fractional polarisation of the AME, at frequencies near the peak of the emission (i.e., 20–30 GHz), are at the level of $\sim 1\%$ (95.4% confidence level). Finally, we compare these constraints with the predictions of some theoretical AME models and discuss the possible impact of polarised AME on future primordial B-mode experiments.

1. Introduction

The anomalous microwave emission (hereafter AME) is an excess of dust-correlated microwave (10–60 GHz) emission [1, 2] which cannot be explained in terms of the standard physical mechanisms of continuum emission in this frequency range: synchrotron, free-free, and/or thermal dust emission. This AME has been measured by multiple cosmic microwave background (CMB) experiments on both large scales (e.g., COBE [1]; OVRO [2]; Saskatoon [3]; 19 GHz [4]; Python V [5]; Tenerife [6, 7]; GBT [8–10]; COSMOSOMAS [11]; WMAP [12–17]; Planck [18, 19]) as well as in pointed observations of specific Galactic dust clouds (e.g., COSMOSOMAS [20, 21]; CBI [22–24]; AMI [25–27]; VSA [28, 29]; RATAN-600 [30]; 8 GHz [31, Conklin data]; Planck [18]). Moreover, recent studies also show evidence of AME in nearby galaxies [32, 33]. A comprehensive review of the status of the AME measurements in intensity can be found in this special issue.

Among the various physical mechanisms proposed to explain the AME, electric-dipole emission [34] from very

small (less than 10^3 atoms) rapidly rotating ($\sim 1.5 \times 10^{10} \text{ s}^{-1}$) dust grains in the interstellar medium (the so-called “spinning dust”) appears to be the most favoured mechanism [18, 20, 22, 35, 36]. However, there are other possible explanations in the literature. For example, magnetic dipole emission [37] from vibrating “magnetic dust” grains has been also discussed. A detailed theoretical description of these models can be found elsewhere [34, 37–42]. A review on the subject is also included in this special issue.

Measurements of the polarisation of the AME may constitute a key tool to distinguish between these models. The polarisation degree of spinning dust emission is predicted to be very small [38], reaching a maximum (6–7%) around 2–3 GHz, and dropping rapidly towards high frequencies (e.g., about 3% polarisation at 10 GHz and less than 0.5% above 30 GHz). Magnetic dust is expected to be, in general, polarised at much higher levels, and more importantly, the predicted frequency behaviour is different [37]. Recently, detailed predictions for the expected polarisation of the magnetic dipole emission, both for aligned free-flying magnetic nanoparticles and for nonspherical silicate host with

randomly oriented magnetic inclusions, have been reported [42]. They showed that the level of linear polarisation depends strongly on the degree of alignment between the dust grains and the magnetic field, having zero polarisation for random alignments. Furthermore, in cases with magnetic inclusions, the polarisation level can be greater than 5% at 30 GHz, while in the range 10–20 GHz all models have polarisation degrees lower than 1% (depending on the magnetic inclusions). A relevant prediction is that the polarisation direction can be reversed in this second case with magnetic inclusions, which could be used as an observational tracer to distinguish between these two models.

In this paper, we present an overview of the current observational status of the measurements of the polarisation of the AME. Although there is little information in the literature on this subject, mainly because the polarisation degree of the AME is known to be very small and thus difficult to measure, it is a field with a rapidly increasing activity. In addition to the importance of understanding the physical processes responsible of the emission in the interstellar medium, the characterisation of all polarised astrophysical foregrounds in the microwave range is very relevant for future CMB experiments aiming to detect a primordial B-mode signal [43, 44].

The structure of the paper is as follows. Section 2 presents some practical issues related to polarisation measurements. The current status of the AME polarisation constraints is presented in the following two sections. In Section 3, we review the six Galactic regions where measurements (or upper limits) have been set in the 10–60 GHz frequency range: Perseus, LPH96, Helix Nebulae, ρ Ophiuchi, LDN1622, and Pleiades. In Section 4, we discuss the current constraints on the polarisation of the diffuse (large-scale) Galactic AME emission. For completeness, we derive in Section 5.2 new constraints on the polarisation of the AME for two of the aforementioned regions (LDN1622 and LPH96) for which WMAP constraints were not available. Finally, the conclusions and implications for future B-mode experiments are presented in Section 6.

2. Polarisation Measurements

Here we review some specific methodologies and conventions of the polarisation measurements. First of all, we will be reporting only linear polarisation measurements, as the physical mechanisms considered in this frequency range do not produce circular polarisation ($V = 0$).

Linear polarisation can be described in terms of two Stokes parameters [45], Q and U . While the intensity (I) is a scalar quantity, Q and U are not: they depend on the selected reference frame. Unless otherwise stated, the values quoted in this paper are referred to Galactic coordinates, and the *HEALPix* polarisation convention [46] is used (i.e., for a given point on sky, y -axis points towards east, and x -axis points south). If, for a certain measurement, (Q, U) are given in another reference system which is rotated by an angle θ

with respect to the previous one, the Stokes parameter in our new frame can be obtained as

$$\begin{aligned} Q' &= \cos(2\theta)Q + \sin(2\theta)U, \\ U' &= -\sin(2\theta)Q + \cos(2\theta)U. \end{aligned} \quad (1)$$

Flux extraction methods used for AME regions are similar to those used for intensity measurements in CMB studies, but now directly applied to the Q and U maps. The most widely used method for polarisation constraints in compact regions is the aperture photometry (e.g., [47–49]), but in principle, other methods could be applied (for a review, see [50]). For example, fitting methods based on different spatial profiles are often used for extracting the intensity in AME regions: either by fitting the beam profile for point-like objects (e.g., [51–53]), or fitting more complex shapes (ellipsoids, multiple Gaussians, etc.) for extended objects (e.g., [20, 28]). Other techniques, as matched filters [54–56], wavelets [57–59], or the recently proposed filtered fusion technique [60], have been used to detect and to measure the polarisation of point-like objects in CMB maps and could in principle be applied to resolve AME regions.

Throughout this paper, we define the polarised intensity as

$$P = \sqrt{Q^2 + U^2} \quad (2)$$

and the fractional polarisation (in per cent units) as

$$\Pi(\%) = 100 \frac{\sqrt{Q^2 + U^2}}{I} = 100 \frac{P}{I}. \quad (3)$$

When placing confidence limits on polarisation measurements, there is an specific issue related to P (and Π) estimates, due to the fact that the posterior distributions of the polarisation level (and angle) do not follow a normal (Gaussian) distribution. This issue is especially relevant for AME measurements, because most of the current constraints are either upper limits or marginal detections with very low S/N ratios, and if not properly taken into account, the polarisation fraction estimates could be biased.

The posterior distribution of the polarisation level P was described elsewhere [61, 62]. Here we follow [63], and first, we introduce the so-called Rice (or Rician) distribution for the polarisation, which gives the probability of measuring a polarisation fraction in the range $[P, P + dP]$,

$$R(P | P_0)dP = \frac{P}{\sigma} \exp\left[-\frac{P^2 + P_0^2}{2\sigma^2}\right] I_0\left(\frac{PP_0}{\sigma^2}\right) \frac{dP}{\sigma}, \quad (4)$$

where P_0 stands for the true (underlying) polarisation value of the object that we are observing; I_0 is the zeroth-order modified Bessel function; σ stands for the uncertainty on the Q (or U) measurements (i.e., $\langle Q^2 \rangle = \langle U^2 \rangle = \sigma^2$). Note that this expression was derived assuming that the underlying observables (Q and U) follow a Gaussian distribution. The n th moment of this Rician distribution is given by

$$E[P^n] = (2\sigma^2)^{n/2} \Gamma\left(1 + \frac{n}{2}\right) {}_1F_1\left(-\frac{n}{2}, 1, -\frac{P_0^2}{2\sigma^2}\right), \quad (5)$$

where Γ stands for the gamma function, and ${}_1F_1$ is the confluent hypergeometric function of the first kind [64]. For example, the mean (or first moment) of the Rician distribution, is thus given by

$$E[P] = \sigma \sqrt{\frac{\pi}{2}} {}_1F_1\left(-\frac{1}{2}, 1, -\frac{P_0^2}{2\sigma^2}\right). \quad (6)$$

Note that this equation has the proper asymptotic limit for large values of P_0/σ , in the sense that $E[P] \rightarrow P_0$ for $P_0^2 \gg \sigma^2$. However, for low signal-to-noise ratios, the mean of this distribution does not coincide with P_0 .

Once we have the Rician distribution, and for the case of a single polarisation measurement, the posterior distribution is given, according to the Bayes' theorem, by

$$\begin{aligned} f(P_0 | P) &= \frac{R(P | P_0)}{\int R(P | P_0) dP_0} \\ &= \sigma^{-1} \sqrt{\frac{2}{\pi}} \exp\left[-\frac{P_0^2}{2\sigma^2}\right] \exp\left[-\frac{P^2}{4\sigma^2}\right] \frac{I_0(PP_0/\sigma^2)}{I_0(P^2/4\sigma^2)} \end{aligned} \quad (7)$$

for the case of a uniform prior in P_0 . This function is plotted in Figure 1 for several values of the measured polarisation (P). Direct integration of (7) can be used to provide an estimate of the true polarisation, \hat{P} , as well as to define the confidence intervals. For example, if we define the cumulant distribution $F(P)$ as

$$F(P) = \int_0^P f(x | P_{\text{obs}}) dx \quad (8)$$

for a certain observed polarisation value P_{obs} , then the 95% confidence limit P_u is derived by solving the implicit equation $F(P_u) = 0.95$.

For practical purposes, the maximum likelihood solution for \hat{P} can be approximated, in the two limits of low and high S/N ratios, by these simple expressions:

$$\begin{aligned} \hat{P} &= 0, \quad \text{for } \frac{P}{\sigma} < \sqrt{2}, \\ \hat{P} &\approx \sqrt{P^2 - \sigma^2}, \quad \text{for } \frac{P}{\sigma} \gtrsim 3. \end{aligned} \quad (9)$$

We note that, in practice, this posterior distribution can be also evaluated numerically by using Monte-Carlo simulations based on the noise properties of the measurements (e.g., [48, 49]). This Monte-Carlo procedure permits us to include not only more complex noise properties, but also the uncertainty in the intensity measurements when deriving the Π estimates. The upper limits reported in Section 5 use this Monte-Carlo approach.

3. Polarisation of the AME in Galactic Regions

Out of the list of compact Galactic regions showing evidence for AME, we have identified in the literature only six with published polarisation constraints: four dust clouds and two HII regions. In order to provide the constraints on P

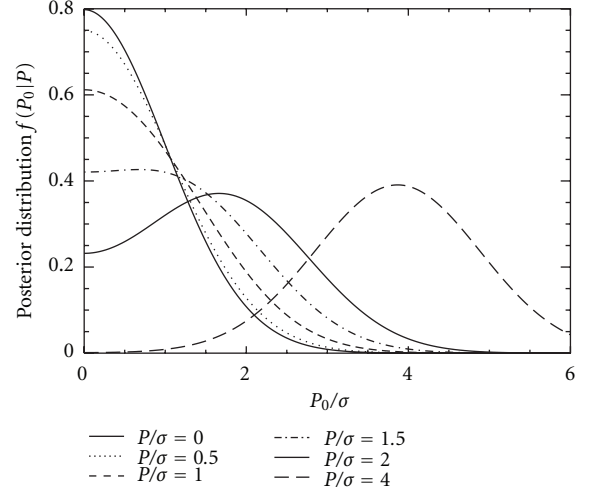


FIGURE 1: Posterior distribution function from the Rician distribution and for the case of a single polarisation measurement, from (7). Note that for measured polarisation values $P/\sigma < \sqrt{2}$, the posterior distribution (as a function of the true polarisation, P_0/σ) peaks at zero polarisation.

and Π and for completeness, we also briefly summarise the status of the intensity measurements of those regions. All values described throughout this section are included both in Table 1 and Figure 2.

3.1. Dust Clouds

3.1.1. G159.6-18.5 (Perseus). The Perseus molecular complex is a giant molecular cloud located at a distance of 260 pc [68]. The G159.6-18.5 dust feature is our region of interest, an expanding HII bubble that has emerged from the outer edge of the cloud [69, 70].

The first detection of AME in G159.6-18.5 was presented in [20] and used the COSMOSOMAS experiment [11, 71] (10–18 GHz) and the WMAP (23–94 GHz) data. The spectral energy distribution (hereafter SED) shows a clear emission excess (e.g., ~ 11.3 Jy and ~ 27.2 Jy at 11 and 16 GHz, resp.), which is well fitted by a spinning dust model in the frequency range 10–60 GHz [34]. A detailed review of the AME in this region is also presented in this special issue.

Using the COSMOSOMAS data at 11 GHz, [65] reported a marginal detection of polarised emission in this region, which in principle could be ascribed to AME. Taken as a face value, the reported polarisation fraction ($\Pi = 3.4_{-1.9}^{+1.5}\%$ at the 95% confidence level) favours electric dipole emission [34] over dipole magnetic emission [37], as the physical mechanism responsible of the observed polarisation. However, a careful study has to be carried out at lower frequencies to confirm the spinning dust hypothesis. Recently, and using new data from the Effelsberg telescope at 2.7 GHz (11 cm), [72] proposed that G159.6-18.5 acts as a Faraday Screen (FR) which rotates the polarisation angle of the background emission, and this might contribute significantly to the COSMOSOMAS measurement at 11 GHz.

TABLE 1: Summary of the current constraints on the fractional polarisation (Π) of the AME both for individual Galactic objects and for large-scale (diffuse) measurements. Columns 1 to 3 indicate the region, the experiment used for this particular constraint, and the angular resolution, respectively. The following four columns indicate the constraints on the fractional polarisation (Π), separated according to the frequency band for an easier comparison. When quoting upper limits, the 95% confidence level is used. Last column provides the relevant references.

Name	Experiment	Resolution	Π (9–11 GHz) [%]	Π (22 GHz) [%]	Π (30–33 GHz) [%]	Π (40 GHz) [%]	References
Galactic AME regions							
G159.6-18.5	COSMOSOMAS	1°	3.4 ^{+1.5} _{-1.9}				[65]
”	WMAP-7	1°		<1.01	<1.79	<2.69	[48]
”	WMAP-7	1°		<1.4	<1.9	<4.7	[49]
ρ Ophiuchi	CBI	~9′			<3.2		[24]
”	WMAP-7	1°		<1.7	<1.6	<2.6	[49]
LDN1622	GBT	~1.3′	<2.7				[10]
”	WMAP-7	1°		<2.6	<4.8	<8.3	This work
Pleiades	WMAP-7	1°		<12.2	<32.0	<95.8	[21], this work
LPH96	CBI	~9′			<10		[23]
”	WMAP-7	1°		<1.3	<2.5	<7.4	This work
Helix	CBI	~9′			<8		[66]
Diffuse Galactic AME							
All sky	WMAP-3	1°		<1	<1	<1	[67]
All sky	WMAP-5	1°		<5			[16]

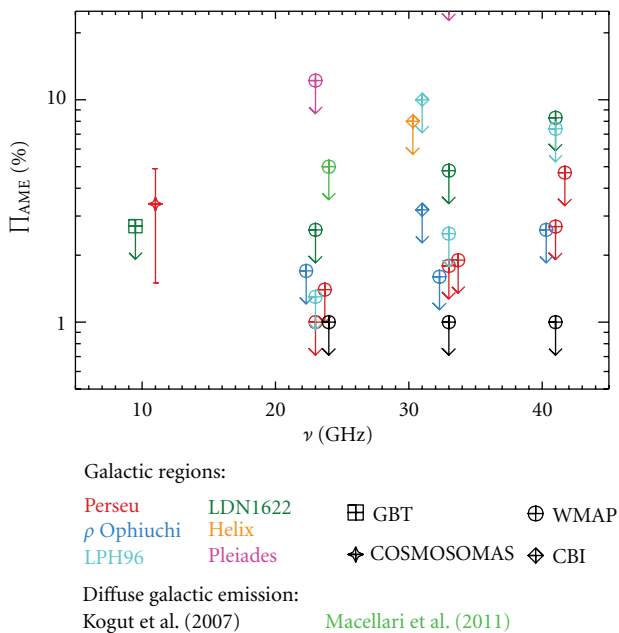


FIGURE 2: Summary of the current constraints on the fractional polarisation (Π) of the AME. Data points are taken from Table 1. All upper limits are given at the 95% confidence level.

Later, [48] studied the polarisation properties of the AME in G159.6-18.5 using the WMAP-7 data, putting constraints on the polarisation fraction of the AME in the region, at an angular resolution of 1°, and using an aperture photometry method on a circular aperture with radius $r_0 = 2^\circ$. All measurements in the five WMAP frequency bands were

found to be compatible with zero polarisation, and thus, only upper limits for P and Π were reported. At 23 GHz, they reported $P_{\text{AME}} < 0.48$ Jy and $\Pi_{\text{AME}} < 1.01\%$, while at 33 GHz, the constraints are 0.86 Jy and 1.79%. Note that at these frequencies, the contribution of a possible FR screen in the region is negligible. Again, these results are consistent with the expected polarisation level from electric dipole emission [38].

More recently, [49] revised the polarisation constraints on the Perseus region using WMAP-7 data, using aperture photometry but with a more detailed treatment of the WMAP instrumental noise properties. Their constraints, properly corrected for the Rice bias, are $P_{\text{AME}} < 0.24$ Jy and $\Pi_{\text{AME}} < 1.4\%$ at 23 GHz and 0.30 Jy and 1.9% at 33 GHz (95% confidence level). These values are fully consistent with those obtained in [48].

3.1.2. ρ Ophiuchi. The ρ Ophiuchi molecular cloud (e.g., [73–75]) lies within the Gould Belt region, at a distance of 135 ± 15 pc [76]. A detailed study of the centimetre-wave continuum radiation in this region was presented in [24], who reported an excess of emission over the expected free-free emission level at 31 GHz, spatially associated with the ρ Ophiuchi West bright feature, thus evidencing the presence of AME. Using the Planck data [18], a high-accuracy SED has been derived. The best-fitting model for this SED requires a spinning dust contribution with two components: a high-density ($\sim 2 \times 10^4 \text{ cm}^{-3}$) molecular gas and a low-density ($\sim 200 \text{ cm}^{-3}$) atomic gas.

A polarised intensity map at 31 GHz was obtained in ρ Ophiuchi with the CBI interferometer, with a synthesised

beam of 9.5×8.3 arcmin² [24]. No obvious polarisation was found in this map, so an upper limit of $\Pi < 3.2\%$ (2σ) was derived for the peak central region and $\Pi < 16\%$ (2σ) for the outer parts. For the integrated flux density, it was set an upper limit of 1% at 3σ .

Recently, [49] also provided constraints on the polarisation fraction in this region, based on WMAP-7 data, at 1° scales. The upper limits, after noise-bias correction, are $P_{\text{AME}} < 0.43$ Jy and $\Pi_{\text{AME}} < 1.7\%$ at 23 GHz; $P_{\text{AME}} < 0.44$ Jy and $\Pi_{\text{AME}} < 1.6$ at 33 GHz (95% confidence level).

3.1.3. LDN1622. Located at a distance of ~ 200 pc [77], Lynds 1622 (hereafter LDN1622) is a dark cloud that lies in the foreground of the Orion B cloud within the Orion East molecular complex [78]. It extends up to 1 pc according to its far-IR emission. Next to LDN1622, we can find a diffuse HII region named Barnard's Loop.

Using the Green Bank Telescope (GBT), [8] reported the first detection of AME in this region, which was later confirmed by [22], using observations with the CBI at 31 GHz, the Parkes-MIT-NRAO survey at 4.85 GHz, WMAP data (23–94 GHz), and IRAS. The CBI measurement yields a (loss-corrected) flux density of 2.90 ± 0.04 Jy, which is basically dominated by the AME contribution.

The only upper limit on the polarised AME in LDN1622 that can be found in the literature was reported in [10]. The GBT Spectrometer at 9.65 GHz was used to obtain observations in the four Stokes parameters, yielding $Q = 35 \pm 30 \mu\text{K}$ and $U = 26 \pm 34 \mu\text{K}$ at an angular resolution of $\sim 6'$. These values were translated into upper limits on the polarisation using a maximum likelihood approach similar to the one described in Section 2, resulting $P < 88 \mu\text{K}$ and $P < 123 \mu\text{K}$ at the 95% and 99.7% confidence levels, respectively. The constraint on the fractional polarisation at 9.65 GHz is $\Pi < 2.7\%$ (95% confidence level).

3.1.4. Pleiades Reflection Nebula. The Pleiades reflection nebula lies within the Taurus complex at a distance of ~ 120 pc [79]. This is a well-known region, and detailed information about the physical properties of the interstellar medium can be found elsewhere (see e.g., [21], and references therein).

The first evidence for AME in the Pleiades reflection nebula was obtained using the WMAP-7 and COSMOS-MAS data [21]. At 23 GHz, the flux density (2.15 ± 0.12 Jy), integrated within a 1° radius, mainly corresponds to the AME intensity. The polarised fluxes at this frequency, also derived using aperture photometry, are $Q = 0.076 \pm 0.071$ Jy and $U = -0.056 \pm 0.091$ Jy. When combining these values with the intensity measurement and taking into account the noise-bias correction described in Section 2, a 2σ upper limit on the polarisation fraction of $\Pi < 10.8\%$ was set at 23 GHz.

3.2. HII Regions. At radio/microwave frequencies ($\lesssim 100$ GHz), HII regions are dominated by free-free (thermal bremsstrahlung) emission from ionised plasma with electron temperatures $T_e \approx 8000$ K. The spectrum of free-free radiation is well understood [80, 81], and it is known to be unpolarised. However, a contribution of AME to the SED of these objects could be in principle expected, since ion

collisions with grains are predicted to be one of the largest contributors in maintaining the large rotational velocities required to produce spinning dust emission [34]. We now review the polarisation measurements associated with two HII regions showing evidence of AME: LPH96 and the Helix Nebulae.

3.2.1. LPH96. LPH96 is a diffuse HII region [82], for which observations with the Green Bank 43-m Telescope between 5 and 10 GHz [8] suggested a rising spectrum compatible with AME. However, later CBI observations at 31 GHz [23] showed no evidence for significant AME. Indeed, the spectral index within the CBI band, and between CBI and Effelsberg data at 1.4 and 2.7 GHz, was found to be $\beta = 2.06 \pm 0.03$, which is consistent with optically thin free-free emission, thus setting an upper limit of 24% (2σ) on the intensity of AME at 31 GHz. A consistent result, showing no evidence of AME, was obtained using the Very Small Array interferometer [28].

In polarisation, [23] reported CBI observations of Stokes Q and U parameters, with a synthesised beam of 7.9×6.5 (FWHM). The polarised emission was found to be negligible, thus setting a 3σ upper limit on the total fractional polarisation of 2%. Depending on the actual intensity of the AME, this limit can be translated into an upper limit on the fractional polarisation of the AME. For instance, [23] argue that if 14% of the total intensity emission at 31 GHz is indeed anomalous, then the polarisation of this component is $\Pi \lesssim 10\%$ (at the 2σ level).

3.2.2. Helix Nebula and Other PNe. The Helix nebula (NGC7293) is an evolved Planetary Nebula (PN), lying at a distance of ~ 200 pc [83]. Its angular size is about $10'$, and its emission extends up to 1 pc [84].

A detailed multifrequency analysis on the region was carried out in [85]. The derived SED shows a dust-correlated 31 GHz excess over free-free emission, which cannot be explained in terms of a synchrotron component, nor with optically thick knots, nor in terms of ultracold grains. However, one of the most interesting aspects of this detection is that very small grains, thought not to survive in evolved Planetary Nebulae (PNe), have not been detected in NGC7293. Therefore, the presence of AME cannot be explained in terms of electric dipole emission from spinning dust grains, and thus, for this particular case, the magnetic dipole emission from ferromagnetic grains is favoured [85]. Because of this particularity, [66] extended the previous work in the Helix, by considering a more extended sample of 37 PNe. Using CBI measurements, they showed that the 31 GHz flux densities in their PNe sample are systematically higher than the level of optically thin free-free continuum extrapolated from 250 GHz. The 31 GHz excess is observed in all 18 PNe with reliable 31 and 250 GHz data and is significant in nine PNe.

Polarisation measurements at 31 GHz were obtained in four objects of the full sample: Helix, NGC7009, NGC1360, and NGC246. No significant polarisation was detected in any of these four PNe, being all Stokes Q and U maps fully consistent with noise. The 99% upper limits on the total

polarisation fraction, after correcting for the noise bias as described in Section 2, are 8.5%, 8.5%, 17%, and 2.4% for NGC7009, NGC1360, NGC246, and NGC7293, respectively.

For the case of the Helix, and since free-free radiation is not polarised, that limit on the total polarisation can be converted into an upper limit for the AME polarisation fraction. For 36–80% free-free emission at 31 GHz, this translates into $\Pi < 3.8$ –12% for the AME, also at the 99% confidence level. The more conservative number (8% at 2-sigmas) is also included in Table 1.

4. Polarisation of the Diffuse Galactic AME

Due to the low-polarisation degree of the AME measured in Galactic regions, most of the component separation methods attempting to separate the AME in polarisation from CMB maps normally assume that this component is unpolarised. Because of this reason, there are only a few constraints in the literature on the polarisation of the (large-scale) diffuse Galactic AME emission. Here we review two papers, both based on WMAP data.

First, [67] used the WMAP 3-year data to constrain the fractional polarisation of the AME. By assuming that the spatial distribution and the polarisation angles of the AME can be traced by dust templates and adopting a spinning dust model [34] for the frequency dependence of the emission, they fitted the polarisation data searching for an AME contribution. Their conclusion is that the spinning dust contribution is less than 1% of the observed polarisation signal variance in any WMAP band (23–94 GHz).

More recently, [16] used a different approach, based on a cross-correlation analysis between the WMAP 5-year polarisation maps and several intensity template maps tracing the Galactic synchrotron, dust, and free-free emissions. They derived the polarisation fraction for all those three components in 48 sky regions (corresponding to the *HEALPix* pixelisation with $N_{\text{side}} = 2$). In intensity, the dust-correlated emission is found to be the dominant signal over the entire sky in the 23–94 GHz range, being the anomalous emission clearly detected at 23 and 33 GHz. At these two frequencies, the AME is found to be the dominant foreground at low Galactic latitudes ($-40^\circ < b < 10^\circ$). The average fractional polarisation of dust-correlated AME at 23 GHz is $3.2 \pm 0.9(\text{stat}) \pm 1.5(\text{sys})$ per cent, or equivalently, $\Pi < 5\%$ at the 95% confidence level. These two results have been included in Table 1 and Figure 2.

5. New Constraints

In the previous sections we have presented a compilation of the up-to-date polarisation measurements of AME in individual regions, as well as in the diffuse Galactic emission, which is summarised in Table 1. Now, we use WMAP 7-year data to expand the spectral range of these constraints in those regions where we have not found WMAP measurements in the literature. For LDN1622, [10] derived an upper limit at 9.65 GHz using data from the GBT telescope, whereas the 31 GHz measurement for LPH96 was obtained by [23] using data from the CBI interferometer. In the Pleiades reflection

nebula, [21] presented an upper limit using only the 23 GHz WMAP channel. Here, we complement the polarisation measurements for those three regions using the WMAP maps. We note that the Helix nebula is not included in our study, because of the low flux density and small angular extent of this object, making the AME emission of this region undetectable in WMAP maps.

5.1. Data and Methodology. We use the WMAP 7-year data products [86], which are publicly available in the *LAMBDA* webpage (<http://lambda.gsfc.nasa.gov/>) in the *HEALPix* pixelisation scheme. Maps are provided for each of the five WMAP frequency bands (K, Ka, Q, V, and W), centred at 22.8, 33.0, 40.7, 60.8, and 93.5 GHz. The original angular resolutions of these bands are, respectively, 0.85° , 0.65° , 0.51° , 0.35° , and 0.25° although, for consistency, we will work with maps degraded to a common resolution of 1° .

Figures 3, 4, and 5 show maps of the *I*, *Q*, and *U* Stokes parameters at LDN1622, LPH96, and the Pleiades reflection nebula, respectively. No clear polarised emission is visible in any of these maps. Thus, we use an aperture photometry integration to derive upper limits on the polarisation fractions. As explained in [48], this is an efficient technique for computing fluxes, or upper limits, in regions of low signal to noise, which at the same time allows a reliable subtraction of the underlying background signal. It consists of an integration of the temperatures of all pixels within a given aperture, after subtracting the mean background level which is calculated by averaging the temperatures of all pixels enclosed in an external annulus. The central coordinates, together with the radii of the inner aperture and of the background ring used in each case, are shown in Table 2. The flux estimate is given by

$$S_\nu = a(\nu) \left[\frac{\sum_{i=1}^{n_1} T_i}{n_1} - \frac{\sum_{j=1}^{n_2} T_j}{n_2} \right], \quad (10)$$

where n_1 and n_2 are, respectively, the number of pixels in the circular aperture and in the background annulus, and T_i and T_j represent the pixel thermodynamic temperatures in the aperture and in the external annulus (here by “temperature” we refer either to total intensity, or temperature in Stokes *Q* and *U*, when we calculate polarised fluxes). The function $a(\nu)$ gives the conversion factor from temperature to flux,

$$a(\nu) = \frac{h^2 \nu^4}{2k_B T_0^2 c^2} \sinh^{-2} \left(\frac{h\nu}{2k_B T_0} \right) n_1 \Omega_{\text{pix}}, \quad (11)$$

where h and k_B are the Planck and Boltzmann constants; $T_0 = 2.725$ K is the CMB temperature today [87]; Ω_{pix} stands for the solid angle subtended by a *HEALPix* pixel (all of them have the same area).

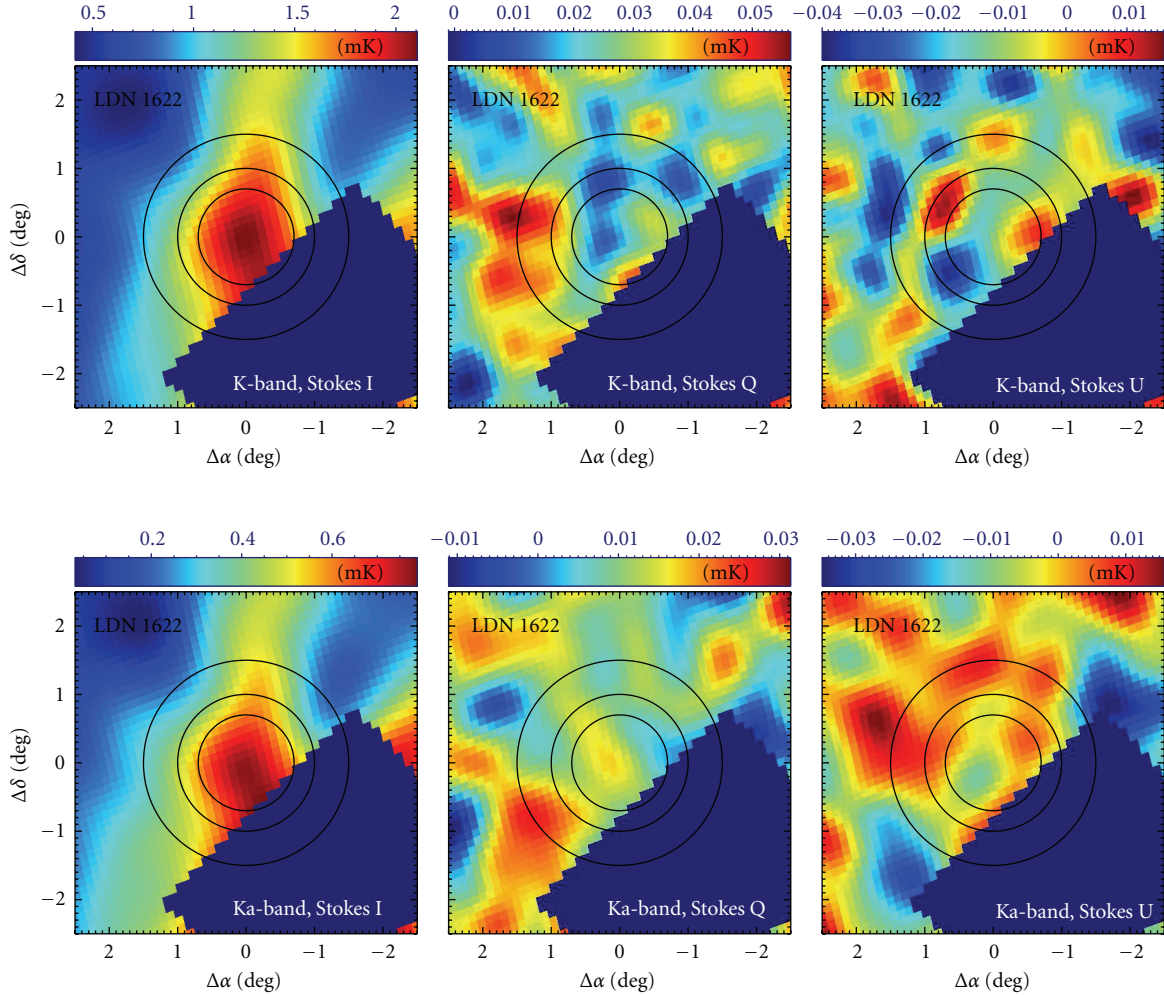


FIGURE 3: The LDN1622 region, as seen by WMAP in Stokes parameters I (left), Q (centre), and U (right column), at 23 GHz (top row) and 33 GHz (bottom row). All maps are displayed at the common angular resolution of 1.0° . The circles ($r_0 = 0.7^\circ$, $r_1 = 1.0^\circ$, and $r_2 = 1.5^\circ$) indicate the main aperture (r_0) and the region for the background correction ($r_1 < r < r_2$) used for the aperture photometry method. The masked regions are not included in the flux density determination (see text for details).

The associated error bar for the flux estimator given (10) can be computed analytically, using the pixel-to-pixel covariance, as

$$\sigma(S_\nu) = a(\nu) \left[\frac{1}{n_1^2} \sum_{i,i'}^{n_1, n_1} C(\theta_{ii'}) + \frac{1}{n_2^2} \sum_{j,j'}^{n_2, n_2} C(\theta_{jj'}) - \frac{2}{n_1, n_2} \sum_{i,j} C(\theta_{ij}) \right]^{1/2}, \quad (12)$$

where the indices i and i' run over pixels in the aperture region, while j and j' run over pixels in the background region. In (12), $C(\theta_{ij})$ is the pixel-to-pixel 2-point correlation function, which is evaluated for any pair of pixels separated by an angle θ_{ij} , and in general, it includes the CMB, the background emission, and the instrumental noise contributions.

In the case of the total intensity estimates, the two main contributions to the error bar are the instrumental noise and

TABLE 2: Central positions and radii used in the aperture photometry analysis for each region.

Name	R.A. (J2000) (deg)	Dec. (deg)	r_0 (deg)	r_1 (deg)	r_2 (deg)
LDN1622	88.64	2.10	0.7	1.0	1.5
LPH96	99.28	10.70	0.7	1.0	1.5
Pleiades	56.24	23.78	1.0	1.7	2.0

the background fluctuations, which chiefly arise from the large-scale Galactic emission and from the CMB. In order to account for the two terms, following [49], we estimate the associated flux error bar through the quadratic sum of the standard deviations in the aperture and in the background:

$$\sigma(S_\nu^t) \approx a(\nu) \sigma(T_{\text{bg}}) \left[\frac{1}{n_{\text{ap}}} + \frac{1}{n_{\text{bg}}} \right]^{1/2}, \quad (13)$$

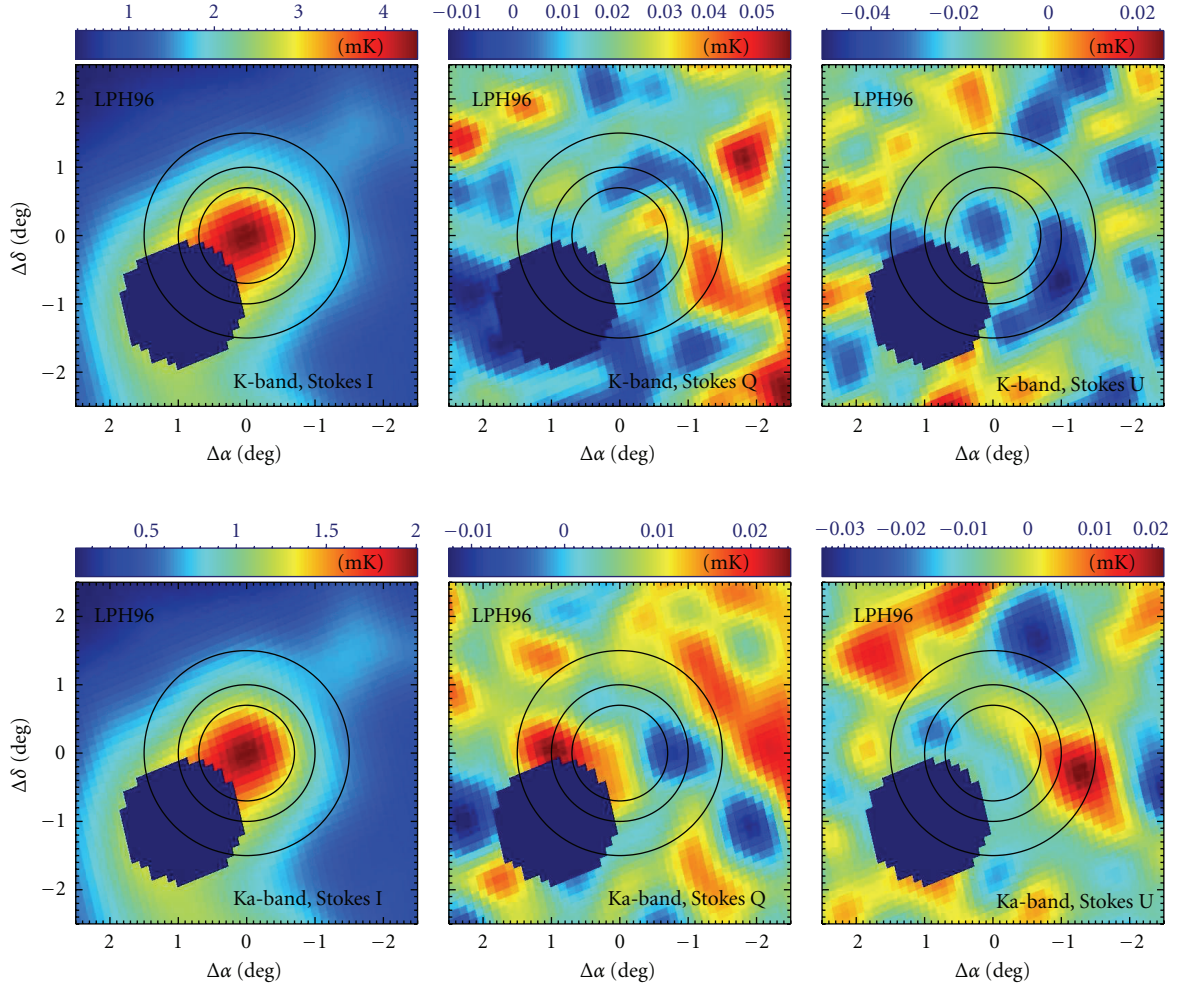


FIGURE 4: The same as Figure 3, but for the LPH96 region.

where $\sigma(T_{\text{bg}})$ represents the pixel-to-pixel standard deviation in the background; n_{ap} and n_{bg} are the number of independent pixels in the aperture and the background, respectively. Those are calculated as the equivalent number of beams that can be accommodated within each aperture. Note that in (13), we do not include the standard deviation on the aperture, as this will be contaminated by the source contribution.

Conversely, when extracting the Q and U fluxes on WMAP data, we have checked that the contributions of the background fluctuations and the CMB are not so critical. Therefore, in this case, we follow [48] and we use (12), being the correlation function entirely due to instrumental noise. Note that, even in this case of almost uncorrelated noise, we still have a contribution which arises from the smoothing process applied to bring all the maps to a common 1° angular resolution.

In order to derive polarisation upper limits associated with the AME, we need to have an estimate of the AME total intensity flux at each of the WMAP frequencies, which might be viewed as the residual flux after subtracting the other contributions, namely, the CMB, the free-free, and the thermal dust emissions. We characterise the free-free

emission as $I_{\text{ff}} = A_{\nu_0}^{\text{ff}} (\nu/\nu_0)^{\beta_{\text{ff}}}$, with $\beta_{\text{ff}} = -0.1$, from low-frequency radio surveys at 0.408 GHz [88], 0.820 GHz [89], and 1.4 GHz [90]. The thermal dust emission is modelled using a modified black-body spectrum, $I_d(\nu, T_d) = \tau_{100} (\nu/(2998 \text{ GHz}))^{\beta_d} B_\nu(T_d)$, using far-infrared data from the DIRBE satellite between 1249 and 2998 GHz [91]. Finally, a CMB component is fitted to the data using a black-body curve. The total AME intensity flux is then calculated as $I_{\text{AME}} = I_{\text{total}} - I_{\text{ff}} - I_d - I_{\text{cmb}}$, and the final AME polarisation fraction as $\Pi_{\text{AME}} = 100P_0/I_{\text{AME}}$, where P_0 is the debiased polarised flux, which is calculated from the measured polarised flux, P , following the formalism presented in Section 2. The uncertainty of those quantities (I_{AME} and Π_{AME}) is derived by propagating the uncertainty of the SED fit.

5.2. Results

5.2.1. LDN1622. After applying a mask to remove the contamination introduced by the neighbouring Barnard's loop HII region (The region masked for our analysis has a rectangular shape, defined by the following four vertices: v1: (R.A. = $87.^\circ 07$; Dec. = $2^\circ.9$), v2: (R.A. = $85^\circ.04$; Dec.

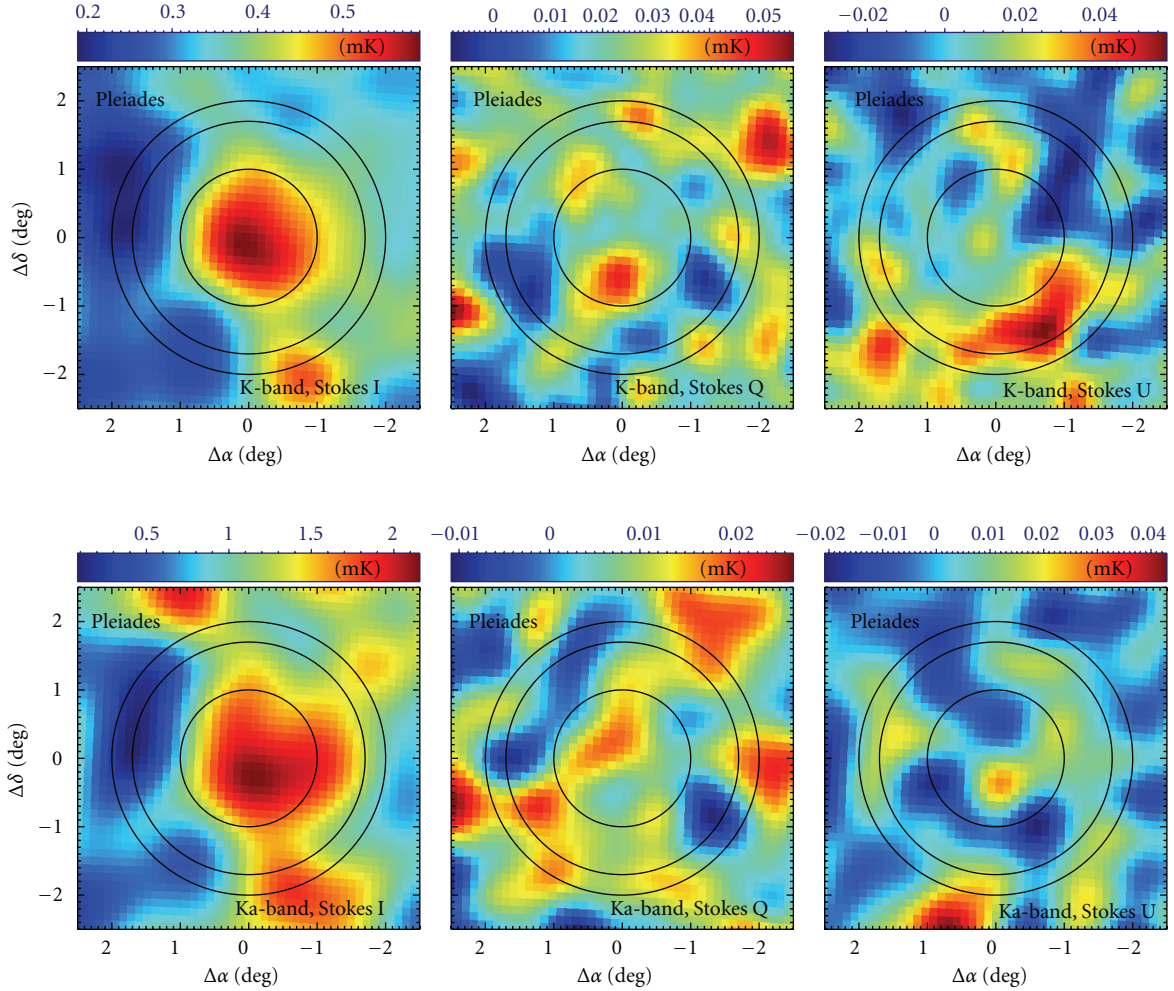


FIGURE 5: The same as Figure 3, but for the Pleiades region. The apertures now correspond to the radii $r_0 = 1^\circ$, $r_1 = 1.5^\circ$, and $r_2 = 2^\circ$.

$= 0^\circ.79$), $v3$: (R.A. = $87^\circ.79$; Dec.: $-1^\circ.53$), and $v4$: (R.A. = $89^\circ.91$; Dec. = $0^\circ.03$), we get the intensity fluxes listed in Table 3. Our derived fluxes at low frequencies (1.9 ± 4.2 and 1.19 ± 0.85 Jy, at 0.40 and 1.42 GHz, resp.), should be considered as upper limits, as they are within the error bars and the maps do not present clear emission. To determine the amplitude of the free-free emission, we instead use the flux density of 0.086 ± 0.042 Jy obtained by [22] at 5 GHz. We then perform a joint fit of the CMB and thermal dust components using the 94 GHz WMAP flux and the DIRBE fluxes in the three bands, after subtracting the free-free emission corresponding to each band. We fix the emissivity index at the value given by [22], $\beta_d = 1.7$, and fit for the remaining three parameters, obtaining $T_d = 17.17 \pm 0.31$ K, $\tau_{100} = (9.53 \pm 1.02) \times 10^{-4}$, and $T_{\text{cmb}} = 35.60 \pm 6.4 \mu\text{K}$. The final AME fluxes are listed in Table 3.

The Q and U WMAP maps of Figure 3 do not show significant signal towards this region, and the computed fluxes are accordingly compatible with the error bars. We therefore derive the 2-sigma upper limits on the fractional polarisation shown in Table 4. These constraints, as well as the 2.7% limit at 9 GHz given by [10], rule out all the models presented in [37] based on magnetic dipole emission

from single-domain dust grains (the magnetic field is aligned either parallel or perpendicular to the largest moment of inertia of the grains), all of which predict higher polarisation fractions. However, a lower polarisation could arise when grains are arranged in different magnetic domains.

5.2.2. LPH96. The WMAP maps at the diffuse HII region LPH96 are shown in Figure 4. A circular mask with radius $0^\circ.8$ has been applied to remove the contamination from the point source located at position R.A. (J2000) = $100^\circ.23$ and Dec. = $9^\circ.70$. Significant emission is visible in the low-frequency maps (8.4 ± 4.4 and 7.2 ± 1.7 Jy at 0.408 and 1.42 GHz, resp.); so we use those values to constrain the amplitude of the free-free component. We perform the joint CMB and thermal dust fit in the same way as it was applied to LDN1622. In this case, we fix $\beta_d = 1.7$ and $T_d = 18.175$ K [9], and fit for the remaining two parameters, obtaining $T_{\text{cmb}} = 85.22 \pm 2.66 \mu\text{K}$ and $\tau_{100} = (8.33 \pm 0.13) \times 10^{-4}$.

The residual AME flux at 33 GHz is 6.91 ± 2.63 Jy, which represents about the 50% of the total (measured) flux. This value supports the results of [8], who first claimed the detection of AME in this region, but apparently contradicts those of [23], who obtained an AME flux of 14% of the total

TABLE 3: Stokes I , Q , and U measured in LDN1622, LPH96, and the Pleiades.

ν (GHz)	I (Jy)	I_{AME} (Jy)	Q (Jy)	U (Jy)
LDN1622				
23	5.64 ± 1.90	5.22 ± 1.90	-0.05 ± 0.05	0.01 ± 0.06
33	4.90 ± 1.70	4.05 ± 1.72	-0.01 ± 0.09	-0.04 ± 0.09
41	4.44 ± 1.77	3.11 ± 1.82	-0.05 ± 0.11	0.04 ± 0.12
61	4.84 ± 2.95	1.42 ± 3.20	0.16 ± 0.27	0.06 ± 0.29
94	9.96 ± 5.89	-0.61 ± 7.80	0.25 ± 0.64	0.05 ± 0.69
LPH96				
23	13.95 ± 2.44	7.86 ± 2.80	-0.00 ± 0.05	0.01 ± 0.06
33	13.65 ± 2.26	6.91 ± 2.63	-0.02 ± 0.08	-0.04 ± 0.10
41	13.37 ± 2.28	5.87 ± 2.63	0.17 ± 0.11	-0.10 ± 0.13
61	14.07 ± 2.49	3.48 ± 2.80	-0.49 ± 0.25	0.20 ± 0.31
94	19.62 ± 5.02	0.12 ± 5.19	-0.08 ± 0.60	0.17 ± 0.74
Pleiades				
23	2.60 ± 0.90	1.94 ± 0.90	0.08 ± 0.07	-0.06 ± 0.09
33	2.55 ± 1.15	1.20 ± 1.15	0.06 ± 0.13	-0.07 ± 0.17
41	2.64 ± 1.26	0.63 ± 1.28	-0.14 ± 0.20	-0.14 ± 0.24
61	4.71 ± 2.49	0.38 ± 2.52	-0.06 ± 0.47	-0.58 ± 0.57
94	9.11 ± 5.19	-0.52 ± 5.26	-1.02 ± 1.16	-1.26 ± 1.40

TABLE 4: Upper limits at the 95% confidence level, on the fractional linear polarisation of the AME measured in LDN1622, LPH96, and Pleiades at the three lowest WMAP frequency bands.

Region	P_0 (Jy)			Π_{AME} (%)		
	23 GHz	33 GHz	41 GHz	23 GHz	33 GHz	41 GHz
LDN1622	<0.12	<0.19	<0.23	<2.6	<4.8	<8.3
LPH96	<0.10	<0.17	<0.34	<1.3	<2.5	<7.4
Pleiades	<0.19	<0.28	<0.51	<12.2	<32.0	<95.8

measured flux at 31 GHz with the CBI interferometer and claimed not to find evidence of AME towards this source. A possible explanation for this inconsistency is given by the fact that [23] focused their analysis on a compact structure ($\sim 6'$) in the region, while in the present analysis, we obtained the flux density by integrating over an area of $\sim 0.7^\circ$, thus also taking into account a possible extended emission which would be resolved out by the CBI interferometer (see [23] for details).

No signal is evident in the Q and U maps at the position of LPH96, and in fact the measured fluxes are compatible with the instrumental noise. We therefore derive the 2-sigma upper limits on the fractional polarisation shown in Table 4. Our result at 33 GHz is about four times more restrictive than the one calculated by [23] at 31 GHz.

5.2.3. Pleiades. The intensity and polarisation WMAP maps in the position of the Pleiades reflection nebula are shown in Figure 5. We have followed the same process as in [21], with the only difference that now we calculate errors in the intensity flux using (13). This barely changes the results of the CMB and thermal dust fits. The fluxes corresponding to total intensity and to polarisation are shown in Table 3. The AME residual flux at 23 GHz is at a less significance

(2.2-sigma) than that obtained in [21], owing to the different approach for calculating error bars. The upper limits on the polarisation fraction shown in Table 4 are less restrictive than those in the other two sources, due to the lower AME intensity.

6. Discussion

The observational study of the polarisation of the AME provides a valuable tool to understand the physical mechanism(s) responsible for the AME and to disentangle among the different models proposed in the literature.

From an observational point of view, exploring the spectral and spatial properties of the polarisation of the AME is a challenge because of the expected low polarisation fraction. Despite this difficulty, in the last few years there has been a sustained observational effort, and nowadays the current upper limits (see Table 1) of the AME polarisation fraction are at the level of $\Pi \approx 1\%$, both for the extended emission and for individual regions. There is only one detection claimed to date, in the Perseus molecular complex [65], but in order to confirm the physical mechanism responsible for the emission, other detections are needed at different wavelengths.

Nevertheless, even if we only have upper limits, we can still significantly constrain some of the models in the literature, in particular those predicting high fractional polarisation degrees. To illustrate this issue, Figures 6 and 7 compare, at 23 GHz and 33 GHz, all the upper limits listed in Table 1, with the predictions of some polarisation models, corresponding to the electric dipole (ED) and magnetic dipole (MD) emissions. For the ED case, we show the polarised Cold Neutral Medium spinning dust model proposed by [34]. Note that, as this model is derived under the assumption of negligible saturation effects, this curve corresponds to the maximal values allowed by the paramagnetic mechanism. Levels of $\lesssim 1\%$ and $\lesssim 0.5\%$ are expected at 23 GHz and 33 GHz, respectively.

For the polarised MD emission we considered two cases: (1) grains with single magnetic domain; (2) grains with magnetic inclusions. For the first case, [37]'s models from perfectly aligned grains consisting of a single magnetic domain are determined by the dotted and dashed lines, for two different grain shapes with axial ratios 1:2:2 and 1:1.25:1.5, respectively. Note that the frequency behaviour depends strongly on the shape and composition of the grains. Recently, [42] showed that the level of linear polarisation can be much lower when the grains are partially aligned, decreasing to zero polarisation for random alignments. Thus, these curves should again be considered as maximal values for this mechanism. In the perfect alignment case, the models predict polarisation fractions between 10 and 20% at 23 GHz (see Figures 6 and 7).

In the second case, the randomly oriented magnetic inclusions models [42] predict at 20 GHz levels lower than 5% (depending on the magnetic inclusions). Meanwhile, at 33 GHz they reach levels between $\sim 5\%$ and $\sim 10\%$.

The low levels of polarised AME emission allow us to rule out several models based on MD emission, in particular

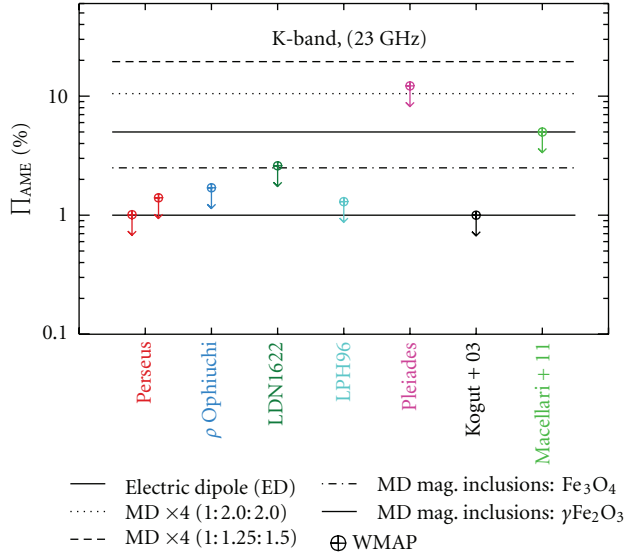


FIGURE 6: Observational constraints on the polarisation fraction of the AME at 23 GHz for individual regions and on all sky (see Table 1). The horizontal lines correspond to different theoretical predictions in this frequency band, both for electric dipole emission (ED) and magnetic dipole emission (MD) models. The solid line shows the expected polarisation fraction for the Cold Neutral Medium (spinning dust) model proposed by [34]. The dotted and dashed lines correspond to the polarisation fraction for MD from perfectly aligned grains consisting of a single magnetic domain [37]. The polarisation fraction from randomly oriented magnetic inclusions [42] is shown by the dot-dashed and dot-dot-dashed lines.

those where the orientation of the magnetic domains is aligned either parallel or perpendicular to the principal axis of the largest moment of inertia. Nevertheless, this does not rule out the magnetic dipole emission as the physical process responsible for the observed polarisation [42]. In particular, there are specific regions, as the Helix Nebulae, where the most plausible mechanism of emission should be the MD, as small grains have not been detected in this evolved PN.

6.1. Implications for Future B-Mode Experiments. CMB polarisation and, in particular, B-mode observations are expected to be a primary source of information about the physics of the very early universe, potentially providing an unambiguous proof of the existence of primordial gravitational waves [92–94], thus opening a unique window to carry out a detailed study of the inflationary epoch.

Consequently, the CMB B-mode observations are a very dynamic area of research in cosmology, with multiple observatories being designed, built, and deployed [43, 44, 95–99].

One of the main challenges in carrying out such a program is to understand (and to correct for) the astrophysical foregrounds with very high accuracy, as they could be ultimate limitations to the exploitation of the CMB B-mode potential [99, 100].

Here, we provide some simple estimates, based on the upper limits reviewed in Table 1, on the contribution of the

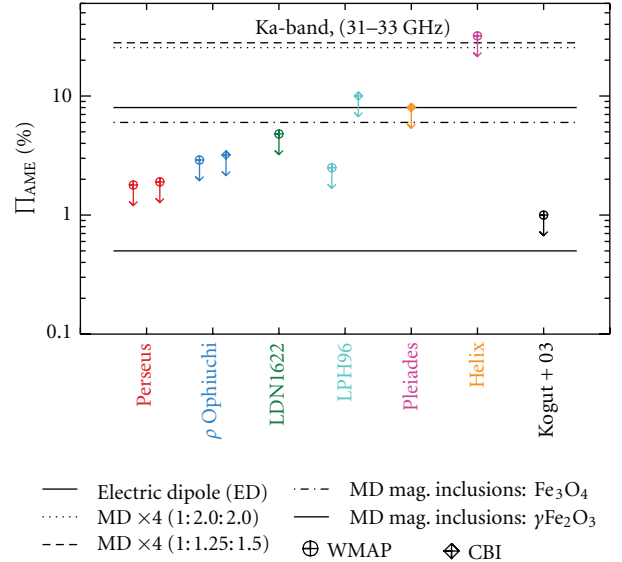


FIGURE 7: The same as Figure 6, but now for the Ka-band (31–33 GHz).

large-scale polarised AME to the detectability of B-modes. For definiteness, we will focus on the case of 30 GHz, as this will be one of the cosmological frequencies of the QUIJOTE-CMB experiment [95]. First, we start by parameterising the contribution of polarised AME to the angular power spectrum as

$$\frac{\ell(\ell+1)C_\ell^{E,AME}}{2\pi} = \frac{\ell(\ell+1)C_\ell^{B,AME}}{2\pi} = A_{AME} \ell^{-\alpha} \Pi_{AME}^2, \quad (14)$$

where Π_{AME} is the average fractional polarisation of the AME. The constant α characterises the angular dependence of the signal. Here, we assume that, at first order, the AME should follow the same dependence as the thermal dust, and we use $\alpha = 0.6$ (see, e.g., [13, 101]). Finally, the normalisation factor A_{AME} can be easily obtained by imposing that the rms (intensity) contribution should be consistent with the results from [16]. In particular, we use here the rms amplitude for the dust contribution at this frequency, derived from an all-sky analysis using the KQ85 mask [101]. Being conservative, this rms value of $27.6 \pm 0.6 \mu\text{K}$ is assumed to be totally due to AME.

Figure 8 presents a sketch of the polarised power spectrum for the AME at 33 GHz, compared with the CMB E- and B-mode angular power spectra for a model with a tensor-to-scalar ratio of $r = 0.1$. For illustration, we consider here three values for the fractional polarisation, namely, $\Pi_{AME} = 1.0\%$, 0.5% , and 0.1% . For comparison, we also include in this figure the contribution to the power spectrum of the polarised synchrotron (C_l^{Synch}) at this frequency (dotted line). The normalisation of this curve is based on the measured rms polarised synchrotron emission measured by [16] ($\Delta T_S^{\text{Pol}} = 3.9 \pm 0.2 \mu\text{K}$).

At 33 GHz, and based on the existing constraints, the polarised AME has a lower contribution to the power spectrum than the polarised synchrotron emission. Nevertheless,

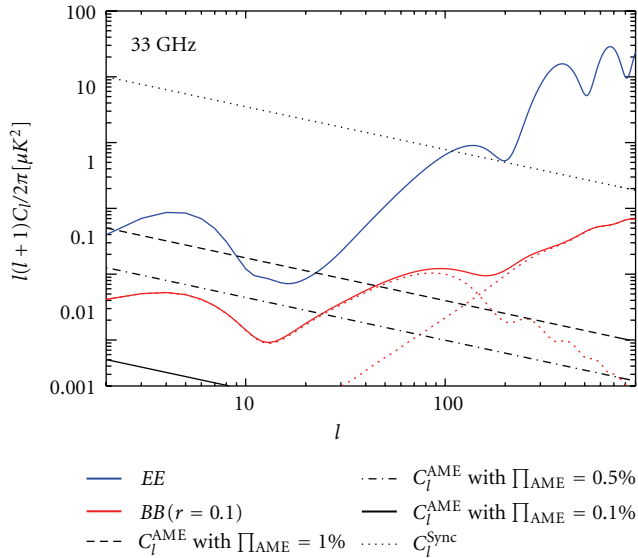


FIGURE 8: Contribution of the polarised AME to the (E and B) angular power spectrum at 33 GHz. The solid *blue* and *red* lines correspond to the CMB polarisation spectrum of E-modes and B-modes for the WMAP-7 cosmology [103] and assuming a tensor-to-scalar ratio of $r = 0.1$. Note that for the B-mode spectrum, the primordial tensor and lensing contributions are also plotted separately. The polarised AME power spectra (C_l^{AME}), for fractional polarisations Π_{AME} equal to 1.0%, 0.5% and 0.1%, are shown as dashed, dotted-dashed, and dotted-dotted-dashed lines, respectively. For comparison, the synchrotron contribution at this frequency is also shown as a black dotted line.

its emission is still larger than the B-mode power spectra for $r = 0.1$ at large angular scales ($l \lesssim 60$ and $\lesssim 30$ for $\Pi = 1.0\%$ and $\Pi = 0.5\%$, resp.). Therefore, and based on existing observational constraints, a polarised diffuse AME component could in principle have an impact on the detectability of primordial B-modes at 33 GHz and at angular scales ($l \lesssim 100$).

Future experiments, like QUIJOTE-CMB [95], will provide very sensitive measurements of the AME polarisation at several frequency channels in the range 10–40 GHz, reaching the required sensitivities to detect a polarisation level of $\Pi = 0.1\%$, in Galactic regions as those discussed in this paper, after a few hours integration time [102].

Acknowledgments

Some of the results in this paper have been derived using the *HEALPix* [46] package. The authors acknowledge the use of the Legacy Archive for Microwave Background Data Analysis (LAMBDA). Support for LAMBDA is provided by the NASA Office of Space Science. J. A. Rubiño-Martín is a Ramón y Cajal Fellow of the Spanish Ministry of Economy and Competitiveness (MINECO). This work has been partially funded by the MINECO under the project AYA2010-21766-C03-02, and the Consolider-Ingenio project CSD2010-00064 (EPI: Exploring the Physics of Inflation).

References

- [1] A. Kogut and G. Hinshaw, “Monte Carlo simulations of medium-scale cosmic microwave background anisotropy,” *The Astrophysical Journal Letters*, vol. 464, no. 1, pp. L39–L41, 1996.
- [2] E. M. Leitch, A. C. S. Readhead, T. J. Pearson, and S. T. Myers, “An anomalous component of galactic emission,” *The Astrophysical Journal Letters*, vol. 486, no. 1, pp. L23–L26, 1997.
- [3] A. de Oliveira-Costa, A. Kogut, M. J. Devlin, C. B. Netterfield, L. A. Page, and E. J. Wollack, “Galactic microwave emission at degree angular scales,” *The Astrophysical Journal Letters*, vol. 482, no. 1, pp. L17–L20, 1997.
- [4] A. de Oliveira-Costa, M. J. Devlin, T. Herbig et al., “Mapping the cosmic microwave background anisotropy: combined analysis of QMAP flights,” *The Astrophysical Journal Letters*, vol. 509, no. 2, pp. L77–L80, 1998.
- [5] P. Mukherjee, K. Coble, M. Dragovan et al., “Galactic foreground constraints from the Python V cosmic microwave background anisotropy data,” *The Astrophysical Journal*, vol. 592, no. 2, pp. 692–698, 2003.
- [6] A. de Oliveira-Costa, M. Tegmark, C. M. Gutiérrez et al., “Cross-correlation of tenerife data with galactic templates—evidence for spinning dust?” *The Astrophysical Journal Letters*, vol. 527, no. 1, pp. L9–L12, 1999.
- [7] A. de Oliveira-Costa, M. Tegmark, R. D. Davies et al., “The quest for microwave foreground X,” *The Astrophysical Journal Letters*, vol. 606, no. 2, pp. L89–L92, 2004.
- [8] D. P. Finkbeiner, D. J. Schlegel, C. Frank, and C. Heiles, “Tentative detection of electric dipole emission from rapidly rotating dust grains,” *The Astrophysical Journal Letters*, vol. 566, no. 2, pp. 898–904, 2002.
- [9] D. P. Finkbeiner, G. I. Langston, and A. H. Minter, “Microwave interstellar medium emission in the green bank galactic plane survey: evidence for spinning dust,” *The Astrophysical Journal*, vol. 617, no. 1, pp. 350–359, 2004.
- [10] B. S. Mason, T. Robishaw, C. Heiles, D. Finkbeiner, and C. Dickinson, “A limit on the polarized anomalous microwave emission of lynds 1622,” *The Astrophysical Journal Letters*, vol. 697, no. 2, pp. 1187–1193, 2009.
- [11] S. R. Hildebrandt, R. Rebolo, J. A. Rubiño-Martín et al., “COSMOSOMAS observations of the cosmic microwave background and Galactic foregrounds at 11 GHz: evidence for anomalous microwave emission at high Galactic latitude,” *Monthly Notices of the Royal Astronomical Society*, vol. 382, no. 2, pp. 594–608, 2007.
- [12] R. D. Davies, C. Dickinson, A. J. Banday, T. R. Jaffe, K. M. Górski, and R. J. Davis, “A determination of the spectra of Galactic components observed by the Wilkinson microwave anisotropy probe,” *Monthly Notices of the Royal Astronomical Society*, vol. 370, no. 3, pp. 1125–1139, 2006.
- [13] L. Page, G. Hinshaw, E. Komatsu et al., “Three-year Wilkinson microwave anisotropy probe (WMAP) observations: polarization analysis,” *The Astrophysical Journal, Supplement Series*, vol. 170, no. 2, pp. 335–376, 2007.
- [14] M. A. Miville-Deschênes, N. Ysard, A. Lavabre et al., “Separation of anomalous and synchrotron emissions using WMAP polarization data,” *Astronomy & Astrophysics*, vol. 490, no. 3, pp. 1093–1102, 2008.
- [15] N. Ysard, M. A. Miville-Deschênes, and L. Verstraete, “Probing the origin of the microwave anomalous foreground,” *Astronomy & Astrophysics*, vol. 509, no. 1, article L1, 2010.
- [16] N. Macellari, E. Pierpaoli, C. Dickinson, and J. E. Vaillancourt, “Galactic foreground contributions to the 5-year

- Wilkinson microwave anisotropy probe maps,” *Monthly Notices of the Royal Astronomical Society*, vol. 418, no. 2, pp. 888–905, 2011.
- [17] T. Ghosh, A. J. Banday, T. Jaffe et al., “Foreground analysis using cross-correlations of external templates on the 7-year Wilkinson microwave anisotropy probe data,” *Monthly Notices of the Royal Astronomical Society*, vol. 422, no. 4, pp. 3617–3642, 2012.
- [18] P. A. R. Ade, N. Aghanim, M. Arnaud et al., “Planck early results. XX. New light on anomalous microwave emission from spinning dust grains,” *Astronomy & Astrophysics*, vol. 536, article A20, 17 pages, 2011.
- [19] A. Abergel, P. A. R. Ade, N. Aghanim et al., “Planck early results. XXI. Properties of the interstellar medium in the galactic plane,” *Astronomy & Astrophysics*, vol. 536, article A21, 18 pages, 2011.
- [20] R. A. Watson, R. Rebolo, J. A. Rubiño-Martín et al., “Detection of anomalous microwave emission in the Perseus molecular cloud with the COSMOSOMAS experiment,” *The Astrophysical Journal Letters*, vol. 624, no. 2, pp. L89–L92, 2005.
- [21] R. Génova-Santos, R. Rebolo, J. A. Rubiño-Martín, C. H. López-Caraballo, and S. R. Hildebrandt, “Detection of anomalous microwave emission in the pleiades reflection Nebula with Wilkinson microwave anisotropy probe and the COSMOSOMAS Experiment,” *The Astrophysical Journal*, vol. 743, no. 1, article 67, 2011.
- [22] S. Casassus, G. F. Cabrera, F. Förster, T. J. Pearson, A. C. S. Readhead, and C. Dickinson, “Morphological analysis of the centimeter-wave continuum in the dark cloud LDN 1622,” *The Astrophysical Journal*, vol. 639, no. 2, pp. 951–964, 2006.
- [23] C. Dickinson, S. Casassus, J. L. Pineda, T. J. Pearson, A. C. S. Readhead, and R. D. Davies, “An upper limit on anomalous dust emission at 31 GHz in the diffuse cloud [LPH96] 201.663+1.643,” *The Astrophysical Journal Letters*, vol. 643, no. 2, pp. L111–L114, 2006.
- [24] S. Casassus, C. Dickinson, K. Cleary et al., “Centimetre-wave continuum radiation from the ρ Ophiuchi molecular cloud,” *Monthly Notices of the Royal Astronomical Society*, vol. 391, no. 3, pp. 1075–1090, 2008.
- [25] A. M. M. Scaife, N. Hurley-Walker, M. L. Davies et al., “AMI limits on 15-GHz excess emission in northern H II regions,” *Monthly Notices of the Royal Astronomical Society*, vol. 385, no. 2, pp. 809–822, 2008.
- [26] A. M. M. Scaife, N. Hurley-Walker, D. A. Green et al., “AMI observations of Lynds dark nebulae: further evidence for anomalous cm-wave emission,” *Monthly Notices of the Royal Astronomical Society*, vol. 400, no. 3, pp. 1394–1412, 2009.
- [27] A. M. M. Scaife, D. A. Green, G. G. Pooley et al., “High-resolution AMI large array imaging of spinning dust sources: spatially correlated $8\ \mu\text{m}$ emission and evidence of a stellar wind in L675,” *Monthly Notices of the Royal Astronomical Society*, vol. 403, no. 1, pp. L46–L50, 2010.
- [28] A. Scaife, D. A. Green, R. A. Battye et al., “Constraints on spinning dust towards Galactic targets with the very small array: a tentative detection of excess microwave emission towards 3C396,” *Monthly Notices of the Royal Astronomical Society*, vol. 377, no. 1, pp. L69–L73, 2007.
- [29] C. T. Tibbs, R. A. Watson, C. Dickinson et al., “Very small array observations of the anomalous microwave emission in the Perseus region,” *Monthly Notices of the Royal Astronomical Society*, vol. 402, no. 3, pp. 1969–1979, 2010.
- [30] T. A. Semenova, Y. N. Pariiskii, and N. N. Bursov, “The ‘X component’ of the radio background,” *Astronomy Reports*, vol. 53, no. 1, pp. 1–8, 2009.
- [31] M. Lu, J. Dunkley, and L. Page, “Evidence for anomalous dust-correlated emission at 8 GHz,” *The Astrophysical Journal*, vol. 749, no. 2, article 165, 2012.
- [32] A. M. M. Scaife, B. Nikolic, D. A. Green et al., “Microwave observations of spinning dust emission in NGC 6946,” *Monthly Notices of the Royal Astronomical Society*, vol. 406, no. 1, pp. L45–L49, 2010.
- [33] P. A. R. Ade, N. Aghanim, M. Arnaud et al., “Planck early results. XVII. Origin of the submillimetre excess dust emission in the magellanic clouds,” *Astronomy & Astrophysics*, vol. 536, article A17, 17 pages, 2011.
- [34] B. T. Draine and A. Lazarian, “Electric dipole radiation from spinning dust grains,” *The Astrophysical Journal Letters*, vol. 508, no. 1, pp. 157–179, 1998.
- [35] S. Iglesias-Groth, “Hydrogenated fullerenes and the anomalous microwave emission of the dark cloud LDN 1622,” *Monthly Notices of the Royal Astronomical Society*, vol. 368, no. 4, pp. 1925–1930, 2006.
- [36] C. Dickinson, R. D. Davies, L. Bronfman et al., “CBI limits on 31 GHz excess emission in southern H II regions,” *Monthly Notices of the Royal Astronomical Society*, vol. 379, no. 1, pp. 297–307, 2007.
- [37] B. T. Draine and A. Lazarian, “Magnetic dipole microwave emission from dust grains,” *The Astrophysical Journal Letters*, vol. 512, no. 2, pp. 740–754, 1999.
- [38] A. Lazarian and B. T. Draine, “Resonance paramagnetic relaxation and alignment of small grains,” *The Astrophysical Journal*, vol. 536, no. 1, pp. L15–L18, 2000.
- [39] Y. Ali-Haïmoud, C. M. Hirata, and C. Dickinson, “A refined model for spinning dust radiation,” *Monthly Notices of the Royal Astronomical Society*, vol. 395, no. 2, pp. 1055–1078, 2009.
- [40] T. Hoang, A. Lazarian, and B. T. Draine, “Spinning dust emission: effects of irregular grain shape, transient heating, and comparison with Wilkinson microwave anisotropy probe results,” *The Astrophysical Journal*, vol. 741, no. 2, article 87, 2011.
- [41] K. Silsbee, Y. Ali-Haïmoud, and C. M. Hirata, “Spinning dust emission: the effect of rotation around a non-principal axis,” *Monthly Notices of the Royal Astronomical Society*, vol. 411, no. 4, pp. 2750–2769, 2011.
- [42] T. Draine and B. Hensley, “Magnetic nanoparticles in the interstellar medium: emission spectrum and polarization,” . In press, <http://arxiv.org/abs/1205.7021>.
- [43] J. Bock, S. Church, M. Devlin et al., “Task force on cosmic microwave background research,” *ArXiv Astrophysics e-prints*. In press, <http://arxiv.org/abs/astro-ph/0604101>.
- [44] J. A. Peacock and P. Schneider, “ESA-ESO Working Group on ‘Fundamental Cosmology,’” Tech. Rep., ESA-ESO Working Group, 2006.
- [45] S. Chandrasekhar, *Radiative Transfer*, Dover, New York, NY, USA, 1960.
- [46] M. Górski, E. Hivon, A. J. Banday et al., “HEALPix: a framework for high-resolution discretization and fast analysis of data distributed on the sphere,” *The Astrophysical Journal*, vol. 622, no. 2 I, pp. 759–771, 2005.
- [47] C. Hernández-Montegudo and J. A. Rubiño-Martín, “On the presence of thermal Sunyaev-Zel’dovich induced signal in the first-year WMAP temperature maps,” *Monthly Notices of the Royal Astronomical Society*, vol. 347, no. 2, pp. 403–410, 2004.
- [48] C. H. López-Caraballo, J. A. Rubiño-Martín, R. Rebolo, and R. Génova-Santos, “Constraints on the polarization of the

- anomalous microwave emission in the perseus molecular complex from seven-year wmap data,” *The Astrophysical Journal Letters*, vol. 729, no. 1, article 25, 2011.
- [49] C. Dickinson, M. Peel, and M. Vidal, “New constraints on the polarization of anomalous microwave emission in nearby molecular clouds,” *Monthly Notices of the Royal Astronomical Society*, vol. 418, no. 1, pp. L35–L39, 2011.
- [50] D. Herranz and P. Vielva, “Cosmic microwave background images,” *IEEE Signal Processing Magazine*, vol. 27, no. 1, pp. 67–75, 2010.
- [51] E. Bertinl and S. Arnouts, “SExtractor: software for source extraction,” *Astronomy & Astrophysics, Supplement Series*, vol. 117, no. 2, pp. 393–404, 1996.
- [52] P. Carvalho, G. Rocha, and M. P. Hobson, “A fast Bayesian approach to discrete object detection in astronomical data sets—PowellSnakes I,” *Monthly Notices of the Royal Astronomical Society*, vol. 393, no. 3, pp. 681–702, 2009.
- [53] S. Mitra, G. Rocha, K. M. Górski et al., “Fast pixel space convolution for cosmic microwave background surveys with asymmetric beams and complex scan strategies: FEBeCoP,” *The Astrophysical Journal, Supplement Series*, vol. 193, no. 1, article 5, 2011.
- [54] M. Tegmark and A. de Oliveira-Costa, “Removing point sources from cosmic microwave background maps,” *The Astrophysical Journal*, vol. 500, no. 2, pp. L83–L86, 1998.
- [55] D. Herranz, M. López-Cañiego, J. L. Sanz, and J. González-Nuevo, “A novel multifrequency technique for the detection of point sources in cosmic microwave background maps,” *Monthly Notices of the Royal Astronomical Society*, vol. 394, no. 1, pp. 510–520, 2009.
- [56] L. F. Lanz, D. Herranz, J. L. Sanz, J. González-Nuevo, and M. López-Cañiego, “A multifrequency method based on the matched multifilter for the detection of point sources in CMB maps,” *Monthly Notices of the Royal Astronomical Society*, vol. 403, no. 4, pp. 2120–2130, 2010.
- [57] L. Cayón, J. L. Sanz, R. B. Barreiro et al., “Isotropic wavelets: a powerful tool to extract point sources from cosmic microwave background maps,” *Monthly Notices of the Royal Astronomical Society*, vol. 315, no. 4, pp. 757–761, 2000.
- [58] P. Vielva, E. Martínez-González, J. E. Gallegos, L. Toffolatti, and J. L. Sanz, “Point source detection using the spherical Mexican hat wavelet on simulated all-sky Planck maps,” *Monthly Notices of the Royal Astronomical Society*, vol. 344, no. 1, pp. 89–104, 2003.
- [59] M. López-Cañiego and P. Vielva, “Biparametric adaptive filter: detection of compact sources in complex microwave backgrounds,” *Monthly Notices of the Royal Astronomical Society*, vol. 421, pp. 2139–2154, 2012.
- [60] M. López-Cañiego, M. Massardi, J. Gonzalez-Nuevo et al., “Polarization of the wmap point sources,” *The Astrophysical Journal Letters*, vol. 705, no. 1, pp. 868–876, 2009.
- [61] S. O. Rice, “Mathematical analysis of random noise-conclusion,” *Bell System Technical Journal*, vol. 24, pp. 46–156, 1945.
- [62] J. F. L. Simmons and B. G. Stewart, “Point and interval estimation of the true unbiased degree of linear polarization in the presence of low signal-to-noise ratios,” *Astronomy & Astrophysics*, vol. 142, no. 1, pp. 100–106, 1985.
- [63] J. E. Vaillancourt, “Placing confidence limits on polarization measurements,” *Publications of the Astronomical Society of the Pacific*, vol. 118, no. 847, pp. 1340–1343, 2006.
- [64] M. Abramowitz and I. A. Stegun, *Handbook of Mathematical Functions*, 1972.
- [65] E. S. Battistelli, R. Rebolo, J. A. Rubiño-Martín et al., “Polarization observations of the anomalous microwave emission in the Perseus molecular complex with the cosmosomas experiment,” *The Astrophysical Journal Letters*, vol. 645, no. 2, pp. L141–L144, 2006.
- [66] S. Casassus, L. Å. Nyman, C. Dickinson, and T. J. Pearson, “A centimetre-wave excess over free-free emission in planetary nebulae,” *Monthly Notices of the Royal Astronomical Society*, vol. 382, no. 4, pp. 1607–1622, 2007.
- [67] A. Kogut, J. Dunkley, C. L. Bennett et al., “Three-year Wilkinson microwave anisotropy probe (WMAP) observations: foreground polarization,” *The Astrophysical Journal*, vol. 665, no. 1, pp. 355–362, 2007.
- [68] J. Cernicharo, R. Bachiller, and G. Duvert, “The Taurus-Auriga-Perseus complex of dark clouds. I—density structure,” *Astronomy & Astrophysics*, vol. 149, no. 2, pp. 273–282, 1985.
- [69] B. G. Andersson, P. G. Wannier, G. H. Moriarty-Schieven, and E. J. Bakker, “The nature of the IRAS ring G159.6-18.5 in Perseus and its exciting star HD 278942,” *Astronomical Journal*, vol. 119, no. 3, pp. 1325–1338, 2000.
- [70] N. A. Ridge, S. L. Schnee, A. A. Goodman, and J. B. Foster, “The complete nature of the warm dust shell in perseus,” *The Astrophysical Journal*, vol. 643, no. 2, pp. 932–944, 2006.
- [71] J. E. Gallegos, J. F. Macías-Pérez, C. M. Gutiérrez et al., “COSMOSOMAS: a circular scanning instrument to map the sky at centimetric wavelengths,” *Monthly Notices of the Royal Astronomical Society*, vol. 327, no. 4, pp. 1178–1186, 2001.
- [72] W. Reich and P. Reich, “Measuring and calibrating galactic synchrotron emission,” in *Proceedings of the International Astronomical Union on Cosmic Magnetic Fields: From Planets, to Stars and Galaxies*, vol. 259 of *IAU Symposium*, pp. 603–612, 2009.
- [73] P. J. Encrenaz, “A new source of intense molecular emission in the Rho Ophiuchi complex,” *The Astrophysical Journal*, vol. 189, pp. L135–L136, 1974.
- [74] C. A. Kulesa, A. L. Hungerford, C. K. Walker, X. Zhang, and A. P. Lane, “Large-scale CO and [C I] emission in the ρ ophiuchi molecular cloud,” *The Astrophysical Journal*, vol. 625, no. 1 I, pp. 194–209, 2005.
- [75] K. E. Young, M. L. Enoch, N. J. Evans et al., “Bolocam survey for 1.1 mm dust continuum emission in the c2d legacy clouds. II. Ophiuchus,” *The Astrophysical Journal*, vol. 644, no. 1, pp. 326–343, 2006.
- [76] M. A. C. Perryman, L. Lindegren, J. Kovalevsky et al., “The HIPPARCOS catalogue,” *Astronomy & Astrophysics*, vol. 323, no. 1, pp. L49–L52, 1997.
- [77] B. A. Wilson, T. M. Dame, M. R. W. Mashed, and P. Thaddeus, “A uniform CO survey of the molecular clouds in Orion and Monoceros,” *Astronomy & Astrophysics*, vol. 430, no. 2, pp. 523–539, 2005.
- [78] R. J. Maddalena, M. Morris, J. Moscowitz, and P. Thaddeus, “The large system of molecular clouds in Orion and Monoceros,” *The Astrophysical Journal*, vol. 303, pp. 375–391, 1986.
- [79] F. van Leeuwen, “HIPPARCOS distance calibrations for 9 open clusters,” *Astronomy & Astrophysics*, vol. 341, no. 3, pp. L71–L74, 1999.
- [80] C. Dickinson, R. D. Davies, and R. J. Davis, “Towards a free-free template for CMB foregrounds,” *Monthly Notices of the Royal Astronomical Society*, vol. 341, no. 2, pp. 369–384, 2003.
- [81] B. T. Draine, *Physics of the Interstellar and Intergalactic Medium*, Princeton University Press, Princeton, NJ, USA, 2011.

- [82] F. J. Lockman, D. J. Pisano, and G. J. Howard, "Detection of 130 "diffuse" galactic H II regions," *The Astrophysical Journal Letters*, vol. 472, no. 1, pp. 173–182, 1996.
- [83] H. C. Harris, C. C. Dahn, D. G. Monet, and J. R. Pier, "Trigonometric parallaxes of Planetary Nebulae (invited review)," in *Planetary Nebulae*, H. J. Habing and H. J. G. L. M. Lamers, Eds., vol. 180 of *IAU Symposium*, p. 40, 1997.
- [84] A. K. Speck, M. Meixner, D. Fong, P. R. McCullough, D. E. Moser, and T. Ueta, "Large-scale extended emission around the Helix Nebula," in *Planetary Nebulae: Their Evolution and Role in the Universe*, S. Kwok, M. Dopita, and R. Sutherland, Eds., vol. 209 of *IAU Symposium*, p. 316, 2003.
- [85] S. Casassus, A. C. S. Readhead, T. J. Pearson, L. Å. Nyman, M. C. Shepherd, and L. Bronfman, "Anomalous radio emission from dust in the Helix," *The Astrophysical Journal*, vol. 603, no. 2, pp. 599–610, 2004.
- [86] N. Jarosik, C. L. Bennett, J. Dunkley et al., "Seven-year Wilkinson microwave anisotropy probe (WMAP*) observations: sky maps, systematic errors, and basic results," *The Astrophysical Journal, Supplement Series*, vol. 192, no. 2, article 14, 2011.
- [87] J. C. Mather, D. J. Fixsen, R. A. Shafer, C. Mosier, and D. T. Wilkinson, "Calibrator design for the COBE far infrared absolute spectrophotometer (FIRAS)," *The Astrophysical Journal Letters*, vol. 512, no. 2, pp. 511–520, 1999.
- [88] C. G. T. Haslam, C. J. Salter, H. Stoffel, and W. E. Wilson, "A 408 MHz all-sky continuum survey. II—the atlas of contour maps," *Astronomy & Astrophysics, Supplement Series*, vol. 47, pp. 1–143, 1982.
- [89] E. M. Berkhuijsen, "A survey of the continuum radiation at 820 MHz between declinations -7 deg and $+85$ deg. I. Observations and reductions," *Astronomy & Astrophysics, Supplement Series*, vol. 5, p. 263, 1972.
- [90] P. Reich and W. Reich, "A radio continuum survey of the Northern sky at 1420 MHz. II," *Astronomy & Astrophysics, Supplement Series*, vol. 63, no. 2, pp. 205–288, 1986.
- [91] M. G. Hauser, R. G. Arendt, T. Kelsall et al., "The COBE diffuse infrared background experiment search for the cosmic infrared background. I. Limits and detections," *The Astrophysical Journal Letters*, vol. 508, no. 1, pp. 25–43, 1998.
- [92] A. G. Polnarev, "Polarization and anisotropy induced in the microwave background by cosmological gravitational waves," *Soviet Astronomy*, vol. 29, no. 6, article 607, 1985.
- [93] M. Kamionkowski, A. Kosowsky, and A. Stebbins, "Statistics of cosmic microwave background polarization," *Physical Review D*, vol. 55, no. 12, pp. 7368–7388, 1997.
- [94] M. Zaldarriaga and U. Seljak, "All-sky analysis of polarization in the microwave background," *Physical Review D*, vol. 55, no. 4, pp. 1830–1840, 1997.
- [95] J. A. Rubiño-Martín, R. Rebolo, M. Tucci et al., "The QUIJOTE CMB experiment," in *Highlights of Spanish Astrophysics V*, J. M. Diego, L. J. Goicoechea, J. I. González-Serrano, and J. Gorgas, Eds., p. 127, 2010.
- [96] K. Arnold, P. A. R. Ade, A. E. Anthony et al., "The POLARBEAR CMB polarization experiment," in *5th Millimeter, Submillimeter, and Far-Infrared Detectors and Instrumentation for Astronomy*, vol. 7741 of *Proceedings of SPIE*, July 2010.
- [97] B. Reichborn-Kjennerud, A. M. Aboobaker, P. Ade et al., "EBEX: a balloon-borne CMB polarization experiment," in *5th Millimeter, Submillimeter, and Far-Infrared Detectors and Instrumentation for Astronomy*, vol. 7741 of *Proceedings of SPIE*, San Diego, Calif, USA, July 2010.
- [98] J. Aguirre, A. Amblard, A. Ashoorioon et al., "Observing the evolution of the universe," In press, <http://arxiv.org/abs/0903.0902>.
- [99] C. Armitage-Caplan, M. Avillez, D. Barbosa et al., "CORe (Cosmic Origins Explorer) a whitepaper," In press, <http://arxiv.org/abs/1102.2181>.
- [100] M. Tucci, E. Martínez-González, P. Vielva, and J. Delabrouille, "Limits on the detectability of the CMB B-mode polarization imposed by foregrounds," *Monthly Notices of the Royal Astronomical Society*, vol. 360, no. 3, pp. 935–949, 2005.
- [101] B. Gold, N. Odegard, J. L. Weiland et al., "Seven-year wilkinson microwave anisotropy probe (WMAP*) observations: galactic foreground emission," *The Astrophysical Journal, Supplement Series*, vol. 192, no. 2, article 15, 2011.
- [102] J. A. Rubiño-Martín, R. Rebolo, M. Aguiar et al., "The QUIJOTE-CMB experiment: studying the polarisation of the Galactic and cosmological microwave emissions," in *4th Ground-Based and Airborne Telescopes*, vol. 8444 of *Proceedings of SPIE*, Amsterdam, the Netherlands, August 2012.
- [103] D. Larson, J. Dunkley, G. Hinshaw et al., "Seven-year wilkinson microwave anisotropy probe (WMAP*) observations: power spectra and WMAP-derived parameters," *The Astrophysical Journal, Supplement Series*, vol. 192, no. 2, article 16, 2011.